Non-Hermitian and Topological Features of Photonic Systems
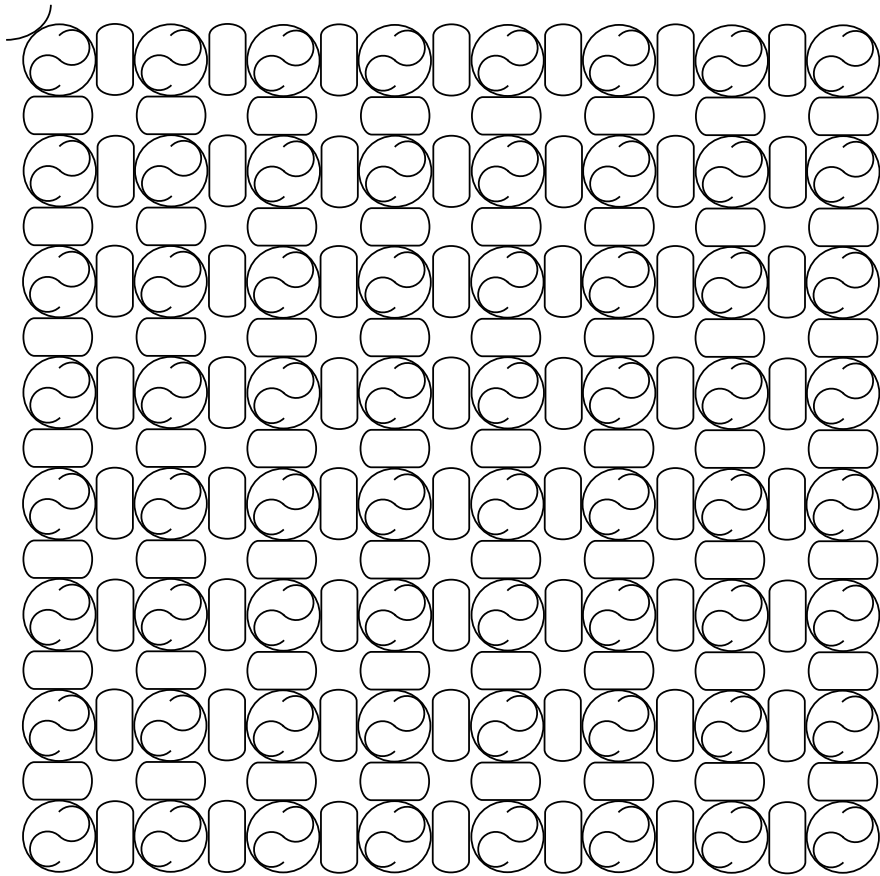
Alberto Muñoz de las Heras

Non-Hermitian and Topological Features of Photonic Systems

Alberto Muñoz de las Heras

A dissertation submitted to the
Dipartimento di Fisica
Università degli Studi di Trento

In fulfilment of the requirements for the Degree of
Philosophiæ Doctor in Physics

Under the Supervision of
Dr. Iacopo Carusotto

Dottorato di Ricerca XXXIV Ciclo
December 15th, 2021

Supervisor:

Dr. Iacopo Carusotto

Co-supervisor:

Prof. Lorenzo Pavesi

Members of the committee:

Prof. Stefano Azzini - Università di Trento

Prof. Alberto Amo García - Université de Lille

Prof. Stefan Rotter - TU Wien

Para mis abuelos, Francisco y María.

Acknowledgements

$\mathbb{I}$ cannot start this section without expressing my greatest gratitude to my supervisor, Iacopo Carusotto. He is not only one of the most talented physicists I have ever met, but also an extraordinary person capable of immediately transmitting his enthusiasm for both physics and life. Without his patient and wise guidance I would not have been able to complete this Thesis.

I am also indebted to my co-supervisor Lorenzo Pavesi and my colleagues Riccardo Franchi and Stefano Biasi from the Nanoscience Laboratory of the University of Trento, as well as to Mher Ghulinyan from Fondazione Bruno Kessler. Although directly working with experimentalists was one of the biggest challenges of the past years, I learned quite a lot from them. This Thesis owes very much to the insight and advice of Prof. Pavesi. Also, it has been a pleasure to collaborate with Franchi and Biasi: they are really talented scientists and I am sure they will have a bright future whatever path they decide to follow.

The members of the BEC Center also deserve my kindest works. Although the pandemic restrictions limited the opportunities to gather together, discussing physics with them has always been both challenging and thrilling. Many thanks to Franco Dalfovo, Gabriele Ferrari, Stefano Giorgini, Philipp Hauke, Giacomo Lamporesi, Chiara Menotti, Lev Pitaevskii, Gianluca Rastelli, Alessio Recati, Matteo Rizzi, Sandro Stringari, Daniele De Bernardis, and Alessandro Zenesini. I feel so proud to say that I wrote my Thesis in such an important group. Last, but not least, I am also grateful to the person without none of this could even exist: the CNR administrative, Beatrice Ricci!

I am also glad to have gone through this experience with such wonderful people by my side: the Quantum at Trento PhD students Louise Wolswijk, Matteo Sighinolfi, Francesco Turro, and (already PhD) Santo Roccuzzo. I am also deeply grateful to the people working with Iacopo for all the physics discussions —and not only!— and good times shared: Francesco Piccioli, Alberto Nardin, Anna Berti, Matteo Seclì, Fabio Caleffi, Onur Umucalilar, Aurelian Loirette-Pelous, and especially to my office mates Elia Macaluso, Ivan Amelio, and Luca Giacomelli, which have also played the role of advisors quite often.

The administrative staff of the PhD in Physics also deserves credit for all our accomplishments, in particular Lucia Appoloni and Micaela Paoli.

I am grateful to have encountered a big group of Spanish people at Trento. Many of them have become very close friends with whom I shared my most enjoyable and —most importantly— difficult moments in this city. In particular, I wish to express my deepest gratitude and friendship to Ana Bejarano, Estefanía Coronado, Gabriel Cebrián, Raúl Bombín, Albert Gallemí, and Rocío Sáez.

The next lines are devoted to my family, in Spanish.

Por último, quiero aprovechar estas últimas líneas para agradecer a mi familia todo el apoyo que me han brindado a lo largo de estos años. Aunque lejos, mi corazón ha estado con ellos en todo momento. No puedo dejar de mencionar a mis abuelos, Josefa y Antonio, de quienes no he podido disfrutar tanto como me hubiera gustado; y sobre todo a mis padres: a ellos les debo haberme convertido en la persona que soy. Les estaré eternamente agradecido por todo lo que me han dado, especialmente por su infinita paciencia y por su amor, apoyo y confianza incondicionales.

Gracias.

Contents

Contents

Introduction

Topology is the branch of mathematics that studies those properties of geometrical objects that remain unaltered under continuous deformations, such as stretching or twisting. This already tells us something very special about this field: it is not concerned with the particular details of a certain object at a local level, but rather with non-local properties known as topological invariants which cannot be changed unless we tear or glue different parts of the object.

Such ideas found an unexpected spin-off in condensed matter physics when the quantization of the Hall resistance occurring in a two-dimensional electron gas subjected to a strong magnetic field was discovered [1]. This phenomenon, part of the so-called integer quantum Hall effect, is a consequence of time-reversal symmetry breaking, which leads to the nontrivial geometrical properties of the quantum wavefunctions [2] associated to the resulting energy spectrum. This is quantized in a set of Landau levels [3], each characterized by a topological invariant known as Chern number whose value cannot be changed unless the gaps separating the levels are closed. Another remarkable consequence of the topological invariant character of the Chern number is the existence of topological insulators [4]. These materials feature fully-occupied energy bands with non-zero Chern numbers. As a result, they exhibit an insulating bulk while simultaneously hosting conducting states at their surface which propagate in a well-defined direction and are protected against local disorder and perturbations by time-reversal symmetry breaking.

Afterwards it was found that such topological phases of matter arise in a variety of quantum (and even classical! [5, 6]) systems. In particular, the development of quantum simulators such as cold atomic gases and photonic systems opened promising perspectives for a deeper understanding of such physics. The main advantage of these platforms is that they offer a larger degree of experimental control over the parameters of the Hamiltonian one wishes to implement, as well as the possibility of employing measurement techniques not available for solid state samples.

In particular, topological photonics aims at exploring topological phases of matter using optical setups [7]. On the one hand, photons pose their own challenges which have no analog in other platforms: they are bosons, massless, do not carry electrical charge, do not interact between each other, and possess an intrinsic driven-dissipative nature. However, on the other hand, these unique features allow to investigate new physics that would be impossible to explore in traditional conservative setups. Moreover, optical systems offer several advantages, like the possibility of directly accessing the system's properties by means of the emission spectrum or to probe specific parts of the system. Since the existence of energy bands is a ubiquitous property of waves inside spatially periodic media, band theory can be applied to photonic crystals realized by subjecting electromagnetic waves to spatially periodic modulations of the electric susceptibility tensor [8, 9].

Several strategies have been employed to obtain a topologically nontrivial band structure in photonic crystals. Perhaps the most straightforward one capitalizes on magneto-optic materials breaking time-reversal symmetry under an external magnetic field [10]. However, magnetic elements are difficult to integrate with state-of-the-art silicon photonics technology. A non-magnetic

1

alternative is posed by quantum spin-Hall insulators: These consist on two copies of a topological insulator, each supporting photons that experience an opposite synthetic magnetic field and therefore display opposite Chern numbers. These are the two pseudospins of the system. For bosonic particles such as photons the absence of coupling between the two pseudospins is required in order to preserve time-reversal symmetry and grant topological protection to the resulting helical modes propagating in the surface. For this reason the experimental realization of bosonic quantum spin-Hall insulators posed a more challenging problem. However, such a system was successfully implemented in a two-dimensional array of silicon ring resonators supporting a pair of whispering-gallery modes circulating in clockwise (CW) and counterclockwise (CCW) directions, which constitute the two pseudospins. These resonators are connected through link resonators introducing opposite complex hopping phases for the two pseudospins, therefore giving rise to opposite synthetic gauge fields for counterpropagating photons [11]. In such a platform disorder and fabrication defects give rise to backscattering coupling the two pseudospins; remarkably, this was sufficiently small to preserve the existence of the helical modes.

The study of topologically nontrivial band structures in systems with gain and losses led to the development of the non-Hermitian topological photonics field. A particularly interesting problem concerns the addition of saturable gain to the chiral edge modes of a topological insulator. These topological lasers have been shown to display several advantages with respect to their trivial counterparts, such as absence of light localization at defects, single-mode lasing, and enhanced slope efficiency [12]. Recently, the active analog [13] of the quantum-spin Hall insulator of Ref. [11] was experimentally demonstrated. However, the existence of this system relies on the presence of a sufficiently weak backscattering as a consequence of well-established fabrication process that do not introduce disorder into the samples, and needs to be robust against operational degradation of the array. To address these concerns, the authors of [13] also implemented a different strategy: promoting lasing in a single pseudospin. This was achieved by employing Taiji resonators (TJRs) as the building block of the quantum spin-Hall array. TJRs consist of a ring resonator embedding an S-shaped element that breaks space-reversal (parity) symmetry as it establishes a unidirectional coupling between the two pseudospins. Such resonators have been extensively employed to obtain unidirectional lasing in a single whispering-gallery mode [14].

Notwithstanding the proved importance of TJRs in the realization of quantum spin-Hall topological lasers, a theoretical description of the physical mechanisms behind single-pseudospin lasing is needed. In fact, the use of TJRs opens up exciting connections with Lorentz reciprocity breaking and optical isolators [15] in which light propagates in a single direction. Besides, the robustness of the resulting helical modes under different levels of backscattering must be assessed. Motivated by these open questions, the first part of this Thesis (Chapters 1 to 5) is devoted to explore the physics of nonlinear TJRs and their use as optical isolators and unidirectional lasers. We finally ascertain their role in quantum spin-Hall insulators in the presence of backscattering in Chapter 5.

Up to this point, strong interactions have been out of the discussion. However, a whole new set of topological phases appear when these are considered. In the case of systems with broken time-reversal symmetry we enter the so-called fractional quantum Hall (FQH) regime. Perhaps one of the most remarkable predictions is that the charged bulk excitations of such a system feature a fraction of the elementary charge and intermediate (fractional) statistics between bosons and fermions. Such objects are known as anyons and they are expected to play a crucial role in the development of fault-tolerant topological quantum computers immune to local perturbations and disorder. In spite of this great incentive, a direct experimental demonstration of fractional statistics remains elusive to date, partially due to the difficulty to perform interferometry experiments in two-dimensional electron gases. However, quantum simulators can provide alternative strategies in order to shine more light into the exotic nature of FQH liquids. In the second part of this Thesis (Chapters 6 and 7) we explore in detail the physics of FQH liquids and propose a scheme to experimentally access the fractional charge and statistics of anyons using cold atomic gases and photonic systems. In particular, our calculations are focused on the former platform due to the well-established and conceptually easier techniques employed to generate synthetic gauge fields and strong interactions for cold atoms. However, our proposal can be directly translated to the scheme of Ref. [16] in which a two-photons FQH state of light was recently demonstrated.

The structure of the Thesis is the following:

Chapter 1. We introduce the concepts of topological invariants and topological insulators and explain the physical origin of topological band structures. We present the theory describing the integer quantum Hall effect, focusing on Landau levels arising in continuum geometries,

and the Harper-Hofstadter model for particles on a square lattice. We also introduce quantum spin-Hall systems displaying a nontrivial topology while preserving time-reversal symmetry. We discuss the concept of quantum simulators, focusing on cold atomic gases and photonic systems, and explore how the integer quantum Hall and spin-Hall effects can be realized in such platforms. Finally, we provide an introduction to the non-Hermitian topological photonics field and review the most relevant realizations of topological insulator lasers in one and two dimensions. A special attention is devoted to the quantum spin-Hall laser of Ref. [13].

Chapter 2. We demonstrate that a single TJR breaks Lorentz reciprocity at high intensities due to the optical nonlinearity. First, we review the Lorentz reciprocity theorem and the proposed strategies to obtain nonreciprocal devices capable of working as optical isolators. We then introduce TJRs and employ the coupled-mode theory equations for the electric field amplitudes in each whispering-gallery mode in order to explain the assymetrical power enhancement leading to reciprocity breaking. We present our joint theoretical and experimental study of the transmittance through TJRs coupled to a bus waveguide. The experiments show a different transmittance when the resonator is pumped in opposite directions. Our results are reproduced by a numerical finite-element model. This Chapter is based on the work published in [17].

Chapter 3. We add a saturable gain to a single TJR and assess the unidirectionality of the laser emission in the presence of backscattering. We first present our theoretical formalism based on the coupled-mode equations of motion and a linearized analysis of the small perturbations around their steady state. In the backscattering-free case we investigate the possible lasing regimes of ring resonators and TJRs depending on the type of saturable gain considered and the strength of the coupling between the ring and the embedded S element. We then include backscattering of different strengths and show that the S element of TJRs imposes unidirectionality to the laser emission. The efficiency of this mode selection process is further enhanced by the Kerr nonlinearity of the material. This Chapter is based on the work published in [18].

Chapter 4. We demonstrate optical isolation in practical conditions over a broad frequency band by employing ring resonators and TJRs strongly pumped in one direction. In the resulting devices, four-wave mixing and transmission of signals are only possible in the pump direction, but not in the opposite one. We first derive the coupled-mode equations for pump, signal, and idler by treating the latter two as small perturbations to the first one. We apply this scheme to coherently pumped passive ring resonators, and to incoherently pumped active ring resonators and TJRs. Further insight about the asymmetrical four-wave mixing leading to reciprocity breaking is obtained by diagonalizing the Bogoliubov matrix and looking at the spectrum of eigenvalues. Our proposal is not subjected to the dynamic reciprocity restrictions [19] present in the nonlinear Taiji studied in Chapter 2, where the strong unidirectional pump was not considered.

Chapter 5. We study quantum spin-Hall topological lasers featuring TJRs as site resonators. After introducing the coupled-mode theory we employ in our simulations, we investigate the effect of backscattering in passive arrays of ring resonators and TJRs. We then consider an active, backscattering-free lattice of ring resonators and study the possible lasing regimes depending on the type of saturable gain employed. Focusing on a local saturable gain, we assess the effect of backscattering. We demonstrate that the sign of the optical nonlinearity determines the topological gap in which the system lases. Finally, we introduce TJRs and show that the resulting quantum spin-Hall laser features an improved unidirectionality, slope efficiency, and lasing threshold even in the presence of backscattering. The combination of TJRs and optical nonlinearities promotes lasing in a single helical mode.

Chapter 6. We review the main features of the FQH effect and justify the Laghlin's Ansatz describing its ground state. We then introduce the plasma analogy and we employ it to assess several properties of FQH liquids, like its incompressibility and the fractional charge and statistics of the bulk excitations. We discuss why FQH phases of matter cannot be described with Landau's theory of symmetry breaking, and we introduce the concept of topological order. We then explore the most interesting properties of Abelian and non-Abelian anyons,

and briefly explain why the latter hold great promise as the qubits of fault-tolerant topological quantum computers. Finally, we review the most promising avenues for realizing FQH liquids using quantum simulators, namely cold atomic gases and photonic systems.

Chapter 7. We propose strategies to experimentally access the fractional charge and statistics of quasihole excitations in atomic FQH liquids. Our key idea is to capture quasiholes by means of impurities, forming composite objects that we label anyonic molecules. We employ a Born-Oppenheimer approximation in order to derive an effective Hamiltonian for such objects. In the single impurity case, we calculate the renormalized mass of the anyonic molecule due to the the motion of the quasihole alongside the impurity, as well as the fractional charge, which features contributions from both the impurity and the quasihole. These two quantities can be measured from the cyclotron orbit described by the anyonic molecule. In the two impurities case, we demonstrate that anyonic molecules inherit fractional statistics from its quasihole part. Finally, we show that the statistics of the molecule can be directly measured in a scattering experiment by looking at the interference fringes in the differential scattering cross section. This Chapter is based on the work published in [20].

Chapter **1**

Review of topological photonics

In the last decades photonic platforms have gained a reputation as quantum simulators, i.e. environments where it is possible to replicate the behavior of more complex systems—such as electron gases in solid state samples—capitalizing on a higher level of control over the experimental parameters, which even allows to implement specific Hamiltonians with a great precision. Furthermore, these systems constitute an ideal playground in which to observe physics without correspondence in other platforms due to the unique properties of photons, like their bosonic, massless, and driven-dissipative nature, the absence of photon-photon interactions in vacuum, etc. In particular, topological photonics is a rapidly-evolving field rooted in the application of the topological concepts originally developed for solid state physics to optical setups like photonic crystals, arrays of coupled propagating waveguides, metamaterials, cavity arrays, etc.

The nontrivial topology of these systems stems from the symmetries of their respective Hamiltonians, that allow the association of topological invariants to the energy bands of the spectrum. As long as the gap structure is preserved the topogical invariants cannot change their values, which makes these systems especially robust against defects, disorder, and local perturbations in general. An important consequence of the nontrivial topology of the energy bands is the appearance of chiral edge states at the system's boundaries. Historically, the first evidence of a nontrivial topology was observed in integer quantum Hall systems which break time-reversal symmetry. Another promising avenue is represented by quantum spin-Hall insulators in which time-reversal symmetry is preserved.

It is precisely the study of the interplay between the nonequilibrium nature of photons and the recently discovered topological effects in optical setups that led to the development of the non-Hermitian topological photonics field. An especially interesting byproduct is the addition of saturable gain to the system's boundaries in order to promote lasing in the topologically protected edge states. The resulting topological laser is expected to outperform trivial lasers and display an extraordinary efficiency and immunity against disorder.

In this Chapter we first provide an introduction to basic topology concepts and their relation with integer quantum Hall and spin-Hall systems of electrons, cold atoms, and photons. We then analyze the most promising platforms enabling topological lasing. We refer the interested reader to the more exhaustive review [7]. Regarding active topological photonics one can consult [12]. [21] is instead devoted to the combination of topological photonics and nonlinear optics effects.

1.1   Why topology? Some basic concepts

In this Section we reveal the connection between topology—which apparently is just a branch of mathematics—and condensed matter physics. We introduce the basic topology concepts that we will employ through this Thesis, and we justify the importance of topology in order to correctly account for the dynamics of quantum particles.

We start by considering non-interacting particles subjected to a periodic potential in a d-dimensional space, as it is the case, for instance, of free electrons in a crystal [22]. This problem is described by the single-particle Hamiltonian $H(\mathbf{r}, \mathbf{p})$ satisfying $H(\mathbf{r}, \mathbf{p}) = H(\mathbf{r} + \mathbf{a}_i, \mathbf{p})$ for a set $\{\mathbf{a}_i\}$ of d lattice vectors.

The spatial periodicity of the Hamiltonian allows us to make use of Bloch's theorem. This warrants that the eigenstates of such a Hamiltonian can be written as a plane wave modulated by a periodic function $u_{n,\mathbf{k}}$, i.e.

$$\psi_{n,\mathbf{k}}(\mathbf{r}) = e^{i\mathbf{k}\cdot\mathbf{r}} u_{n,\mathbf{k}}(\mathbf{r}), \tag{1.1}$$

where n is the band index, and $\mathbf{k}$ is the crystal momentum defined within the first Brillouin zone. $u_{n,\mathbf{k}}$ is the so-called *Bloch wavefunction*, which inherits the spatial periodicity from its parent Hamiltonian, i.e. $u_{n,\mathbf{k}}(\mathbf{r} + \mathbf{a}_i) = u_{n,\mathbf{k}}(\mathbf{r})$. A corollary of Bloch's theorem implies that the Bloch wavefunction is an eigenstate of the Bloch Hamiltonian $H_{\mathbf{k}}$, i.e.

$$H_{\mathbf{k}} u_{n,\mathbf{k}}(\mathbf{r}) = E_n(\mathbf{k}) u_{n,\mathbf{k}}(\mathbf{r}), \tag{1.2}$$

where $E_{n,\mathbf{k}}$ is the energy dispersion of the n-th band. The Bloch Hamiltonian is defined by the rotation

$$H_{\mathbf{k}} = e^{-i\mathbf{k}\cdot\mathbf{r}} H(\mathbf{r}, \mathbf{p}) e^{i\mathbf{k}\cdot\mathbf{r}} \tag{1.3}$$

on the parent Hamiltonian $H(\mathbf{r}, \mathbf{p})$.

Usually, in standard solid state undergraduate courses we learn that the electron dynamics inside a crystal is solely determined by the band structure $E_{n,\mathbf{k}}$ of the Hamiltonian. However, the key idea that led to physicists employing topology concepts to study solid state physics is that there is a missing ingredient in such a description: the geometrical properties of the electronic bands in the crystal momentum space.

Let us consider a localized wavepacket built from states in a certain band n. If such a state is adiabatically moved along a closed path C in momentum space, according to the adiabatic theorem it will acquire the standard dynamical phase, which is given by the time integral of $E_n(\mathbf{k})$. However, due to the dependence of the Bloch wavefunctions $u_{n,\mathbf{k}}$ on the crystal momentum $\mathbf{k}$, the state will also pick an additional geometrical phase given by

$$\gamma = \oint_C \mathcal{A}_n(\mathbf{k}) \cdot d\mathbf{k}, \tag{1.4}$$

which is called *Berry phase*. In general, a similar reasoning can be followed for any Hamiltonian depending on some set of external parameters. In the case of electrons in a periodic potential, it is the crystal momentum $\mathbf{k}$ which plays the role of the external parameter.

In Eq. (1.4) $\mathcal{A}_n(\mathbf{k})$ is the so-called *Berry connection*, defined as

$$\mathcal{A}_n(\mathbf{k}) = i \langle u_{n,\mathbf{k}} | \nabla_{\mathbf{k}} | u_{n,\mathbf{k}} \rangle. \tag{1.5}$$

Note that the Berry connection is not a gauge-invariant quantity, as under a gauge transformation $u_{n,\mathbf{k}} \to e^{i\chi(\mathbf{k})} u_{n,\mathbf{k}}$ it transforms as $\mathcal{A}_n(\mathbf{k}) \to \mathcal{A}_n(\mathbf{k}) + \nabla_{\mathbf{k}}\chi(\mathbf{k})$. Nevertheless, the phase $e^{i\chi(\mathbf{k})}$ must be single-valued at the beginning and at the end of the closed path C, imposing that the Berry phase must be gauge invariant modulo 2π.

It is also possible to define a gauge-invariant *Berry curvature* encoding the geometrical properties of the n-th band as

$$\mathbf{\Omega}_n(\mathbf{k}) = \nabla_{\mathbf{k}} \times \mathcal{A}_n(\mathbf{k}). \tag{1.6}$$

The next question we should ask ourselves is whether we can find a *topological invariant*, i.e. some quantity describing the topological properties of the band which is invariant under smooth transformations (known as *homeomorphisms* in a more mathematical language). On more physical grounds, such a transformation of the Hamiltonian must preserve the gap structure of the energy bands.

This topological invariant is known as *Chern number* and it is defined as

$$\mathcal{C}_n = \frac{1}{2\pi} \int_{\text{BZ}} d^2\mathbf{k} \cdot \mathbf{\Omega}_n(\mathbf{k}). \tag{1.7}$$

The Chern number reflects the continuity of the phase of the Bloch wavefunction along a closed path encircling the whole Brillouin zone (BZ). If the phase of the Bloch wavefunction is continuous over the Brillouin zone, then the Berry connection will be also a continuous function of $\mathbf{k}$. Therefore, Eq. (1.6) and Stokes' theorem imply that the Chern number must be necessarily zero. On the other hand, a finite Chern number implies a discontinuous Bloch wavefunction $u_{n,\mathbf{k}}$ and Berry connection $\mathcal{A}_n(\mathbf{k})$.

It can be easily proven that the Chern number can only take integer values [23]. For the sake of simplicity we focus on the two-dimensional (2D) case where particles live in the $x-y$ plane and only the z component of the Berry curvature takes a finite value. This can therefore be rewritten as a scalar quantity as follows:

$$\Omega_n(k_x, k_y) = i \left(\langle \partial_{k_x} u_{n,\mathbf{k}} | \partial_{k_y} u_{n,\mathbf{k}} \rangle - \langle \partial_{k_y} u_{n,\mathbf{k}} | \partial_{k_x} u_{n,\mathbf{k}} \rangle \right). \tag{1.8}$$

We now consider a closed path ∂S inside the Brillouin zone, separating the enclosed surface S from the external one S'. We can then use Stokes' theorem to rewrite the Chern number in terms of the common boundary $\partial S = -\partial S'$, i.e.

$$\begin{aligned} C_n &= \frac{1}{2\pi} \int_S d^2k \, \Omega_n(k_x, k_y) + \frac{1}{2\pi} \int_{S'} d^2k \, \Omega_n(k_x, k_y) \\ &= \frac{1}{2\pi} \oint_{\partial S} d\mathbf{k} \cdot \mathcal{A}_n(k_x, k_y) - \frac{1}{2\pi} \oint_{\partial S} d\mathbf{k} \cdot \mathcal{A}'_n(k_x, k_y) \\ &= \frac{1}{2\pi}(\gamma - \gamma') \end{aligned} \tag{1.9}$$

where $\mathcal{A}_n$ and $\mathcal{A}'_n$ are the Berry connections calculated using the gauge choices for S and S', respectively, and γ and γ' are the corresponding Berry phases. Since γ and γ' have been calculated along the same path, they can only differ by a multiple of 2π, implying that the Chern number must be an integer.

The topological invariant character of the Chern number is manifested as it remains constant under smooth perturbations preserving the gap structure of the electronic energy spectrum [24, 25, 26]. A fermionic system in which bands displaying finite Chern numbers are completely filled is known as *Chern insulator*.

Obviously, in this Thesis we are interested in systems displaying finite Chern numbers. The question we should be asking ourselves now is: How can we generate a nontrivial topology? It turns out that the system symmetries have some words to say. In particular, when time-reversal symmetry is present we have that the Berry curvature is an odd function of $\mathbf{k}$, i.e. $\boldsymbol{\Omega}_n(-\mathbf{k}) = -\boldsymbol{\Omega}_n(\mathbf{k})$. When we integrate such a quantity over the whole BZ the contributions from $\mathbf{k}$ and $-\mathbf{k}$ cancel out. Applying this identity to the definition of Chern number (1.7) we see that

$$2\pi \mathcal{C}_n = \int_{\mathrm{BZ}} \boldsymbol{\Omega}_n(\mathbf{k}) \cdot d^2\mathbf{k} = \int_{\mathrm{BZ}} \boldsymbol{\Omega}_n(-\mathbf{k}) \cdot d^2\mathbf{k} = - \int_{\mathrm{BZ}} \boldsymbol{\Omega}_n(\mathbf{k}) \cdot d^2\mathbf{k} \rightarrow \mathcal{C}_n = 0, \tag{1.10}$$

i.e. under time-reversal symmetry the Chern number must be zero. A straightforward route to guarantee a non-vanishing Chern number is to break time-reversal symmetry while preserving spatial-inversion symmetry (also known as parity symmetry). A system invariant under spatial-inversion features $\boldsymbol{\Omega}_n(-\mathbf{k}) = \boldsymbol{\Omega}_n(\mathbf{k})$ and therefore we will have that

$$2\pi \mathcal{C}_n = \int_{\mathrm{BZ}} \boldsymbol{\Omega}_n(\mathbf{k}) \cdot d^2\mathbf{k} = \int_{\mathrm{BZ}} \boldsymbol{\Omega}_n(-\mathbf{k}) \cdot d^2\mathbf{k} = \int_{\mathrm{BZ}} \boldsymbol{\Omega}_n(\mathbf{k}) \cdot d^2\mathbf{k}, \tag{1.11}$$

which a priori does not impose any value of $\mathcal{C}_n$.

Time-reversal symmetry breaking is the key ingredient of the so-called *integer quantum Hall* (IQH) systems, which constitute, historically, the first category in which topological effects were observed. However, we can also capitalize in the coupling between the electron spin and momentum in order to obtain a nontrivial topology while preserving time-reversal symmetry. These are the so-called *quantum spin-Hall* systems, in which two spin species feature opposite Chern numbers, which globally add up to zero. The next Sections of this Chapter are devoted to introduce the two kinds of systems.

Note that up to this point we have only relied on the band theory for noninteracting particles in a crystal. However, the previous discussion can be generalized in order to account for interactions between particles [26]. When these become very strong the particles form an exotic, strongly correlated phase known as *fractional quantum Hall* (FQH) fluid. We will devote more attention to this physics in Chapter 6.

1.1.1   The zoo of topological insulators

Finally, prior to studying into detail the IQH and quantum spin-Hall effects, we would like to point out that these are not the only possible systems exhibiting a nontrivial topology. *Topological insulators* generalize the concept of Chern insulators beyond time-reversal symmetry breaking to systems in which different symmetries are broken and preserved. In any case, topological insulators feature an insulating bulk with a topological band structure preserved by the symmetries of the system, and host topologically protected chiral edge states by virtue of the bulk-edge correspondence (that we will study into detail in Sec. 1.2.5). There exists a myriad of topological insulator phases classified according to their symmetries, and characterized by topological invariants that can be different from the Chern number [4, 27]. Topological insulators emerge in both bosonic and fermionic systems, and in different dimensions beyond the paradigmatic 2D case. For instance, the one-dimensional SSH model that we will discuss in the context of the topological laser (see Sec. 1.6.1) features a chiral symmetry as its Hamiltonian commutes with the σ_z Pauli matrix. As a consequence, a pair of zero-dimensional edge states appear inside the topological gap. The topological invariant in this case is known as *winding number*. In this Thesis, we will focus on IQH and quantum spin-Hall systems, and therefore we will use interchangeably the terms *Chern insulator* and *topological insulator*.

1.2   The integer quantum Hall effect in the continuum

In this Section we will briefly discuss the most prominent features of the integer quantum Hall (IQH) effect in the continuum (i.e. without considering an external periodic potential). This phenomenon can be understood without taking into account the interaction between particles. The interested reader can widen the information about this topic in the more exhaustive notes by [28, 29, 30]. The IQH effect in a discrete lattice will be studied in Sec. 1.3.

We concluded the previous Section wondering what kind of physical mechanisms could lead to the observation of a nontrivial topology. One of the possibilities consisted on breaking time-reversal symmetry while preserving spatial-inversion symmetry. This can be achieved, for instance, by subjecting a collection of charged particles to a magnetic field.

This is exactly what happened in the pioneering experiments of von Klitzing [1], where the IQH effect was observed for the first time. The setup consisted on a MOSFET transistor where a 2D electron gas was subjected to a strong magnetic field perpendicular to the confinement plane. We know from our undergraduate physics textbooks that in the classical Hall effect the Hall resistance R_{H} [1] follows a linear dependence with respect to the magnetic field strength B. Quite unexpectedly, von Klitzing found that R_{H} forms a plateaux structure as a function of B. Inside each plateau the value of R_{H} is determined by universal constants, namely h, the Planck's constant, and e, the electron charge. More precisely, R_{H} can be expressed as

$$R_{\mathrm{H}} = \left(\frac{h}{e^2} \right) \frac{1}{\nu}, \tag{1.12}$$

where ν was found to be a positive integer characterizing each plateau. This is why this phenomenon was labeled as IQH effect. The experimental results of von Klitzing are shown in Fig. 1.1.

As we advanced before, it turns out that this physics can be understood in the single-particle picture, without taking into account the Coulomb repulsion between electrons. In the next Subsection we will derive the energy spectrum of a noninteracting 2D electron gas under a strong perpendicular magnetic field, which is organized in bands known as *Landau levels* (LL).

1.2.1   Landau levels

In this Subsection we present the quantum mechanical treatment of the dynamics of noninteracting charged particles in 2D under a strong magnetic field perpendicular to the plane of motion. As we will see, the single-particle energy spectrum is quantized, forming macroscopically degenerate energy bands known as *Landau levels* (LLs) [3]. A very clear analogy can be established between these energy levels and those of a 1D harmonic oscillator featuring the cyclotron frequency $\omega_{\mathrm{c}} =$

---

[1]In two dimensions, resistance and resistivity are interchangeable concepts, and the same occurs between conductance and conductivity.
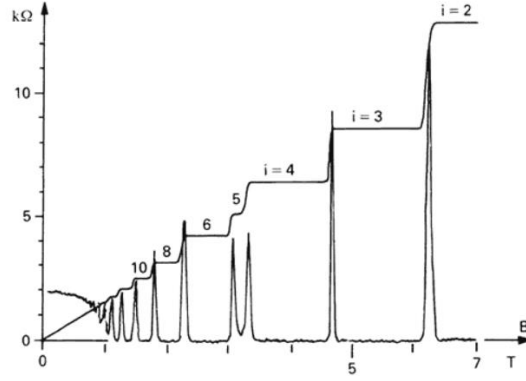
Figure 1.1: *The integer quantum Hall effect.* Hall and longitudinal resistances as a function of the magnetic field strength B. The Hall resistance forms a series of plateaux, while the longitudinal resistance vanishes in each of them. Figure taken from The Nobel Prize website.

qB/m as its natural frequency (in our notation B is the magnetic field, q the particle charge, and m is its mass).

The Lagrangian of a spinless electron of charge $q = -e$ and mass m inside a background magnetic field $\mathbf{B} = \nabla \times \mathbf{A} = B\mathbf{u}_z$ is given by

$$\mathcal{L} = \frac{1}{2}m\dot{\mathbf{r}}^2 - e\dot{\mathbf{r}} \cdot \mathbf{A}. \tag{1.13}$$

Here $\mathbf{A}$ is the vector potential and $\mathbf{u}_z$ is an unit vector perpendicular to the 2D plane where the electron motion is restricted (namely the $x - y$ plane). The canonical momentum can then be calculated in the following form:

$$\mathbf{p} = \frac{\partial \mathcal{L}}{\partial \dot{\mathbf{r}}} = m\dot{\mathbf{r}} - e\mathbf{A}. \tag{1.14}$$

A closer inspection of the last equation reveals that the canonical momentum is not invariant under a gauge transformation $\mathbf{A} \to \mathbf{A} + \nabla\alpha$. Instead, one can define a gauge-invariant *mechanical momentum* $\mathbf{\Pi}$ as

$$\mathbf{\Pi} = \mathbf{p} + e\mathbf{A} = m\dot{\mathbf{r}}. \tag{1.15}$$

The Hamiltonian can now be computed as

$$H = \dot{\mathbf{r}} \cdot \mathbf{p} - \mathcal{L} = \frac{1}{2m}(\mathbf{p} + e\mathbf{A})^2 = \frac{\mathbf{\Pi}^2}{2m}, \tag{1.16}$$

which is obviously a gauge-invariant quantity.

In order to promote this so far classical Hamiltonian function to a quantum operator we will employ the canonical quantization formalism. We start by writing the Poisson brackets for the canonical variables, which are the electron's position $\mathbf{r} = (x, y)$ and canonical momentum $\mathbf{p} = (p_x, p_y)$:

$$\{r_i, p_j\} = \delta_{ij}, \quad \{r_i, r_j\} = \{p_i, p_j\} = 0. \tag{1.17}$$

We now consider $\mathbf{r}$ and $\mathbf{p}$ to be operators and replace the Poisson brackets by the corresponding canonical commutation relations

$$[r_i, p_j] = i\hbar\delta_{ij}, \quad [r_i, r_j] = [p_i, p_j] = 0. \tag{1.18}$$

For the gauge-invariant mechanical momentum operator Π these commutation relations translate into

$$[\Pi_x, \Pi_y] = -ie\hbar B = -i\frac{\hbar^2}{\ell_B^2}, \tag{1.19}$$

where $\ell_{\mathrm{B}} = \sqrt{\hbar/eB}$ is the so-called magnetic length, which is the length scale that characterizes the quantum dynamics of the particles inside a magnetic field.

We now introduce a couple of creation and annihilation operators operators, entirely analogous to those employed to describe the spectrum of a 1D quantum harmonic oscillator. They are defined as

$$a = \frac{\ell_{\mathrm{B}}}{\sqrt{2}\hbar}(\Pi_x - i\Pi_y), \quad a^\dagger = \frac{\ell_{\mathrm{B}}}{\sqrt{2}\hbar}(\Pi_x + i\Pi_y). \tag{1.20}$$

The normalization prefactor ensures that they satisfy the same commutation relations as the ladder operators of the harmonic oscillator:

$$[a, a^\dagger] = 1. \tag{1.21}$$

Inverting Eq. (1.20) and inserting it into Eq. (1.16) we find that the system's Hamiltonian can be written in the very familiar form

$$H = \hbar\omega_{\mathrm{c}} \left(a^\dagger a + \frac{1}{2} \right), \tag{1.22}$$

which is identical to that of a 1D harmonic oscillator of characteristic frequency ω_{c}. We can now exploit this resemblance in order to construct the Hilbert space of the Hamiltonian (1.22) as it is done for a quantum harmonic oscillator. We first consider the ground state $|0\rangle$ obeying $a|0\rangle = 0$ and then build the rest of the Hilbert space acting with the creation operator $a^\dagger$. By applying the ladder operators on a general state $|n\rangle$, where n is a non-negative integer, we get

$$a^\dagger |n\rangle = \sqrt{n+1}\, |n+1\rangle, \quad a|n\rangle = \sqrt{n}\, |n-1\rangle. \tag{1.23}$$

Such a general state $|n\rangle$ can then be written as

$$|n\rangle = \frac{(a^\dagger)^n}{\sqrt{n!}} |0\rangle. \tag{1.24}$$

By applying the Hamiltonian (1.22) to the state (1.24) we can calculate its energy:

$$E_n = \hbar\omega_{\mathrm{c}} \left(n + \frac{1}{2} \right). \tag{1.25}$$

Therefore we conclude that the energy spectrum of a 2D charged particle inside a perpendicular magnetic field consists of equally-spaced levels separated by energy gaps determined by the cyclotron frequency $\hbar\omega_{\mathrm{c}}$. These are the so-called Landau levels (LLs).

At first glance it may seem that something is missing from the previous derivation of the LL spectrum: we started from a 2D system and we arrived at a seemingly one-dimensional Hilbert space completely determined by just a non-negative integer number which labels the different LLs. If we take a closer look at the Hamiltonian (1.16) we see that it is a function of two couples of conjugate operators: (x, p_x) and (y, p_y). Therefore, our guess would have been that a pair of quantum numbers are needed in order to describe its energy spectrum. The important point here is that the Hamiltonian solely depends on the mechanical momentum $\mathbf{\Pi}$, i.e. on just one pair of conjugate operators. This means that each LL $|n\rangle$ must be degenerate. In order take this into account we need to construct a second operator that depends on the other pair of conjugate operators and that commutes with the Hamiltonian.

In this sense we introduce the *pseudomomentum*

$$\tilde{\mathbf{\Pi}} = \mathbf{p} - e\mathbf{A}, \tag{1.26}$$

which, remarkably, is not a gauge-invariant quantity. Its commutation relations differ from those of the mechanical momentum (1.19) by a minus sign, i.e.

$$[\tilde{\Pi}_x, \tilde{\Pi}_y] = i\frac{\hbar^2}{\ell_{\mathrm{B}}^2}. \tag{1.27}$$

We choose to calculate the commutators $[\Pi_i, \tilde{\Pi}_j]$ and $[H, \tilde{\Pi}_i]$ in the symmetric gauge, which is defined by the vector potential

$$\mathbf{A} = -\frac{1}{2}\mathbf{r} \times \mathbf{B} = \frac{B}{2}(-y, x). \tag{1.28}$$

This gauge choice breaks translational symmetry in the x and y directions; in spite of this, it has the great advantage of preserving rotational symmetry around the z axis. As we will see, this means that the third component of the angular momentum will be a good quantum number. Choosing Eq. (1.28) as our vector potential $\mathbf{A}$ we get the commutation relations

$$[\Pi_x, \tilde{\Pi}_x] = [\Pi_y, \tilde{\Pi}_y] = [\Pi_x, \tilde{\Pi}_y] = 0. \tag{1.29}$$

Furthermore, all the pseudomomentum components commute with the Hamiltonian (1.16):

$$[H, \tilde{\Pi}_x] = [H, \tilde{\Pi}_y] = 0. \tag{1.30}$$

At this point we can introduce a second couple of ladder operators

$$b = \frac{\ell_B}{\sqrt{2}\hbar}(\tilde{\Pi}_x + i\tilde{\Pi}_y), \quad b^\dagger = \frac{\ell_B}{\sqrt{2}\hbar}(\tilde{\Pi}_x - i\tilde{\Pi}_y) \tag{1.31}$$

which satisfy the commutation relation $[b, b^\dagger] = 1$. In the symmetric gauge both pairs of ladder operators (a and b) commute with each other, and therefore we have that $[H, b] = [H, b^\dagger] = 0$.

Following the same reasoning as for the a ladder operators we can introduce a ground state $|0\rangle$ and apply $b^\dagger$ in order to construct the corresponding Hilbert space. This latter set of dagger operators allows us to account for the degeneracy of the LLs. The (normalized) most general state now takes the form

$$|n, m\rangle = \frac{(a^\dagger)^n (b^\dagger)^m}{\sqrt{n!m!}} |0, 0\rangle. \tag{1.32}$$

In the equation above we have introduced the second quantum number m that can take any non-negative value and that was missing in our first description. This explicitly shows the degeneracy of the LLs and, as we will see, it is actually the quantum number related to the z-component of the angular momentum. By $|0, 0\rangle$ we label the ground state, which is annihilated both by a and b. The most general state $|n, m\rangle$ accounting for the degeneracy of the LLs is still an eigenstate of the Hamiltonian (1.22) and its energy is given again by Eq. (1.25), which only depends on the quantum number n corresponding to the a set of ladder operators.

So far we have elaborated the spectrum of eigenstates and eigenvalues of 2D charged particles in a uniform magnetic field. At this point we can ask ourselves a couple of interesting questions: How does the ground state of such a system look like? And what is the degeneracy of each Landau level? These questions will be addressed in the following Subsections.

1.2.2 The lowest Landau level wavefunction

In this Subsection we will construct the wavefunction for the ground state of a system of 2D particles under a uniform perpendicular magnetic field in the position representation—that is, we will compute

$$\psi_{0,0}(x, y) = \langle x, y | n = 0, m = 0 \rangle. \tag{1.33}$$

The ground state receives the name of *lowest Landau level* (LLL). For this calculation we will work in the symmetric gauge introduced in the previous Subsection (i.e. with the vector potential in Eq. (1.28)).

We know that the LLL must be annihilated by the a lowering operator:

$$a|0, m\rangle = 0 \quad \forall m. \tag{1.34}$$

We would like to associate a differential equation to the expression above. With this objective in mind we write the annihilation operator as

$$
\begin{aligned}
a &= \frac{\ell_{\mathrm{B}}}{\sqrt{2}\hbar}(\Pi_x - i\Pi_y) \\
&= \frac{\ell_{\mathrm{B}}}{\sqrt{2}\hbar}[p_x - ip_y + e(A_x - iA_y)] \\
&= \frac{\ell_{\mathrm{B}}}{\sqrt{2}\hbar}\left[-i\hbar(\partial_x - i\partial_y) + \frac{eB}{2}(-y - ix)\right]
\end{aligned}
\tag{1.35}
$$

using Eqs. (1.15) and (1.28), and the position representation of the momentum operator $\mathbf{p} = -i\hbar\nabla = -i\hbar(\partial_x, \partial_y)$. In order to simplify the notation, at this point it is useful to introduce the complex coordinates

$$
z = x - iy, \quad \bar{z} = x + iy.
\tag{1.36}
$$

We warn the reader that, from now on, the variable z does not represent a position in the third spatial coordinate. We define the corresponding partial derivatives as

$$
\partial = \frac{1}{2}(\partial_x + i\partial_y), \quad \bar{\partial} = \frac{1}{2}(\partial_x - i\partial_y),
\tag{1.37}
$$

which obey $\partial z = \bar{\partial}\bar{z} = 1$ and $\partial\bar{z} = \bar{\partial}z = 0$.

We can now rewrite the ladder operators a, $a^\dagger$ as a function of the complex coordinates as

$$
a = -i\sqrt{2}\left(\ell_{\mathrm{B}}\bar{\partial} + \frac{z}{4\ell_{\mathrm{B}}}\right), \quad a^\dagger = -i\sqrt{2}\left(\ell_{\mathrm{B}}\partial - \frac{\bar{z}}{4\ell_{\mathrm{B}}}\right).
\tag{1.38}
$$

By implementing this change of variables we can now simplify the differential equation (1.34) for the annihilation of the LLL wavefunctions $\psi_{0,m}(z,\bar{z}) \equiv \psi_m(z,\bar{z})$:

$$
\left(\ell_{\mathrm{B}}\bar{\partial} + \frac{z}{4\ell_{\mathrm{B}}}\right)\psi_m(z,\bar{z}) = 0.
\tag{1.39}
$$

In general, the set of solutions to this equation can be written as

$$
\psi_m(z,\bar{z}) = f_m(z)e^{-|z|^2/4\ell_{\mathrm{B}}^2},
\tag{1.40}
$$

for any holomorphic function $f_m(z)$ [2].

Such an indefiniteness on the ground state wavefunction is again telling us that the LLL is degenerate. To sort this out and find the explicit form of the functions $f_m(z)$ we can follow a similar procedure as we did for the annihilation of the $n = 0$ states by associating another differential equation to the annihilation of the $m = 0$ states by the b lowering operator, i.e. $b\,|n,0\rangle = 0$. In this case, the b ladder operators can be written as

$$
b = -i\sqrt{2}\left(\ell_{\mathrm{B}}\partial + \frac{\bar{z}}{4\ell_{\mathrm{B}}}\right), \quad b^\dagger = -i\sqrt{2}\left(\ell_{\mathrm{B}}\bar{\partial} - \frac{z}{4\ell_{\mathrm{B}}}\right),
\tag{1.41}
$$

which leads to

$$
\left(\ell_{\mathrm{B}}\partial + \frac{\bar{z}}{4\ell_{\mathrm{B}}}\right)\psi_{n,0}(z,\bar{z}) = 0.
\tag{1.42}
$$

Similarly to Eq. (1.39), the most general solution to the equation above is

$$
\psi_{n,0}(z,\bar{z}) = g_n(\bar{z})e^{-|z|^2/4\ell_{\mathrm{B}}},
\tag{1.43}
$$

where $g_n(\bar{z})$ can be any antiholomorphic function. Specifically, $\psi_0 \equiv \psi_{0,0}$ must be a solution to both Eqs. (1.39) and (1.43). The requirement that the function outside the Gaussian exponential must

---

[2] A complex-valued function $f(z)$ is holomorphic in a certain domain if for every point z of that domain the function is differentiable in a neighbourhood of the point. Similarly, a complex-valued function $f(\bar{z})$ is anti-holomorphic if it is differentiable with respect to $\bar{z}$ in a neighbourhood of every point of its domain.

---

be holomorphic and antiholomorphic at the same time leaves a constant as the only possibility, which will be determined by the normalization of ψ_0. This leads to

$$\psi_0(z, \bar{z}) = \frac{1}{\sqrt{2\pi \ell_{\mathrm{B}}^2}} e^{-|z|^2/4\ell_{\mathrm{B}}^2}. \tag{1.44}$$

We can now construct the rest of degenerate states within the LLL by using the differential equation (1.41) for $b^\dagger$. This gives

$$\psi_m(z, \bar{z}) = \frac{1}{\sqrt{2\pi \ell_{\mathrm{B}}^2 m!}} \left(\frac{z}{\sqrt{2}\ell_{\mathrm{B}}}\right)^m e^{-|z|^2/4\ell_{\mathrm{B}}^2}. \tag{1.45}$$

The wavefunctions (1.45) constitute a basis for the LLL. They also have the further advantage of being eigenstates of the z-component of angular momentum. We can clearly see this if we look at the definition of the angular momentum operator L_z:

$$L_z = i\hbar \left(x\partial_y - y\partial_x\right) = \hbar(z\partial - \bar{z}\bar{\partial}). \tag{1.46}$$

Acting with this operator on the set of LLL wavefunctions we get

$$L_z \psi_m(z, \bar{z}) = \hbar m \psi_m(z, \bar{z}). \tag{1.47}$$

Since the expression above is nothing but the eigenvalue equation for the L_z operator, we have therefore discovered that m is the angular momentum quantum number.

1.2.3 The degenaracy of the Landau levels

Here we explicitly calculate the degeneracy of a given Landau level. To make this calculation, we will employ the Landau gauge, which features a vector potential of the form

$$\mathbf{A} = (0, x, 0). \tag{1.48}$$

Although this gauge choice breaks both rotational symmetry around the z axis and translation invariance in the x direction, it preserves translation invariance along the y direction.

The Hamiltonian (1.16) can now be written in the form

$$H = \frac{1}{2m} \left[p_x^2 + (p_y + eBx)^2\right]. \tag{1.49}$$

Due to the explicit translational invariance of the Hamiltonian in the y direction, we can simultaneously diagonalize the Hamiltonian H and the y component of the canonical momentum p_y. The common basis of eigenstates will of course consist on plane waves in the y direction, which motivates the Ansatz

$$\psi_k(x, y) = e^{iky} f_k(x). \tag{1.50}$$

The action of the Hamiltonian (1.49) on ψ_k gives

$$H\psi_k(x, y) = \frac{1}{2m} \left[p_x^2 + (\hbar k + eBx)^2\right] \psi_k(x, y) = H_k \psi_k(x, y), \tag{1.51}$$

where the effective Hamiltonian H_k mimics that of a harmonic oscillator in the x direction, with its center displaced from the origin and located at a position $x = -k\ell_{\mathrm{B}}^2$. The oscillation frequency is again given by the cyclotron frequency ω_{c}. In order to show explicitly these properties we rearrange the effective Hamiltonian in the more simple shape

$$H_k = \frac{1}{2m} p_x^2 + \frac{m\omega_{\mathrm{c}}}{2}(x + k\ell_{\mathrm{B}}^2)^2. \tag{1.52}$$

The eigenvalues of H_k are the LLs

$$E_n = \hbar\omega_{\mathrm{B}} \left(n + \frac{1}{2}\right), \tag{1.53}$$

which are labeled by the set of $\{n\}$ non-negative integers and do not depend on the y-momentum quantum number k. The corresponding eigenstates in the position representation can be written as

$$\psi_{n,k}(x,y) \propto e^{iky} H_n(x + k\ell_{\mathrm{B}}^2) e^{-(x+k\ell_{\mathrm{B}}^2)^2/2\ell_{\mathrm{B}}^2}, \tag{1.54}$$

where H_n is the n-th Hermite polynomial.

So far we have arrived at the same results as we had obtained in the previous Subsection using the symmetric gauge. However, the main advantage of the Landau gauge is that we can calculate the degeneracy of each LL in a very straightforward manner. Let us ask ourselves how many states fit inside a rectangle of side lengths L_x and L_y in the x and y directions, respectively, for fixed n. We know that the effect of the finite size in the y direction will be the quantization of the k momentum in units of $2\pi/L_y$. Instead, in the x direction translational symmetry is broken due to the Landau gauge choice, and therefore the finite size of our rectangle does not result in an analog quantization of the x momentum. Nevertheless, since the wavefunctions (1.54) are exponentially localized around $x = -k\ell_{\mathrm{B}}^2$, for a finite sample restricted to $0 \le x \le L_x$ we will have k values laying within the range $-L_x/\ell_{\mathrm{B}}^2 \le k \le 0$. With this in mind we can compute the number of states in a LL inside the rectangle as

$$\mathcal{N} = \frac{L_y}{2\pi} \int_{-L_x/\ell_{\mathrm{B}}^2}^{0} dk = \frac{A}{2\pi\ell_{\mathrm{B}}^2} = \frac{eBA}{2\pi\hbar} = \frac{BA}{\Phi_0}. \tag{1.55}$$

Here, $A = L_x L_y$ is the area of the sample and $\Phi_0 = 2\pi\hbar/e$ is the magnetic flux quantum. This result implies that the number of states inside each LL is simply given by the number of magnetic flux quanta trespassing the sample. The reader should keep in mind that, in general, this can be a macroscopically large quantity. This will be important when we try to add interactions to this picture in Chapter 6. Note that, even though we chose a rectangular shape to make the calculation, this result holds under a different sample shape choice.

1.2.4 The quantization of the Hall conductance

We are now in a position to explain the quantization of the Hall conductance $\sigma_{\mathrm{H}} = R_{\mathrm{H}}^{-1}$ in units of e^2/h giving rise to the plateaux structure shown in Fig. 1.1. How does this correlate with the quantization of the energy spectrum of the electrons in terms of the LLs? The fact that both phenomena are described in terms of non-negative integer numbers should raise suspicions. Indeed, such a connection exists and, as we will see, the Hall resistance takes the value in Eq. (1.12) precisely when ν LLs are fully occupied.

So far we have talked extensively about the energy spectrum of a 2D electron gas in a magnetic field, but we have not mentioned topology in our discussion. Soon after the discovery of von Klitzing, Thouless [2] used linear response theory [31] in order to show that the IQH effect could be understood in terms of the nontrivial topology of the LLs. Applying for the first time topological concepts to condensed matter physics, Thouless demonstrated that the Hall conductance of an electron gas in a two-dimensional periodic potential and subjected to a uniform magnetic field can be related to the Chern numbers of the occupied bands, i.e.

$$\sigma_{\mathrm{H}} = -\frac{e^2}{h} \sum_{n \in \mathrm{occ.}} \mathcal{C}_n. \tag{1.56}$$

In our case, it can be shown that each LL features a Chern number $\mathcal{C}_n = -1$. The equation above is known as *TKNN formula* (after Thouless, Kohomoto, Nightingale, and den Nijs), and it provides an explanation for the plateaux structure found in the Hall resistance: each time a LL is completely filled the sum in the right-hand side of Eq. (1.56) increases by -1. The Hall conductance is therefore proportional to the number of fully occupied LLs.

An important consequence of the topological invariant character of the Chern number is that the value that it takes in a given LL cannot change unless the energy gap separating it from other LLs is closed. As a consequence, what Eq. (1.56) is telling us is that the Hall conductance itself is another topological invariant. This is why it exhibits a special robustness against the presence of disorder in the samples and other local perturbations.

Prior to concluding our discussion about the TKNN formula, we warn the reader that there is a subtle point here: the definition of the Chern number (1.7) as an integral over the whole

BZ works fine for periodic Hamiltonians but breaks down when we consider a continuum system. However, the Chern number of LLs can be calculated by discretizing space employing the so-called Harper-Hofstadter model (that will be studied in detail in Sec. 1.3) and then taking the limit of small flux per plaquette, in which the LLs energy spectrum is recovered, as was demonstrated by Harper in Ref. [32].

The role of disorder

We will now make some remarks about the role of disorder in the quantization of the Hall resistance. The experimental samples inevitably contain impurities that can be modelled with a random potential $V(\mathbf{r})$. If the strength of disorder is weak compared to the gap separating the LLs ($V \ll \hbar\omega_c$), then it follows from quantum perturbation theory that disorder will break the degeneracy inside each LL. A further consequence of disorder will be to turn some of the quantum states from extended to localized. It can be shown (see [30]) that for each band only the states close to its center will be extended, while those close to the edges of the band will be localized. This is important if we want to explain the behavior of conductance because only the extended states can give a contribution to it.

Consider a LL with fully-filled extended states. According to Eq. (1.55) as B is decreased the LL can accomodate fewer electrons, and as a consequence the Fermi energy will increase. This means that the localized states will begin to be populated. Since these states cannot give a contribution to the conductance, this quantity does not change. Only when the extended states located at the center of the bands are populated the value of the conductance experiences a sudden change. This is the origin of the plateaux that were observed in von Klitzing's experiments where the Hall resistance takes constant values over certain ranges of B. Quite remarkably, this explains why Eq. (1.12) is still valid even when a LL is not fully occupied.

1.2.5 Chiral edge states and the bulk-edge correspondence

Up to this point we have focused our attention in bulk properties only. However, the story is not complete if we do not look at the sample edges as well. Even in classical physics we know that, as a result of the cyclotron motion of the electrons inside a uniform magnetic field, the boundaries of the sample will host an electron current moving in a single direction.

In the case of topologically nontrivial materials there exists an intimate relation between the topology of the energy bands in the bulk and the edge modes propagating along the surface of the sample. This is the so-called *bulk-edge correspondence*: when two materials featuring different topological invariants are put into contact, their interface must host spatially localized edge states at energies within the energy gap of the surrounding bulk materials [33, 34]. Of course, this statement also holds in the case of a topologically nontrivial material surrounded by the trivial vacuum, leading as well to the appearance of edge states [4]. The bulk-edge correspondence can be understood in terms of the different topological invariants exhibited by both materials: if the value of such a quantity must be changed, then the only possiblity is that the energy gap has to be closed somewhere, leading to the appearance of the boundary states.

This kind of edge modes is also characterized by a well-defined chirality: each of them propagates in a particular direction around the bulk of the sample, but not in the opposite. The absence of degenerate surface states featuring an opposite group velocity makes the chiral edge modes resulting from the bulk-edge correspondence topologically protected against backscattering caused, for example, by the presence of impurities in the system.

In the case of the IQH effect, the sum of the Chern numbers associated to the occupied bulk bands is equal to the difference between the number of edge modes featuring a positive and a negative chirality. Since all LLs have $\mathcal{C}_n = -1$, all edge modes propagate in the same direction and give the same contribution to the edge current, therefore explaining once again the quantization of the Hall conductance reviewed in the previous Subsection. The chirality of the edge states is actually determined by the sign of the Chern number: -1 implies a counterclockwise propagating edge state, while $+1$ means that the edge state propagates in the clockwise direction.

1.3   The IQH effect in a lattice: the Harper-Hofstadter model

Of course, the nontrivial topology of the energy spectrum is not an exclusive property of electrons in the continuum under a magnetic field. Tight-binding Hamiltonians for spatial-periodic potentials can also display a band structure with a nontrivial topology if they feature the key ingredient: time-reversal symmetry breaking. In particular, this Section is devoted to review the Harper-Hofstadter model [35, 36], which is the tight-binding version on a square lattice of the continuum IQH effect. Again, interactions play no role and it is sufficient to look at the single-particle spectrum.

The magnetic flux trespassing each plaquette of the square lattice can be accounted for in the tight-binding Hamiltonian by including a complex hopping phase between neighboring sites known as *Peierls phase* [37, 38]. From the definiton of magnetic flux, employing the Stokes' theorem it is straightforward to show that such a phase takes the form

$$\Phi_{\mathbf{r}_1 \to \mathbf{r}_2} = \frac{e}{\hbar} \int_{\mathbf{r}_1}^{\mathbf{r}_2} \mathbf{A}(\mathbf{r}) \cdot d\mathbf{r}, \tag{1.57}$$

for a particle hopping from $\mathbf{r}_1$ to $\mathbf{r}_2$, in terms of the magnetic vector potential $\mathbf{A}(\mathbf{r})$.

In order to include this complex hopping phase in the system's Hamiltonian we can use the Landau gauge, in which the vector potential takes the especially appealing form $\mathbf{A}(\mathbf{r}) = (-By, 0, 0)$. The Hamiltonian of the Harper-Hofstadter model reads

$$H = -J \sum_{x,y} (e^{-i2\pi\alpha y/d} a_{x+d,y}^\dagger a_{x,y} + a_{x,y+d}^\dagger a_{x,y} + \text{H.c.}), \tag{1.58}$$

where $a_{x,y}^\dagger$ ($a_{x,y}$) is the creation (annihilation) operator of a particle at a site (x, y), J is the hopping amplitude and d is the lattice spacing. The parameter α takes into account the number of flux quanta piercing each plaquette, i.e. $\alpha = Bd^2/\Phi_0$, where $\Phi_0 = 2\pi\hbar/e$ is the magnetic flux quantum.

Unlike the continuum IQH effect, the physics described by the Harper-Hofstadter model is governed by the competition between the magnetic length $\ell_\text{B} = \sqrt{\hbar/eB}$ and an additional lengthscale d describing the site separation of the lattice. As a consequence, the allowed energy bands adopt a fractal structure as a function of α. This energy spectrum, plotted in Fig. (1.2), is commonly known as *Hofstadter butterfly* and was experimentally observed for the first time in a microwave waveguide by exploiting the analogy between the transfer matrix governing its transmittance and the eigenvalues of the Harper-Hofstadter Hamiltonian [39].

We can shine more light into the particular structure of the spectrum by considering rational values of α, i.e. $\alpha = p/q$, where p and q are integer numbers. Due to the spatial dependence of the hopping phase describing the gauge field in Eq. (1.58) the d periodicity of the square lattice is not inherited by the Hamiltonian. Nevertheless, periodicity is recovered if one considers the so-called *magnetic unit cell*, consisting of a $1 \times q$ plaquette. Therefore, a Harper-Hofstadter model featuring a magnetic flux $\alpha = p/q$ will have q bands, since in a tight-binding model the number of bands is determined by the number of sites per unit cell.

We can now apply the concepts introduced in Sec. 1.1 in order to study the nontrivial topology of the bulk energy bands and the robust chiral modes of the surface. The Chern number $\mathcal{C}_\nu$ of the ν-th band is given by Eq. (1.7) and depends on the magnetic flux α trespassing each plaquette of the system. For instance, it can be shown [40] that the $\alpha = 1/4$ Harper-Hofstadter model features four bands of Chern numbers

$$\mathcal{C}_1 = -1, \quad \mathcal{C}_2 + \mathcal{C}_3 = 2, \quad \mathcal{C}_4 = -1. \tag{1.59}$$

If one considers a semi-infinite lattice with a finite number of sites in the y direction then the TKNN formula [2, 26, 41, 42] dictates that the Hall conductance is given again by Eq. (1.56).

When a finite number of bands are completely filled the system behaves as a topological insulator, i.e. it features an insulating bulk but it can also host topologically protected chiral modes at its surface according to the bulk-edge correspondence. The sum of the Chern numbers of the occupied bands below a given gap determines the difference between the number of edge modes with positive (N_+) and negative (N_-) chirality that exist inside that gap, i.e.

$$N_+ - N_- = \sum_{E_\nu < E_\text{gap}} \mathcal{C}_\nu. \tag{1.60}$$
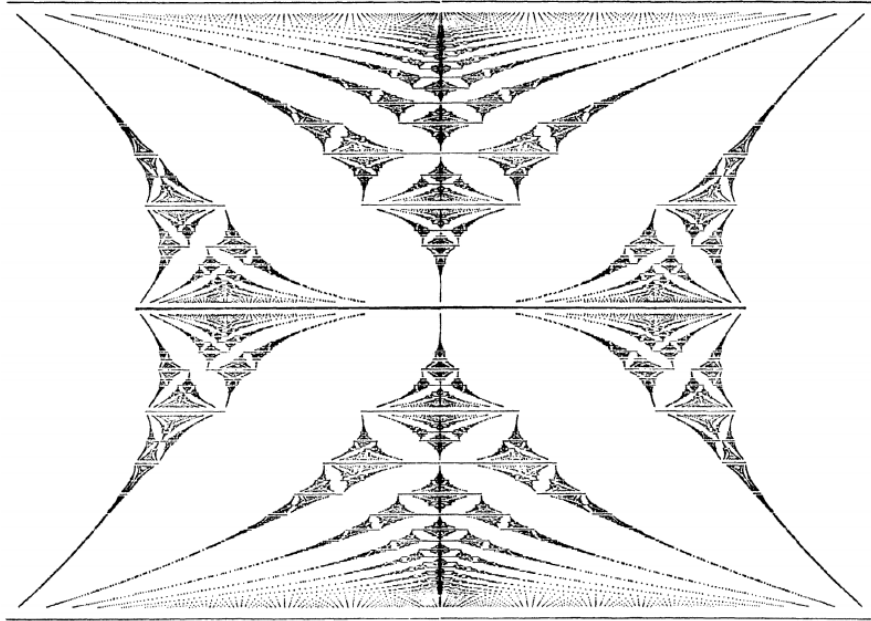
Figure 1.2: Energy bands of the Harper-Hofstadter model. The vertical axis is the magnetic flux Φ running from 0 to Φ_0, while the horizontal axis represents the energy, running from $-4J$ to $4J$. Figure taken from [36].

In the equation above, E_ν is the energy of the ν-th band and E_{gap} is the energy of the considered gap. For instance, in the case of the Harper-Hofstadter model with $\alpha = 1/4$ the bottom gap features an edge state with CCW chirality, the central gap is not well-defined as the two central bands touch at several Dirac points and therefore no propagating edge states can exist, and in the upper gap we find an edge sate propagating in the CW direction.

To conclude this Section, we note that the Landau level energy structure of the continuum IQH effect can be recovered from the butterfly-like Harper-Hofstadter spectrum in the limit of small flux density, i.e. $\alpha = 1/q$ and $q \to \infty$. In fact, in Ref. [32] it was demonstrated that the Harper-Hofstadter energy bands near rational values of α can be written as a superposition (given by a unitary matrix) of the continuum Landau levels. When $q \to \infty$ this unitary change of basis is given by the identity matrix, granting a one-to-one correspondence.

1.4 Quantum spin-Hall systems

In this Section we introduce quantum spin-Hall systems, which exhibit a nontrivial topology and at the same time preserve time-reversal symmetry.

Both the continuum IQH effect and the Harper-Hofstadter model relied on the presence of a magnetic field breaking time-reversal symmetry in order to generate a nontrivial topology, i.e. an energy band structure featuring finite Chern numbers. On the other hand, in systems with time-reversal symmetry, the Berry curvature satisfies $\Omega_n(-\mathbf{k}) = -\Omega_n(\mathbf{k})$ and, as we saw with Eq. (1.10), this implies that the Chern number of non-degenerate bands must be zero. Even in the case of degenerate bands the definition (1.7) can be straightforwardly generalized [43, 44] in order to show that their Chern numbers must also be zero for 2D systems in which time-reversal symmetry is preserved [45].

Apparently we are left with the intuition that time-reversal symmetry breaking is necessary to obtain a nontrivial topology, at least in momentum space. However, in 2005 a new class of time-reversal symmetry-preserving topological phase was proposed: the so-called *quantum spin-Hall insulators* [46, 47]. Such systems are often called $\mathbb{Z}_2$ insulators, as they are characterized by a topological invariant which can only take the values 0 or 1 depending on its trivial or nontrivial nature, respectively. Quantum spin-Hall insulators consist of two copies of a Chern insulator, each one associated to an opposite spin: up ($\uparrow$) and down ($\downarrow$). The magnetic field acting on each spin points in opposite directions, and as a consequence the Chern numbers for spin up and down

are the opposite, i.e. $\mathcal{C}_\downarrow = -\mathcal{C}_\uparrow$. Overall, the total magnetic field applied is zero, time-reversal symmetry is preserved, and the sum of the Chern numbers for the two spins is zero. As long as spin-flipping processes are not present in the system, both spin components can be treated as two uncoupled Chern insulators. From the the bulk-edge correspondence it follows that the number of topologically protected edge states will be the same for each spin; however, they will propagate with opposite chirality. These kind of surface modes are known as *helical* edge states.

In fermionic systems preserving time-reversal symmetry, even when spin-flip processes are present, Kramers' theorem grants topological protection for at least one pair of edge modes. The theorem implies that given an eigenstate with a certain energy, its time-reversal counterpart must be degenerate, forming a so-called *Kramers pair*. More importantly, a couple of helical states forming a Kramers pair are orthogonal, meaning that no backscattering coupling both states can be introduced without breaking time-reversal symmetry, for instance by means of the presence of magnetic impurities. The first experimental realization of such a system was due to [48] using HgTe quantum wells. Generalizations of quantum spin-Hall systems to higher dimensions have also been proposed [49].

In the case of bosonic particles Kramers' theorem does not hold anymore. This means that the helical states of such a system will not be robust against terms coupling the two pseudospin degrees of freedom. This poses a big challenge in order to study analogs of quantum-spin Hall systems using photons or bosonic atoms. However, if no such coupling exists then the resulting edge states will be granted topological protection even if one is dealing with bosonic particles [50, 11]. In Sec. 1.5.2 we will see an example of such a system.

1.5 Beyond electron gases: quantum simulators

So far, we have focused on the topological properties of 2D electron gases in solid state systems. However, Bloch's theorem does not care about the particular nature of the particles involved: it reflects a universal property of waves under spatially-periodic Hamiltonians. The same occurs regarding the topology of the wavefunction describing some quantum-mechanical system: the concepts presented in Sec. 1.1, such as the Berry curvature and the topological invariant Chern number, are still valid beyond electron gases. Actually, even classical setups like acoustic structures [5] and arrays of coupled pendula [6] can be engineered to display a topological dispersion. The question arising at this point is whether there are advantages in studying topology in alternative systems. Both from the theoretical and experimental point of view, the objective would be to employ quantum systems granting a large degree of control over them, to the point that one could implement particular Hamiltonians (such as the Harper-Hofstadter model introduced in Sec. 1.3) in wide parameter ranges, and allowing to produce neat measurements of the physically relevant quantities. This would facilitate the exploration and understanding of new physics which otherwise would be difficult to study using traditional solid state samples.

The idea of such a platform, whose scope goes far beyond that of topology, was proposed back in 1982 by Richard Feynman [51] and receives the name of *quantum simulator*. Of course, the study of the topological properties of electron gases in solid state materials continues attracting attention and generating valuable results with a great impact in society. However, the complexity of these systems and the little room for tuning the experimental parameters can pose extraordinary challenges.

A plethora of systems have been proposed to be employed as quantum simulators and, in fact, many of them serve very well this purpose. The most popular ones include ultracold atoms [52], quantum fluids of light [53], photonic systems [54], superconducting circuits [55], and trapped ions [56]. Today, these artificial systems are interesting on their own, leading to completely new observations beyond their electronic counterpart, and some implementations are even strong candidates to build a functional quantum computer.

In this Thesis we will focus on the case of ultracold atoms and, especially, photonic systems. This, of course, arises some particular difficulties: we saw that breaking time-reversal symmetry is a necessary condition to reproduce IQH physics. Nevertheless, atoms and photons are neutrally charged particles, and therefore, it seems impossible that they can mimic the dynamics of charged particles in a magnetic field. In both cases several strategies have been developed in order to design synthetic gauge fields. For photons, however, even more challenges are present: they are bosons, massless, and they have an intrinsic non-equilibrium nature. In the following Subsections we will see how to overcome these difficulties.

1.5.1   Cold atoms

Dilute gases of neutral atoms cooled down to a temperature range between 10^{-6} and 10^{-9} K have gained a reputation as the leading platform where to study Bose-Einstein condensation and superfluidity [57]. This is a consequence of the highly-developed experimental techniques available to manipulate neutral atoms using laser light and magnetic fields [58]. In addition, one can explore the cloud properties by means of time-of-flight experiments, absorption imaging, and even quantum gas microscopes with single-atom resolution [59, 60].

For instance, the laser beams can be appropriately designed in order to subject the atoms to different trapping potentials (harmonic, box-like, etc.) and, even more importantly, to trap them in optical lattices with the desired spatial periodicity [61, 62, 63]. This opened the door to the study of topological band structures using neutral atoms [64, 65].

In the particular case of quantum Hall physics, neutral atoms can mimic the behavior of charged particles under a magnetic field by employing different strategies resulting in an effective magnetic field.

The most straightforward one [66, 67] relies on a mathematical analogy between the Lorentz force experienced by a charged particle in a magnetic field and the Coriolis force in a rotating reference frame, i.e.

$$\mathbf{F}_{\text{Lorentz}} = q\mathbf{v} \times \mathbf{B}, \quad \mathbf{F}_{\text{Coriolis}} = -2M\boldsymbol{\Omega} \times \mathbf{v}. \tag{1.61}$$

In the equation above M and q are the mass and charge of the particle, $\mathbf{v}$ is its velocity, $\mathbf{B} = B\mathbf{u}_z$ is the orthogonal magnetic field and $\boldsymbol{\Omega} = \Omega\mathbf{u}_z$ is the rotation frequency of the trap. We see that if we set $2M\boldsymbol{\Omega} = q\mathbf{B}$ the two expressions are the same.

It is also worthwhile to look at this analogy at the level of the Hamiltonian. A general Hamiltonian in a reference frame rotating at a frequency $\boldsymbol{\Omega}$ is given by

$$H_\Omega = \frac{\mathbf{p}^2}{2M} + V(\mathbf{r}) - \boldsymbol{\Omega} \cdot \mathbf{L}, \tag{1.62}$$

where $V(\mathbf{r})$ is a trapping potential in the $x - y$ plane and $\mathbf{L}$ is the angular momentum operator. This Hamiltonian can be rewritten in the more suggestive form

$$H = \frac{(\mathbf{p} - q\mathbf{A}(\mathbf{r}))^2}{2M} + V(\mathbf{r}) + V_{\text{c}}(\mathbf{r}), \tag{1.63}$$

where the effective vector potential $\mathbf{A}$ and the effective centrifugal potential $V_{\text{c}}(\mathbf{r})$ are given by

$$q\mathbf{A}(\mathbf{r}) = M\Omega(x\mathbf{u}_y - y\mathbf{u}_x), \quad V_{\text{c}}(\mathbf{r}) = -\frac{1}{2}M\Omega^2\mathbf{r}^2. \tag{1.64}$$

It can be easily shown that $\nabla \times \mathbf{A}$ gives $\mathbf{B} = 2M\boldsymbol{\Omega}/q$, therefore justifying the analogy between the Lorentz and Coriolis forces. The resulting centrifugal potential can be countered by adding an additional harmonic trapping of the same frequency, i.e.

$$V_{\text{h}}(\mathbf{r}) = \frac{1}{2}M\Omega^2\mathbf{r}^2. \tag{1.65}$$

However, this approach requires a perfect balance between the centrifugal potential V_{c} and the harmonic confinement V_{h}. This can be circumvented by resorting to an additional quartic potential like in Ref. [68]. The setup can also suffer from anisotropies in the harmonic potential that make difficult to balance the centrifugal one. This inconvenient can be tackled by employing more refined experimental techniques like the so-called evaporative spin-up method [69].

Alternate strategies to generate a synthetic magnetic field for neutral particles include the association of a Berry phase to the atom dynamics by employing appropriate optical and magnetic fields [70, 71, 72, 73]. The Berry phase can mimic the Aharonov-Bohm phase collected by the wavefunction of an electron in a magnetic field. As we already know, this leads to the introduction of an effective vector potential known as Berry connection in the Hamiltonian [67]. This solution was exploited by [74] in order to observe the nucleation of quantized vortices in a rubidium Bose-Einstein condensate, therefore proving the existence of a synthetic gauge field for neutral atoms. Nevertheless, this approach suffers from undesired thermal issues due to spontaneous emission and the subsequent recoil heating in the atomic cloud.

Artificial gauge fields can also be designed for neutral atoms in periodic potentials. The seminal work of [75] introduced the fundamental concept of laser-assisted tunneling. This proposal consists on a 2D lattice alternating columns loaded with atoms in two different internal states. In such a system tunneling in the horizontal direction is only possible by means of laser beams coherently transferring the atoms between the two internal states. This allowed to implement complex hoppings in the lattice whose effect on the atom dynamics resembles those of charged particles in a magnetic field. This idea led to the experimental realization of the Harper-Hofstadter model for cold atoms [76, 77].

Finally, it is worth mentioning an alternative approach which relies on the temporal modulation of some external parameters of the Hamiltonian. This is known as Floquet engineering. In the case of a shaken optical lattice in which the modulation breaks time-reversal symmetry complex hoppings can be obtained [78]. This led to the first experimental realization of the Haldane model [79].

1.5.2   Photonic systems

Possibly the most fundamental difference between solid state setups and photonic systems is the nature of the constituent particles: electrons are fermions, while photons are bosons. We have already encountered one of the consequences of such a difference: in the case of bosonic quantum spin-Hall systems studied in Sec. 1.4 Kramers' theorem does not hold and the helical surface modes lose their topological protection whenever the two pseudospins are coupled.

At the many body level, the different quantum statistics translate in the different states that these particles occupy at low temperatures. In the case of fermions, all the states below the Fermi level are occupied with just one particle, while bosons form Bose-Einstein condensates where a macroscopic number of particles occupies the lowest-energy state. In the case of optical systems this picture is a bit different due to the intrinsic driven-dissipative nature of photons. This implies that, typically, the ground state is the trivial vacuum and, in order to circumvent the absorption by the material medium and the radiative losses, an external pumping mechanism is needed in order to refill the system with photons. As a consequence of this balance between pumping and losses, optical systems are far from thermal equilibrium.

This, however, is not bad news at all, as the nonequilibrium nature of photons provides us with a formidable set of probes and measurement tools which are not available in the solid state or ultracold atoms cases. In fact, light radiated away by the system contains fundamental information about the field distribution and the photon statistics inside the device. We can directly access this information by imaging the emission in free space, or by collecting it locally by means of antennas or waveguides. It is also possible to probe different parts of the system by injecting light only into them.

Concerning the massless nature of photons, it does not constitute a problem as it is well-known that the confinement inside a cavity provides the photons with an effective mass [80].

As we discussed at the beginning of the present Section, Bloch's theorem is also valid for electromagnetic waves under spatially-periodic Hamiltonians. This allows the existence of electromagnetic bands and gaps in metamaterials known as *photonic crystals*, which are engineered by means of a spatially periodic variation of the electric permittivity and magnetic permeability tensors [8, 9]. Such photonic bands are also characterized by Chern numbers that vanish unless time-reversal symmetry is broken. This key idea is at the bottom of the topological photonics field.

It turns out that, as in the case of dilute atomic gases, it is possible to design artificial gauge fields for photons. The first proposal due to Haldane and Raghu [81, 82] contemplated the realization of photonic crystals using magneto-optic materials that break time-reversal symmetry. This led to the observation of the photonic equivalent of the chiral edge modes of the IQH effect in the microwave regime [10]. These works represent the roots of the topological photonics field.

After that, many alternative structures have been proposed in order to develop a better integration with state of the art silicon photonics technology operating at telecommunication wavelengths (around 1.5 μm). An important example is the all-dielectric quantum spin-Hall photonic crystal designed by [11], which realizes two copies of a Harper-Hofstadter topological insulator. This platform consists on an array of silicon ring resonators, each supporting a pair of degenerate whispering-gallery modes which propagate in clockwise and counterclockwise directions. These constitute the two pseudospins of the system. Globally, time-reversal symmetry is preserved, but the links connecting different resonators realize opposite complex hopping phases for the two pseudospins.

Therefore, photons belonging to different pseudospins experience opposite artificial magnetic fields and belong in photonic bands featuring opposite Chern numbers. An optimized design guarantees a negligible backscattering coupling the two pseudospins, which preserves the robustness of the topological helical modes.

It is also worth mentioning that propagating geometries in which the z coordinate plays the role of time can also be employed to mimic the effects of the temporal modulation of the Hamiltonian. A seminal example is provided by the evanescently coupled helical waveguides of [83].

Regarding the generation of synthetic gauge fields for photons in the continuum, the experiment of [84] employed a twisted multimode cavity which induces a photon rotation in each round-trip. Due to the previously commented analogy between rotating reference frames and magnetic fields, this design allowed the observation of photonic Landau levels as in the IQH effect.

1.6 Non-Hermitian topological photonics

In the previous Sections we reviewed the fascinating properties that topologically nontrivial materials can display. We learned that, although originally developed for electron gases in solid state devices, topology in physics is a universal phenomenon emerging from the geometrical properties of the wavefunction of a quantum system. Therefore, all these concepts and ideas can also be applied in other platforms, like cold atomic gases and photonic setups. The latter, in particular, promise exciting applications like waveguide propagation immune to backscattering, but also pose exciting challenges rooted in the nonequilibrium nature of photon gases.

What sets topological photonics apart from every other field is the possiblity to introduce active materials into such topologically nontrivial structures in order to study the interplay between gain and losses. This gave rise to the so-called *topological lasers* or, in short, *topolasers*. Of course, the most promising application is to promote lasing in the topologically protected chiral edge modes.

In general, disorder is present in laser cavities due to fabrication defects, operational degradation, malfunctioning, etc. Disorder gives rise to light localization at defects, ultimately resulting in a degraded overlap between the lasing mode and the gain profile. As a consequence, the laser performance decreases due to lower output coupling, multimode lasing, and reduced slope efficiency. These issues are enhanced in arrays of coupled laser resonators featuring a large number of elements (employed to produce high output powers). The topological protection of the edge modes against local perturbations, however, can lead to an improved performance with respect to topologically trivial lasing, and it is expected to grant robust single-mode emission.

The existence of non-Hermitian topological insulators and the robustness of the protected edge modes under the presence of gain remained as open questions for a long time [85, 86]. Recently, several experiments have demonstrated that lasing in topologically protected edge states is possible in such systems. In this Chapter we discuss the most promising platforms in which topological lasing has been achieved. For a more comprehensive review, we refer the reader to [12].

1.6.1 The one-dimensional topolaser

In this Subsection we focus on the first experimental realization of a topolaser: a one-dimensional (1D) chain of exciton-polariton micropillars implementing the Su–Schrieffer–Heeger (SSH) model [87].

A schematic illustration of the SSH model can be found in panels (a) and (b) of Fig. 1.3. It consists on a 1D chain with a unit cell formed by two sites, labeled a and b, each hosting one state of the same energy. The intracell coupling t is, however, different from the intercell coupling t'. The Hamiltonian reads

$$H = \sum_j \left(t b_j^\dagger a_j + t' a_{j+1}^\dagger b_j + h.c. \right), \tag{1.66}$$

where a_j (b_j) are the annihilation operators on the site a (b) of the unit cell j. As we known from textbook solid state physics, a tigh-binding model featuring a two-sites unit cell will have two bands separated by a gap.

The topology of the system is encoded in the so-called *winding number*, which is a topological invariant, analog of the Chern number in 1D. It is given by

$$\mathcal{W} = \frac{1}{2\pi} \int_{\text{BZ}} \frac{\partial \phi(k)}{\partial k} dk. \tag{1.67}$$
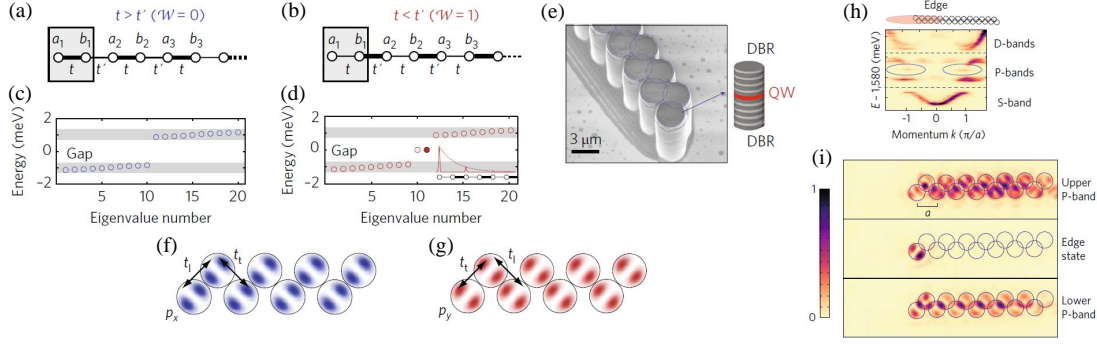
Figure 1.3: **(a)** and **(b)** show sketches of the SSH model in the trivial and topological cases, respectively. The resulting energy eigenvalues are found in panels **(c)** (trivial) and **(d)** (topological). **(e)** shows a SEM image of the zig-zag micropillars chain. **(f)** and **(g)** show a sketch of the spatial distribution of the p_x and p_y modes in the lattice, respectively. **(h)** displays the photoluminiscence emission of the bands as a function of their energy and crystal momentum when the edge of the chain is excited. **(i)** shows the emission in real space of some of the bands displayed in **(h)**. Figure adapted from [87].

The winding number reflects the number of times that the phase of the energy eigenvectors ϕ winds around the origin. It can only take the values 0 (trivial) when $t > t'$, or 1 (nontrivial) when $t' > t$. If one considers an infinite chain, no physical consequence should emerge from this distinction, as one is free to choose a different unit cell, therefore interchanging the values of t and t'. However, in a finite lattice the unit cell is univocally determined by the first site. As a consequence, when $\mathcal{W} = 0$ no edge states appear within the gap (Fig. 1.3c), but when $\mathcal{W} = 1$ each edge site hosts a zero-dimensional (0D) topological edge state (Fig. 1.3d) in the middle of the gap.

The reader may wonder what is the origin of the nontrivial behavior of the SSH model. After all, time-reversal symmetry is preserved, and the model does not fall into the category of quantum spin-Hall systems. Topology in this case stems from the geometry of the model: the SSH Hamiltonian anticommutes with the σ_z Pauli matrix, and therefore presents a chiral symmetry (manifested in the fact that the Hamiltonian is purely off-diagonal in the basis of the (a,b) sites of each unit cell). This means that the lasing edge modes will be robust against disorder in the hopping parameters t, t', which preserves the chiral symmetry. Remarkably, the edge modes also exhibit robustness against local perturbations breaking chiral symmetry, such as a change in the onsite energy of a micropillar, as long as these perturbations remain smaller than the bandgap.

The experimental implementation of the SSH model of [87] consists on an active zig-zag chain of semiconductor micropillars (Fig. 1.3e). The coupling between photons and excitons gives rise to hybrid quasiparticles with both light and matter properties known as polaritons [53]. Each micropillar hosts a quantum well embedded by distributed Bragg reflectors to confine photons inside it. These display a series of collective photonic modes labelled by their angular momentum symmetry: s, p, d, etc. The SSH model is reproduced by exploiting the different spatial shape of the p_x and p_y modes, which controls the strength of the overlap between intracell and intercell micropillars: The subspace of the p_x modes (Fig. 1.3f) gives rise to the trivial case at if features $t > t'$, while that of the p_y modes (Fig. 1.3g) exhibits a nontrivial topology as couplings in this case satisfy $t' > t$.

In order to obtain polariton lasing, the authors of Ref. [87] optimized the gain for the p modes and optically pumped the chain using a continuous-wave laser. When the elliptical spot of the laser is placed at the edge of the lattice, emission in momentum space (Fig. 1.3h) reveals the s, p and d bands, but also the appearance of an edge mode within the p bands. When we look at the emitted intensity in real space (Fig. 1.3i) we observe that, at the corresponding energies, the p modes are extended in all the optically pumped area, while the edge state is confined to the edge micropillar.
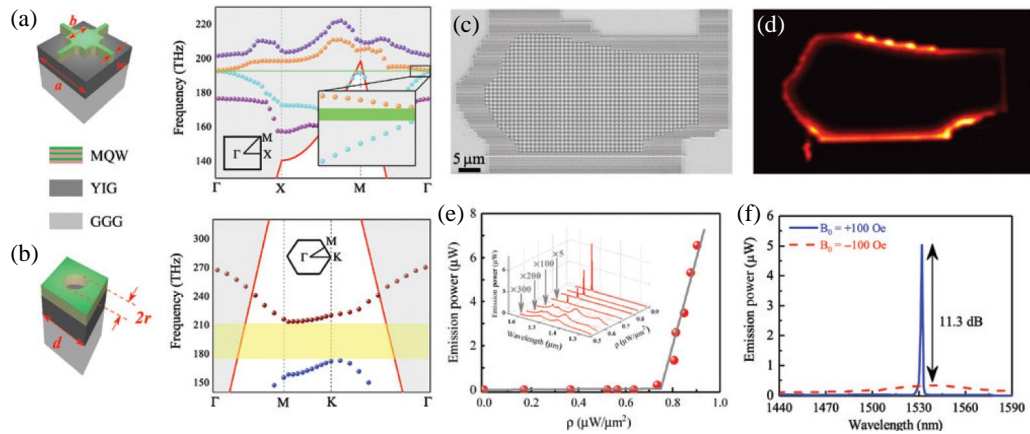
Figure 1.4: Sketches of the unit cell of the nontrivial square lattice **(a)** and of the trivial triangular lattice **(b)**. To their right one can find their respective energy band diagrams. **(c)** SEM picture of the topolaser. **(d)** Real-space camera image of the optically-pump device. **(e)** Emission power as a function of the pump density of the driving laser ρ and of wavelength. **(f)** Emission power as a function of wavelength for opposite directions of the magnetic field. Figure taken from [12], who adapted it from [88].

1.6.2   The two-dimensional IQH laser

Of course, having a point-like topologically-protected edge state was already a great success. However, 0D modes do not propagate, which leaves out of reach some of the most appealing properties of topological laser emission, like chiral transport immune to backscattering defects. Propagating 1D edge modes can instead be obtained by employing a 2D photonic topological insulator. We know from Sec. 1.1 that the most straightforward route to open a topological gap is to rely on time-reversal symmetry breaking. This is exactly what was proposed by Haldane and Raghu in Ref. [81, 82] in order to produce the analog IQH effect for photons. Such a system was first implemented by Ref. [10] in the microwave regime using a 2D photonic crystal made of ferrite rods, which is a magneto-optic material that breaks time-reversal symmetry for photons when an external magnetic field is applied. This led to the first observation of unidirectional photonic edge modes, which furthermore were found to be topologically protected against backscattering caused by a defect inserted in the lattice boundaries.

Motivated by the promising perspectives that the addition of gain to such a system holds, the first 2D topolaser was built by Ref. [88]. The authors employed a square lattice formed by star-like unit cells made of an active multi-quantum well structure on top a magneto-optic material (Fig. 1.4a). The band structure of this lattice under a uniform magnetic field perpendicular to the lattice plane shows a topological band gap (green-shaded region). The sum of the Chern numbers of the bands below this gap gives $|\sum \mathcal{C}| = 1$, which implies the existence of a chiral edge state in the lattice surface. This nontrivial square lattice was embedded inside a trivial triangular lattice with cylindrical air-hole unit cells (Fig. 1.4b). The band structure of this lattice features a broad gap (yellow-shaded area) even in the absence of the external magnetic field. In this case the sum of the Chern numbers of the bands below this band gap gives $\sum \mathcal{C} = 0$, and therefore this lattice cannot host chiral surface modes. The dimensions of the two lattices were chosen to overlap their band gaps around 1.5 μm, where the gain of the active material peaks. The edge modes are probed by means of a defect waveguide evanescently coupled to the square lattice. This was created by removing a line of air holes in the triangular lattice.

In order to test the topological protection of the edge states against local perturbations, an arbitrary-deformed geometry square lattice was designed (Fig. 1.4c) [3]. The external magnetic field was turned on and the system was probed by means of optical pumping with a laser. Fig. 1.4d shows a real-space camera image of the device, where the edge mode is clearly seen in the boundary between the two lattices. The authors also showed that this edge mode disappears when the

---

[3]The authors claim that their topological photonic crystal has a USA map-like shape. We kindly advise the reader to consult a tea leaves reader in order to get a more founded insight.
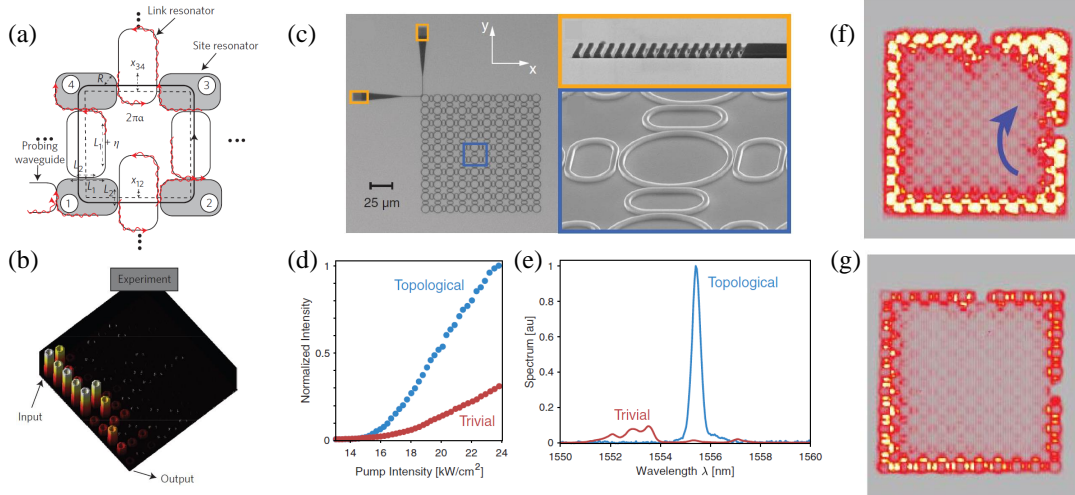
Figure 1.5: **(a)** Plaquette of the quantum spin-Hall insulator based on an array of silicon ring resonators implementing two copies of the Harper-Hofstadter model (see [11]). **(b)** The chiral helical mode is able to bypass a defect as a consequence of its topological protection. **(c)** SEM image of the active spin-Hall topolaser of [13]. **(d)** Output intensity as a function of the pump intensity for topological (with flux per plaquette $\alpha = 1/4$) and trivial ($\alpha = 0$) lattices. **(e)** Emission spectra for the two lattices. **(f)** Lasing response of the topological lattice in the presence of two defects intentionally inserted in the perimeter. **(g)** The same for the trivial lattice. Figure adapted from [11] and [13].

external magnetic field is removed (not shown in the Figure). Fig. 1.4e displays the emission power as a function of both the pump power density of the driving laser ρ and of wavelength. By increasing ρ, a threshold appears separating the trivial (non-lasing) regime from the spontaneous emission (lasing) regime. Remarkably, laser emission takes place at a single wavelength. The chiral character of the edge mode is confirmed by Fig. 1.4f, which shows the output of the probing waveguide. When the direction of the external magnetic field is reversed, the emission through the output waveguide is strongly suppressed, indicating that the edge mode has switched its propagation direction.

1.6.3 Quantum spin-Hall lasers

This Section is devoted to present topological lasers based on quantum spin-Hall insulators where time-reversal symmetry breaking is not required in order to obtain a nontrivial topology. Such systems were introduced in Sec. 1.4.

In particular, we will focus on topological lasers built upon the work of [11] in a passive (without gain) platform. This system consists on a 2D square lattice of silicon ring resonators, each supporting two degenerate whispering-gallery modes that propagate in clockwise (CW) and counterclockwise (CCW) directions. As a result, counterpropagating photons can be considered as carrying an opposite pseudospin-1/2. The site resonators forming the square lattice are connected via anti-resonant link resonators whose position and length is designed in such a way that photons circulating in a closed path around a plaquette in different directions get the opposite complex phase (see Fig. 1.5a). This implements two copies of the Harper-Hofstder model where photons belonging to different pseudospins experience opposite synthetic gauge fields. However, time-reversal symmetry is globally preserved as the magnetic fields for each pseudospin add up to zero.

As we learned in Sec. 1.4, a bosonic quantum spin-Hall system requires a negligible coupling between the two pseudospins in order to grant topological protection to the helical edge modes. This is, of course, the most critical point of the realization of [11]. However, the authors optimized the lattice by using directional couplers between ring resonators in order to obtain a very weak backscattering causing photons to change propagation direction. As a result, they observed the chiral helical states and demonstrated their immunity against local disorder such as a missing resonator on the lattice boundary (Fig. 1.5b).

The active version of such a platform was implemented by [13] by employing ring resonators built on top of InGaAsP quantum wells (Fig. 1.5c). One of the corner resonators is coupled to
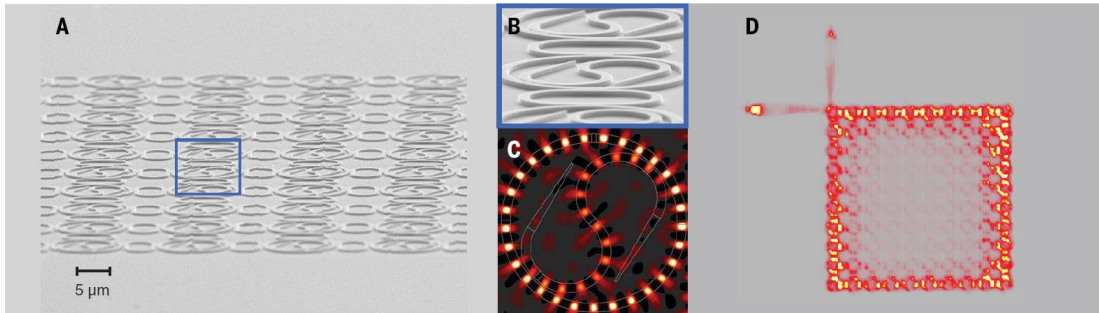
Figure 1.6: **(a)** SEM image of the quantum spin-Hall lattice of Taiji resonators (TJRs). **(b)** SEM image of the unit cell of the lattice. **(c)** Field distribution in an individual TJR, as obtained from finite-element simulations. **(d)** Measured spatial intensity profile when the perimeter of a lattice with flux per plaquette $\alpha = 1/4$ is optically pumped. Figure taken from [13].

an output waveguide that can be harnessed to assess the edge modes chirality. When the authors optically pumped the perimeter resonators of the lattice, they observed lasing in the helical modes. The topolaser features a larger slope efficiency compared with trivial lasing in a lattice with $\alpha = 0$ (Fig. 1.5d) and a single-wavelength spectrum around 1.5 μm (Fig. 1.5e). The topological protection is demonstrated when one of the resonators is removed from the perimeter: the helical modes are able to circumvent the defect and continue propagating (Fig. 1.5f), while in the trivial lattice lasing occurs in separated sections (Fig. 1.5g).

Of course, lasing in the topologically protected helical modes of a quantum spin-Hall lattice relies on the absence of coupling between the two pseudospins, i.e. on the lack of backscattering causing photons to reverse their propagation direction. In the setups of [11, 13] this is measured to be negligible thanks to an optimized lattice design and a well-established fabrication process leading to the absence of defects. However, even if these conditions are met, operational degradation can introduce disorder and rule out the topological protection of the helical modes.

In the next Subsection we will comment about the use of nonreciprocal elements in the experiments of [13] in order to grant topological protection to a single pseudospin even in arrays featuring spurious backscattering.

1.6.4 Nonreciprocity and quantum spin-Hall helical modes

Lorentz reciprocity is a general property of linear media characterized by spatially-symmetric electric permittivity and magnetic permeability tensors. In practice it implies that the transmittance through a reciprocal device must be direction-independent. Nonreciprocal devices are therefore necessary in order to build optical isolators allowing light to propagate in a certain direction only. The most common pathway employed in order to break reciprocity relies on the use of magneto-optic materials that break time-reversal symmetry. However, this is not the only possibility. For instance, as we will show in Chapter 2 one can exploit the Kerr nonlinearity of the material in devices breaking spatial-reversal symmetry in order to achieve a direction-dependent transmittance. We will study into detail Lorentz reciprocity and its implications in Sec. 2.2.

The authors of [13] decided to employ the latter route in order to preserve the topological protection of a single pseudospin of the quantum spin-Hall laser even in the presence of backscattering. The key ingredient is the so-called *Taiji resonator* (TJR), an all-silicon dielectric device breaking reciprocity solely due to the combination of nonlinearities and its parity-symmetry breaking shape. This consists of a ring resonator embedding an S-shaped waveguide which recirculates light from one of the two degenerate whispering-gallery modes supported into the other one, but forbids the opposite process. Of course, the direction of the S waveguide can be arbitrarily chosen in order to promote lasing in the desired pseudospin.

The TJR was employed as the site resonator of the active quantum spin-Hall insulator of [13] (see Fig. 1.6). The authors found that power recirculation through the S-like waveguide of the TJRs led to lasing in the favored pseudospin with more than 12 dB of intensity difference with respect to the opposite pseudospin. Fig. 1.6d shows the emitted intensity when the perimeter of a lattice featuring flux per plaquette $\alpha = 1/4$ is optically pumped. It can be clearly seen that the

majority of light exits the system via one of the two output couplings. This implies that intensity in the lattice is circulating predominantly in the CCW pseudospin.

This is great news: TJRs can be employed to solve the problem of pseudospin coupling in active bosonic quantum spin-Hall insulators, as they rule out the possibility of lasing in the unfavored pseudospin. However, a clear theoretical analysis of the pseudospin selection by active TJRs is still needed. Such a theory must take into account how does backscattering affect this process, and what level is tolerable. Also, further research about the mode competition for the gain saturation between the two surviving helical modes belonging to the same pseudospin is necessary. In the following Chapters we will shine more light on these open questions regarding the nonreciprocal behavior of TJRs and their role in quantum spin-Hall topolasers.

1.7 Concluding remarks

Prior to start discussing our original results, we would like to summarize the most important messages of the present Chapter.

The nontrivial topology of the energy bands of a given physical system stems from the geometrical properties of the wavefunction that describes it, which are encoded by means of an integer number known as Chern number. This is a topological invariant: its value cannot be changed by local perturbations preserving the band structure of the system. This has the remarkable consequence of producing chiral edge states at the boundaries of a topologically nontrivial material where the topological gap must be closed. A material hosting topological edge states while simultaneously presenting an insulating bulk is known as topological insulator. Although generalizations for interacting particles exist, in this Chapter we have focused on the noninteracting single-particle picture.

The most straightforward path to obtain a finite Chern number is to break time-reversal symmetry, for example by means of an external magnetic field. These are the so-called integer quantum Hall (IQH) systems. However, it is also possible to achieve a nontrivial topology while preserving time-reversal symmetry. This is realized in the so-called quantum spin-Hall effect, which features particles belonging to two different spins that are subjected to opposite gauge fields. As a result one has two copies of a topological insulator, one for each spin, that display counterpropagating edge modes labelled as helical modes. For fermionic particles even though spin-coupling processes are present at least a pair of helical modes is preserved; however in bosonic spin-Hall systems the helical modes are not robust against spin coupling.

Even though this physics was discovered in 2D electron gases the same behavior arises in quantum simulators like cold atoms and photonic systems. These platforms have the advantage of offering a larger degree of experimental control and parameter tunability, as well as highly-developed measurement techniques that cannot be applied in electron gases. In particular, the advent of topological photonics expanded the landscape of topological phases of matter due to the unique features of photons, like their bosonic and non-conservative nature. For instance, non-Hermitian topological photonics aims at exploring the interplay between topology and systems with gain and losses. The so-called topological lasers result from the addition of a saturable gain to the chiral edge states of a topological insulator, and have been shown to display an enhanced efficiency and robustness against disorder which outperforms their trivial analogs.

Very recently, a quantum spin-Hall laser was realized in a lattice of silicon ring resonators in which the two counterpropagating whispering-gallery modes supported by each resonator play the role of the two opposite pseudospins [13]. Backscattering coupling counterpropagating photons was very small and the topological protection of the helical modes was preserved. However, Ref. [13] also showed that a better strategy consists on promoting lasing in a single pseudospin by employing the so-called Taiji resonators (TJRs) instead of ring resonators. TJRs are ring resonators embedding an S-shaped element that recirculates the backscattered light into the lasing pseudospin.

The next Chapters are devoted to a complete study of nonlinear TJRs and their connections with Lorentz reciprocity breaking (Chap. 2), dynamical time-reversal symmetry breaking in the presence of a saturable gain (Chap. 3), and their use as optical isolators blocking counterpropagating light (Chap. 4). We finally capitalize on our insight about such devices to investigate the quantum spin-Hall laser made of TJRs (Chap. 5).

Chapter **2**

Lorentz reciprocity breaking in a single nonlinear Taiji resonator

In this Chapter we demonstrate an effective, nonlinearity-induced non-reciprocal behavior in a passive non-magnetic multi-mode Taiji resonator. Non-reciprocity is achieved by a combination of an intensity-dependent refractive index and of a broken spatial reflection symmetry. The work presented in this Chapter was carried out in collaboration with the experimental group of Prof. Lorenzo Pavesi at the University of Trento [1]. Our main results were published in [17].

Continuous wave power dependent transmission experiments show non-reciprocity and a direction dependent optical bistability loop. These can be explained in terms of the unidirectional mode coupling that causes an asymmetric power enhancement in the resonator. The observations are quantitatively reproduced by a numerical finite-element theory and physically explained by an analytical coupled-mode theory. Our results represent an important step towards the miniaturization of nonreciprocal elements for photonic integrated networks. Overall, Taiji resonators have exciting applications regarding single-mode lasing (see Chapter 3), optical isolators (see Chapter 4), and large arrays where to study the interplay between topological and non-Hermitian effects (see Chapter 5).

2.1 Introduction

Lorentz reciprocity is a fundamental property of electromagnetic fields propagating in linear and non-magnetic media [89]. In optics, it imposes that transmission through any device built by such media is independent on the direction of propagation. However, nonreciprocal elements such as optical isolators [15] play a crucial role in a variety of technological applications. Such devices only allow the transmission of signals in a certain direction: hence, they are employed to grant the appropriate operation of lasers in spite of spurious back-reflections and noise, and as the analog of diodes for photonic integrated circuits [90, 91, 92].

The usual path to optical non-reciprocity relies on employing magnetic elements that explicitly break the time-reversal $\mathcal{T}$ symmetry [93, 94, 10, 95, 96, 97, 98]. Due to the technical challenges associated to the monolithic integration of such elements into integrated photonics devices, alternative strategies compatible with state-of-the-art photonic technologies are being explored to circumvent Lorentz reciprocity. Time-dependent modulations of the material refractive index have been used but their operation requires an external driving field for the modulation and a large on-chip footprint [99, 100, 101, 102, 103]. Since the reciprocity theorem crucially relies on the linearity of the field equations, another promising avenue is to exploit optical nonlinearities of materials. A first configuration involved a cascade of two nonlinear resonators with different properties, which made transmission strongly direction-dependent [104]. Similar non-reciprocal devices were then

---

[1] R. Franchi and S. Biasi performed the experiments. A. Muñoz de las Heras derived the theoretical models and performed the numerical simulations.
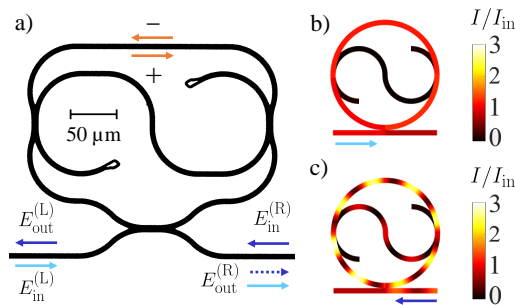
Figure 2.1: **a)** Optical image of the Taiji resonator (TJR) coupled to a bus waveguide. In the *forward* configuration (light blue arrows) light enters the sample from the left; in the *reverse* configuration (dark blue arrows) light is injected from the right. The dashed arrow represents the reflected light in the reverse case. The orange arrows indicate the propagation direction of clockwise ($+$) and counterclockwise ($-$) modes. **b,c)** Simulated intensity I (in units of the input intensity I_{in}) inside a TJR operating in the forward (b) and reverse (c) configurations for the same excitation frequency and power. The intensity maps are produced using the finite-element approach of Eq. (2.17). The physical parameters were chosen in order to improve the readability of the Figure.

studied exploiting complex resonator designs [105, 106], $\mathcal{PT}$-symmetric coupled cavities [107, 108], and two-beam interactions [109, 110]. Related nonlinearity-induced topology and unidirectional propagation phenomena were experimentally realized in [111].

In this Chapter, we combine material nonlinearities and a broken spatial reflection symmetry to observe an effective breaking of Lorentz reciprocity in a single multi-mode Taiji resonator. Taiji micro-ring resonators (TJRs) are formed by a microring with an S-shaped waveguide across as sketched in Fig. 2.1a. In the linear regime, reciprocity of the transmission across a TJR coupled to a bus waveguide is preserved and the effect of the S-shaped waveguide element is limited to an efficient unidirectional reflection [112]. Still, different optical powers are accumulated in the TJR depending on the direction of illumination (Fig. 2.1b,c). At large input powers this leads to a direction-dependent effective nonlinearity and, thus, to an effective non-reciprocal transmission. In addition to providing an intuitive explanation to the mechanism underlying this key nonreciprocal behavior, we also show the important practical advantages offered by TJR-based nonreciprocal elements in silicon photonics: a smaller footprint than previous non-magnetic proposals; an intrinsic degeneracy of the resonator modes which is protected by $\mathcal{T}$-reversal without the need for any fine tuning of the resonant frequencies of several devices; a reduced power threshold to non-reciprocity due to the use of the inter-mode nonlinearity and of the spatial overlap of the two degenerate modes.

The structure of the Chapter is the following: In Sec. 2.2 we study into detail Lorentz reciprocity theorem, the restrictions it imposes on the transmittance through a photonic device, and how we can overcome them. In Sec. 2.3 we develop an analytical coupled-mode theory of light propagation across the TJR and we make use of it to illustrate the reciprocity breaking for a TJR operating in the nonlinear regime. Sec. 2.4 presents all technical details of the experimental samples and the optical setup and summarizes the finite-element model used to describe *ab initio* the light propagation in our device. The experimental results are shown in Sec. 2.5 and compared to the theory. Conclusions are finally drawn in Sec. 2.6.

2.2   Lorentz reciprocity theorem and Taiji resonators

In this Section we would like to say a few words about what is Lorentz reciprocity, where does it stem from, its implications in the quest for optical isolation, and what strategies we can implement in order to construct nonreciprocal devices. At the end of the Section we introduce nonlinear TJRs and explain the physical mechanism by which they break reciprocity. More information about Lorentz reciprocity and optical isolators can be found in [15].

Lorentz reciprocity is a general property of linear media featuring spatially-symmetric electric permittivity ϵ and magnetic permeability μ tensors. Consider a couple of solutions to the Maxwell

equations in a source-free medium. They must satisfy

$$\nabla \times \mathbf{E}_{1,2} = -i\omega\mu\mathbf{H}_{1,2}, \quad \nabla \times \mathbf{H}_{1,2} = i\omega\epsilon\mathbf{E}_{1,2}. \tag{2.1}$$

After a bit of manipulation we can transform the equations above into the identity

$$\nabla \cdot (\mathbf{E}_1 \times \mathbf{H}_2 - \mathbf{E}_2 \times \mathbf{H}_1) = i\omega(\mathbf{E}_2\epsilon\mathbf{E}_1 - \mathbf{E}_1\epsilon\mathbf{E}_2 - \mathbf{H}_2\mu\mathbf{H}_1 + \mathbf{H}_1\mu\mathbf{H}_2). \tag{2.2}$$

In the case in which ϵ and μ are symmetric tensors the right-hand side of Eq. (2.2) is zero and thus we have

$$\nabla \cdot (\mathbf{E}_1 \times \mathbf{H}_2 - \mathbf{E}_2 \times \mathbf{H}_1) = 0. \tag{2.3}$$

This is the Lorentz reciprocity theorem. We can get a more profound physical insight about it by considering the electric currents $\mathbf{J}_{1,2}$ that give rise to the electric and magnetic fields $\mathbf{E}_{1,2}$ and $\mathbf{H}_{1,2}$, respectively. Using Maxwell's equations we can rewrite Eq. (2.3) as

$$\mathbf{J}_1 \cdot \mathbf{E}_2 = \mathbf{E}_1 \cdot \mathbf{J}_2. \tag{2.4}$$

This means that the field measured at one point generated by a source at a second point is the same as the field measured at the second point due to the same source at the first point.

An important corolary of Lorentz reciprocity theorem is that, in the case of photonic devices, transmission through such a reciprocal system must be identical if we interchange input and output. Hence, isolation cannot be realized if the system is reciprocal. In order to understand this we consider the scattering matrix S of such a device

$$\mathbf{b} = S\mathbf{a}, \tag{2.5}$$

which relates the input $\mathbf{a} = (a_1, a_2, ..., a_n)^T$ and output $\mathbf{b} = (b_1, b_2, ..., b_n)^T$ field amplitudes in the ports $1, 2, ..., n$. We assume that each port supports only one mode.

We can write the guided electric and magnetic fields orthogonal to the propagation direction as

$$\mathbf{E}_{t,m} = (a_m e^{-i\beta_m z} + b_m e^{i\beta_m z})\mathbf{e}_{t,m}, \tag{2.6}$$

$$\mathbf{H}_{t,m} = (a_m e^{-i\beta_m z} - b_m e^{i\beta_m z})\mathbf{h}_{t,m}, \tag{2.7}$$

where z points in the forward direction of each waveguide, $\mathbf{e}_{t,m}$ and $\mathbf{h}_{t,m}$ are unit vectors lying on the transverse $x-y$ plane, and β_m is the propagation constant of mode m. The orthonormalization condition between modes at different ports reads

$$\frac{1}{2} \int \int \mathbf{e}_m \times \mathbf{h}_n^* \cdot d\mathbf{S} = \delta_{m,n}, \tag{2.8}$$

where $\delta_{m,n}$ is the Kronecker delta.

In particular, if we take the surface of the optical device to lie at $z = 0$, we can express the electric and magnetic fields there as

$$\mathbf{E}_{t,m} = (a_m + b_m)\mathbf{e}_{t,m}, \tag{2.9}$$

$$\mathbf{H}_{t,m} = (a_m - b_m)\mathbf{h}_{t,m}. \tag{2.10}$$

For the sake of simplicity let us consider a device with two ports, labelled 1 and 2. Applying Gauss' theorem to a pair of electric and magnetic fields satisfying Eq. (2.3) (namely $\mathbf{E}'$, $\mathbf{H}'$, and $\mathbf{E}''$, $\mathbf{H}''$) and using the orthonormalization relation (2.8) we can write

$$\int \mathbf{E}' \times \mathbf{H}'' \cdot d\mathbf{S} = (a_1' + b_1')(a_1'' - b_1'') + (a_2' + b_2')(a_2'' - b_2'')$$

$$= \int \mathbf{E}'' \times \mathbf{H}' \cdot d\mathbf{S} = (a_1'' + b_1'')(a_1' - b_1') + (a_2'' + b_2'')(a_2' - b_2'). \tag{2.11}$$

The equation above can be simplified by employing the definition of the vectors $\mathbf{a}$ and $\mathbf{b}$, giving

$$\mathbf{b}' \cdot \mathbf{a}'' = \mathbf{a}' \cdot \mathbf{b}''. \tag{2.12}$$

We now introduce the scattering matrix (2.5), and thus we get

$$\mathbf{a}'^T S^T \mathbf{a}'' = \mathbf{a}'^T S \mathbf{a}''. \tag{2.13}$$

This implies that the scattering matrix must be symmetric, i.e.

$$S^T = S. \tag{2.14}$$

In particular, this means that the off-diagonal elements must be equal, i.e. $S_{12} = S_{21}$. Therefore, transmission must be the same if we switch the input and output directions. This fact forbids the possibility to build an optical isolator using reciprocal media. Such devices only display a non-zero transmittance in a certain direction, and therefore we would need $S_{12} \neq 0$ and $S_{21} = 0$ at the same time.

A crucial question at this point is how we can circumvent the Lorentz reciprocity theorem. Probably the most common path relies on breaking time-reversal symmetry by means of magneto-optic materials. In the presence of a magnetic field (either externally applied or because the material itself is ferromagnetic) this would result in asymmetric electric permittivity ϵ and magnetic permeability μ tensors. As a consequence, the right-hand side of Eq. (2.2) will in general yield a finite quantity, because matrix multiplication is not commutative. For example, the textbook Faraday effect produces a polarization rotation with opposite signs for backwards and forwards propagation. Some of the proposals relying on magneto-optic materials are based on waveguides displaying different propagation constants when light travels in opposite directions [93, 96], non-reciprocal losses [113], frequency splitting in resonators [94, 95], and the IQH effect for light in topological photonic crystals [10].

It is also possible to obtain an asymmetric scattering matrix by means of a time-dependent refractive index. This strategy relies on the presence of an external driving field producing a propagating perturbation of the refractive index which couples two specific forward-propagating modes but does not couple pairs of backward-propagating modes [114, 100].

However, time-reversal symmetry breaking is not the only possibility to break reciprocity. For a nonlinear material one has that the electric permittivity tensor ϵ depends on the electric field, and therefore $\mathbf{E}_1 \epsilon(\mathbf{E}_2) \mathbf{E}_2 \neq \mathbf{E}_2 \epsilon(\mathbf{E}_1) \mathbf{E}_1$. This implies that in general one cannot neglect the right-hand side of Eq. (2.2), as we did to demonstrate Lorentz reciprocity theorem in linear media. Therefore, another class of nonreciprocal systems rely on exploiting optical nonlinearities. We can mention devices based on Raman amplification [115], stimulated Brillouin scattering [116], chirped nonlinear photonic crystals [117, 118], and the direction-dependent resonance frequency shift produced by a Kerr optical nonlinearity [109, 110].

The nonlinear Taiji resonator (TJR) studied in this Thesis falls in the latter category. As it is shown in Fig. 2.1a, TJRs support whispering-gallery modes propagating in clockwise (CW) and counter-clockwise (CCW) directions, whose pairwise degeneracy is protected by $\mathcal{T}$-reversal. The effect of the S-shaped waveguide is to unidirectionally couple light from the CW mode into the CCW one, while both modes display the same effective loss rate. In the *forward* configuration (Fig. 2.1b), light accesses the bus waveguide from its left side and excites the CCW mode of the resonator through a directional coupler, but does not propagate into the S-shaped waveguide. On the other hand, in the *reverse* configuration (Fig. 2.1c) light enters the bus waveguide from the right and excites the CW mode; via the S-shaped waveguide it partially transfers excitation into the CCW one. The resulting increase of the total light intensity stored in the resonator, combined with an intensity-dependent nonlinear refractive index, is at the heart of the Lorentz reciprocity breaking.

In the following Section we will employ the coupled-mode equations for the field amplitudes in each mode to demonstrate that this asymmetry leads to a different transmittance in each configuration.

2.3 Theory

This Section is devoted to introduce the temporal coupled-mode theory [119, 120] that will guide our experimental analysis. In particular, here we make use of this simplified model in order to show that the optical power inside a nonlinear TJR exhibits a direction-dependent bistability loop when probed with large-intensity signals. This ultimately gives rise to parameter ranges where transmittance is very different in the two configurations.
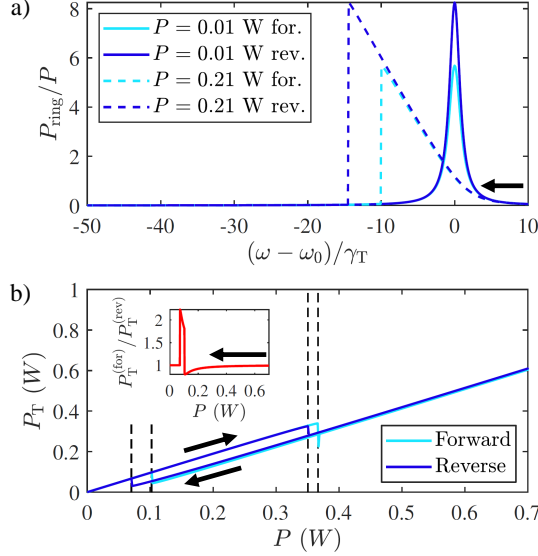
Figure 2.2: **a)** Simulated internal power P_{ring} for a downwards frequency sweep (black arrow) at two input powers P. Light (dark) blue curves refer to the forward (reverse) configuration. **b)** Simulated transmitted power P_{T} for a fixed frequency $\omega - \omega_0 \simeq -4\gamma_{\text{T}}$ in the forward and reverse configurations. Black arrows indicate the sweep direction. Black dashed lines label the threshold powers. The inset shows the ratio $P_{\text{T}}^{(\text{for})}/P_{\text{T}}^{(\text{rev})}$ of the transmitted powers in the forward and reverse configurations along a decreasing P ramp. Parameters for both panels: $L \simeq 850$ μm, $L_{\text{S}} = L/2$, $k_{\text{w}} = k_{\text{S}} = 0.14$, $\gamma_{\text{A}} = 5.7 \times 10^9$ s^{-1}, $n_{\text{L}} = 1.83$, $n_{\text{T}} = 8.8 \times 10^{-13}$ cm^2/W, $A = 0.66$ μm^2, and $g = 1$.

We start by writing the coupled-mode equations describing the electric field amplitudes in each counterpropagating mode of the TJR. A complete derivation of these equations can be found in Appendix A. Focusing on the neighborhood of a TJR resonance (with resonance frequency ω_0), let us assume a monochromatic excitation at ω, a weak coupling of the microring to the S-shaped waveguide and to the bus waveguide (real valued coupling coefficients $k_{\text{S}}, k_{\text{w}} \ll 1$), and a power dependent refractive index of the TJR $n = n_{\text{L}} + n_{\text{NL}}I$, where I is the optical intensity in the TJR (see Fig. 2.1b,c) and n_{L}, n_{NL} are the linear refractive index and the nonlinear coefficient, respectively. The steady state of the electric field amplitudes $E_{\pm}$ in the CW (+) and CCW (−) modes reads

$$\omega E_+ = \omega_0 E_+ - \frac{n_{\text{NL}}}{n_{\text{L}}}\omega_0(|E_+|^2 + g|E_-|^2)E_+ - i\gamma_{\text{T}}E_+$$
$$- \frac{c}{Ln_{\text{L}}}k_{\text{w}}E_{\text{in}}^{(\text{R})}, \tag{2.15}$$

$$\omega E_- = \omega_0 E_- - \frac{n_{\text{NL}}}{n_{\text{L}}}\omega_0(|E_-|^2 + g|E_+|^2)E_- - i\gamma_{\text{T}}E_-$$
$$- \frac{c}{Ln_{\text{L}}}k_{\text{w}}E_{\text{in}}^{(\text{L})} - i\frac{c}{Ln_{\text{L}}}2k_{\text{S}}^2 e^{i\frac{\omega}{c}n_{\text{L}}L_{\text{S}}}E_+ . \tag{2.16}$$

The intensity inside the TJR is then given by $I = \epsilon_0 cn_{\text{L}}|E_+ + E_-|^2/2$ (where ϵ_0 is the vacuum permittivity and c is the vacuum speed of light). In the equations above, L and L_{S} are the microring and the S-shaped waveguide lengths, and γ_{T} is the TJR loss rate (see later). $E_{\text{in}}^{(\text{L})}$ and $E_{\text{in}}^{(\text{R})}$ are the input fields exciting the ring from the left and the right of the bus waveguide, while the output fields to the left and to the right are $E_{\text{out}}^{(\text{L})} = \sqrt{1 - k_{\text{w}}^2}\, E_{\text{in}}^{(\text{R})} + ik_{\text{w}}E_+$ and $E_{\text{out}}^{(\text{R})} = \sqrt{1 - k_{\text{w}}^2}\, E_{\text{in}}^{(\text{L})} + ik_{\text{w}}E_-$, respectively.

The strength of the nonlinearity is quantified by $n_{\text{NL}} = n_{\text{K}} + n_{\text{T}}$ which is the sum of the Kerr n_{K} and thermal n_{T} nonlinearities. Of particular interest is the parameter g which describes the nature of the TJR nonlinearity. $g = 2$ represents a spatially local Kerr nonlinearity [121, 122, 123]: this value can be understood by thinking in terms of the Feynman diagrams from the two possible processes in which counterpropagating photons can locally interact. On the other hand, $g = 1$ describes a thermo-optic nonlinearity [124] mediated by a homogeneous heating of the TJR
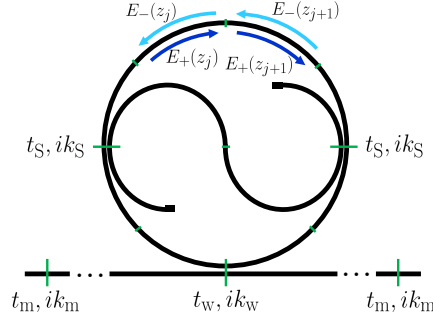
Figure 2.3: Scheme of the modelled Taiji resonator (TJR) showing the electric field amplitudes E inside each segment z_j (delimited by the short transverse lines) and the transmission and coupling amplitudes at each directional coupler (represented by the long transverse lines) $t_{\mathrm{w,S,m}}$ and $ik_{\mathrm{w,S,m}}$.

depending on the total energy that is dissipated in it. Appendix A includes an explicit derivation of these different factors, and also shows that intermediate situations in which both processes contribute to n_{NL} are described by $g = (2n_{\mathrm{K}} + n_{\mathrm{T}})/(n_{\mathrm{K}} + n_{\mathrm{T}})$. In our specific silicon-based TJR, we have $n_{\mathrm{T}} \gg n_{\mathrm{K}}$ and thus $g \simeq 1$.

The total effective loss rate $\gamma_{\mathrm{T}} = \gamma_{\mathrm{A}} + ck_{\mathrm{w}}^2/(2Ln_{\mathrm{L}}) + ck_{\mathrm{S}}^2/(Ln_{\mathrm{L}})$ is the same for the CW and CCW modes. It results from the sum of absorption γ_{A} and radiative losses into the bus and the S-shaped waveguides. Yet, the last term of (2.16) shows the asymmetric mode coupling introduced by the S-shaped waveguide: while all light lost by the CCW mode into the S-shaped waveguide is radiated away, part of the light transferred by the CW mode into the S-shaped waveguide is re-injected in the CCW mode. This is illustrated in Fig. 2.1b,c: In the forward configuration, only the CCW mode is excited and no reflection occurs. In the reverse one, both modes are excited, and marked interference fringes are visible in the intensity profile. As a result, for the same frequency and input power, the unidirectional mode coupling leads to a larger intensity inside the TJR in the reverse configuration than in the forward one.

While this asymmetry does not affect reciprocity in the linear regime of weak excitations [112], it has a major impact on the nonlinear response to strong fields. In Fig. 2.2a, we show the numerical prediction of the coupled-mode equations (2.15-2.16) for the internal power propagating in the ring $P_{\mathrm{ring}} = AI$ (with A the waveguide cross section). The input power $P = A\epsilon_0 cn_{\mathrm{L}}|E_{\mathrm{in}}|^2/2$ is kept at constant values while the frequency is scanned downwards across a resonance in forward and reverse configurations. At low input power the usual Lorentzian peak is found; though, because of the S-shaped waveguide, the internal power P_{ring} is higher in the reverse configuration. For a larger input power, the nonlinear refractive index causes a shift of the resonance proportional to the TJR internal power. In our $n_{\mathrm{NL}} > 0$ case, the shift is towards lower frequencies. At sufficiently large powers, both curves display a sudden downward jump right after the resonance, as typical in optical bistability [125, 126, 127, 128, 129]. Note that the position of the jump depends on the direction: the larger internal intensity in the reverse configuration allows for a larger shift of the resonance before jumping. This difference is responsible for a frequency window where the internal intensity in the two configurations is strikingly different.

This key feature is an example of the nonlinear breaking of reciprocity and is further illustrated in Fig. 2.2b. Here, we show the simulated transmitted power P_{T} as a function of the input power P for a fixed incident frequency $\omega - \omega_0 \simeq -4\gamma_{\mathrm{T}}$ in the optical bistability regime. As the input power grows, P_{T} displays a linear increase up to a threshold P_1 where a sudden jump down onto another stable solution occurs. On the way back, for decreasing P, the threshold P_2 for the upwards jump is such that $P_2 \ll P_1$. Thus, a bistability loop opens that can be understood as a metastability in a first order phase transition. Once again, the different values of the internal intensity P_{ring} in the forward and reverse cases lead to markedly different values for P_1 and P_2. This results in intensity windows where the transmitted powers in the two directions are very different, as shown in the inset.
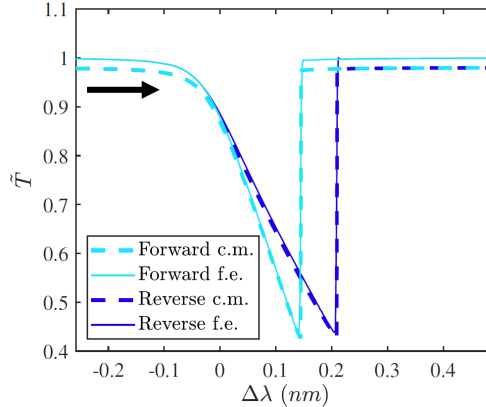
Figure 2.4: Normalized transmittance $\tilde{T}$ as a function of the relative wavelength shift with respect to the resonance wavelenght ($\Delta\lambda$) in an upwards ramp (indicated by the black arrow) for a TJR in the forward (light blue) and reverse (dark blue) configurations. The dashed curves were calculated by using the coupled-mode theory (c.m.), whereas the solid lines were obtained with the finite-element model (f.e.). The incident power is taken to be $P = 0.21$ W. The parameters of the simulations are those of Fig. 2.2.

2.4   Samples and optical setup

In order to verify our predictions, we fabricated integrated TJR devices using silicon oxynitride (SiON) single mode channel waveguides as shown in Fig. 2.1a [112]. The waveguide cross section is $A = 0.66$ μm^2. As measured in [130] at a wavelength $\lambda \simeq 1550$ nm, $n_L = 1.83$ and the linear absorption coefficient $\alpha = 3.5 \times 10^{-5}$ μm^{-1}. We estimated $n_T = (8.8 \pm 0.4) \times 10^{-13}$ cm^2/W from the fit of our experimental data, much larger than the typical Kerr nonlinear refractive index $n_K = 8 \times 10^{-16}$ cm^2/W of the material [130]. The length of the bus waveguide is approximately the same on both sides of the TJR. In order to avoid undesired mode couplings, the ends of the S-shaped waveguide have been designed with a particular geometry (looking as rhomboids in Fig 2.1a) which prevents back-reflections [131].

The optical setup employs a fiber-coupled continuous wave tunable laser operating at the wavelength range spanning from 1490 nm to 1640 nm. Its output is coupled to an Erbium-Doped Fiber Amplifier to get high power. Then, a polarization control stage sets the input light to the TM (transverse magnetic) polarization. Light is coupled in the bus waveguide by butt-coupling through a tapered fiber. The transmitted light is collected by a fiber and sent to an InGaAs detector. In order to switch between the forward and the reverse configurations, the sample is simply turned without any other change in the setup.

As it was reported in [112], the response of our samples is made more complicated by Fabry-Pérot oscillations in the transmittance due to reflections at the bus waveguide facets. Even though this does not affect the qualitative predictions of the coupled mode theory (2.15-2.16), a quantitative description requires taking this effect into account [2]. Besides, the coupled-mode theory is truncated at second order in the couplings $k_{w,S}$, and therefore it is not valid if the condition $k_{w,S} \ll 1$ is not met, as occurs for some of our fit parameters (see next Section). To this purpose, we have built a more refined finite-element model based on the solution of the nonlinear Helmholtz equation in our specific geometry. As it is detailed in Appendix B and in [112], the ring resonator as well as the S-shaped and the bus waveguides are appropriately segmented and propagation of the forward- and reverse-propagating waves along each segment of length $\Delta z \gg \lambda$ is described by the steady-state condition

$$E_{\pm}(z \pm \Delta z) = \exp\left\{i\left[\left(n_L + i\alpha\frac{c}{\omega}\right)\right.\right. \tag{2.17}$$

$$\left.\left. + n_T\frac{\Delta z}{L}\sum_{j=1}^{N}\left(|E_{\pm}(z_j)|^2 + |E_{\mp}(z_j)|^2\right)\right]\frac{\omega}{c}\Delta z\right\}E_{\pm}(z).$$

---

[2]A complete study regarding the role of the reflections at the bus waveguide facets can be found in the follow-up work [132].
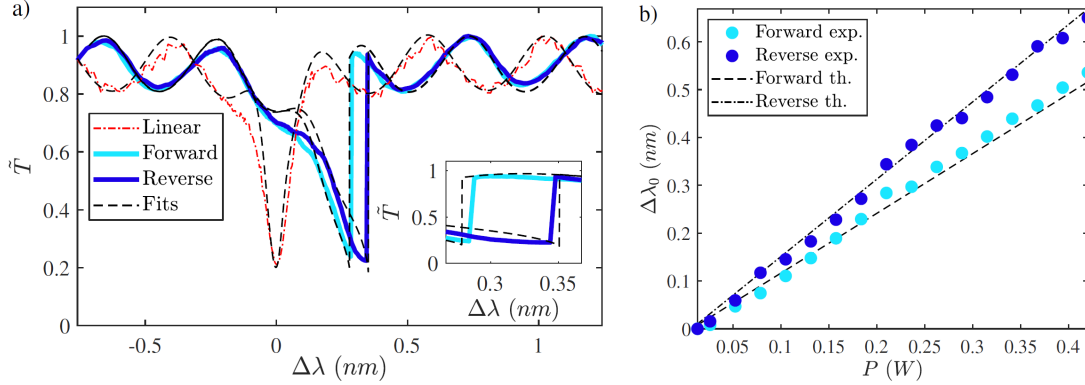
Figure 2.5: **a)** Normalized transmittance $\tilde{T} = T/T_{\max}$ as a function of the detuning $\Delta\lambda = \lambda - \lambda_0$ from the linear resonance wavelength for an upwards wavelength sweep (black arrow). The red dotted line represents the experimental transmittance in the linear regime for an input power $P \simeq 0.01$ W. The light (dark) blue solid curve corresponds to the experimental transmittance in forward (reverse) configuration at a fixed input power $P = 0.21$ W. The black dashed lines are theoretical fits of each experimental curve produced using Eq. (2.17). The inset gives a magnified view of the region of strongest nonreciprocal behavior. **b)** Shift $\Delta\lambda_0$ of the resonance wavelength as a function of the input power P for the resonance displayed in panel a). Light (dark) blue circles correspond to experimental data in forward (reverse) configuration. The black dashed (dotted) line is a linear fit to the theoretically calculated $\Delta\lambda_0$ in forward (reverse) configuration.

where the thermo-optic nonlinear refractive index of each element results from the averaged power within it. In the equation above we are neglecting the contribution of the local Kerr nonlinearity which, as we saw at the beginning of the present Section, is three order of magnitude smaller than the nonlocal thermo-optic nonlinearity. A complete expression accounting for the two types can be found in Appendix B. Mixing of the field in the different elements is provided by directional couplers, while reflection at both ends of the bus waveguide is taken as lossless with reflection amplitude ik_{m}.

A diagram of the simulated device is shown in Fig. 2.3. The TJR is assumed to be at the center of the bus waveguide. Whilst the sample employed in the experiment features an asymmetrical TJR with an optimized shape in order to reduce backscattering of light, to facilitate the calculations we employed a circular TJR with the same ring length.

In the following Subsection we show that this finite-element theory matches the coupled-mode theory in the appropriate limits and can be used to quantitatively fit our experimental data.

2.4.1   Coupled-mode theory and finite-element model in the weak coupling regime

Here we show that the finite-element simulations recover the coupled-mode theory results for the transmittance across the single nonlinear Taiji resonator in the weak coupling limit ($k_{\mathrm{w,S}} \ll 1$) without Fabry-Pérot oscillations ($k_{\mathrm{m}} = 0$). Fig. 2.4 displays the normalized transmittance $\tilde{T} = T/T_{\max}$ for a TJR operating in forward and reverse configurations as obtained by using both formalisms. The parameters of the simulations are those employed in Fig. 2.2 for an incident power $P = 0.21$ W. The agreement between both models is best found around resonance where the coupled-mode equations are valid. The discontinuities and the non-reciprocal window are found to lie at the same wavelengths in both simulations.

2.5   Experimental results

To probe the TJR response, we performed sweeps of the laser wavelength at fixed powers around the cold TJR resonance at $\lambda_0 = 1545.76$ nm. When operated at a small input power, $P \lesssim 0.03$ W, the thermal nonlinearity plays no role and the cold sample behaves as a linear device. Indeed, we observed the same transmittance T when pumped from the left or from the right. The linear transmittance normalized to its maximum value $\tilde{T} = T/T_{\max}$ is shown as a function of the detuning
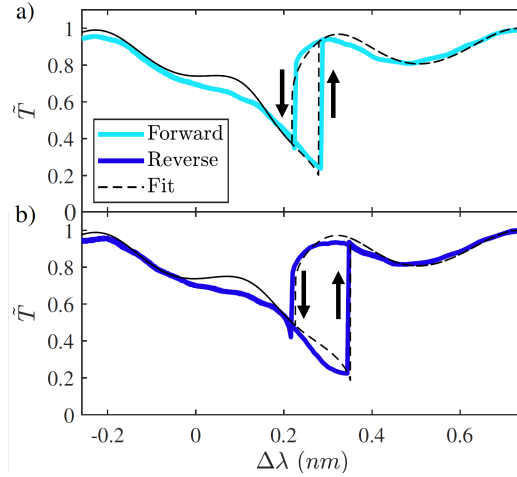
Figure 2.6: Optical bistability in the normalized transmittance $\tilde{T} = T/T_{\max}$ along a round-trip sweep of the laser detuning $\Delta\lambda$ across the resonance at a fixed input power $P = 0.21$ W. The ramp direction is indicated by the black arrows. Experimental data are shown as solid lines while the black dashed lines are the fits obtained with the finite-element theory of Eq. (2.17). **a)** Forward configuration (light blue). **b)** Reverse configuration (dark blue).

$\Delta\lambda = \lambda - \lambda_0$ from the resonance wavelength as the red dash-dotted line of Fig. 2.5a. From a fit of this curve with the theoretical model (black dashed lines), we extracted the coefficients $k_{\mathrm{w}} = 0.49 \pm 0.02$, $k_{\mathrm{S}} = 0.14 \pm 0.03$ and $k_{\mathrm{m}} = 0.24 \pm 0.04$. A list of all parameters employed in the fits of the experimental data can be found in Table 2.1.

R_{r}	135.11 μm	n_{L}	1.83
R_{S}	62.45 μm	n_{K}	8×10^{-16} cm^2/W
L_{L}	687.50 μm	n_{T}	$(8.8 \pm 0.4) \times 10^{-13}$ cm^2/W
L_{R}	687.50 μm	α	0.3454×10^{-4} μm^{-1}
A	0.66×10^{-8} cm^2	k_{w}	0.49 ± 0.02
N_{r}	8	k_{S}	0.14 ± 0.03
N_{S}	2	k_{m}	0.24 ± 0.04
N_{w}	4		

Table 2.1: Fit parameters: ring radius R_{r}, S waveguide radius R_{S}, bus waveguide length to the left L_{L} and right L_{R} of the TJR, waveguide cross section A, number of segments in which the ring, S and bus waveguides are divided $N_{\mathrm{r,S,w}}$, linear refractive index n_{L}, nonlinear Kerr refractive coefficient n_{K}, nonlinear thermal refractive coefficient n_{T}, absorption losses α, coupling parameters $k_{\mathrm{w,S}}$ for the ring-bus waveguide and ring-S waveguide couplers, and reflection amplitude k_{m} at the bus waveguide facets.

In order to investigate the nonlinear response, we then performed upwards wavelength ramps at larger input powers (an example for $P = 0.21$ W is shown in Fig. 2.5a). As predicted by the model (Fig. 2.2), the resonance dip in $\tilde{T}$ is pushed towards longer wavelengths by the nonlinearity due to the accumulated power in the TJR up to the threshold where $\tilde{T}$ jumps back to a value close to one. In the reverse configuration, since a larger intensity is present inside the resonator for the same input power, the resonance wavelength experiences a larger displacement than in the forward configuration. This is our first evidence of a nonlinearity-induced nonreciprocal behavior. A magnified view around the transition points where the difference is the largest is shown in the inset of Fig. 2.5a. Here, the ratio of the transmittance in the two directions reaches a value $T_{\mathrm{for}}/T_{\mathrm{rev}} \simeq 6$ dB at $\Delta\lambda \simeq 0.34$ nm. The displacement $\Delta\lambda_0$ of the resonance from its linear position as a function of the input power P is displayed in Fig. 2.5b: the non-reciprocity is clearly visible as a larger slope in the reverse case because of the higher internal power. The small deviations of the experimental points (circles) from a linear fit of the theory (lines) are mostly due to the Fabry-Pérot oscillations.

Further insight in this physics is provided by the bistability loops that are observed when
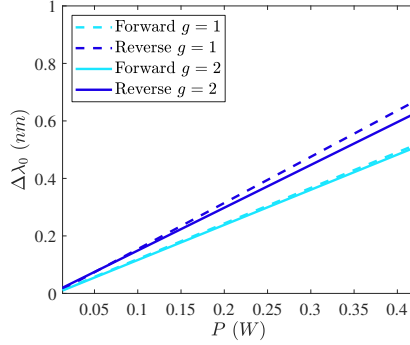
Figure 2.7: Shift of the resonance wavelength $\Delta\lambda_0$ with respect to its linear value $\lambda = 1545.76$ nm as a function of the input power P. All curves are linear fits of the numerically calculated data using the finite-element model. Dashed lines are the curves displayed in Fig. 2.5b for the experimental case of a thermo-optic nonlinearity with $n_{\mathrm{T}} = 8.8 \times 10^{-13}$ cm^2/W. Solid lines are obtained by employing a purely Kerr nonlinearity ($n_{\mathrm{T}} = 0$) whose strength has been artificially increased to $n_{\mathrm{K}} = 8.8 \times 10^{-13}$ cm^2/W to match the strength of the thermo-optic nonlinearity of the experiment. Light (dark) blue lines correspond to the forward (reverse) configuration.

comparing the transmittance along frequency ramps in upwards and downwards directions at the same fixed input power. In agreement with the coupled-mode theory of Fig. 2.2, the experimental observations in Fig. 2.6 show that the bistable loop observed in the reverse configuration (bottom) is wider than the one in the forward configuration (top), due to the different feedback caused by the S-shaped waveguide in the TJR. This is also reproduced by the finite element model (dashed lines).

Finally, it is worth wondering what would be different if our samples displayed a Kerr non-linearity instead of a thermo-optic one. In the following Subsection we investigate the difference between the resonance shift shown in Fig. 2.5b and that produced by a Kerr nonlinearity of the same magnitude.

2.5.1 Resonance shift for equivalent thermo-optic and Kerr nonlineari-ties

Here we compare the resonance shift $\Delta\lambda_0$ produced by the thermo-optic nonlinearity displayed by the single nonlinear Taiji resonator (TJR) with the one that would exhibit a fictitious TJR featuring a Kerr nonlinear parameter of the same magnitude $n_{\mathrm{K}} = 8.8 \times 10^{-13}$ cm^2/W and a negligible $n_{\mathrm{T}} \simeq 0$. In all calculations, $\Delta\lambda_0$ is measured with respect to the linear position of the resonance at $\lambda = 1545.76$ nm. Fig. 2.7 shows linear fits of the numerical results of the finite-element model in each case, which slightly deviate from the linear behaviour due to Fabry-Pérot oscillations: quite unexpectedly, for a given value of the input power the Kerr nonlinearity with $g = 2$ gives a slightly smaller nonlinear shift $\Delta\lambda_0$ than the thermo-optic nonlinearity ($g = 1$).

These numerical results can be physically understood using the coupled-mode equations (2.15-2.16). In the forward configuration light circulates in the CCW mode only and no significant difference between both kinds of nonlinearity arises. In the reverse configuration, one could have expected that the presence of the $g = 2$ factor in the Kerr nonlinear term of Eq. (2.16) would give a larger nonlinear shift $\Delta\lambda_0$ compared to the thermo-optical case. The complete calculation displayed here shows that this is not the case, since the very presence of this factor $g = 2$ quickly pushes the CCW mode out of resonance from the CW one and the pump laser. This results in a smaller value of the intensity in the CCW mode, which may well overcompensate the factor 2. As a result, the net effective nonlinear shift $\Delta\lambda_0$ turns out to be a bit smaller for a Kerr nonlinearity than for a thermal one at the same input power.

2.6   Conclusions and perspectives

In this Chapter we have demonstrated how the combination of optical nonlinearities and a spatially asymmetric design gives rise to an effective violation of reciprocity in a single non-magnetic multi-

mode Taiji resonator (TJR). This device goes one step beyond previous multi-resonator proposals and realizations in terms of integrability in silicon photonics circuits. The simplicity of its design allows a transparent theoretical analysis and facilitates its use as the unit cell of more complex structures.

The effective breaking of reciprocity is visible in the dependence of both the nonlinear shift of the resonance wavelength and the width of the optical bistability loop on the direction of illumination. The experimental observations are quantitatively reproduced by a finite-element model and the effect is intuitively understood by a coupled-mode theory in terms of the asymmetric coupling introduced by the S-shaped waveguide and the consequently different strength of the nonlinear feedback effect.

The nonreciprocal bandwidth can be extended by engineering TJRs built of highly nonlinear materials in a properly designed critical coupling regime maximizing the optical power inside the resonator, and by employing an optimized coupling with the S-shaped waveguide allowing to achieve simultaneously a high quality factor and a larger exchange of energy between the counterpropagating modes.

Once the nonreciprocal behavior of the passive nonlinear TJR is understood, our next step will be to consider the addition of a saturable gain to the coupled-mode equations (2.15-2.16) and investigate the role of the unidirectional coupling enabled by the embedded S element in promoting unidirectional lasing under strong incoherent pumping of the TJR [14]. Moreover, we will address whether unidirectional lasing in this device is also possible in the presence of spurious backscattering coupling the two counterpropagating modes. This will be the subject of Chapter 3.

Even though the work presented in the present Chapter demonstrates nonreciprocal transmission when waves are injected in the forward and reverse directions, in practice an optical isolator needs to block reverse-propagating noise while a forward-propagating signal is being simultaneously transmitted. Ref. [19] showed that if the frequency spectrum of the two counterpropagating waves does not overlap, nonreciprocity breaks down in the latter case. This is called *dynamic reciprocity*. We will propose an alternative that circumvents this problem and grants isolation under practical working conditions in Chapter 4.

Finally, in Chapter 5 we will explore the richer variety of nonlinearity-induced nonreciprocal effects in quantum spin-Hall topological insulator lasers made of TJRs in which backscattering is also present [97, 12, 21].

Chapter 3

Unidirectional lasing in a single nonlinear Taiji resonator

$\mathcal{I}$n this Chapter we develop a general formalism to study laser operation in active microring resonators supporting two counterpropagating modes. Our formalism is based on the coupledmode equations of motion for the field amplitudes in the two counterpropagating modes and a linearized analysis of the small perturbations around the steady state. We show that Taiji resonators introduced in Chapter 2 —i.e. devices including an additional S-shaped waveguide establishing an unidirectional coupling between both modes— feature a preferred chirality on the laser emission and can ultimately lead to unidirectional lasing even in the presence of sizable backscattering. The efficiency of this mode selection process is further reinforced by the Kerr nonlinearity of the material. This stable unidirectional laser operation can be seen as an effective breaking of $\mathcal{T}$-reversal symmetry dynamically induced by the breaking of the $\mathcal{P}$-symmetry of the underlying device geometry. This mechanism appears as a promising building block to ensure non-reciprocal behaviors in integrated photonic networks and topological lasers without the need for magnetic elements. The latter spin-off will be the core subject of Chapter 5. The main results of the present Chapter were published in [18].

3.1 Introduction

Ring resonator lasers have always received a great attention for both the interesting physics they host and their rich technological applications [133]. These systems support two degenerate counterpropagating modes in clockwise (CW) and counterclockwise (CCW) directions which are in strong mode competition. It has been shown that ring lasers can host stable unidirectional lasing in each direction [134], yet with the undesired possibility of spontaneous switching between the two states due to quantum fluctuations [135, 136, 137, 138]. Other unsought features include backscattering processes coupling the two counterpropagating modes and even light localization at defects [139, 140, 141, 142, 143]. This leads to a finite emission in the two directions and a spectral broadening of the emission with possible multi-mode behaviours and can even place the system in a self-oscillation regime where the intensity and phase of the emission periodically vary in time.

Preferential laser oscillation in one of the two counterpropagating modes is an appealing milestone due to the features that come alongside: increased output power, single-frequency spectrum, closer overlap with the gain profile, and improved mode stability, among others [144]. Stable unidirectional lasing in ring resonators has been investigated by adding an S-shaped waveguide element to the ring resonator, so to form a Taiji resonator (TJR). As we saw in Chapter 2, this S-shaped element breaks spatial reflection $\mathcal{P}$-symmetry as it allows light of one mode to couple into the other one but forbids the opposite process. Robust unidirectional operation in this laser was first demonstrated in the near-infrared in [14, 145] and then has been further extended to other wavelengths and cavity designs [146, 147, 148].
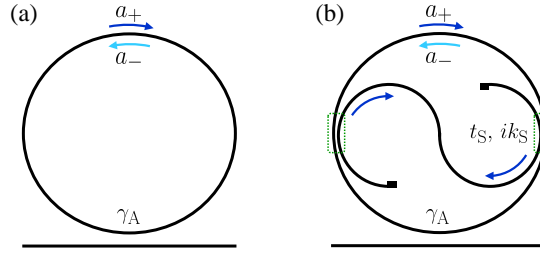
Figure 3.1: Schematic diagrams of the ring **(a)** and "Taiji" **(b)** microresonators. The field amplitudes of the clockwise (CW) and counterclockwise (CCW) modes are denoted by a_+ and a_-, respectively. In the Taiji microresonator (TJR) directional couplers of transmittance (coupling) amplitude t_S (ik_S) are signalized with the dashed green rectangles. The loss rate γ_A accounts for absorption and radiative couplings, for instance with a bus waveguide.

The active TJR has found further application in parity-time ($\mathcal{PT}$) symmetric micro-ring lasers [149] and non-Hermitian active structures [150], and holds great promise to explore the physics of exceptional points [151]. The idea of controlling the chirality of the laser emission via $\mathcal{P}$-symmetry breaking has also been exploited by establishing a loss imbalance [152], a coupling asymmetry between the two counterpropagating modes using two non-Hermitian nanoscatterers [153], and a bias in the pump direction [154]. As we saw in Chapter 1, active TJRs have started being employed [155, 13] as the building block of 2D topological lasers [7, 12] in order to select a preferential chirality for the surface modes and prevent backscattering reflections.

Notwithstanding the proven importance of TJRs to achieve unidirectional lasing and their connections with deeply rooted physical ideas, we still lack a complete theory describing their operation. In this Chapter we develop a general theory of lasing in active resonators featuring sizable couplings between counter-propagating modes such as ring and Taiji resonators. We analyze the steady-state solutions of the coupled-mode equations of motion for the fields' amplitudes and we study their stability by looking at the small fluctuations dynamics. In this way we prove the crucial advantage of including an S-shaped element to guarantee robust unidirectional lasing and protect it against spurious backscattering-mediated mode couplings, e.g. by disorder in the resonator and interface roughness. Finally, we show how this protection is reinforced in nonlinear resonators displaying an intensity-dependent refractive index.

The Chapter is organized as follows: In Sec. 3.2 we present the coupled-mode theory equations describing the system and the linearized approximation employed to assess the stability of their steady-state solutions. Sec. 3.3 makes use of these theoretical tools in order to study the laser emission of backscattering-free ring resonators (Sec. 3.3.1) and TJRs (Sec. 3.3.2). The effect of a weak backscattering is explored in Sec. 3.4, where we show the robustness of unidirectional lasing in TJRs. This analysis is then extended to larger values of the backscattering in Sec. 3.5. The positive effect of the optical nonlinearity on the unidirectional lasing is highlighted in Sec. 3.6. Conclusions are finally drawn in Sec. 3.7.

3.2   The physical system and the theoretical model

In this Section we mathematically describe an active resonator using the coupled-mode equations of motion for the field amplitudes of the CW and CCW modes. We then solve these equations for the long-time steady states for different values of the system parameters. We also present the linearized approximation that allows us to study the stability of the steady-states under small fluctuations.

We consider a ring resonator of circumference L_0 (see Fig. 3.1a) and the equivalent TJR with the same perimeter enclosing an S-shaped waveguide (shown in Fig. 3.1b). Without loss of generality the S waveguide was chosen to couple the CW into the CCW mode but not viceversa. The two elements of the TJR are coupled at two points separated by a distance L_S via lossless and reciprocal directional couplers with transmission and coupling amplitudes given by t and ik, respectively (t and k are real numbers satisfying $t^2 + k^2 = 1$). The S waveguide tips are assumed to feature a *reflection killer* geometry where light is scattered away, thus preventing back-reflections [131].

The ring resonator case is recovered from the TJR equations by setting $t = 1$. Even though we considered a circular external perimeter, the model and its results are still valid for any other shape, like racetrack or square-like resonators. In realistic experiments the shape of the external waveguide can be optimized to reduce backscattering.

In all cases the resonator supports two counterpropagating modes in CW ($+$) and CCW ($-$) directions whose amplitudes $a_\pm$ can be described using an extended version of the coupled-mode equations of motion introduced in Chapter 2 which accounts for the saturable gain [156, 157, 158, 159]

$$i\dot{a}_\pm = \omega_0 a_\pm - \frac{n_{\mathrm{NL}}}{n_{\mathrm{L}}}\omega_0 \left(|a_\pm|^2 + g|a_\mp|^2\right) a_\pm + i\frac{P_0}{1 + \frac{1}{n_{\mathrm{S}}}(|a_\pm|^2 + \xi|a_\mp|^2)} a_\pm - i\gamma_T a_\pm + \beta_{\pm,\mp} a_\mp, \quad (3.1)$$

where ω_0 is the resonance frequency of the resonator, n_{L} is the dimensionless linear refractive index, n_{NL} quantifies the strength of the optical nonlinearity, and g is a dimensionless parameter describing the character of the nonlinearity. As discussed in Chapter 2, $g = 1$ represents a nonlocal thermo-optic nonlinearity, while $g = 2$ describes a purely local Kerr-like one.

The key novelty of Eq. (3.1) with respect to the coupled-mode theory equations (2.15-2.16) for the passive TJR is the introduction of a saturable gain term featuring an amplification rate P_0 and a gain saturation coefficient n_{S}. The nature of the saturable gain is summarized in the cross-coupling parameter ξ: while a homogeneously broadened gain medium yields a spatially local saturable gain described by $\xi = 2$, an inhomogeneously broadened gain medium gives rise to a spatially non-local saturable gain featuring $\xi < 2$ [160]. As we will see in Sec. 3.3, the value of ξ ultimately governs the mode competition for gain: in particular, for $\xi \simeq 1$ lasing can be obtained simultaneously in the two modes of a backscattering-free ring resonator. However, the saturable gain in ring resonator lasers is usually provided by a collection of quantum wells, and therefore falls in the $\xi = 2$ category. Therefore, in this Chapter we will focus on lasers featuring either $\xi = 1$ or $\xi = 2$, even though the results in this latter case also apply to media described by $1 < \xi < 2$. In any case, we will always consider a class-A laser in which the dynamics of the reservoir of incoherent excitations giving rise to the saturable gain is very fast in comparison with all the other timescales of the problem, and therefore can be integrated out in the saturable gain term [161, 162]. In practice, this implies that the response of the gain medium to the light intensity in the resonator is instantaneous.

The total losses $\gamma_{\mathrm{T}} = \gamma_{\mathrm{A}} + \gamma_{\mathrm{S}}$ include the intrinsic absorption and radiative losses γ_{A} of the ring (which for instance account for the coupling with a bus waveguide) and the effective losses due to radiation into the S waveguide $\gamma_{\mathrm{S}} = c\kappa_{\mathrm{S}}^2/L_0 n_{\mathrm{L}}$ (where c is the vacuum speed of light and κ_s is the amplitude for light insertion into the S waveguide). The generalized coupling coefficients $\beta_{\pm,\mp}$ account for all kinds of mode coupling, including backscattering and the S-waveguide couplings. A backscattering-free ring resonator features $\beta_{\pm,\mp} = 0$, while our backscattering-free TJR is described by $\beta_\pm = 0$, $\beta_\mp = -i2ck_{\mathrm{S}}^2 e^{i\omega_0 n_{\mathrm{L}} L_{\mathrm{S}}/c}/L_0 n_{\mathrm{L}}$ [1].

In this coupled-mode formalism, the loss $\gamma_{\mathrm{S,A,T}}$ and amplification P_0 rates as well as the generalized coupling coefficients $\beta_{\pm,\mp}$ have the same units of inverse time as the resonance frequency ω_0. On the other hand, some arbitrariness exists for the choice of the normalization and, even, the units of the field amplitudes $a_\pm$: in the quantum literature, they are often normalized so that their squared modulus $|a_\pm|^2$ give the number of photons present in each mode. In the photonics literature, one rather normalizes them so that their squared modulus $|a_\pm|^2$ corresponds to the light intensity (usually expressed in W/cm^2) circulating around the cavity in each mode. With this choice, n_{S} also has the dimension of an intensity, while n_{NL} has the usual meaning of a non-linear refractive index with the dimension of an inverse intensity and can be directly extracted from tables of material parameters.

Our calculations have been carried out with a silicon photonics implementation in mind. As typical parameters, we considered a resonator of perimeter $L_0 = 20$ μm and S-waveguide length $L_{\mathrm{S}} = L_0/2$, a refractive index $n_{\mathrm{L}} = 3.5$ and a loss rate $\gamma_{\mathrm{A}} = 6.8 \times 10^9$ s^{-1} (or equivalently $\gamma_{\mathrm{A}} n_{\mathrm{L}}/c = 8 \times 10^{-5}$ μm^{-1}). For a resonance wavelength of 1.55 μm, corresponding to a frequency $\omega_0 \sim 2\pi \times 194$ THz, this gives a quality factor for the ring resonator (without S element) of about $Q \sim 1.5 \times 10^5$.

But a key advantage of our coupled-mode formalism is its independence from the specific physical realization, where all physical parameters of the system are summarized into a few parameters.

---

[1] Of course all results in this Chapter are directly transferred to TJRs where the S waveguide recirculates light in the opposite direction from the CCW mode into the CW one. To do this, it is enough to exchange the indices $+ \leftrightarrow -$.

As one can see in what follows, all figures can be plotted in terms of adimensional quantities of transparent physical meaning: rates are normalized in units of the (experimentally accessible) loss rate or linewidth $\gamma_{A,T}$ of the passive system; the amplification appears in the ratio P_0/γ_T characterizing the relative pumping compared to the laser threshold. These choices make the translation of our results into physical units a straightforward task for any given system once its basic parameters are known.

In order to simulate the response of the resonators we numerically solved Eq. (3.1) for the long-time ($t \to \infty$) steady states $a_\pm^{(0)}$ employing a 4th order Runge-Kutta algorithm and starting from random initial conditions at $t = 0$. As we will see in the following Sections, in general the steady states oscillate at a single frequency and therefore it is useful to define $\tilde{a}_\pm = a_\pm e^{-i\omega t}$, where ω is a reference frequency. The stationary values of the field amplitudes $\tilde{a}_\pm^{(0)} = \tilde{a}_\pm(t \to \infty)$ satisfy $\partial_t \tilde{a}_\pm^{(0)} = 0$ and therefore we can write the steady-state equation

$$0 = (\omega_0 - \omega)\tilde{a}_\pm^{(0)} - \frac{n_{\mathrm{NL}}}{n_{\mathrm{L}}}\omega_0 \left(|\tilde{a}_\pm^{(0)}|^2 + g|\tilde{a}_\mp^{(0)}|^2\right)\tilde{a}_\pm^{(0)} + i\frac{P_0}{1 + \frac{1}{n_{\mathrm{S}}}(|\tilde{a}_\pm^{(0)}|^2 + \xi|\tilde{a}_\mp^{(0)}|^2)}\tilde{a}_\pm^{(0)} - i\gamma_{\mathrm{T}}\tilde{a}_\pm^{(0)}$$
$$+ \beta_{\pm,\mp}\tilde{a}_\mp^{(0)} . \tag{3.2}$$

We now describe the linearized approximation employed to assess the stability of the steady-state solutions to Eq. (3.1). We start by writing the field amplitudes $\tilde{a}_\pm$ as the sum of the stationary states $\tilde{a}_\pm^{(0)}$ satisfying Eq. (3.2) and the small fluctuations $|\delta\tilde{a}_\pm| \ll |\tilde{a}_\pm^{(0)}|$, i.e. $\tilde{a}_\pm = \tilde{a}_\pm^{(0)} + \delta\tilde{a}_\pm$. Introducing these expressions into Eq. (3.1) and keeping fluctuations at linear order $\mathcal{O}(\delta\tilde{a}_\pm)$ we arrive to the equations

$$i\frac{d}{dt}\begin{bmatrix}\delta\tilde{a}_+ & \delta\tilde{a}_+^* & \delta\tilde{a}_- & \delta\tilde{a}_-^*\end{bmatrix}^T = A\begin{bmatrix}\delta\tilde{a}_+ & \delta\tilde{a}_+^* & \delta\tilde{a}_- & \delta\tilde{a}_-^*\end{bmatrix}^T, \tag{3.3}$$

where the matrix A is given by

(3.4)

Altogether, Eqs. (3.3-3.4) describe the fluctuation dynamics. The steady states described by Eq. (3.2) are asymptotically stable whenever all eigenvalues of the matrix A in Eq. (3.4) have a negative imaginary part. This means that fluctuations are damped out as $t \to \infty$ and the steady states behave as attractors in the (a_+, a_-) space.

Figure 3.2: **(a,b)** Steady-state intensity of the CW ($|\tilde{a}_+^{(0)}|^2$) and CCW ($|\tilde{a}_-^{(0)}|^2$) modes for a backscattering-free ring resonator laser as a function of the pump rate P_0. Panel (a) refers to an inhomogeneously broadened gain medium with $\xi = 1$, while panel (b) corresponds to a homogeneously broadened gain medium ($\xi = 2$). The black dashed line represents the total intensity summed over the two directions. **(c,d)** Imaginary part of the system eigenvalues λ for a ring resonator laser as a function of the pump rate P_0. Panel (c) refers to an inhomogeneously broadened gain medium with $\xi = 1$, while panel (d) corresponds to a homogeneously broadened gain medium ($\xi = 2$). The numbers below the curves indicate their degeneracy.

Figure 3.3: **(a,b)** Steady-state intensity of the CW ($|\tilde{a}_+^{(0)}|^2$) and CCW ($|\tilde{a}_-^{(0)}|^2$) modes for a backscattering-free TJR laser as a function of the pump rate P_0. Panel (a) refers to an inhomogeneously broadened gain medium with $\xi = 1$, while panel (b) corresponds to a homogeneously broadened gain medium ($\xi = 2$). The black dashed line represents the total intensity summed over the two directions. **(c,d)** Imaginary part of the system eigenvalues λ for a TJR laser as a function of the pump rate P_0. Panel (c) refers to an inhomogeneously broadened gain medium with $\xi = 1$, while panel (d) corresponds to a homogeneously broadened gain medium ($\xi = 2$). The numbers below the curves indicate their degeneracy.

3.3 Backscattering-free resonators

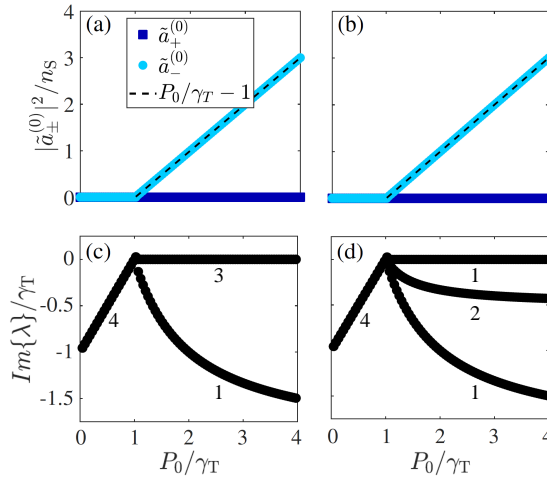In this Section we present the results for the paradigmatic cases of a ring resonator and a TJR without backscattering. We solve Eq. (3.1) to find the possible steady-state solutions and plug them into Eqs. (3.3-3.4) in order to determine their stability. We will also address the role of the cross-coupling parameter ξ in the saturable gain. The analysis in this Section is valid in both the linear and nonlinear regimes, regardless of the optical nonlinearity kind (given by g). Without loss of generality, the field amplitudes $\tilde{a}_\pm$ can be taken as real quantities by choosing a rotating reference frame co-moving with the (possibly nonlinear-shifted) resonance frequency of the resonator.

3.3.1 Ring resonator

We begin by studying the solutions to Eq. (3.1) in the simplest backscattering-free ring resonator case (i.e. $t = 1$, $\beta_{\pm,\mp} = 0$). Fig. 3.2 shows the steady-state intensities $|\tilde{a}_\pm^0|^2$ of both modes (panels (a) and (b)) together with the imaginary parts of the eigenvalues of the fluctuation dynamics matrix (3.1) (panels (c) and (d)) for growing values of the pump rate from $P_0 = 0$ to $P_0 = 4\gamma_{\rm T}$ in the $\xi = 1$ (panels (a) and (c)) and $\xi = 2$ (panels (b) and (d)) cases. In both situations, below the lasing threshold $P_0 < \gamma_{\rm T}$ the intensity $|\tilde{a}_\pm^{(0)}|^2$ of both modes is zero and the four eigenvalues

$$\lambda_{1,2} = +(\omega_0 - \omega) + i(P_0 - \gamma_{\rm T}), \tag{3.5}$$

$$\lambda_{3,4} = -(\omega_0 - \omega) + i(P_0 - \gamma_{\rm T}), \tag{3.6}$$

feature the same negative imaginary part. Since gain saturates with $\tilde{a}_\pm^{(0)}$, in this regime the only possible stable solution is that no coherent light is present. Above the lasing threshold $P_0 > \gamma_{\rm T}$ the eigenvalues change to

$$\lambda_1/\gamma_{\rm T} = -\frac{n_{\rm NL}}{n_{\rm L}}\omega_0(g-1)n_{\rm S}\left(\frac{P_0}{\gamma_{\rm T}} - 1\right) + i\left(\frac{P_0/\gamma_{\rm T}}{1 + \xi(P_0/\gamma_{\rm T} - 1)} - 1\right), \tag{3.7}$$

$$\lambda_2/\gamma_{\rm T} = +\frac{n_{\rm NL}}{n_{\rm L}}\omega_0(g-1)n_{\rm S}\left(\frac{P_0}{\gamma_{\rm T}} - 1\right) + i\left(\frac{P_0/\gamma_{\rm T}}{1 + \xi(P_0/\gamma_{\rm T} - 1)} - 1\right), \tag{3.8}$$

$$\lambda_3 = 0, \tag{3.9}$$

$$\lambda_4/\gamma_{\rm T} = -2i\frac{P_0/\gamma_{\rm T} - 1}{P_0/\gamma_{\rm T}}. \tag{3.10}$$

The $\xi = 1$ case presents a particular behaviour as it is the only situation in which the system shows effective gain in both directions and features a threefold degenerate imaginary part $Im\{\lambda_{1,2,3}\} = 0$. This is due to the phase freedom of each direction and the CW $\leftrightarrow$ CCW symmetry which is present in this case only. Beyond the bifurcation point both intensities depart linearly with randomly-chosen values satisfying $(|\tilde{a}_+^{(0)}|^2 + |\tilde{a}_-^{(0)}|^2)/n_{\rm S} = P_0/\gamma_{\rm T} - 1$.

For a homogeneously broadened gain medium ($\xi = 2$) the resonator lases randomly in one mode only with equal probability as $|\tilde{a}_\pm^{(0)}|^2/n_{\rm S} = P_0/\gamma_{\rm T} - 1$, while the other one remains unamplified. This is also true for intermediate values $1 < \xi < 2$. In contrast to the $\xi = 1$ case, now the linearized analysis features a single imaginary part (since $Im\{\lambda_{1,2,4}\} \neq 0$) corresponding to the Goldstone mode $\lambda_3 = 0$. Due to the asymmetric gain amplification terms in Eq. (3.1) a larger intensity in a certain direction randomly determined by the initial conditions leads to a smaller amplification in the other one. As t evolves this asymmetry drives the system into a unidirectional lasing state in the randomly favored mode, while the other is killed.

By employing a Fourier transform we were able to ascertain that for $P_0 > \gamma_{\rm T}$ the steady-state field amplitudes $a_\pm^{(0)}$ oscillate in time at the nonlinear-shifted resonance frequencies $\omega_\pm$ of each mode. In the $\xi = 1$ case these are given by

$$\omega_\pm = \omega_0 - \frac{n_{\rm NL}}{n_{\rm L}}\omega_0(|\tilde{a}_\pm^{(0)}|^2 + g|\tilde{a}_\mp^{(0)}|^2), \tag{3.11}$$

while for $\xi > 1$ the intensity in one of the two directions vanishes and one has either

$$\omega_\pm = \omega_0 - \frac{n_{\rm NL}}{n_{\rm L}}\omega_0|\tilde{a}_\pm^{(0)}|^2 \tag{3.12}$$

for unidirectional lasing in the CW or CCW direction, respectively.

In general, we found that no bidirectional lasing is observed for $\xi > 1$. This fact can be put on more solid grounds as follows. From Eq. (3.2) one sees that if both field amplitudes $\tilde{a}_{\pm}^{(0)}$ are taken as real numbers a finite intensity in the two directions (i.e. $\tilde{a}_{\pm}^{(0)} \neq 0$) would simultaneously imply

$$\frac{P_0}{1 + \frac{1}{n_{\mathrm{S}}}(|\tilde{a}_{\pm}^{(0)}|^2 + \xi|\tilde{a}_{\mp}^{(0)}|^2)} = \gamma_{\mathrm{T}}, \tag{3.13}$$

which necessarily sets $|\tilde{a}_{+}^{(0)}|^2 = |\tilde{a}_{-}^{(0)}|^2$. Diagonalizing the matrix in this case, one obtains the eigenvalues

$$\lambda_{1,2} = 0, \tag{3.14}$$

$$\lambda_3/\gamma_{\mathrm{T}} = +2i\frac{P_0/\gamma_{\mathrm{T}} - 1}{P_0/\gamma_{\mathrm{T}}}\frac{\xi - 1}{\xi + 1}, \tag{3.15}$$

$$\lambda_4/\gamma_{\mathrm{T}} = -2i\frac{P_0/\gamma_{\mathrm{T}} - 1}{P_0/\gamma_{\mathrm{T}}}. \tag{3.16}$$

Having $\xi > 1$ implies $\mathrm{Im}\{\lambda_3\} > 0$ and therefore this solution is unstable. We conclude that for $\xi > 1$ the only possible stable solutions involve unidirectional lasing in one of the two counter-propagating modes, randomly chosen by the initial conditions.

3.3.2   TJR

We now move on to the study of the stability of an active TJR under the same ramp in the pump rate employed in the previous Subsection. For these simulations we set $\gamma_{\mathrm{S}} = 0.2\gamma_{\mathrm{A}}$, $\beta_{\pm} = 0$, and $\beta_{\mp} = -i2ck_{\mathrm{S}}^2 e^{i\omega_0 n_{\mathrm{L}} L_{\mathrm{S}}/c}/L_0 n_{\mathrm{L}}$. We have neglected the nonlinear phase shift inside the S waveguide as the optical power inside it is very small compared to that circulating along the external waveguide.

Fig. 3.3 shows the steady-state intensities $|\tilde{a}_{\pm}^{(0)}|^2$ (in panels (a) and (b) for $\xi = 1$ and $\xi = 2$, respectively) and the imaginary part of the eigenvalues (in panels (c) and (d) for $\xi = 1$ and $\xi = 2$, respectively) for the family of steady-state solutions that are most commonly reached. Below the lasing threshold $P_0 < \gamma_{\mathrm{T}}$ the two directions feature a zero intensity for both interaction types. Above the lasing threshold $P_0 > \gamma_{\mathrm{T}}$ the intensity of the mode in which the S-waveguide coupling is directed (in our case the CCW) departs linearly from the bifurcation as $|\tilde{a}_{-}^{(0)}|^2/n_{\mathrm{S}} = P_0/\gamma_{\mathrm{T}} - 1$, while the other mode (the CW one) remains empty. The off-diagonal S-waveguide coupling in Eq. (3.4) does not change the eigenvalues of the linearized theory with respect to the ring resonator case and therefore they are given again by Eqs. (3.5-3.6) below threshold and by Eqs. (3.7-3.10) above threshold. As opposed to the ring resonator case, not even for $\xi = 1$ one can have a finite intensity in both modes simultaneously: the presence of the S waveguide breaks in fact the CW $\leftrightarrow$ CCW symmetry and favors unidirectional lasing in the CCW direction. As in the previous Subsection using a Fourier transform we found that above $P_0 > \gamma_{\mathrm{T}}$ the steady-state field amplitudes $a_{\pm}^{(0)}$ oscillate at the nonlinear-shifted resonance frequency of the resonator, which is taken as the reference frequency ω. For our TJR this is given by

$$\omega = \omega_0 - \frac{n_{\mathrm{NL}}}{n_{\mathrm{L}}}\omega_0|\tilde{a}_{-}^{(0)}|^2 \tag{3.17}$$

for any value of ξ.

While the unidirectional CCW-only solutions depicted in Fig. 3.3 are the steady-state that is most frequently reached by the numerics, it is important to verify whether other solutions are possible in specific parameter regimes. To this purpose, we considered Eq. (3.2) assuming a finite intensity in both modes, i.e. $\tilde{a}_{\pm}^{(0)} \neq 0$. Without loss of generality $\tilde{a}_{+}^{(0)}$ is taken to be a real number. From Eq. (3.2) this would require

$$\omega_0 - \omega = \frac{n_{\mathrm{NL}}}{n_{\mathrm{L}}}\omega_0(|\tilde{a}_{+}^{(0)}|^2 + g|\tilde{a}_{-}^{(0)}|^2), \tag{3.18}$$

$$\frac{P_0}{1 + \frac{1}{n_{\mathrm{S}}}(|\tilde{a}_{+}^{(0)}|^2 + \xi|\tilde{a}_{-}^{(0)}|^2)} = \gamma_{\mathrm{T}}, \tag{3.19}$$

$$\tilde{a}_{-}^{(0)} = \frac{i\frac{c}{L_0 n_{\mathrm{L}}}2\kappa_{\mathrm{S}}^2 e^{i\omega_0 n_{\mathrm{L}} L_{\mathrm{S}}/c}}{(\omega_0 - \omega) - \frac{n_{\mathrm{NL}}}{n_{\mathrm{L}}}\omega_0\left(|\tilde{a}_{-}^{(0)}|^2 + g|\tilde{a}_{+}^{(0)}|^2\right) + i\frac{P_0}{1 + \frac{1}{n_S}(|\tilde{a}_{-}^{(0)}|^2 + \xi|\tilde{a}_{+}^{(0)}|^2)} - i\gamma_T}\tilde{a}_{+}^{(0)}. \tag{3.20}$$
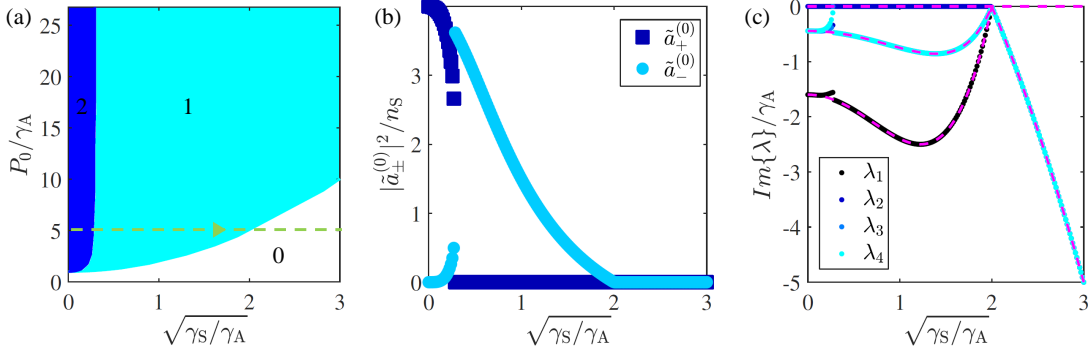
Figure 3.4: **(a)** Pump rate P_0 vs. square root of the S-coupling losses $\sqrt{\gamma_S}$ diagram for a backscattering-free TJR with $\xi = 2$ and $n_{NL} = 0$. The region where only the trivial solution is present is depicted in white. The light blue region represents the parameter range where only CCW lasing is possible. In the dark blue region two solutions exist: single-mode lasing in the preferred CCW direction and bidirectional lasing with $|\tilde{a}_+^{(0)}| \gg |\tilde{a}_-^{(0)}|$. Each region is labeled by the numbers 0, 1, and 2, respectively. **(b)** Normalized steady-state intensity $|\tilde{a}_\pm^{(0)}|^2$ obtained by numerically solving Eq. (3.1) as a function of $\sqrt{\gamma_S}$ for a fixed $P_0 = 5\gamma_A$ as indicated by the dashed horizontal line in (a). **(c)** Imaginary part of the system eigenvalues λ as a function of $\sqrt{\gamma_S}$ corresponding to the path shown as the dashed horizontal line of panel (a). The points are numerically calculated by diagonalizing the matrix A in Eq. (3.4) for the steady-state solutions displayed in panel (b). The dashed lines correpond to the analytic eigenvalues (3.5-3.10).

In particular, in the $g = \xi = 1$ case the first two conditions impose the denominator in Eq. (3.20) to vanish, which implies that $\tilde{a}_+^{(0)} = 0$.

To carry on this analysis when we have $g > 1$, $\xi > 1$, or both, we explored the phase space of the problem by numerically solving Eq. (3.1) using different values of P_0 and γ_S in order to explore its possible steady-state solutions. We found that stable bidirectional lasing is possible for values of P_0 and γ_S within the dark blue region of Fig. 3.4a. This kind of solutions involve a strong lasing in the CW direction and a smaller intensity populating the CCW due to the presence of a weak S coupling. For larger values of γ_S, $|\tilde{a}_-^{(0)}|^2$ increases up to a threshold in which the $\tilde{a}_+^{(0)} \neq 0$ solution disappears and only the $\tilde{a}_-^{(0)} \neq 0$ one remains. While this figure is plotted in the linear ($n_{NL} = 0$) regime and for a local saturable gain ($\xi = 2$), we have verified that the same conclusion holds for $n_{NL} \neq 0$ and other values of the g and ξ parameters. However, the larger the values of g and n_{NL} employed, the smaller is $|\tilde{a}_-^{(0)}|^2$ in the bidirectional solution and the larger the value of γ_S at which the transition to the single solution region takes place for a fixed P_0. This is a consequence of the different shifts of the resonance frequency for opposite directions introduced by nonlinearities with $g > 1$. On the other hand, when both $g, \xi \to 1$ the region featuring the bidirectional solution shrinks to smaller values of γ_S, ultimately disappearing for $g = \xi = 1$.

The light blue parameter range of Fig. 3.2 features a single solution with emission in the CCW mode only. The lower limit is given by the pump threshold $P_0 = \gamma_T$. Of course, this CCW-mode lasing solution also extends in the dark-blue region of Fig. 3.2 where it coexist with the other, bidirectional solution. Which of the two solutions is actually chosen by the system will depend on the initial conditions.

Panels (b) and (c) show the lasing intensity and the imaginary part of the eigenvalues (calculated by diagonalizing the matrix A in Eq. (3.4)) for the ramp depicted as the dashed line in panel (a), respectively. The initial conditions correspond to unidirectional lasing in the CW direction. As γ_S is increased the initially unfavored CCW mode gets rapidly populated and the emission intensity in the CW mode decreases. As this happens the imaginary part of one of the eigenvalues grows and eventually crosses zero towards positive values. At this point the solution becomes unstable and the system experiences a transition towards a unidirectional lasing regime in the CCW direction. Note that as γ_S grows, the total loss rate γ_T is also enhanced so that the CCW intensity decreases until the system ends up in the trivial solution.

We conclude that the presence of the S-shaped element breaking $\mathcal{P}$-symmetry in Eq. (3.1) rules out the possibility of pure unidirectional lasing solutions in the unfavored direction. For $g = \xi = 1$

not even bidirectional emission is possible and beyond the lasing threshold the system compulsory lases in a single direction with the preferential chirality introduced by the S waveguide. For other choices of the g, ξ coefficients bidirectional lasing is possible for a small enough S-coupling, but only for particular values of the parameters and always giving $|\tilde{a}_+^{(0)}|^2 \gg |\tilde{a}_-^{(0)}|^2$.

From a more abstract perspective, we can conclude this section by noting that, in contrast to what happens in a passive device or for a pump rate $P_0 < \gamma_\mathrm{T}$, the solution for $P_0 > \gamma_\mathrm{T}$ is not invariant under $\mathcal{T}$-reversal even though the underlying equations of motion are fully $\mathcal{T}$-reversal symmetric. We can therefore state that the presence of the $\mathcal{P}$-breaking S-shaped element induces a dynamical breaking of $\mathcal{T}$-symmetry above the lasing threshold.

3.4   Small backscattering

In this Section we study how the laser emission of active ring resonators and TJRs is affected by a random backscattering smaller in modulus than the intrinsic absorption and radiative loss rate γ_A of the ring. The analog analysis for a backscattering larger than γ_A can be found in Sec. 3.5. In both Sec. 3.4 and Sec. 3.5 the nonlinear shift of the resonance frequency of the resonator is neglected (i.e. we set $n_\mathrm{NL} = 0$). This effect will be studied in Sec. 3.6. As an inhomogeneously broadened medium yielding a nonlocal gain saturation is not representative of a semiconductor-based laser, starting from the present Section we will focus in the $\xi = 2$ case, although our results are also valid for values of ξ within the range $1 < \xi \leq 2$. As in Sec. 3.3 we employ the reference frequencies (3.12) and (3.17) which for $n_\mathrm{NL} = 0$ reduce to the resonance frequency of the resonator $\omega = \omega_0$.

In general, the effect of backscattering can be summarized by the Hermitian and non-Hermitian coefficients

$$h = -\frac{\beta_\mp + \beta_\pm^*}{2}, \tag{3.21}$$

$$n = i\frac{\beta_\mp - \beta_\pm^*}{2}, \tag{3.22}$$

defined in [163]. The former gives rise to a symmetric, conservative exchange of energy between the CW and CCW modes, while the latter introduces a different balance between the back-reflection in each mode that can lead to gain and losses beyond the saturable gain ($\propto P_0$) and losses ($\propto \gamma_\mathrm{T}$) terms in Eq. (3.1). Therefore we need $|n| \leq \gamma_\mathrm{T}$ in order to preserve the validity of our model.

The distinction between *small* and *large* backscattering made through this Chapter is referred to the loss rate without S couplings γ_A. By small backscattering we intend that it is at least one order of magnitude smaller than γ_A, i.e. $|h|, |n| \lesssim 10^{-1} \times \gamma_\mathrm{A}$. On the other hand, we labeled as large backscattering that which is at least comparable with γ_A, i.e. $|h| \gtrsim 10^{-1}\gamma_\mathrm{A}$. For all parameter choices, simulations are carried by solving Eq. (3.1) for different values of n and h and finding the $t \to \infty$ steady states $\tilde{a}_\pm^{(0)}$. As usual, the stability of the solutions is assessed by calculating the corresponding eigenvalues of the fluctuation dynamics matrix in Eq. (3.4).

3.4.1   Perturbative solution

Prior to the numerics we discuss the perturbative analytical solution of Eq. (3.1) valid for both the ring resonator and the TJR as microscopic backscattering is added. We assume that this is so small that the backscattering-free solution of Eq. (3.1) involving unidirectional lasing does not substantially change. In order to account for the small intensity in the suppressed mode we considered the backscattering couplings $\tilde{\beta}_{\pm,\mp}$ as the small perturbations to the backscattering-free ring resonator and TJR solutions explored in Sec. 3.3. The new coupling parameters for the ring resonator are $\beta_{\pm,\mp} = \tilde{\beta}_{\pm,\mp}$, while those for the TJR are $\beta_\pm = \tilde{\beta}_\pm$ and $\beta_\mp = -i2ck_\mathrm{S}^2 e^{i\omega_0 n_\mathrm{L} L_\mathrm{S}/c}/L_0 n_\mathrm{L} + \tilde{\beta}_\mp$. Without loss of generality, and in order to use the same indices in both cases, we considered an unperturbed solution in which the ring resonator lases unidirectionally in the CCW mode. We can then write the perturbed solutions as $\tilde{a}_\pm^{(0)} = \tilde{a}_{\pm,\mathrm{un}}^{(0)} + \delta\tilde{a}_\pm^{(0)}$, where $\tilde{a}_{\pm,\mathrm{un}}^{(0)}$ are the unperturbed solutions with $\tilde{\beta}_{\pm,\mp} = 0$. As shown in Sec. 3.3 these are given by $\tilde{a}_{+,\mathrm{un}}^{(0)} = 0$ and $|\tilde{a}_{-,\mathrm{un}}^{(0)}|^2/n_\mathrm{S} = P_0/\gamma_\mathrm{T} - 1$. On the other hand $\delta\tilde{a}_\pm^{(0)}$ are the first-order perturbative corrections. Introducing the perturbed solution into the steady-state given by Eq. (3.2) and staying at linear order $\mathcal{O}(\tilde{\beta}_{\pm,\mp})$, $\mathcal{O}(\delta\tilde{a}_\pm^{(0)})$ in
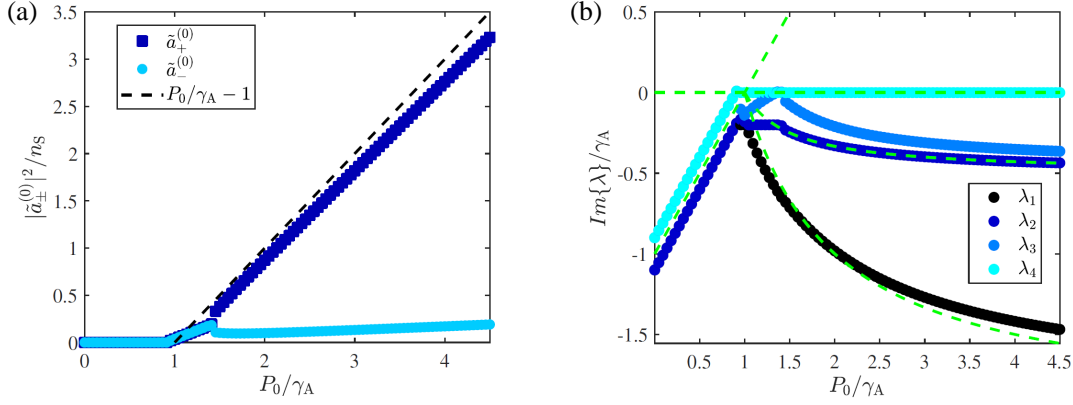
Figure 3.5: Ring resonator with $\xi = 2$ and backscattering parameters $|n| = 0.1\gamma_A$ and $h = 0$. **(a)** Steady-state intensity $|\tilde{a}_\pm^{(0)}|^2$ in each mode as a function of the pump rate P_0. The dashed line is the backscattering-free intensity. **(b)** Imaginary part of the fluctuation dynamics eigenvalues λ as a function of P_0. The dashed lines represent the imaginary part of the backscattering-free eigenvalues (3.5-3.10).
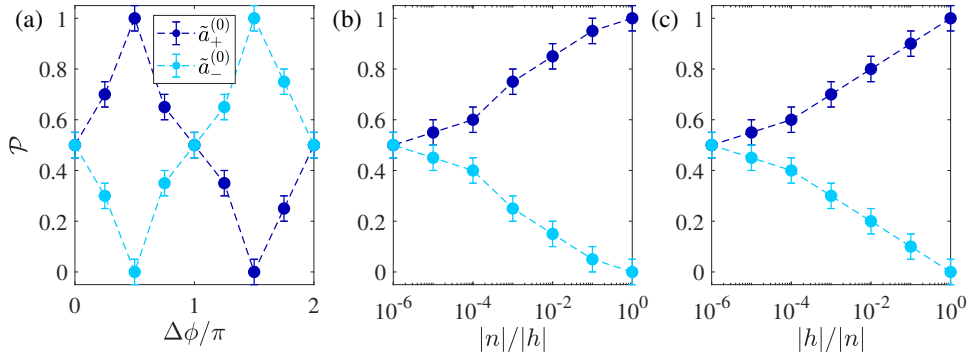
Figure 3.6: Probability of a ring resonator with $\xi > 1$ to lase preferentially in the CW (dark blue) and CCW (light blue) direction for different values of the backscattering. **(a)** Fixed modulus $|h| = |n| \simeq 5 \times 10^{-4}\gamma_A$ as a function of the relative phase angle $\Delta\phi = \phi_n - \phi_h$. **(b)** Fixed $\Delta\phi = \pi/2$ and $|h| \simeq 5 \times 10^{-4}\gamma_A$ as a function of $|n|$. **(c)** Fixed $\Delta\phi = \pi/2$ and $|n| \simeq 5 \times 10^{-4}\gamma_A$ as a function of $|h|$.

the perturbation we arrive at

$$\delta\tilde{a}_+^{(0)} = \frac{i\tilde{\beta}_\pm}{\frac{P_0}{1+\frac{\xi}{n_S}|\tilde{a}_{-,\text{un}}^{(0)}|^2} - \gamma_\text{T}} \tilde{a}_{-,\text{un}}^{(0)}. \tag{3.23}$$

The intensity in the perturbatively populated CW mode is given by $|\delta\tilde{a}_+^{(0)}|^2$. This means that as long as backscattering couples light from the CCW into the CW mode (i.e. for $\tilde{\beta}_\pm \neq 0$) the CW mode will host a finite emission. Note that the intensity in the CW mode increases whenever the system features a smaller value of ξ, that is a more nonlocal gain saturation. The perturbation theory breaks down for $\xi = 1$ as Eq. (3.23) diverges at such a value. This is a consequence of the threefold-degenerate Goldstone mode that appears in this case (see Eqs. (3.7-3.10) for $n_\text{NL} = 0$ and $\xi = 1$).

Our simulations confirm that Eq. (3.23) correctly accounts for the intensity of the perturbatively populated CW mode as long as $|\tilde{\beta}_\pm| \ll \gamma_\text{T}$. The intensity in the preferred mode is still given with a large precision by the unperturbed solution $|\tilde{a}_{-,\text{un}}^{(0)}|^2$ and the eigenvalues of the matrix A in Eq. (3.4) do not significantly change. Therefore we conclude that in the presence of perturbative backscattering both the ring resonator and the TJR lase unidirectionally to a great extent, although some light is also present in the unfavored mode at the same frequency, with an intensity proportional to the backscattering coupling in its direction.

3.4.2   Ring resonator

Here we demonstrate how the values of the Hermitian and non-Hermitian coefficients describing backscattering (3.21-3.22) control the lasing chirality in a ring resonator. This fact can be employed to construct unidirectional lasers by properly engineering the resonator's microscopic backscattering, for example by means of one or more nanotips coupled with the evanescent field of the resonator, similarly to the experiment of [153]. Note that in a ring resonator $\gamma_\text{S} = 0$ and therefore $\gamma_\text{T} = \gamma_\text{A}$.

As was shown in Sec. 3.4.1 the presence of perturbative backscattering does not appreciably change the fluctuation dynamics eigenvalues and the system lases unidirectionally to a great extent. Nevertheless, for values $|\tilde{\beta}_{\pm,\mp}| \gtrsim 10^{-2}|\gamma_\text{A}|$ the perturbation theory (3.23) breaks down, a significant intensity populates the unfavored lasing direction and the intensity in the preferred direction falls below its usual value $P_0/\gamma_\text{A} - 1$. Fig. 3.5 shows the intensities (panel (a)) and imaginary part of the eigenvalues of matrix A (panel (b)) for a ring resonator featuring $\xi = 2$, $h = 0$ and $|n| = 0.1\gamma_\text{A}$. Above the lasing threshold located at $P_0 \simeq 0.9\gamma_\text{A}$ both counterpropagating modes are amplified with the same intensity and oscillate simultaneously in a coherent way. As P_0 and $|\tilde{a}_\pm^{(0)}|^2$ grow the effect of mode competition in the gain saturation gets reinforced and intensity fluctuations become more susceptible of breaking the symmetry of the laser emission. This is evident from panel (b), where one of the imaginary parts quickly grows as P_0 increases and at some point turns positive. Here, the system undergoes a transition towards a regime with a larger lasing intensity in a preferred mode. The larger ξ (that is, the larger the local character of the gain saturation), the smaller the value of P_0 necessary to drive the system out of the bidirectional emission state as gain saturation asymmetry becomes more important. Nevertheless, the unfavored mode maintains a small intensity due to the finite backscattering in both directions.

The smaller lasing threshold obtained in Fig. 3.5 can be understood by diagonalizing the matrix A of Eq. (3.4). In the general coupling case $\beta_{\pm,\mp} \neq 0$ below the lasing threshold (i.e. for $|\tilde{a}_\pm^{(0)}|^2 = 0$) the eigenvalues are

$$\lambda_1 = +(\omega_0 - \omega) + i(P_0 - \gamma_\text{A}) + (\beta_\pm\beta_\mp)^{1/2}, \tag{3.24}$$

$$\lambda_2 = -(\omega_0 - \omega) + i(P_0 - \gamma_\text{A}) - (\beta_\pm^*\beta_\mp^*)^{1/2}, \tag{3.25}$$

$$\lambda_3 = +(\omega_0 - \omega) + i(P_0 - \gamma_\text{A}) - (\beta_\pm\beta_\mp)^{1/2}, \tag{3.26}$$

$$\lambda_4 = -(\omega_0 - \omega) + i(P_0 - \gamma_\text{A}) + (\beta_\pm^*\beta_\mp^*)^{1/2}. \tag{3.27}$$

The terms in the square roots can modify their imaginary parts, therefore shifting the threshold position with respect to the backscattering-free case, where these terms were zero. The new lasing threshold takes place at a power $P_0 = \gamma_\text{A} - Im\{(\beta_\pm\beta_\mp)^{1/2}\}$. If $n = 0$ one has that $\beta_\mp = \beta_\pm^*$ and the square roots are purely real. In this case the lasing threshold remains at its usual position
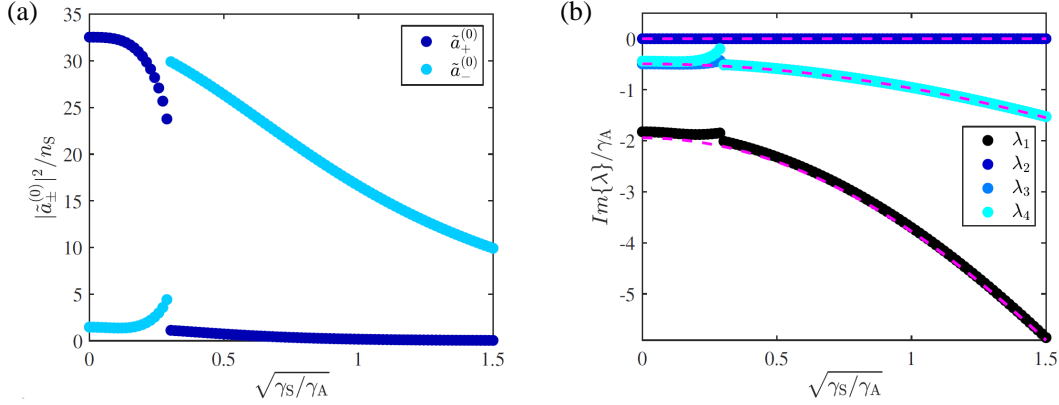
Figure 3.7: Ramp in the S-waveguide coupling from $\gamma_S = 0$ to $\sqrt{\gamma_S/\gamma_A} = 1.5$ for a ring resonator with $\xi = 2$ in the presence of a backscattering described by $|n| = 0.1\gamma_A$ and $h = 0$ for a fixed pump rate $P \simeq 36\gamma_A$. **(a)** Intensities in each mode $|\tilde{a}_\pm^{(0)}|^2$ as a function of the square root of the S-coupling losses $\sqrt{\gamma_S}$. **(b)** Imaginary part of the linearized fluctuation dynamics eigenvalues λ as a function of $\sqrt{\gamma_S}$. The dashed lines correspond to the backscattering-free eigenvalues (3.7-3.10).

$P_0 = \gamma_A$. The same is true for a unidirectional coupling (featuring either $\beta_\pm = 0$ or $\beta_\mp = 0$). The maximum shift for fixed $|\beta_{\pm,\mp}|$ occurs for $h = 0$ and is given by $P_0 = \gamma_A - |\beta_\pm|$.

In spite of the finite intensity circulating in the unfavored direction, in the small backscattering regime the majority of the ring resonator's emission still takes place in a preferential direction determined by the particular choice of backscattering coefficients. Fig. 3.6 shows the probability of a ring resonator featuring $\xi > 1$ to lase preferentially in a certain direction as a function of the Hermitian and non-Hermitian parameters. Here, the probability is calculated by averaging over many independent realizations of the initial noise used to seed the laser operation.

We first study the situation in which both of them are finite and of equal strength, i.e. $|h| = |n| \neq 0$. In panel (a) these are kept at a fixed modulus $|h| = |n| \simeq 5 \times 10^{-4}\gamma_A$ while the phase angle between them $\Delta\phi = \phi_n - \phi_h$ is varied. For $\Delta\phi = 0, \pi$ (which implies $|\beta_\pm| = |\beta_\mp|$) the system has equal probabilities of lasing in each mode, while for $\Delta\phi = \pm\pi/2$ the emission preferentially takes place in one particular direction with 100% probability. It is easy to realize that $\Delta\phi = +\pi/2$ implies $\beta_\mp = 0$ while $\Delta\phi = -\pi/2$ corresponds to having $\beta_\pm = 0$. These results are in perfect agreement with the behavior of passive microdisk resonators reported in [163].

However, this is only valid when $|h| = |n| \neq 0$. If one of the two parameters is kept fixed and the other is reduced to zero, the lasing probability in each direction tends to $\mathcal{P} = 0.5$ regardless of the phase difference $\Delta\phi$, as shown in panels (b) and (c). This is easily understood by exploring Eqs. (3.21-3.22): either $n = 0$ or $h = 0$ imply in fact an equal coupling strength in the two directions, i.e. $|\beta_\pm| = |\beta_\mp|$.

3.4.3 TJR

In the case of a TJR coupling unidirectionally the CW into the CCW direction one has that $|\beta_\mp| \gg |\beta_\pm|$ and therefore

$$h \simeq -\frac{\beta_\mp}{2}, \tag{3.28}$$

$$n \simeq i\,\frac{\beta_\mp}{2}, \tag{3.29}$$

which falls into the $|n| = |h|$, $\Delta\phi = -\pi/2$ case. As already shown in this Section, this implies that even though the resonator hosts a small intensity in the CW mode due to the finite coupling $\beta_\pm \neq 0$, the majority of the system emission takes place in the CCW mode. The presence of additional backscattering coupling light into the CCW direction does not have any visible effect as it does not modify the coupling $\beta_\mp$ significantly [2].

---

[2]For a TJR with an oppositely oriented S-element, one still has $|n| = |h|$ but $\Delta\phi = \pi/2$. As expected, this implies a preferred emission in the CW direction.
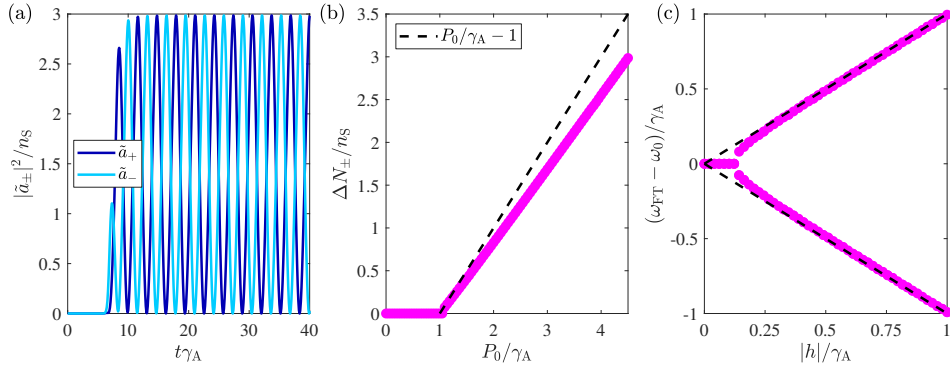
Figure 3.8: Ring resonator with $\xi = 2$ and backscattering given by $|h| = \gamma_A$ and $n = 0$. **(a)** Intensity in each mode $|\tilde{a}_\pm|^2$ as a function of time t. The pump rate is fixed at $P_0 = 4.5\gamma_A$. **(b)** Amplitude $\Delta N_\pm$ of the oscillations of the intensity in each mode as a function of the pump rate P_0 (pink circles). The amplitude is the same in the two directions. The dashed line corresponds to the usual dependence in the absence of backscattering. **(c)** Frequencies ω_{FT} of the two emission components (whose beating leads to the intensity oscillations visible in panel **(a)**) as a function of the Hermitian backscattering coefficient $|h|$. The pump rate is fixed at $P_0 = 4.5\gamma_A$. The frequencies are the same in the two directions.

In order to shine more light into the role of the S waveguide we performed a coupling ramp from $\gamma_S = 0$ (which corresponds to a ring resonator) to $\sqrt{\gamma_S/\gamma_A} = 1.5$ in a resonator featuring $\xi = 2$ and a fixed pump rate $P_0 \simeq 36\gamma_A$. The initial situation is described by the backscattering parameters employed in Fig. 3.5, namely $|n| = 0.1\gamma_A$ and $h = 0$, for which the two directions have equal probabilities of hosting the preferential lasing emission. Our results are displayed in Fig. 3.7. As γ_S grows $\beta_\mp$ increases: This leads to an intensity transfer from the CW to the CCW mode. For $\sqrt{\gamma_S/\gamma_A} \gtrsim 0.25$ the S-waveguide coupling strength grows beyond the backscattering couplings and the imaginary part of one of the eigenvalues of matrix (3.4) crosses zero from below. The system then experiences a transition towards a state with preferential lasing in the CCW direction. As γ_S continues growing the relative importance of backscattering with respect to the S coupling decreases. For $\sqrt{\gamma_S/\gamma_A} \simeq 1$ the ratio between backscattering in the CW direction $\beta_\pm$ and the total loss rate γ_T already gives $|\beta_\pm| \simeq 5 \times 10^{-2}\gamma_T$, which means that the system is approaching the perturbative backscattering regime described in Sec. 3.4.1. As this happens the spectrum of eigenvalues of the matrix A in Eq. (3.4) approaches the backscattering-free eigenvalues (3.7-3.10) and the intensity ratio between the two directions already gives a sizable value $|\tilde{a}_-^{(0)}|^2 \simeq 250|\tilde{a}_+^{(0)}|^2$ for $\sqrt{\gamma_S/\gamma_A} = 1.5$. The eventual decrease of the intensity also in the CCW direction that is observed at higher γ_S is due to the growth of the total loss rate γ_T that is naturally associated to the increasing γ_S.

These results confirm the possibility to use the S waveguide in order to guarantee unidirectional lasing. The necessary condition is to implement a sufficiently large coupling allowing to treat backscattering as a microscopic perturbation to unidirectional lasing, which according to our model is legitimate at least up to $|\tilde{\beta}_{\pm,\mp}| \lesssim 10^{-2}\gamma_T$.

3.5   Large backscattering

In this Section we investigate lasing in ring resonators and TJRs characterized by the presence of a large Hermitian backscattering compared with the resonator loss rate in the absence of the S element, i.e. $|h| \gtrsim \gamma_A$. As we will show such a coupling introduces self-oscillations of the intensity in the two directions. The requirement $|n| \leq \gamma_T$ that is needed to avoid an unphysical backscattering-induced gain implies that our model can only account for a large Hermitian backscattering. For simplicity, we will then consider $n = 0$ throughout this Section. The addition of a non-Hermitian coupling would only introduce an asymmetry between the two counter-propagating directions that damps the oscillating behavior for values of n approaching γ_T. As in Sec. 3.4, the analysis carried in this Section does not take into account the resonance shift due to the nonlinearity, i.e. $n_{\mathrm{NL}} = 0$. This additional effect will be studied in Sec. 3.6. Under this condition, lasing occurs at the resonator
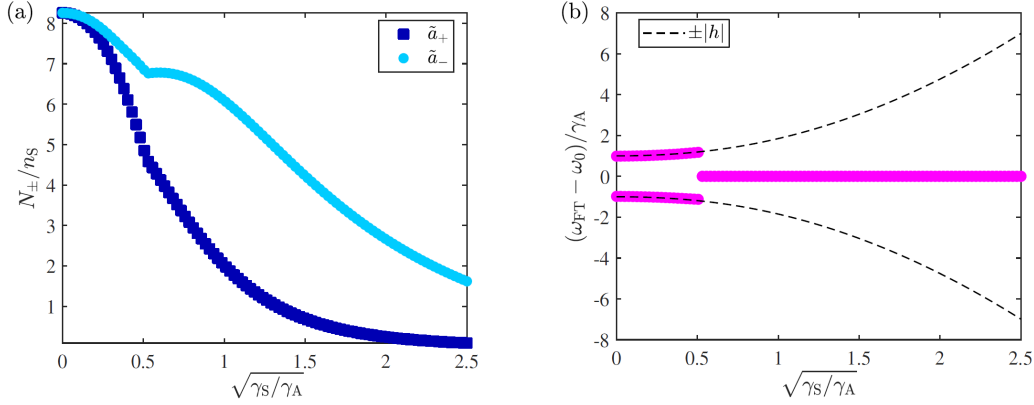
Figure 3.9: Ramp in S-waveguide coupling from $\gamma_S = 0$ (ring resonator) to $\sqrt{\gamma_S/\gamma_A} = 2.5$ for a ring resonator with $\xi = 2$ in the presence of a backscattering given by $n = 0$ and $|h| = \gamma_A$ for a fixed pump rate $P \simeq 20\gamma_A$. **(a)** Mean value between intensity maxima and minima in each direction $N_\pm$ as a function of the square root of the S-coupling losses $\sqrt{\gamma_S}$. Data corresponding to $\sqrt{\gamma_S/\gamma_A} \lesssim 0.5$ falls into the oscillation regime. **(b)** Frequency of the field amplitudes in the two directions ω_{FT} as a function of $\sqrt{\gamma_S}$.

frequency ω_0.

Fig. 3.8a shows the time evolution of the intensity in each mode for a ring resonator featuring $\xi = 2$, $n = 0$, and $|h| = \gamma_A$ at a pump rate $P_0 = 4.5\gamma_A$. As observed in previous works [141, 143] for such a large backscattering coupling the resonator enters a regime in which the intensity in the two directions oscillates in phase opposition at a frequency given by twice the modulus of the backscattering coupling $|h|$. Panel (b) shows the amplitude $\Delta N_\pm$ of these oscillations as a function of P_0. This is equal in the two directions and is slightly smaller than the backscattering-free amplitude, which is given by $P_0/\gamma_A - 1$. The frequency at which the field amplitudes $\tilde{a}_\pm$ oscillate ω_{FT} is extracted from a Fourier transform, and displayed in panel (c) for a fixed pump rate $P_0 = 4.5\gamma_T$ as a function of $|h|$. As shown in Sec. 3.4 for a small backscattering in our reference frame rotating at a frequency $\omega = \omega_0$ the field amplitudes do not oscillate. As $|h|$ grows beyond approximately $0.1\gamma_A$ both field amplitudes start oscillating with two opposite frequency components which rapidly approach $\pm|h|$ as the Hermitian backscattering grows.

This situation changes dramatically when the S-shaped waveguide of the TJR is introduced. In Fig. 3.9 a ring resonator featuring the same ξ parameter and backscattering coefficients as in the simulation displayed in Fig. 3.8 is subjected to an S-coupling ramp. The pump rate is fixed at $P_0 = 20\gamma_A$. Panel (a) shows the mean value between the maximum and minimum intensities $N_\pm = (max\{|\tilde{a}_\pm|^2\} + min\{|\tilde{a}_\pm|^2\})/2$ emitted in each direction. In the oscillatory regime that takes place for $\sqrt{\gamma_S/\gamma_A} \lesssim 0.5$ this quantity corresponds to half the amplitude of the oscillations. In the nonoscillatory regime (for $\sqrt{\gamma_S/\gamma_A} \gtrsim 0.5$) one has that $max\{|\tilde{a}_\pm|^2\} = min\{|\tilde{a}_\pm|^2\}$ and therefore $N_\pm = |\tilde{a}_\pm^{(0)}|^2$. On the other hand, Fig. 3.9b shows the oscillation frequency ω_{FT} extracted from a Fourier transform of the field amplitudes $\tilde{a}_\pm$ in each direction for the same ramp in γ_S. In the oscillatory regime the two amplitudes oscillate with two frequency components given by the Hermitian backscattering coefficient $\pm|h|$. For $\sqrt{\gamma_S/\gamma_A} \gtrsim 0.5$ the coupling strength with the S waveguide increases beyond the backscattering couplings given by $|h| = \gamma_A$ and the oscillations disappear (see panel (b)). This regime is equivalent to the situation studied in Sec. 3.4.3. Panel (a) shows that the S-shaped waveguide imposes a definite chirality in the laser emission, as the CCW mode becomes the favored mode when γ_S is increased. Once again, the eventual decrease of the intensity in the two directions that is visible at larger γ_S is due the growth of the total loss rate γ_T. Interestingly, this effect mainly affects the unfavored CW mode, whose emission becomes rapidly negligible. For instance, already at $\sqrt{\gamma_S/\gamma_A} = 2.5$ the intensity ratio between both directions is $|\tilde{a}_-^{(0)}|^2 \simeq 17|\tilde{a}_+^{(0)}|^2$.
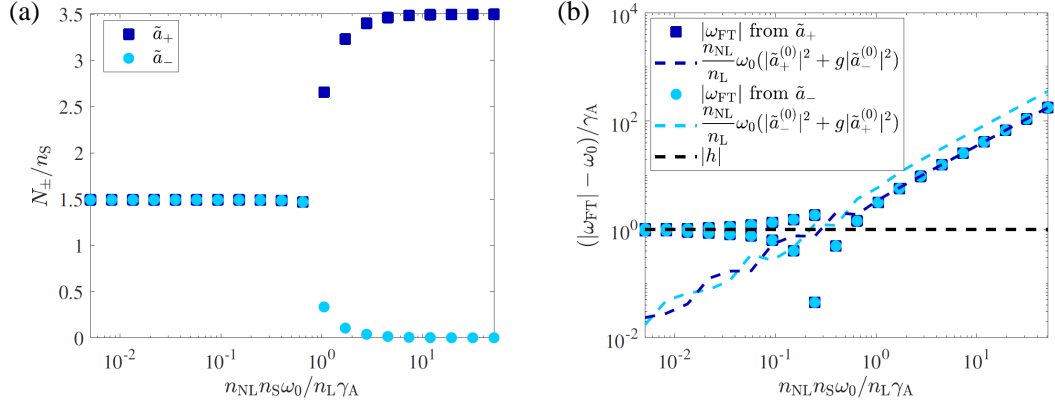
Figure 3.10: **(a)** Mean value between intensity maxima and minima $N_\pm$ as a function of the nonlinear refractive index n_{NL} for a ring resonator featuring an optical Kerr nonlinearity ($g = 2$) and a local gain saturation ($\xi = 2$). The backscattering parameters are $n = 0$, $|h| = \gamma_{\mathrm{A}}$. The pump rate is fixed at $P_0 = 4.5\gamma_{\mathrm{A}}$. Data corresponding to $n_{\mathrm{NL}} n_{\mathrm{S}} \omega_0 / n_{\mathrm{L}} \gamma_{\mathrm{A}} \lesssim 1$ fall into the oscillatory regime. **(b)** Absolute values of the oscillation frequencies ω_{FT} of the field amplitudes $\tilde{a}_\pm$ as a function of n_{NL}. Squares and circles are the values extracted from the Fourier transform (FT) of the data presented in panel (a). Dashed lines represent the expected oscillation frequency in the linear regime $|h|$ and the nonlinear frequency shifts for each mode.

3.6 Effect of the optical nonlinearities

In this Section we show that the local Kerr nonlinearity indigenous to the waveguide material reinforces the unidirectionality of the ring laser emission. This effect can be combined with the action of the S-waveguide in order to further reinforce unidirectional lasing even in the large backscattering regime. The nonlinearity modifies the resonance frequency of each mode $\omega_\pm^{(0)}$ according to

$$\omega_\pm^{(0)} = \omega_0 \left[1 - \frac{n_{\mathrm{NL}}}{n_{\mathrm{L}}} (|\tilde{a}_\pm^{(0)}|^2 + g|\tilde{a}_\mp^{(0)}|^2) \right]. \tag{3.30}$$

In the backscattering-free ring resonator and unidirectional TJR lasers the nonlinearity has no effects beyond the shift of the resonance frequency. The behavior is therefore the same as the one described in Sec. 3.3 for the linear regime. The same is true for a pure thermo-optic nonlinearity with $g = 1$ even in the presence of backscattering. In this case the resonance frequency of the two modes is in fact shifted by equal amounts and therefore the coupling between them is not perturbed by the nonlinearity. On the other hand, if one has $g > 1$ and finite and unequal intensities in the two modes, as is possible for a sufficiently large backscattering in a ring resonator, the resonance frequency in the two directions will be different. This fact further suppresses the intermodal coupling as it reduces the probability of light to scatter from one mode to another.

Fig. 3.10a shows the mean value between the intensity maxima and minima $N_\pm$ as the nonlinear refractive index n_{NL} is varied. In the nonoscillatory regime this quantity reduces to the steady-state intensity $|\tilde{a}_\pm^{(0)}|^2$. Panel (b) of the same figure shows the field oscillation frequencies ω_{FT} in the two directions for the same n_{NL} ramp, as extracted from a Fourier transform of the field amplitudes. Once again we chose a rotating reference frame at the linear resonance frequency ω_0. The calculation was made for a ring resonator featuring a $g = 2$ optical nonlinearity and a $\xi = 2$ saturable gain. The backscattering parameters are $n = 0$, $|h| = \gamma_{\mathrm{A}}$, which fall into the large backscattering regime described in Sec. 3.5. The pump rate is fixed at $P_0 = 4.5\gamma_{\mathrm{A}}$. Similarly to Fig. 3.9, as n_{NL} increases oscillations disappear, leading to a regime in which the laser emission is concentrated in a randomly chosen direction (the CW one in the figure), each with 50% of probability. This effect is reinforced as n_{NL} grows, ultimately achieving a pure unidirectional emission for $n_{\mathrm{NL}} n_{\mathrm{S}} \omega_0 / n_{\mathrm{L}} \gamma_{\mathrm{A}} \gtrsim 10$. For the largest value of n_{NL} calculated, the intensity ratio gives $|\tilde{a}_+^{(0)}|^2 \simeq 10^4 |\tilde{a}_-^{(0)}|^2$.

As shown in panel (b), for negligible values of n_{NL} both modes oscillate with two frequency components given by the Hermitian backscattering coefficient $\pm|h|$, as demonstrated in Sec. 3.5. For the purpose of using a logarithmic scale, the absolute values $|\omega_{\mathrm{FT}}|$ are displayed. As n_{NL} increases,
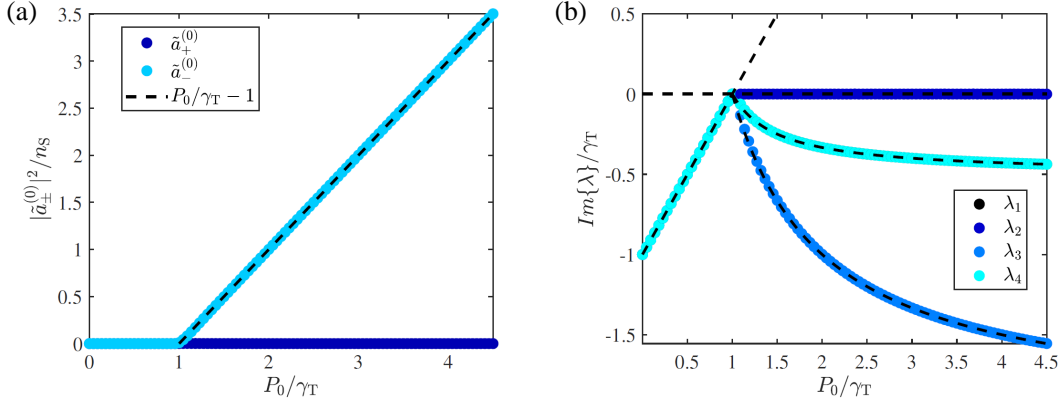
Figure 3.11: Pump rate ramp in a TJR featuring an S-waveguide coupling $\sqrt{\gamma_S/\gamma_A} = 2.5$, a $\xi = 2$ gain saturation, a $g = 2$ nonlinearity given by $n_{NL} n_S \omega_0 / n_L \gamma_A = 50$, and backscattering parameters $n = 0$ and $|h| = \gamma_A$. **(a)** Steady-state intensity $|\tilde{a}_{\pm}^{(0)}|^2$ in each mode as a function of the pump rate P_0. The dashed line is the backscattering-free intensity. **(b)** Imaginary part of the fluctuation dynamics eigenvalues λ as a function of P_0. The dashed lines correspond to the imaginary parts of the backscattering-free eigenvalues given by Eqs. (3.5-3.10). The black circles are not visible as they lay below the light blue ones.

the frequencies blue shift until a transition takes place at $n_{NL} n_S \omega_0 / n_L \gamma_A \gtrsim 1$ back to a regime with stationary intensity values, in which the two field amplitudes oscillate at a single frequency given by the nonlinear displacement of the resonance frequency of the resonator (Eq. (3.30)) for the preferred lasing direction. This is telling us that the unfavored CCW direction does no longer feature laser oscillations at its own resonance frequency but that all the light that populates it is being backscattered from the preferential CW direction.

Finally, Fig. 3.11 displays the steady-state intensities $|\tilde{a}_{\pm}^{(0)}|^2$ and the corresponding imaginary part of the eigenvalues of matrix A (Eq. (3.4)) for a pump rate ramp in a TJR featuring an S-waveguide coupling $\sqrt{\gamma_S/\gamma_A} = 2.5$, a $g = 2$ Kerr nonlinearity of strength $n_{NL} n_S \omega_0 / n_L \gamma_A = 50$, a $\xi = 2$ saturable gain, and large backscattering parameters $n = 0$ and $|h| = \gamma_A$. In the absence of the S-waveguide and the nonlinearity, the corresponding ring resonator would feature intensity oscillations at a frequency given by $2|h|$. Instead, the nonlinear TJR capitalizing on these two crucial elements shows unidirectional lasing with a preferred CCW chirality with 100% probability. The intensity in the CW direction is four orders of magnitude smaller than that in the CCW one and can therefore be safely neglected. The Bogoliubov analysis of the small perturbations to this steady state reveals that the eigenvalues of the linearized fluctuation dynamics matrix A are identical to those calculated in the backscattering-free case, ensuring the stability of the unidirectional emission.

3.7   Conclusions

In this Chapter we demonstrated that an active "Taiji" micro-ring resonator (TJR) formed by a standard ring resonator supplemented by an S-shaped element unidirectionally coupling the two counterpropagating modes shows a preferential chirality in the laser oscillation even in the presence of a large backscattering. The presence of the S-shaped element implies robust unidirectional lasing in the favored direction and restricts the emission in the other direction to negligible values.

Our theoretical investigation is based on the most general version of the coupled-mode equations of motion for the field amplitudes in the two counter-propagating modes. These equations are first solved for the steady-states. The dynamical stability of these latter against small perturbations is then assessed within a linearized theory by looking at the imaginary part of the eigenvalues of the linearized fluctuations dynamics matrix.

In the absence of backscattering, one of the two counterpropagating lasing solutions of the ring resonator disappears for a sufficiently strong coupling by the S-element, leaving a single stable solution with laser emission only in the mode which is favored by the S-shaped element. This unidirectional emission remains stable even in the presence of backscattering effects due, e.g.,

to the roughness of the resonator surface, as long as the coupling by the S-element exceeds the backscattering strength. The robustness of the unidirectional laser emission is further reinforced by a Kerr nonlinearity shifting the resonance of the two counterpropagating modes by different amounts.

While unidirectional laser emission in a random direction in ring resonators can be seen as a spontaneous breaking of the time-reversal $\mathcal{T}$-symmetry in the lasing state above threshold, the explicit breaking of $\mathcal{P}$-symmetry in the geometrical shape of our Taiji resonator leads to a preferred chirality of the laser emission. This can be understood as an explicit dynamical breaking of $\mathcal{T}$-symmetry induced by the broken $\mathcal{P}$-symmetry in an otherwise $\mathcal{T}$-symmetric device.

This novel mechanism for breaking $\mathcal{T}$-reversal appears of great interest in view of realizing optical isolators and other non-reciprocal devices based on wave-mixing phenomena without the need for magnetic elements. Further research along these lines will be the subject of Chapter 4.

Furthermore, as we will demonstrate in Chapter 5, in the context of topological photonics [7, 13] TJRs allow to dynamically generate a topological Chern insulator using structures based on non-magnetic active dielectric materials.

Chapter 4

Optical isolators based on parity-symmetry breaking and four-wave mixing

Ⅰn this Chapter we numerically demonstrate effective optical isolation over a broad frequency range in all-dielectric and non-magnetic devices operating at telecommunication frequencies. The proposed strategy capitalizes on the reciprocity breaking due to the asymmetric action of four-wave mixing coupling a large intensity pump with the transmitted signal but not with reverse-propagating undesired ones. This allows our devices to circumvent the dynamic reciprocity restrictions [19]. Our theoretical formalism is based on a linearized analysis of the signal and idler fields which are treated as small perturbations in the temporal coupled-mode theory equations for the large intensity pump. Nonreciprocity is further investigated by diagonalizing the Bogoliubov matrix for fields propagating in the two directions and examining the resulting spectrum of eigenvalues and the norm of the associated eigenvectors. We propose three setups where this one scheme can be realized in different flavors: a passive ring resonator in add-drop configuration optically pump from one side, an active ring resonator in which an external bias triggers lasing in the forward direction, and an incoherently pumped active Taiji resonator.

4.1   Introduction

Optical isolators [15] —introduced in Chapter 2— are devices that allow the transmission of light in a certain direction (known as *forward*) while simultaneously preventing light propagation in the opposite direction (labelled *reverse*). As reviewed in Sec. 2.2, isolation requires breaking Lorentz reciprocity [89]. For this purpose many strategies have been proposed: Some authors employed magneto-optic materials that break time-reversal symmetry in the presence of an external magnetic field [93, 95, 96, 98]. Others relied on an external driving field producing a time-dependent modulation of the material's refractive index [99, 100, 101, 102, 103]. A more promising strategy to break reciprocity consists on exploiting the optical nonlinearity of the employed dielectric material. Such isolators have the further advantage of offering a smaller on-chip footprint and an easier integration with state-of-the-art silicon-based photonic networks.

Along the latter line, several devices have demonstrated non-reciprocal transmittance when light is injected first in the forward and then in the reverse direction [104, 164, 107, 108, 17]. However, the work of Ref. [19] showed that such systems cannot grant isolation against arbitrary backwards-propagating noise when a strong signal is being transmitted in the forward direction. This is called *dynamic reciprocity*, and it constitutes an extremely important weak point as these are the usual operation conditions in which an optical isolator is expected to work.

Nevertheless, there are some exceptions to dynamic reciprocity. Ref. [19] demonstrated that when the frequency spectrum of the noise overlaps with that of the forward signal, four-wave mixing (FWM) coupling between the two fields preserves nonreciprocity. A specific case in this class is obtained when both signal and noise are monochromatic waves featuring the same frequency. An

example is provided by Ref. [110], who capitalized on the different Kerr nonlinearity shifts of the resonance frequencies of two counterpropagating whispering gallery modes in a silicon ring resonator [109], namely clockwise (CW) and counterclockwise (CCW). After being transmitted through the device, light was reflected at a mirror and could not couple to the counterpropagating mode of the resonator.

In this Chapter we show that all-dielectric ring resonators strongly pumped in a single direction behave as optical isolators over a broad frequency range as they permit the propagation of signals in the pump direction while preventing transmission in the opposite one. This asymmetry stems from the fact that FWM coupling pump and signal is only possible when both propagate in the same direction. This allows our proposal to circumvent the restrictions imposed by dynamic reciprocity.

We consider three different setups where isolation can be realized, all based in very similar concepts. The first one is a passive ring resonator coupled to a pair of bus waveguides in add-drop configuration. The system is coherently pumped through one of the bus waveguides. The second one corresponds to its active analog where an incoherent pumping promotes lasing in a randomly chosen whispering-gallery mode. By means of a small driving injected through one of the bus waveguides one can unambiguously select the lasing chirality. After lasing is triggered the bias driving can be switched off. In the third one, we consider replacing the ring resonator by a Taiji resonator (TJR) laser which eliminates the need for the bias in order to determine its emission direction. Introduced in Chapter 2, TJRs are ring resonators embedding an S-shaped waveguide which couples light propagating in one direction of the external ring into the opposite one, but forbids the inverse process. They have been extensively employed to promote unidirectional lasing [14, 145] (see Chapter 3) and play a central role in order to preserve the topological protection of a pair of chiral surface modes in quantum spin-Hall topological insulator lasers [13, 155, 7, 12] due to the high immunity of their unidirectional emission against backscattering coupling light in counterpropagating modes. The interplay between TJRs and topological band structures will be the subject of Chapter 5.

In order to study this behavior we make use of a time-dependent coupled mode theory. We consider the signal and idler fields as small perturbations to the pump, whose intensity is assumed to be much larger than that of any other field inside the resonator. We then linearize the dependence on the field amplitudes of signal and idler in the coupled-mode equations. By solving for the steady state of the resulting system of equations we are able to ascertain the signal transmittance across such systems and to probe optical isolation from signals propagating in the reverse direction. In order to further investigate the role of the FWM asymmetry we set up the 4×4 Bogoliubov matrix connecting the signal and idler fields in the two directions and diagonalize it to obtain the frequency of the transmittance peaks and assess the stability of the considered modes. This is also employed to highlight a connection between our passive and active optical diodes, and coherently and incoherently pumped polariton condensates [53].

The Chapter is organized as follows. Sec. 4.2 introduces the coupled-mode theory and the linearized approximation employed in our simulations. Our results for a passive ring resonator coherently pumped from one side are shown in Sec. 4.3. Sec. 4.4 is devoted to a similar setup based on active ring resonators. Our results for the TJR laser isolator can be found in Sec. 4.5. Conclusions are finally drawn in Sec. 4.6.

4.2   The physical system and the theoretical model

Light propagating inside a ring resonator of radius R and linear refractive index n_{L} (nonlinear effects are neglected here) is restricted to discrete modes featuring a free-space wavelength

$$\lambda_\ell = \frac{2\pi R n_{\mathrm{L}}}{|\ell|} \tag{4.1}$$

where ℓ is an integer number, namely determining the angular momentum of the mode. The sign of ℓ describes its propagation direction: $\ell > 0$ indicates a CCW-propagating mode, while $\ell < 0$ corresponds to CW modes.

Since resonators are a material medium, the dispersion relation for light inside them is not linear on the angular momentum ℓ and features higher order terms due to the dependence of the linear refractive index n_{L} on the probing wavelength λ, which ultimately results in n_{L} being a

function of ℓ. We can then write the dispersion relation as

$$\omega_\ell^{(0)} = \frac{c}{n_{\mathrm{L}}(\ell)} \frac{|\ell|}{R}, \tag{4.2}$$

where $\omega_\ell^{(0)}$ is the resonance frequency of mode ℓ and c is the vacuum speed of light. We now consider the Taylor expansion of n_{L} around a certain angular momentum mode, which we label ℓ_{P}:

$$n_{\mathrm{L}}(\ell) = n_{\mathrm{L}}(|\ell_{\mathrm{P}}|) + \left(\frac{dn_{\mathrm{L}}}{d|\ell|}\right)_{|\ell_{\mathrm{P}}|} (|\ell| - |\ell_{\mathrm{P}}|) + \mathcal{O}(\ell^2). \tag{4.3}$$

By combining Eqs. (4.2-4.3) we arrive at the expression

$$\omega_\ell^{(0)} = \frac{c}{n_{\mathrm{L}}(|\ell_{\mathrm{P}}|)} \left[1 + \frac{1}{n_{\mathrm{L}}(|\ell_{\mathrm{P}}|)} \left(\frac{dn_{\mathrm{L}}}{d|\ell|}\right)_{|\ell_{\mathrm{P}}|} |\ell_{\mathrm{P}}|\right] \frac{|\ell|}{R}$$
$$- \frac{c}{n_{\mathrm{L}}^2(|\ell_{\mathrm{P}}|)} \left(\frac{dn_{\mathrm{L}}}{d|\ell|}\right)_{|\ell_{\mathrm{P}}|} \frac{\ell^2}{R}, \tag{4.4}$$

which is valid whenever the condition

$$\left(\frac{dn_{\mathrm{L}}}{d|\ell|}\right)_{|\ell_{\mathrm{P}}|} \gg \left(\frac{d^2 n_{\mathrm{L}}}{d|\ell|^2}\right)_{|\ell_{\mathrm{P}}|} |\ell_{\mathrm{P}}| \tag{4.5}$$

is satisfied. We now capitalize on Eq. (4.1) in order to rewrite Eq. (4.4) in terms of the derivative $dn_{\mathrm{L}}/d\lambda$:

$$\omega_\ell^{(0)} = \frac{c}{|\ell_{\mathrm{P}}|} \left[1 - \frac{2\pi R}{|\ell_{\mathrm{P}}|} \left(\frac{dn_{\mathrm{L}}}{d\lambda}\right)_{\lambda_{\mathrm{P}}}\right] \frac{|\ell|}{R}$$
$$+ \frac{c}{n_{\mathrm{L}}(|\ell_{\mathrm{P}}|)} \frac{2\pi}{\ell_{\mathrm{P}}^2} \left(\frac{dn_{\mathrm{L}}}{d\lambda}\right)_{\lambda_{\mathrm{P}}} \ell^2, \tag{4.6}$$

where the derivatives are evaluated at $\lambda_{\mathrm{P}} = 2\pi R n_{\mathrm{L}}/|\ell_{\mathrm{P}}|$. For instance, around $\lambda_{\mathrm{P}} = 1500$ nm SiON waveguides of transverse area 1200 nm $\times$ 570 nm display an effective linear refractive index (including the effect of confinement) $n_{\mathrm{L}} \simeq 1.59$. Its first derivative gives $(dn_{\mathrm{L}}/d\lambda)_{\lambda_{\mathrm{P}}} = -1.42 \times 10^{-4}$ nm^{-1}. The second derivative is zero with a large precision [130]. Thus, in that case the condition (4.5) is met and the quadratic approximation for the dispersion relation is valid.

Eq. (4.6) can be recast in the more suggestive form

$$\omega_\ell^{(0)} = \omega_{\mathrm{P}}^{(0)} + v\left(|\ell| - |\ell_{\mathrm{P}}|\right) + \frac{\alpha}{2}\left(|\ell| - |\ell_{\mathrm{P}}|\right)^2, \tag{4.7}$$

by defining

$$\omega_{\mathrm{P}}^{(0)} = \frac{c|\ell_{\mathrm{P}}|}{n_{\mathrm{L}}(|\ell_{\mathrm{P}}|)R}, \tag{4.8}$$

$$v = \frac{c}{n_{\mathrm{L}}(|\ell_{\mathrm{P}}|)R} \left[1 + \frac{2\pi R}{|\ell_{\mathrm{P}}|} \left(\frac{dn_{\mathrm{L}}}{d\lambda}\right)_{\lambda_{\mathrm{P}}}\right], \tag{4.9}$$

$$\alpha = 2\frac{c}{n_{\mathrm{L}}(|\ell_{\mathrm{P}}|)} \frac{2\pi}{\ell_{\mathrm{P}}^2} \left(\frac{dn_{\mathrm{L}}}{d\lambda}\right)_{\lambda_{\mathrm{P}}}. \tag{4.10}$$

It is instructive to compare Eq. (4.7) with the dispersion of a polariton condensate moving at a constant velocity v [53]. In this sense, $\omega_{\mathrm{P}}^{(0)} \equiv \omega_{\ell_{\mathrm{P}}}^{(0)}$ is the bare resonance frequency of the ℓ_{P} mode, analogous to the ground state frequency at the bottom of the lower polariton branch; $v(|\ell| - |\ell_{\mathrm{P}}|)$ plays the role of the Doppler shift, and $\alpha(|\ell| - |\ell_{\mathrm{P}}|)^2/2$ sets the curvature of the dispersion, where α^{-1} represents an effective mass.

A sketch of the dispersion relation given by Eq. (4.7) can be found in Fig. 4.1a. The key idea behind our proposal for optical isolators is to pump with a large intensity at a frequency ω_{P} in
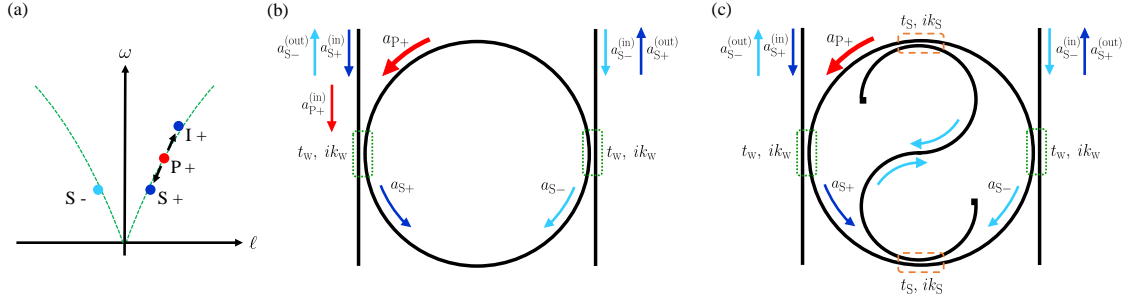
Figure 4.1: **(a)** Frequency ω as a function of the angular momentum ℓ of the modes of a ring resonator and TJR. The green dashed lines are the dispersion relations for CCW ($\ell > 0$) and CW ($\ell < 0$) modes including the curvature given by Eq. (4.7). **(b)** Scheme of a ring resonator pumped in the CCW direction by an external field $a_{\mathrm{P}+}^{(\mathrm{in})}$. The dashed rectangles signal directional couplers of transmission and coupling parameters t_{w} and ik_{w}, respectively. The field amplitude $a_{\mathrm{P}+}$ corresponds to the large intensity pump mode inside the resonator. The system is probed in the two directions by the external fields $a_{\mathrm{S}\pm}^{(\mathrm{in})}$. The field amplitudes of these modes inside the resonator are given by $a_{\mathrm{S}\pm}$. **(c)** Similar scheme for a TJR in which light is unidirectionally coupled from the CW into the CCW direction. The transmission and coupling parameters for the directional couplers between the ring and the S waveguides are given by t_{S} and ik_{S}, respectively.

the vicinity of the resonance frequency $\omega_{\mathrm{P}}^{(0)}$. Without loss of generality we take the corresponding angular momentum to be positive (i.e. $\ell_{\mathrm{P}} > 0$), implying propagation in a CCW whispering-gallery mode of the resonator. This mode is labeled P+ [1]. Due to the intrinsic optical nonlinearity of the material, a couple of photons from the P+ mode can scatter into the S+ (signal) and I+ (idler) modes featuring angular momenta (frequencies) ℓ_{S} (ω_{S}) and $\ell_{\mathrm{I}} = 2\ell_{\mathrm{P}} - \ell_{\mathrm{S}}$ ($\omega_{\mathrm{I}} = 2\omega_{\mathrm{P}} - \omega_{\mathrm{S}}$), respectively. Such a process is known as *four-wave mixing* (FWM). Due to the dependence $n_{\mathrm{L}}(\lambda)$ and the frequency detuning of the pump the S+ and I+ modes will also be detuned with respect to the corresponding resonance frequencies $\omega_{\mathrm{S}}^{(0)} \equiv \omega_{\ell_{\mathrm{S}}}^{(0)}$ and $\omega_{\mathrm{I}}^{(0)} \equiv \omega_{\ell_{\mathrm{I}}}^{(0)}$ given by the dispersion relation (4.7). Furthermore, as we will see, when the optical nonlinearity of the material is considered the resonance frequencies $\omega_{\mathrm{P,S,I}}^{(0)}$ of pump, signal, and idler will also be shifted with respect to the linear value appearing in Eq. (4.7). Such a deviation is proportional to the pump intensity.

The resonator is then probed in opposite directions around the $\omega_{\mathrm{S}}^{(0)}$ resonance by means of a signal with a smaller intensity than that of the pump. When the signal is coupled into the S+ mode propagating in the CCW direction FWM alters its transmittance spectrum. However, a signal S− propagating in the CW direction cannot be coupled with the pump P+ though FWM because no available resonance exists in the vicinity of the resulting I− mode, which is determined by conservation of energy and angular momentum.

Such an asymmetry sets the pump direction as the *forward* operation direction (in our case we chose the CCW) for the optical isolator, and its opposite direction as the *reverse* one (in our case the CW). Therefore, reciprocity is broken for signals propagating in the two directions. The two ingredients allowing this are the $\mathcal{P}$-symmetry (parity) breaking due to the unidirectional pump and the optical nonlinearity giving rise to FWM.

The proposed setup consists on a ring resonator (see Fig. 4.1b) or TJR (see Fig. 4.1c) coupled to a pair of bus waveguides located at opposite sides (i.e. the so-called *add-drop* configuration). Light is injected into the resonator through one of the bus waveguides and transmittance is measured at the output of the other bus waveguide. In this Chapter we follow three different strategies in order to achieve a large intensity in the P+ mode. In a passive ring resonator one can optically pump through one of the bus waveguides at the desired frequency ω_{P}. Taking ideas from Chapter 3 of this Thesis, an alternative strategy consists on employing active resonators and incoherently pump above the lasing threshold. In this Chapter we will assume that the system features an instantaneous saturable gain (i.e. we consider class-A lasers where the dynamics of the reservoir

---

[1]Note that in this Chapter, contrary to the usual notation employed thorough the rest of this Thesis, CW (CCW) modes are identified with the − (+) sing. This is done in order to allow a straightforward identification with the sign of their angular momenta.

giving rise to light amplification is fast enough and has been integrated out in the saturable gain [161, 162]) and that only a pair of counterpropagating modes P$\pm$ can compete for it. In the case of an active ring resonator, if undesired backscattering coupling modes propagating in opposite directions is sufficiently small, the system will host unidirectional emission in a randomly chosen direction. This can be set by means of an external driving propagating in the desired forward direction with a small intensity and a frequency in the vicinity of $\omega_\mathrm{P}^{(0)}$. Once lasing is triggered such a bias can be turned off. Finally, in an active TJR the laser emission already features a well-defined chirality without the need for an external driving. Besides, its unidirectionality is further protected against spurious backscattering.

In order to model the system we consider perfect directional couplers between all its components. These are described by transmission and coupling amplitudes $t_\mathrm{w,S}$ and $ik_\mathrm{w,S}$, respectively, being $t_\mathrm{w,S}$ and $k_\mathrm{w,S}$ real numbers satisfying $t_\mathrm{w,S}^2 + k_\mathrm{w,S}^2 = 1$. The subindices w, S refer to the bus waveguide-resonator and S waveguide-resonator couplings, respectively. The couplings of a ring of perimeter $L = 2\pi R$ with the bus waveguides and the S waveguide introduce the loss rates $\gamma_\mathrm{w} = ck_\mathrm{w}^2/(Ln_\mathrm{L})$ and $\gamma_\mathrm{S} = ck_\mathrm{S}^2/(Ln_\mathrm{L})$, respectively.

We start by writing the most general version of the temporal coupled-mode equations for the P$\pm$ modes, valid for both passive and active ring resonators and TJRs. Let us express the spatio-temporal dependence of the field amplitudes $a_{\mathrm{P}\pm}(z,t) = \tilde{a}_{\mathrm{P}\pm}(t)e^{i(\pm\ell_\mathrm{P}z/R-\omega_\mathrm{P}t)}$ with respect to the angular momentum $\pm\ell_\mathrm{P}$ and the frequency ω_P. The intensity in the P$\pm$ modes is then given by $|\tilde{a}_{\mathrm{P}\pm}|^2$. The coupled-mode equations read

$$i\dot{\tilde{a}}_{\mathrm{P}\pm} = (\omega_\mathrm{P}^{(0)} - \omega_\mathrm{P})\tilde{a}_{\mathrm{P}\pm} - \frac{n_\mathrm{NL}}{n_\mathrm{L}}\omega_\mathrm{P}^{(0)}\left(|\tilde{a}_{\mathrm{P}\pm}|^2 + 2|\tilde{a}_{\mathrm{P}\mp}|^2\right)\tilde{a}_{\mathrm{P}\pm}$$

$$+ i\frac{P_0}{1 + \frac{1}{n_\mathrm{S}}\left(|\tilde{a}_{\mathrm{P}\pm}|^2 + 2|\tilde{a}_{\mathrm{P}\mp}|^2\right)}\tilde{a}_{\mathrm{P}\pm} - i\gamma_\mathrm{T}\tilde{a}_{\mathrm{P}\pm}$$

$$+ \beta_{\pm,\mp}^{(\mathrm{P})}\tilde{a}_{\mathrm{P}\mp} - \frac{c}{Ln_\mathrm{L}}\kappa_\mathrm{w}\tilde{a}_{\mathrm{P}\pm}^{(\mathrm{in})}. \tag{4.11}$$

In this Chapter we will assume that our system features a $g = 2$ local Kerr nonlinearity described by a nonlinear refractive index n_NL, and a $\xi = 2$ local saturable gain with P_0 the pump rate and n_S the gain saturation coefficient (see Chapters 2 and 3). We label $\gamma_\mathrm{T} = \gamma_\mathrm{A} + \gamma_\mathrm{w} + \gamma_\mathrm{S}$ the total loss rate including absorption losses γ_A. We can define a k_A parameter entirely analogous to the coupling coefficients $k_\mathrm{w,S}$ to ensure a better comparison between absorption and radiative losses. This will be given by $k_\mathrm{A} = \sqrt{Ln_\mathrm{L}\gamma_\mathrm{A}/c}$. The coupling parameters between counterpropagating modes for a ring resonator are $\beta_{\pm,\mp}^{(\mathrm{P})} = 0$, while in the case of a TJR featuring an S element of length L_S that couples light from the CW into the CCW direction one has $\beta_\mp^{(\mathrm{P})} = 0$ and $\beta_\pm^{(\mathrm{P})} = -i2ck_\mathrm{S}^2 e^{i\omega_\mathrm{P}^{(0)}n_\mathrm{L}L_\mathrm{S}/c}/Ln_\mathrm{L}$ (nonlinear effects can be safely neglected in the exponential factor). The last term of Eq. (4.11) represents the coupling with an external driving field $a_{\mathrm{P}\pm}^{(\mathrm{in})} = \tilde{a}_{\mathrm{P}\pm}^{(\mathrm{in})}e^{i(\pm\ell_\mathrm{P}z/R-\omega_\mathrm{P}t)}$ featuring a frequency ω_P, which can account for the coherent pump of a passive ring resonator or for the small driving setting the lasing direction of the active ring resonator.

We now introduce the signal $a_{\mathrm{S}\pm}$ and idler $a_{\mathrm{I}\pm}$ fields as small perturbations to the pump with frequency (angular momentum) $\omega_\mathrm{S,I}$ ($\pm\ell_\mathrm{S,I}$), respectively, i.e.

$$\tilde{a}_{\mathrm{P}\pm}e^{i(\pm\ell_\mathrm{P}z/R-\omega_\mathrm{P}t)} \rightarrow \tilde{a}_{\mathrm{P}\pm}e^{i(\pm\ell_\mathrm{P}z/R-\omega_\mathrm{P}t)} + \tilde{a}_{\mathrm{S}\pm}e^{i(\pm\ell_\mathrm{S}z/R-\omega_\mathrm{S}t)} + \tilde{a}_{\mathrm{I}\pm}e^{i(\pm\ell_\mathrm{I}z/R-\omega_\mathrm{I}t)}. \tag{4.12}$$

Making this replacement into Eq. (4.11), staying at linear order $\mathcal{O}(a_{\mathrm{S}\pm}, a_{\mathrm{I}\pm})$ in the perturbations, and neglecting the terms representing nonlinear processes that do not conserve energy or angular momentum we arrive to the following equations for the amplitudes of signal and idler inside the

resonator

$$
i\dot{\tilde{a}}_{S\pm} = (\omega_S^{(0)} - \omega_S)\tilde{a}_{S\pm} - 2\frac{n_{NL}}{n_L}\omega_S^{(0)}\left(|\tilde{a}_{P\pm}|^2 + |\tilde{a}_{P\mp}|^2\right)\tilde{a}_{S\pm} - \frac{n_{NL}}{n_L}\sqrt{\omega_S^{(0)}\omega_I^{(0)}}\tilde{a}_{P\pm}^2\tilde{a}_{I\pm}^*
$$
$$
+ i\frac{P_0}{1 + \frac{1}{n_S}\left(|\tilde{a}_{P\pm}|^2 + 2|\tilde{a}_{P\mp}|^2\right)}\tilde{a}_{S\pm} - i\frac{P_0/n_S}{\left[1 + \frac{1}{n_S}\left(|\tilde{a}_{P\pm}|^2 + 2|\tilde{a}_{P\mp}|^2\right)\right]^2}\left(|\tilde{a}_{P\pm}|^2\tilde{a}_{S\pm} + \tilde{a}_{P\pm}^2\tilde{a}_{I\pm}^*\right)
$$
$$
- i\gamma_T\tilde{a}_{S\pm} + \beta_{\pm,\mp}^{(S)}\tilde{a}_{\mp}^{(S)} - \frac{c}{Ln_L}\kappa_w\tilde{a}_{S\pm}^{(in)} \tag{4.13}
$$

$$
i\dot{\tilde{a}}_{I\pm} = (\omega_I^{(0)} - \omega_I)\tilde{a}_{I\pm} - 2\frac{n_{NL}}{n_L}\omega_I^{(0)}\left(|\tilde{a}_{P\pm}|^2 + |\tilde{a}_{P\mp}|^2\right)\tilde{a}_{I\pm} - \frac{n_{NL}}{n_L}\sqrt{\omega_S^{(0)}\omega_I^{(0)}}\tilde{a}_{P\pm}^2\tilde{a}_{S\pm}^*
$$
$$
+ i\frac{P_0}{1 + \frac{1}{n_S}\left(|\tilde{a}_{P\pm}|^2 + 2|\tilde{a}_{P\mp}|^2\right)}\tilde{a}_{I\pm} - i\frac{P_0/n_S}{\left[1 + \frac{1}{n_S}\left(|\tilde{a}_{P\pm}|^2 + 2|\tilde{a}_{P\mp}|^2\right)\right]^2}\left(|\tilde{a}_{P\pm}|^2\tilde{a}_{I\pm} + \tilde{a}_{P\pm}^2\tilde{a}_{S\pm}^*\right)
$$
$$
- i\gamma_T\tilde{a}_{I\pm} + \beta_{\pm,\mp}^{(I)}\tilde{a}_{\mp}^{(I)}, \tag{4.14}
$$

Similarly to what applies for the pump's equation (4.11), only when the TJR is present the couplings $\beta_{\pm}^{(S,I)} = -i2ck_S^2 e^{i\omega_{S,I}^{(0)}n_L L_S/c}/Ln_L$ are non-zero; otherwise we have that $\beta_{\pm,\mp}^{(S,I)} = 0$. In each equation we have substituted $\omega_P^{(0)}$ by the corresponding resonance frequency $\omega_{S,I}^{(0)}$ to include in our description a signal and idler belonging to different modes. The second term in the right-hand side of Eqs. (4.13-4.14) is the usual Kerr nonlinearity which is also present in Eq. (4.11). However, the coupled-mode equations for signal and idler feature further nonlinear terms describing FWM which are proportional to $\tilde{a}_{P\pm}^2\tilde{a}_{I\pm}^*$ and $\tilde{a}_{P\pm}^2\tilde{a}_{S\pm}^*$ in each case. The different frequencies $\omega_S^{(0)}$ and $\omega_I^{(0)}$ in the FWM terms break the intrinsic Hermiticity of the linearized equations provided that gain and losses are not present into the system (i.e. when $P_0 = \gamma_T = 0$). Such a problem stems from the fact that we did not consider the dependence of the nonlinear refractive index $n_{NL}(\omega_S, \omega_I)$ on the frequency of signal and idler. In order to cure this issue we made the following approximation

$$
-\frac{n_{NL}(\omega_S, \omega_I)}{n_L}\omega_{S,I}^{(0)}\tilde{a}_{P\pm}^2\tilde{a}_{S,I\pm}^* \simeq -\frac{n_{NL}}{n_L}\sqrt{\omega_S^{(0)}\omega_I^{(0)}}\tilde{a}_{P\pm}^2\tilde{a}_{S,I\pm}^*, \tag{4.15}
$$

and employed a geometric mean of the frequencies on the FWM terms. Overall, the linearity of the coupled-mode equations for signal (4.13) and idler (4.14) in $\tilde{a}_{S\pm}$ and $\tilde{a}_{I\pm}$ will be of crucial importance for demonstrating the isolator character of our devices. In the last term of Eq. (4.13), $\tilde{a}_{S\pm}^{(in)}$ is an external forcing for the signal featuring a frequency ω_S.

In the following Sections we solve Eqs. (4.11, 4.13, 4.14) for the steady state of the field amplitudes $\tilde{a}_{P,S,I\pm}^{(0)} = \tilde{a}_{P,S,I\pm}(t \to \infty)$ using a 4th order Runge-Kutta algorithm. As typical parameters for a realistic silicon photonics implementation we choose $R = 20\ \mu m$, $n_L = 1.59$, $\gamma_A n_L/c = 8 \times 10^{-6}$ μm^{-1} (which implies $k_A = 0.032$), and $\omega_P^{(0)} = 2\pi \times 200$ THz, corresponding to the mode $\ell_P = 133$, for which we can employ the value of the derivative $(dn_L/d\lambda)_{\lambda_P} = -1.42 \times 10^{-4}$ nm^{-1} presented at the beginning of this Section. These values yield $v = 8.20$ THz and $\alpha = -18.8$ GHz for the dispersion relation (4.7).

The forward (reverse) normalized transmittances T_{for} (T_{rev}) for a signal exiting the resonator from the opposite waveguide to that in which it was injected are defined as

$$
T_{for} = \frac{|\tilde{a}_{S+}^{(out)}|^2}{|\tilde{a}_{S+}^{(in)}|^2} = \frac{|ik_w\tilde{a}_{+}^{(0)}|^2}{|\tilde{a}_{S+}^{(in)}|^2}, \tag{4.16}
$$

$$
T_{rev} = \frac{|\tilde{a}_{S-}^{(out)}|^2}{|\tilde{a}_{S-}^{(in)}|^2} = \frac{|ik_w\tilde{a}_{-}^{(0)}|^2}{|\tilde{a}_{S-}^{(in)}|^2}. \tag{4.17}
$$

As pump, signal and idler feature different frequencies, a frequency filter at the output of the bus waveguide will allow us to get the signal of interest.

In the following Sections we present our results for the transmittance spectrum of forward and reverse-propagating signals in the presence of a large intensity pump in the forward direction. We start with the optically pumped passive ring resonator.
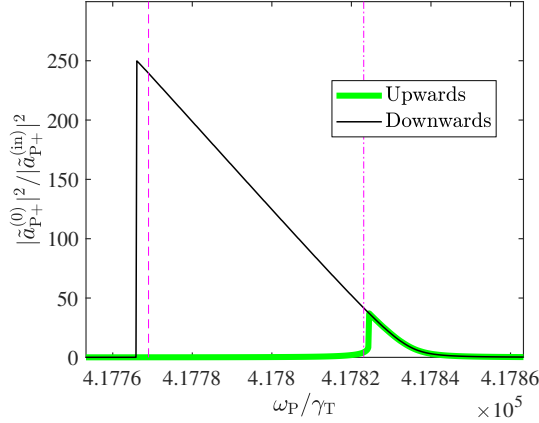
Figure 4.2: Optical bistability in the passive ring resonator described in Sec. 4.3. The figure shows the pump intensity inside the resonator $|\tilde{a}_{P+}^{(0)}|^2$ circulating in the $\ell_P = 133$ mode in units of the incident pump intensity $|\tilde{a}_{P+}^{(in)}|^2$ as a function of frequency ω_P. When frequency is scanned upwards, the intensity is given by the thick green curve (lower branch). In a downwards frequency ramp the intensity is instead given by the thin black line (upper branch). The vertical dashed line indicates the frequency $\omega_P \simeq 4.1777\gamma_T$ in which we pumped in the upper branch. The vertical dashed-dotted line signals the frequency $\omega_P \simeq 4.1782\gamma_T$ in which we pumped in the lower branch.

4.3   Passive ring resonator

In this Section we demonstrate isolation for signals propagating in the reverse direction of a passive ring resonator optically pumped in the $\ell_P = 133$ mode. No saturable gain is present in this case and therefore we take $P_0 = 0$. We employ a nonlinear refractive index $n_{NL} = 10^{-14}$ cm^2/W. As coupling parameters between the ring resonator and the bus waveguides we take $k_w = k_A = 0.032$ to set the system on critical coupling. No S waveguide is present in this case and therefore $k_S = 0$. The corresponding quality factor for such a ring resonator is $Q \simeq 4.2 \times 10^5$.

The coherent pump with frequency ω_P and incident intensity $|\tilde{a}_{P+}^{(in)}|^2$ injected through the left-hand waveguide sets the CCW mode as the forward operation direction. Due to the optical nonlinearity the resonance frequency given in the linear regime by Eq. (4.7) is red-shifted (as our material features $n_{NL} > 0$) and the pump intensity inside the resonator $|\tilde{a}_{P+}^{(0)}|^2$ describes a hysteresis cycle as a function of ω_P known as optical bistability. Such a phenomenon is well-known from Chapter 2. A frequency scan of $|\tilde{a}_{P+}^{(0)}|^2$ is shown in Fig. 4.2, displaying the two intensity branches. Thus, the value of $|\tilde{a}_{P+}^{(0)}|^2$ will depend on whether we are pumping in the upper or lower branch of this hysteresis cycle. An appropriate choice of initial conditions allows us to pump in the upper branch, which features a larger intensity than the lower one. This enhances the effect of FWM. For the same reason we pump at a frequency $\omega_P \simeq 4.1777\gamma_T$, close to the downwards intensity jump of the upper branch, yielding a pump intensity inside the resonator $|\tilde{a}_{P+}^{(0)}|^2 \simeq 240|\tilde{a}_{P+}^{(in)}|^2$.

We then probe the device in the forward direction by sending through the left-hand bus waveguide a signal of incident intensity $|\tilde{a}_{S+}^{(in)}| = 10^{-1}|\tilde{a}_{P+}^{(in)}|^2$. The forward transmittance T_{for} as a function of the signal frequency ω_S is plotted in Fig. 4.3a around a single resonance corresponding to the mode with angular momentum $\ell_S = 131$. The spectrum exhibits a characteristic doublet: The left-hand peak corresponds to the resonance frequency of the signal, whose position is shifted due to the nonlinear terms in Eq. (4.13). The right-hand peak, on the other hand, appears as a consequence of conservation of energy and momentum in FWM processes coupling the pump with the resonance frequency of the idler.

We now send a reverse-propagating signal of identical incident intensity $|\tilde{a}_{S-}^{(in)}| = 10^{-1}|\tilde{a}_{P+}^{(in)}|^2$ through the right-hand bus waveguide and look at the transmittance T_{rev} as its frequency ω_S is varied around the resonance corresponding to the CW mode with angular momentum $\ell_S = -131$. Since FWM is absent, in this case no photons from the pump are scattered into the idler resonance, and therefore T_{rev} displays a single peak. However, this is located at a different frequency from that of the left-hand peak of the T_{for} doublet. This is also due to the lack of FWM coupling between

pump, signal, and idler: in the reverse direction the only contribution to the nonlinear shift of the resonance peak comes from the Kerr nonlinearity. As can be seen in Fig. 4.3a, T_{rev} is negligible over a broad frequency range, including the frequencies at which the doublet in T_{for} appears. In particular, at the frequency $\omega_S \simeq 4.1228\gamma_T$ (or equivalently $[\omega_S - \omega_P^{(0)} - v(|\ell_S| - |\ell_P|)] = -103.47\gamma_T$) in which the forward-propagating signal achieves its maximum transmittance, the ratio between the two transmittances reaches 33 dB, thus demonstrating the isolator character of our device. Since Eqs. (4.13-4.14) are linear in $\tilde{a}_{S\pm}$ and $\tilde{a}_{I\pm}$, the forward and reverse signals cannot interact between each other and therefore the transmittance spectra in the two directions are unaltered even when the two signals are propagating though the device at the same time. As a consequence our device is not subjected to the dynamic reciprocity restrictions and hence it can work as an optical isolator.

The different effect of FWM for counterpropagating signals can be further investigated by means of a Bogoliubov analysis of the dynamics of signal and idler both in forward and reverse directions, which are treated as linearized perturbations to the large intensity pump present in the forward direction only. From Eqs. (4.13-4.14) it is straightforward to set up the Bogoliubov system of equations

$$
i\frac{d}{dt}\begin{bmatrix} \tilde{a}_{S+} & \tilde{a}_{I+}^* & \tilde{a}_{S-} & \tilde{a}_{I-}^* \end{bmatrix}^T
$$
$$
= \begin{bmatrix}
\begin{array}{c} \omega_S^{(0)} - \omega_S - i\gamma_T \\ -2\frac{n_{\text{NL}}}{n_L}\omega_S^{(0)}|\tilde{a}_{P+}^{(0)}|^2 \\ +\frac{n_{\text{NL}}}{n_L}\sqrt{\omega_S^{(0)}\omega_I^{(0)}}\tilde{a}_{P+}^{(0)*2} \end{array} & \begin{array}{c} -\frac{n_{\text{NL}}}{n_L}\sqrt{\omega_S^{(0)}\omega_I^{(0)}}\tilde{a}_{P+}^{(0)2} \\ -\omega_I^{(0)} + 2\omega_P - \omega_S - i\gamma_T \\ +2\frac{n_{\text{NL}}}{n_L}\omega_I^{(0)}|\tilde{a}_{P+}^{(0)}|^2 \end{array} & 0 & 0 \\
0 & 0 & \begin{array}{c} \omega_S^{(0)} - \omega_S - i\gamma_T \\ -2\frac{n_{\text{NL}}}{n_L}\omega_S^{(0)}|\tilde{a}_{P+}^{(0)}|^2 \end{array} & 0 \\
0 & 0 & 0 & \begin{array}{c} -\omega_I^{(0)} + 2\omega_P - \omega_S - i\gamma_T \\ +2\frac{n_{\text{NL}}}{n_L}\omega_I^{(0)}|\tilde{a}_{P+}^{(0)}|^2 \end{array}
\end{bmatrix}
$$
$$
\times \begin{bmatrix} \tilde{a}_{S+} & \tilde{a}_{I+}^* & \tilde{a}_{S-} & \tilde{a}_{I-}^* \end{bmatrix}^T. \tag{4.18}
$$

The next step is to diagonalize the 4×4 matrix above in order to find the eigenvalues ω_S and their corresponding (normalized) eigenvectors $\mathbf{v}$ for several pairs of counterpropagating signals coupled to modes with opposite angular momentum $\pm|\ell_S|$ in a range of $|\ell_S|$ around ℓ_P. On the one hand, the real part of the eigenvalues $Re\{\omega_S\}$ will tell us the position of the transmittance peaks for each pair of signals. On the other hand, a positive imaginary part $Im\{\omega_S\} > 0$ for some ℓ_S implies that the system is dynamically unstable around that mode. A negative imaginary part $Im\{\omega_S\} < 0$ at ℓ_S signals instead the dynamical stability of that mode.

The normalization condition for each eigenvector $\mathbf{v} = [v_1, v_2, v_3, v_4]^T$ reads

$$
\sqrt{v_1^2 + v_2^2 + v_3^2 + v_4^2} = 1. \tag{4.19}
$$

We will classify the four eigenvectors according to their Bogoliubov norms. This quantity is defined as

$$
\|\mathbf{v}\| = |v_1|^2 - |v_2|^2 + |v_3|^2 - |v_4|^2, \tag{4.20}
$$

and quantifies the coupling between signal and idler. It follows from Eq. (4.19) that the Bogoliubov norm is restricted to values in the range

$$
-1 \leq \|\mathbf{v}\| \leq 1. \tag{4.21}
$$

A negative norm implies an idler-dominated response, while a positive norm corresponds to a larger contribution of the signal.

After diagonalizing the matrix in Eq. (4.18) we find four eigenvectors labelled $\mathbf{v}_{I+}$, $\mathbf{v}_{S+}$, $\mathbf{v}_{I-}$, and $\mathbf{v}_{S-}$ featuring norms

$$
\|\mathbf{v}_{I+}\| = -0.724, \quad \|\mathbf{v}_{S+}\| = 0.724, \quad \|\mathbf{v}_{I-}\| = -1, \quad \|\mathbf{v}_{S-}\| = 1. \tag{4.22}
$$

Note that the norms of the eigenvectors belonging to the reverse-propagating idler $\mathbf{v}_{I-}$ and signal $\mathbf{v}_{S-}$ take the extreme values $\|\mathbf{v}_{I-}\| = -1$ and $\|\mathbf{v}_{S-}\| = 1$, signaling that there is no coupling between

them. On the other hand, the norms of the eigenvectors belonging to the forward-propagating idler $\mathbf{v}_{\mathrm{I}+}$ and signal $\mathbf{v}_{\mathrm{S}+}$ feature values closer to zero due to the FWM terms coupling them.

We will label the eigenvalues associated to these eigenvectors as $\omega_{\mathrm{S}}(\mathbf{v}_{\mathrm{I}+})$, $\omega_{\mathrm{S}}(\mathbf{v}_{\mathrm{S}+})$, $\omega_{\mathrm{S}}(\mathbf{v}_{\mathrm{I}-})$, and $\omega_{\mathrm{S}}(\mathbf{v}_{\mathrm{S}-})$, respectively. Panels (b) and (c) of Fig. 4.3 display respectively the real and imaginary parts of the four eigenvalues as a function of the absolute value of the angular momentum $|\ell_{\mathrm{S}}|$ of the pair of counterpropagating signals. For completeness, in these panels we have added the results for non-integer values of $|\ell_{\mathrm{S}}|$. Although they are not relevant to study the transmittance across our device, since only integer values of $|\ell_{\mathrm{S}}|$ are accessible, they will allow us to understand the physics with more clarity, as we will see. For the reverse-propagating signal, as it is evident from the form of the Bogoliubov matrix in Eq. (4.18), the real part of the eigenvalue $\omega_{\mathrm{S}}(\mathbf{v}_{\mathrm{S}-})$ is solely determined by the Kerr nonlinearity shift of the resonance frequency of the mode with angular momentum $-\ell_{\mathrm{S}}$ in which the signal is coupled, i.e.

$$Re\{\omega_{\mathrm{S}}(\mathbf{v}_{\mathrm{S}-})\} = \omega_{\mathrm{S}}^{(0)} \left[1 - 2\frac{n_{\mathrm{NL}}}{n_{\mathrm{L}}} |\tilde{a}_{\mathrm{P}+}^{(0)}|^2 \right]. \tag{4.23}$$

On the other hand, the real part of the eigenvalue $\omega_{\mathrm{S}}(\mathbf{v}_{\mathrm{I}-})$ is given by the frequency at which FWM would couple the pump light into the signal mode due to its interaction with pump photons scattered into the idler resonance frequency, which is as well shifted by the Kerr nonlinearity, i.e.

$$Re\{\omega_{\mathrm{S}}(\mathbf{v}_{\mathrm{I}-})\} = 2\omega_{\mathrm{P}} - \omega_{\mathrm{I}}^{(0)} \left[1 - 2\frac{n_{\mathrm{NL}}}{n_{\mathrm{L}}} |\tilde{a}_{\mathrm{P}+}^{(0)}|^2 \right]. \tag{4.24}$$

As shown in Fig. 4.3b the real parts of these eigenvalues form two branches separated by a gap that takes its minimum frequency width at the angular momentum of the pump ℓ_{P}. The real part of $\omega_{\mathrm{S}}(\mathbf{v}_{\mathrm{S}-})$ gives the frequency at which the reverse transmittance T_{rev} displays its maximum value: to demonstrate this we plotted a dashed-dotted line at the frequency $Re\{\omega_{\mathrm{S}}(\mathbf{v}_{\mathrm{S}-})\}$ corresponding to the mode with angular momentum $\ell_{\mathrm{S}} = -131$ in Fig. 4.3a. We also plotted a second dashed-dotted line at the frequency $Re\{\omega_{\mathrm{S}}(\mathbf{v}_{\mathrm{I}-})\}$ belonging to the mode $\ell_{\mathrm{S}} = -131$. However, as we can ascertain from the Bogoliubov norm of its associated eigenvector ($\|\mathbf{v}_{\mathrm{I}-}\| = -1$), this eigenvalue only features a contribution from the idler, and since FWM is not present for the reverse signal, no peak is displayed by T_{rev} at $Re\{\omega_{\mathrm{S}}(\mathbf{v}_{\mathrm{I}-})\}$. Regarding the imaginary parts, both of them are given by the total loss rate of the resonator, i.e. $Im\{\omega_{\mathrm{S}}(\mathbf{v}_{\mathrm{S},\mathrm{I}-})\} = -\gamma_{\mathrm{T}}$ for all values of angular momentum $|\ell_{\mathrm{S}}|$, as shown in Fig. 4.3c, probing the pump stability against the presence of small reverse-propagating signals regardless of ℓ_{S}.

On the other hand, the eigenvalues $\omega_{\mathrm{S}}(\mathbf{v}_{\mathrm{S},\mathrm{I}+})$ associated to forward signals are given by the diagonalization of the top-left 2×2 block of the Bogoliubov matrix. Again, their real parts give rise to a couple of branches separated by a gap, as shown in Fig. 4.3b. However, in the case of the forward signal FWM results in an effective attraction between the two branches, that get closer together with respect to the reverse signal case. The gap between them remains nevertheless open, and features its minimum frequency width at the pump angular momentum ℓ_{P}. To demonstrate that $Re\{\omega_{\mathrm{S}}(\mathbf{v}_{\mathrm{S},\mathrm{I}+})\}$ give the frequencies of the peaks in T_{for} for each mode, we plotted their values at an angular momentum $\ell_{\mathrm{S}} = 131$ as dashed vertical lines in Fig. 4.3a. Also for the forward signal, the two real parts agree perfectly with the transmittance maxima. Concerning the imaginary parts, these are plotted in Fig. 4.3c and form a flat band given by the total loss rate $Im\{\omega_{\mathrm{S}}(\mathbf{v}_{\mathrm{S},\mathrm{I}+})\} = -\gamma_{\mathrm{T}}$ regardless of the particular value of $|\ell_{\mathrm{S}}|$, implying again that the pump is dynamically stable in the presence of signal and idler in the forward direction.

Note that no unstable behaviors arise in the upper branch of the optical bistability as the imaginary parts of the eigenvalues are always negative. As we mentioned before this is the branch in which we are interested as it provides a larger pump intensity that enhances FWM mixing. However, for completeness we will now take a look at the physics in the lower intensity branch of the bistability loop. We set a pump frequency $\omega_{\mathrm{P}} \simeq 4.1782\gamma_{\mathrm{T}}$ close to the upwards intensity jump (see Fig. 4.2) and use an appropriate choice of initial conditions such that we obtain a pump intensity $|\tilde{a}_{\mathrm{P}+}^{(0)}|^2 \simeq 4.3|\tilde{a}_{\mathrm{P}}^{(\mathrm{in})}|^2$ in the lower branch. As shown in Fig. 4.3d in this case the pump intensity is not sufficiently large to give rise to a sizable FWM. As a consequence, the transmittance spectrum $T_{\mathrm{for,rev}}(\omega_{\mathrm{S}})$ for the pair of counterpropagating modes with absolute angular momenta $|\ell_{\mathrm{S}}| = 131$ is identical in the two directions and features a single peak determined by the Kerr nonlinearity shift of the resonance frequency, i.e. located at $\omega_{\mathrm{S}} = \omega_{\mathrm{S}}^{(0)}[1 - 2n_{\mathrm{NL}}|\tilde{a}_{\mathrm{P}+}^{(0)}|^2/n_{\mathrm{L}}]$.

In this case the Bogoliubov norms of the four eigenvectors are

$$\|\mathbf{v}_{\mathrm{I}+}\| = -0.999, \quad \|\mathbf{v}_{\mathrm{S}+}\| = 0.999, \quad \|\mathbf{v}_{\mathrm{I}-}\| = -1, \quad \|\mathbf{v}_{\mathrm{S}-}\| = 1, \tag{4.25}$$
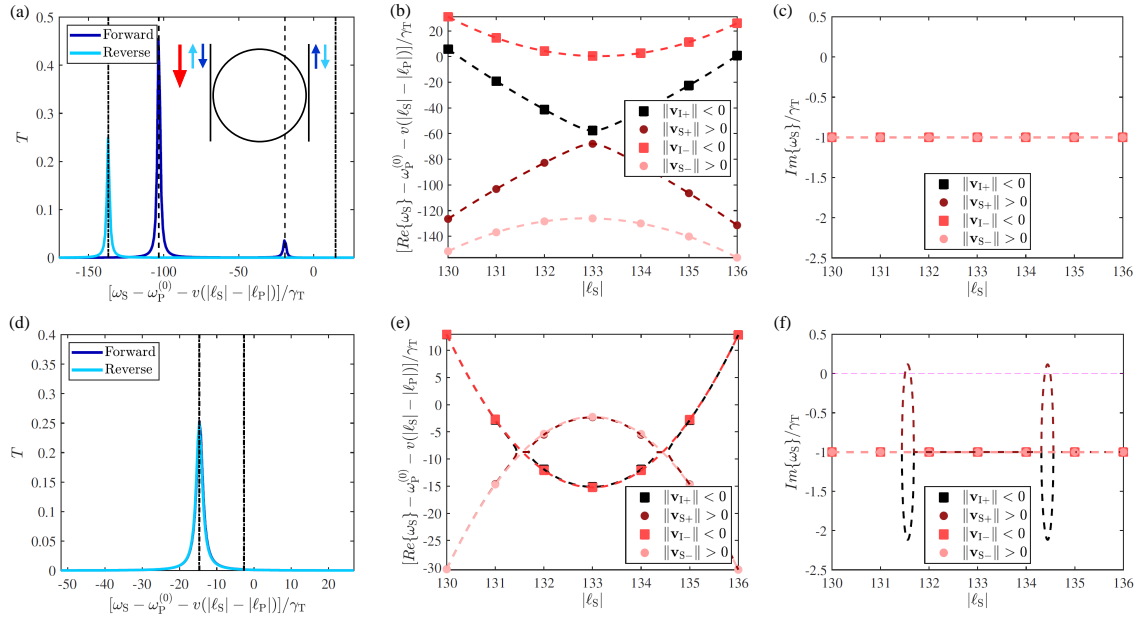
Figure 4.3: **(a,d)** Transmittance T in forward (dark blue) and reverse (light blue) directions across an optically pumped passive ring resonator in add-drop configuration as a function of the signal frequency ω_S for a pair of counterpropagating modes with absolute angular momenta $|\ell_S| = 131$. Panels (a) and (d) display the results when we pump in the upper and lower bistability branches, respectively. A sketch of the device is found in the upper-right part of panel (a). The big, red arrow represents the incident pump, while the small arrows describe the probing with the signal. The vertical dashed-dotted and dashed lines signal respectively the real parts of the Bogoliubov eigenvalues corresponding to the reverse and forward-propagating signals. **(b,c)** Real and imaginary parts of the Bogoliubov eigenvalues ω_S for a pump in the upper bistability branch as a function of the angular momenta $\pm|\ell_S|$ of two signals propagating in the forward and reverse directions which are varied around $\pm\ell_P = \pm133$. The eigenvalues are labelled according to the Bogoliubov norm $\|\mathbf{v}_{S,I\pm}\|$ of the associated eigenvectors. Squares and circles are the values corresponding to the modes of integer angular momenta $|\ell_S|$. The dashed lines are calculated for non-integer values of $|\ell_S|$. Panels **(e,f)** show analogous plots for the case in which we pump in the lower bistability branch. The horizontal dashed pink line in panel (f) indicates the position of zero.

signaling a negligible but finite coupling between signal and idler in the forward case.

The corresponding real and imaginary parts of the Bogoliubov eigenvalues $\omega_S(\mathbf{v}_{S,I\pm})$ are shown in Fig. 4.3e,f, respectively. The two real parts $Re\{\omega_S(\mathbf{v}_{S,I-})\}$ belonging to the reverse-propagating signal intersect at two non-integer values of angular momentum in the neighborhood of the pump angular momentum ℓ_P, therefore closing the gap. However, their corresponding imaginary parts are still given by the total loss rate $Im\{\omega_S(\mathbf{v}_{S,I-})\} = -\gamma_T$ as in the upper bistability branch. This grants the dynamical stability of the pump against reverse signals also in the lower bistability branch. The situation is more interesting in the case of the forward-propagating signal: for non-integer angular momenta around the two intersection points of $Re\{\omega_S(\mathbf{v}_{S,I-})\}$ the two real parts $Re\{\omega_S(\mathbf{v}_{S,I+})\}$ coalesce and the corresponding imaginary parts $Im\{\omega_S(\mathbf{v}_{S,I+})\}$ are split. When the pump frequency ω_P approaches the upwards intensity jump of the bistability loop, the imaginary part of $\omega_S(\mathbf{v}_{S+})$ turns positive in the aforementioned regions of ℓ_S and therefore the system would become dynamically unstable for such non-integer values of angular momenta.

Even though non-integer values of $|\ell_S|$ are not accessible, the width of the two regions at which $Im\{\omega_S(\mathbf{v}_{S,I+})\}$ are split can be broadened by employing materials featuring a smaller (negative) curvature α in the dispersion relation. Eventually some integer values of ℓ_S will fall within these regions.

It is interesting to note that a similar physics arises in coherently pumped polariton condensates, in which the polariton density also features a bistable behavior [53].

4.4   Active ring resonator

Here we investigate isolation in the active analog of the passive ring resonator studied in the previous Section. By incoherently pumping the resonator above the lasing threshold $P_0 > \gamma_T$ we can trigger lasing in the $\pm\ell_P$ counterpropagating modes. On the following we will assume that only this pair of modes competes for the gain. If backscattering is negligible, a local saturable gain will grant unidirectional lasing with a well-defined chirality in one of these two modes, as we probed in Chapter 3. However, for this system to work as an isolator we need to deterministically set one of the operation directions as the forward one. Otherwise the lasing chirality and thus the forward and reverse directions are randomly set every time the device is pumped. Without loss of generality, in our case we choose the CCW as the forward direction by means of a small driving $\tilde{a}_{P+}^{(in)}$ coupling into the $\ell_P > 0$ mode. The presence of the driving triggers lasing in the CCW-propagating ℓ_P mode under an incoherent pumping $P_0 > \gamma_T$. Of course, changing the driving direction will result in a resonator lasing in the opposite mode with angular momentum $-\ell_P$. Nevertheless, once lasing in the desired direction is triggered, one could switch off the driving. In order to check how does the driving alter the features of the transmittance spectrum, we first analyze the case in which it is switched on during the probing with the signal in forward and reverse directions, and at the end of this Section we will also take a look at the case in which the driving is turned off prior to injecting the signals in the two directions.

As parameters for our simulations we employed a ring-bus waveguide coupling $k_w = 0.04$, absorption losses $k_A = 0.032$ (yielding a quality factor $Q \simeq 7.6 \times 10^4$), and a nonlinear refractive index $n_{NL} n_S \omega_P^{(0)}/(n_L \gamma_T) \simeq 9.6$. As done for the passive ring resonator, we choose a pump mode of angular momentum $\ell_P = 133$. We set a pump rate $P_0 = 2\gamma_T$, which gives a pump intensity inside the resonator $|\tilde{a}_P^{(0)}|^2/n_S = P_0/\gamma_T - 1 = 1$. The lasing frequency will then be determined by the Kerr nonlinear shift of the pump resonance frequency, i.e. $\omega_P = \omega_P^{(0)}(1 - n_{NL}/n_L n_S)$.

For now we consider that the driving $\tilde{a}_{P+}^{(in)}$ is present into the system. This features an incident intensity $|\tilde{a}_{P+}^{(in)}|^2 = 10^{-2} n_S$ and a frequency $\omega_P = \omega_P^{(0)}(1 - n_{NL}/n_L n_S)$. The latter coincides with the emission frequency of the laser in the ℓ_P mode. Nevertheless, a driving displaying any other frequency in the neighborhood of ω_P will also trigger lasing in the ℓ_P mode.

In order to demonstrate the isolation of reverse-propagating signals we follow the same strategy as in Sec. 4.3. By means of a signal $\tilde{a}_{S+}^{(0)}$ propagating in the forward direction with incident intensity $|\tilde{a}_{S+}^{(in)}|^2 = 10^{-1} n_S$ we first probe the system around the resonance frequency $\omega_S^{(0)}$ of the mode with positive angular momentum $\ell_S = 131$. The transmittance is shown in Fig. 4.4a and it displays the characteristic doublet spectrum resulting from FWM. We then probe the system using a reverse-propagating signal $\tilde{a}_{S-}^{(0)}$ of the same incident intensity $|\tilde{a}_{S-}^{(in)}|^2 = 10^{-1} n_S$ that couples to the mode with opposite angular momentum $\ell_S = -131$. Fig. 4.4a shows that T_{rev} is negligible over a broad

frequency range and, as we will see, due to the absence of FWM in this case it features its maximum at a frequency given by the Kerr nonlinearity shift of $\omega_S^{(0)}$. This is different from the frequencies at which we obtained the doublet in T_{for}. In fact, at a frequency $\omega_S = 7.5132 \times 10^4 \gamma_T$ (i.e. $[\omega_S - \omega_P^{(0)} - v(|\ell_S| - |\ell_P|)] = -16.52\gamma_T$) where T_{for} achieves its maximum value, the ratio between transmittance in the two directions reaches 23 dB. As in Sec. 4.3, the linearity of Eqs. (4.13-4.14) with respect to the signal and idler fields makes the transmittance spectra $T_{\text{for,rev}}$ unaffected by the presence of each other, therefore preserving the optical isolator character of our device.

Similarly to what we did in the previous Section we now study the asymmetry between forward and reverse signals by setting up the Bogoliubov system of equations for the linearized signal and idler fields in the two directions and diagonalizing the resulting Bogoliubov matrix in a range of angular momenta $\pm|\ell_S|$ around $\pm\ell_P$. In the case of an active ring resonator the system of differential equations reads

$$
i\frac{d}{dt}\begin{bmatrix} \tilde{a}_{S+} & \tilde{a}_{I+}^* & \tilde{a}_{S-} & \tilde{a}_{I-}^* \end{bmatrix}^T
$$

$$
=
\begin{bmatrix}
\begin{matrix} \omega_S^{(0)} - \omega_S - i\gamma_T \\ -2\frac{n_{NL}}{n_L}\omega_S^{(0)}|\tilde{a}_{P+}^{(0)}|^2 \\ +i\frac{P_0}{1+\frac{1}{n_S}|\tilde{a}_{P+}^{(0)}|^2} \\ -i\frac{P_0/n_S}{\left[1+\frac{1}{n_S}|\tilde{a}_{P+}^{(0)}|^2\right]^2}|\tilde{a}_{P+}^{(0)}|^2 \end{matrix} & \begin{matrix} -\frac{n_{NL}}{n_L}\sqrt{\omega_S^{(0)}\omega_I^{(0)}}\tilde{a}_{P+}^{(0)2} \\ -i\frac{P_0/n_S}{\left[1+\frac{1}{n_S}|\tilde{a}_{P+}^{(0)}|^2\right]^2}\tilde{a}_{P+}^{(0)2} \end{matrix} & 0 & 0 \\[2em]
\begin{matrix} +\frac{n_{NL}}{n_L}\sqrt{\omega_S^{(0)}\omega_I^{(0)}}\tilde{a}_{P+}^{(0)*2} \\ -i\frac{P_0/n_S}{\left[1+\frac{1}{n_S}|\tilde{a}_{P+}^{(0)}|^2\right]^2}\tilde{a}_{P+}^{(0)*2} \end{matrix} & \begin{matrix} -\omega_I^{(0)} + 2\omega_P - \omega_S - i\gamma_T \\ +2\frac{n_{NL}}{n_L}\omega_I^{(0)}|\tilde{a}_{P+}^{(0)}|^2 \\ +i\frac{P_0}{1+\frac{1}{n_S}|\tilde{a}_{P+}^{(0)}|^2} \\ -i\frac{P_0/n_S}{\left[1+\frac{1}{n_S}|\tilde{a}_{P+}^{(0)}|^2\right]^2}|\tilde{a}_{P+}^{(0)}|^2 \end{matrix} & 0 & 0 \\[2em]
0 & 0 & \begin{matrix} \omega_S^{(0)} - \omega_S - i\gamma_T \\ -2\frac{n_{NL}}{n_L}\omega_S^{(0)}|\tilde{a}_{P+}^{(0)}|^2 \\ +i\frac{P_0}{1+2\frac{1}{n_S}|\tilde{a}_{P+}^{(0)}|^2} \end{matrix} & 0 \\[2em]
0 & 0 & 0 & \begin{matrix} -\omega_I^{(0)} + 2\omega_P - \omega_S - i\gamma_T \\ +2\frac{n_{NL}}{n_L}\omega_I^{(0)}|\tilde{a}_{P+}^{(0)}|^2 \\ +i\frac{P_0}{1+2\frac{1}{n_S}|\tilde{a}_{P+}^{(0)}|^2} \end{matrix}
\end{bmatrix}
$$

$$
\times \begin{bmatrix} \tilde{a}_{S+} & \tilde{a}_{I+}^* & \tilde{a}_{S-} & \tilde{a}_{I-}^* \end{bmatrix}^T . \tag{4.26}
$$

By diagonalizing the 4×4 matrix above we get the four eigenvectors $\mathbf{v}_{S,I\pm}$ and their corresponding eigenvalues $\omega_S(\mathbf{v}_{S,I\pm})$. In this case, the Bogoliubov norms of the eigenvectors are

$$
\|\mathbf{v}_{I+}\| = -0.759, \quad \|\mathbf{v}_{S+}\| = 0.759, \quad \|\mathbf{v}_{I-}\| = -1, \quad \|\mathbf{v}_{S-}\| = 1, \tag{4.27}
$$

Similarly to the coherently pumped passive resonator studied in Sec. 4.3, only in the forward case there exists a finite coupling between signal and idler.

The real and imaginary parts of the eigenvalues are displayed in panels (b) and (c) of Fig. 4.4, respectively. As in the previous Section, we can obtain more insight about the underlying physics by plotting the whole spectrum of eigenvalues also for non-integer values of $|\ell_S|$. Similarly to the passive ring resonator pumped in the upper branch of the bistability loop, the real parts are arranged in four branches separated by a gap that takes its minimum width at $|\ell_S| = \ell_P$.

For the reverse-propagating signal, FWM is not present and the $Re\{\omega_S(\mathbf{v}_{S,I-})\}$ branches are completely determined by the Kerr nonlinear shift of the resonance frequency of the corresponding modes for signal and idler, i.e. they are given again by Eqs. (4.23-4.24). The value of $Re\{\omega_S(\mathbf{v}_{S-})\}$ can be associated to the frequency at which T_{rev} features its maximum. However, as we can ascertain by examining the Bogoliubov norm of the eigenvectors (4.27), T_{rev} does not display a peak at $Re\{\omega_S(\mathbf{v}_{I-})\}$ because FWM is not present for the reverse signal and therefore no light from the pump can be coupled at this frequency while simultaneously satisfying the conservation of energy and angular momentum. Both $Re\{\omega_S(\mathbf{v}_{S,I-})\}$ at an angular momentum $\ell_S = -131$ are plotted as vertical dashed-dotted lines in Fig. 4.4a. The corresponding imaginary parts $Im\{\omega_S(\mathbf{v}_{S,I-})\}$ take the value

$$
Im\{\omega_S(\mathbf{v}_{S,I-})\} = \frac{P_0}{1+2\frac{1}{n_S}|\tilde{a}_{P+}^{(0)}|^2} - \gamma_T = -\frac{\gamma_T}{3} \tag{4.28}
$$

independently of ℓ_S. This means that the pump is dynamically stable in the presence of the reverse signal.
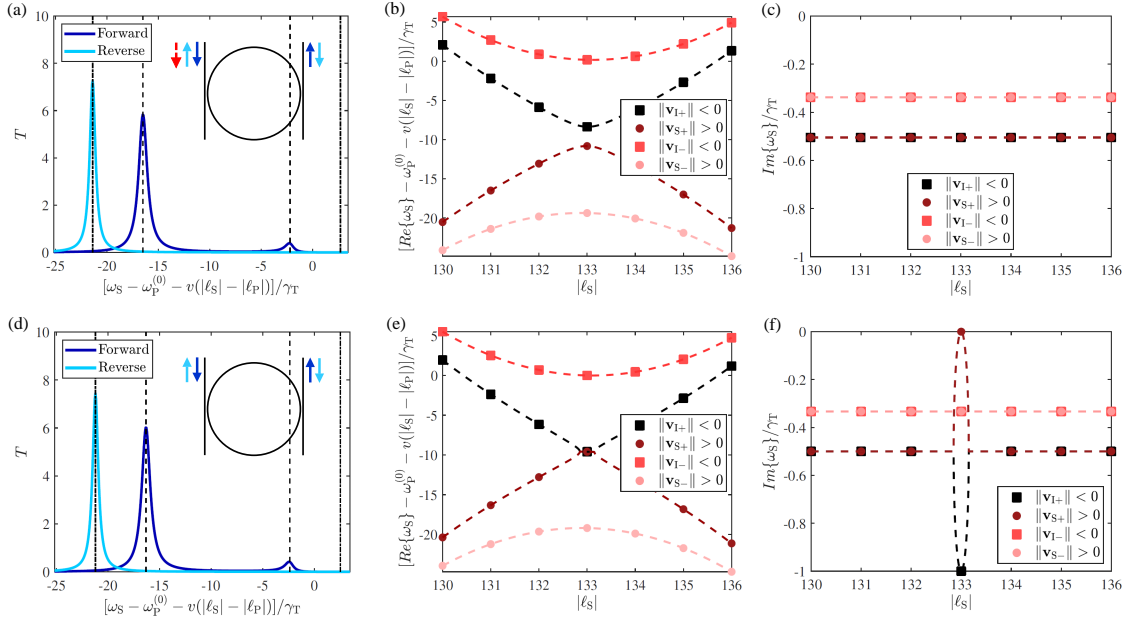
Figure 4.4: **(a,d)** Transmittance T in forward (dark blue) and reverse (light blue) directions across an incoherently pumped active ring resonator in add-drop configuration lasing in the $\ell_P = 133$ mode as a function of the signal frequency ω_S for a pair of counterpropagating modes with angular momenta $|\ell_S| = 131$. Panels (a) and (d) display the results when a small driving employed to trigger lasing is present and absent, respectively. A sketch of the device is found in the upper-right part of panels (a,d). The red, dashed arrow represents the incident driving, while the solid arrows describe the probing with the signal. The vertical dashed-dotted and dashed lines signal respectively the values of the real part of the Bogoliubov eigenvalues corresponding to the reverse and forward-propagating signals. **(b,c)** Real and imaginary parts of the Bogoliubov eigenvalues ω_S in the presence of the driving as a function of the angular momenta $\pm|\ell_S|$ of two signals propagating in the forward and reverse directions which are varied around $\pm\ell_P = \pm133$. The eigenvalues are labelled according to the Bogoliubov norm $\|\mathbf{v}_{S,I\pm}\|$ of the corresponding eigenvectors. Squares and circles are the values corresponding to the modes of integer angular momenta $|\ell_S|$. The dashed lines are calculated for non-integer values of $|\ell_S|$. Panels **(e,f)** show analogous plots for the case in which the driving has been switched off.

On the other hand, as demonstrated by the Bogoliubov norms (4.27) of the corresponding eigenvectors, in the forward case FWM couples the pump with the resonance frequencies of signal and idler. This results in a doublet of peaks in T_{for} at frequencies given by $Re\{\omega_S(\mathbf{v}_{S,I+})\}$. As can be seen in Fig. 4.4b, FWM results in an effective attraction between transmittance peaks as it brings the two eigenvalues branches closer together and narrows the gap. For an angular momentum $\ell_S = 131$ the values of $Re\{\omega_S(\mathbf{v}_{S,I+})\}$ are plotted as vertical dashed lines in Fig. 4.4a. In this case the imaginary parts form a flat band that takes the value

$$Im\{\omega_{S+}^{(\text{up,down})}\} = -\frac{P_0/n_S}{\left[1 + \frac{1}{n_S}|\tilde{a}_{P+}^{(0)}|^2\right]^2}|\tilde{a}_{P+}^{(0)}|^2 = -\frac{\gamma_T}{2}. \tag{4.29}$$

At this point we would like to address the role of the driving $\tilde{a}_{P+}^{(\text{in})}$ in the spectrum of eigenvalues. To do this we will compare these results with those obtained for the same active ring resonator where the driving has been switched off after triggering lasing in the $\ell_S = 133$ mode.

We first focus on evaluating the signal transmittance in the two directions around the resonance frequency $\omega_S^{(0)}$ of the modes with $|\ell_S| = 131$. We use the same procedure that we followed in the presence of the driving: the results for $T_{\text{for,rev}}$ are shown in Fig. 4.4d and they are identical to those obtained when the driving was switched on. This is not a surprise as the driving intensity is so small that it does interact with the signal via the nonlinearities. We then diagonalize the 4×4 Bogoliubov matrix in Eq. (4.26) for several pairs of counterpropagating modes with angular momenta $|\ell_S|$ in a neighborhood of ℓ_P in order to look at the driving-free eigenvalues and eigenvectors. These latter
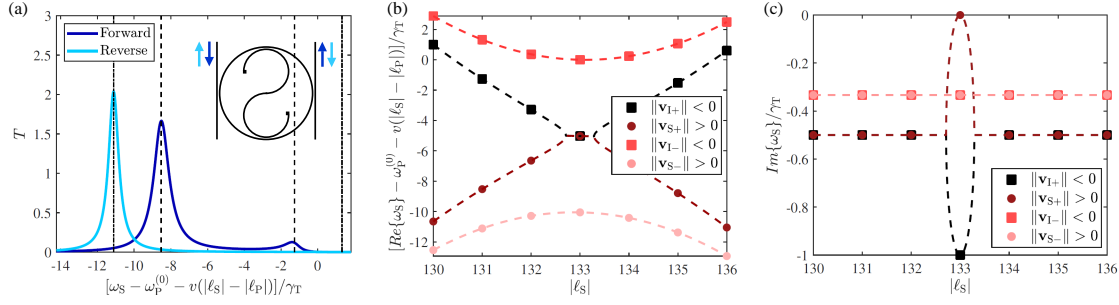
Figure 4.5: **(a)** Transmittance T in forward (dark blue) and reverse (light blue) directions across an optically pumped active TJR in add-drop configuration as a function of the signal frequency ω_S, for counterpropagating modes with angular momenta $|\ell_S| = 131$. The pump rate is fixed at $P_0 = 2\gamma_T$. A sketch of the device is found in the upper-right part of the panel. The arrows describe the probing with the signal. The vertical dashed-dotted and dashed lines signal respectively the values of the real part of the Bogoliubov eigenvalues corresponding to the reverse and forward-propagating signals. **(b,c)** Real and imaginary parts of the Bogoliubov eigenvalues ω_S as the angular momenta $\pm|\ell_S|$ of the modes in which the counterpropagating signals are coupled is varied around $\pm\ell_P = \pm133$. Squares and circles are the values corresponding to the modes of integer angular momenta $|\ell_S|$. The dashed lines are calculated for non-integer values of $|\ell_S|$.

are only slightly modified by the absence of the driving:

$$\|\mathbf{v}_{I+}\| = -0.758, \quad \|\mathbf{v}_{S+}\| = 0.758, \quad \|\mathbf{v}_{I-}\| = -1, \quad \|\mathbf{v}_{S-}\| = 1. \tag{4.30}$$

The real and imaginary parts of the corresponding eigenvalues $\omega_S(\mathbf{v}_{S,I\pm})$ are displayed in Fig. 4.4e,f, respectively. In the case of the reverse-propagating signal and idler we obtain the same values of $\omega_S(\mathbf{v}_{S,I-})$ both in the presence and absence of the driving. However, the eigenvalues $\omega_S(\mathbf{v}_{S,I+})$ corresponding to the forward case are modified in a region of non-integer angular momenta around the pump angular momentum ℓ_P: their real parts coalesce at $Re\{\omega_S(\mathbf{v}_{S,I+})\} = \omega_P^{(0)}[1 - n_{NL}|\tilde{a}_{P+}^{(0)}|^2/n_L]$ (i.e. the frequency of the Kerr-shifted resonance at $\ell_P = 133$), while simultaneously their imaginary parts depart and take the values $Im\{\omega_S(\mathbf{v}_{S+})\} = 0$ and $Im\{\omega_S(\mathbf{v}_{I+})\} = -\gamma_T$ at $\ell_S = \ell_P$. These correspond to the characteristic Goldstone and amplitude modes arising under a U(1) symmetry breaking, which in our case corresponds to the phase of the pump laser field amplitude $\tilde{a}_{P+}^{(0)}$. Such a symmetry breaking is ruled out when the driving is switched on: in that case the incident field $\tilde{a}_{P+}^{(in)}$ fixes the phase of the laser emission and as a consequence the Goldstone and amplitude modes disappear. However, the phase of the pump only enters Eq. (4.26) via the FWM terms. Therefore the eigenvalues corresponding to the reverse-propagating signal are unaffected by the U(1) symmetry breaking. As in the switched on driving case, we plot $Re\{\omega_S(\mathbf{v}_{S,I\pm})\}$ as vertical lines in Fig. 4.4a which give the position of the respective transmittance peaks (except for $Re\{\omega_S(\mathbf{v}_{I-})\}$, as no FWM is present for the reverse signal). By employing materials displaying a smaller (negative) value of the curvature α one can access the Goldstone and amplitude modes at integer values of ℓ_S, as the width of the region in which the imaginary parts $Im\{\omega_S(\mathbf{v}_{S,I+})\}$ split will be broadened.

Also in this case, it is interesting to note that an analog behavior is obtained in the case of an incoherently pumped polariton condensate [53].

4.5   Active TJR

In this Section we demonstrate that our asymmetric FWM scheme can also be applied using a TJR laser. When incoherently pumped above the lasing threshold, active TJRs impose a well-defined chirality to the laser emission without relying on an external bias (see Chapter 3 of this Thesis). As for the active ring resonator studied in the previous Section, we set a pump rate $P_0 = 2\gamma_T$ which gives an intensity $|\tilde{a}_P^{(0)}|^2 = n_S$ circulating in the $\ell_P = 133$ mode only. We employ the usual absorption losses $k_A = 0.032$, the coupling parameters $k_w = 0.04$ and $k_S = 0.04$ (yielding a quality factor $Q \simeq 4 \times 10^4$), and a nonlinear refractive index $n_{NL} n_S \omega_P^{(0)}/(n_L \gamma_T) \simeq 5$.

As in the previous Sections of this Chapter, we first probe the system in the forward direction using an signal whose frequency ω_S is varied around the resonance frequency $\omega_S^{(0)}$ corresponding

to the $\ell_S = 131$ mode. The forward signal features an input intensity $|\tilde{a}_{S+}^{(in)}|^2 = 10^{-1}n_S$. The characteristic doublet structure of the forward transmittance spectrum T_{for} originating from FWM is displayed in Fig. 4.5a. We then probe the system in the reverse direction with a signal of the same incident intensity $|\tilde{a}_{S-}^{(in)}|^2 = 10^{-1}n_S$ around the resonance frequency $\omega_S^{(0)}$ of the $\ell_S = -131$ mode. Similarly to what we obtained in Secs. 4.3 and 4.4, T_{rev} is negligible over a broad frequency range and due to the absence of FWM it features a single peak at a frequency given by the Kerr nonlinearity shift of the mode's resonance (shown in Fig. 4.5a). This is different from the frequencies of the doublet in T_{for}. In fact, at the frequency $\omega_S = 3.9359 \times 10^4 \gamma_T$ (i.e. $[\omega_S - \omega_P^{(0)} - v(|\ell_S| - |\ell_P|)] = -8.51\gamma_T$) where we find the maximum T_{for} we get a 17 dB suppression of the T_{rev} signal. In the frequency range in which the reverse transmittance is negligible, the presence of the reverse-propagating signal does not affect the value of the forward transmittance in spite of the coupling established by the S element of the TJR. This fact, together with the linearity of the coupled-mode equations (4.13-4.14), ensures that the TJR laser can also function as an optical isolator in such a frequency range.

Finally, we also studied the eigenvalues and eigenvectors of the Bogoliubov matrix coupling the forward and reverse signal and idler as a function of the angular momentum $|\ell_S|$ of counterpropagating modes. In this case the system of differential equations is given by

$$
i\frac{d}{dt}\begin{bmatrix}\tilde{a}_{S+} & \tilde{a}_{I+}^* & \tilde{a}_{S-} & \tilde{a}_{I-}^*\end{bmatrix}^T
$$

$$
=\begin{bmatrix}
\begin{matrix}\omega_S^{(0)}-\omega_S-i\gamma_T \\ -2\frac{n_{NL}}{n_L}\omega_S^{(0)}|\tilde{a}_{P+}^{(0)}|^2 \\ +i\frac{P_0}{1+\frac{1}{n_S}|\tilde{a}_{P+}^{(0)}|^2} \\ -i\frac{P_0/n_S}{\left[1+\frac{1}{n_S}|\tilde{a}_{P+}^{(0)}|^2\right]^2}|\tilde{a}_{P+}^{(0)}|^2\end{matrix} & \begin{matrix}-\frac{n_{NL}}{n_L}\sqrt{\omega_S^{(0)}\omega_I^{(0)}}\tilde{a}_{P+}^{(0)2} \\ -i\frac{P_0/n_S}{\left[1+\frac{1}{n_S}|\tilde{a}_{P+}^{(0)}|^2\right]^2}\tilde{a}_{P+}^{(0)2}\end{matrix} & \beta_\pm & 0 \\[3em]
\begin{matrix}+\frac{n_{NL}}{n_L}\sqrt{\omega_S^{(0)}\omega_I^{(0)}}\tilde{a}_{P+}^{(0)*2} \\ -i\frac{P_0/n_S}{\left[1+\frac{1}{n_S}|\tilde{a}_{P+}^{(0)}|^2\right]^2}\tilde{a}_{P+}^{(0)*2}\end{matrix} & \begin{matrix}-\omega_I^{(0)}+2\omega_P-\omega_S-i\gamma_T \\ +2\frac{n_{NL}}{n_L}\omega_I^{(0)}|\tilde{a}_{P+}^{(0)}|^2 \\ +i\frac{P_0}{1+\frac{1}{n_S}|\tilde{a}_{P+}^{(0)}|^2} \\ -i\frac{P_0/n_S}{\left[1+\frac{1}{n_S}|\tilde{a}_{P+}^{(0)}|^2\right]^2}|\tilde{a}_{P+}^{(0)}|^2\end{matrix} & 0 & -\beta_\pm^* \\[3em]
0 & 0 & \begin{matrix}\omega_S^{(0)}-\omega_S-i\gamma_T \\ -2\frac{n_{NL}}{n_L}\omega_S^{(0)}|\tilde{a}_{P+}^{(0)}|^2 \\ +i\frac{P_0}{1+2\frac{1}{n_S}|\tilde{a}_{P+}^{(0)}|^2}\end{matrix} & 0 \\[3em]
0 & 0 & 0 & \begin{matrix}-\omega_I^{(0)}+2\omega_P-\omega_S-i\gamma_T \\ +2\frac{n_{NL}}{n_L}\omega_I^{(0)}|\tilde{a}_{P+}^{(0)}|^2 \\ +i\frac{P_0}{1+2\frac{1}{n_S}|\tilde{a}_{P+}^{(0)}|^2}\end{matrix}
\end{bmatrix}
$$

$$
\times\begin{bmatrix}\tilde{a}_{S+} & \tilde{a}_{I+}^* & \tilde{a}_{S-} & \tilde{a}_{I-}^*\end{bmatrix}^T, \tag{4.31}
$$

where the 4×4 Bogoliubov matrix features additional terms with respect to Eq. (4.26) that account for the coupling of the CW modes into the CCW ones enabled by the S waveguide of the TJR. Nevertheless, it follows from the theory of block matrices that the couplings $\beta_\pm$ do not modify the eigenvalues, which as we will see coincide with those of the active ring resonator in the absence of the external bias.

However, the eigenvectors $\mathbf{v}_{S,I\pm}$ do get modified due to the intermode couplings. In particular, their Bogoliubov norms now take the values

$$
\|\mathbf{v}_{I+}\| = -0.756, \ \ \|\mathbf{v}_{S+}\| = 0.756, \ \ \|\mathbf{v}_{I-}\| = -0.948, \ \ \|\mathbf{v}_{S-}\| = 0.948. \tag{4.32}
$$

Contrary to what we had observed in Secs. 4.3 and 4.4, in the TJR case the unidirectional coupling between the CW and CCW modes introduced by the S element grants Bogoliubov norms in the reverse direction different than -1 and 1 for $\mathbf{v}_{I-}$ and $\mathbf{v}_{S-}$, respectively.

The real and imaginary parts of the corresponding eigenvalues $\omega_S(\mathbf{v}_{S,I\pm})$ are shown in Fig. 4.5b and c, respectively. To get a complete picture of the underlying physics, the eigenvalues are calculated also for non-integer values of $|\ell_S|$. As in the driving-less active ring resonator, the real parts $Re\{\omega_S(\mathbf{v}_{S,I-})\}$ corresponding to the reverse signal are distributed in two bands separated by a gap which achieves its minimum frequency width at $|\ell_S| = \ell_P = 133$. $Re\{\omega_S(\mathbf{v}_{S-})\}$ determines the frequency at which the reverse transmittance T_{rev} takes its maximum vale, which is again given by the resonance frequency of the $-\ell_S$ mode shifted by the Kerr nonlinearity (see Eq. (4.23)). On the other hand, no peak appears at the frequency given by $Re\{\omega_S(\mathbf{v}_{I-})\}$ due to the absence of FWM in the reverse direction. This is confirmed for the particular angular momentum $\ell_S = -131$

in Fig. 4.5a, where we have plotted both $Re\{\omega_{\mathrm{S}}(\mathbf{v}_{\mathrm{S,I-}})\}$ as vertical dashed-dotted lines. The corresponding imaginary parts take the same value $Im\{\omega_{\mathrm{S}}(\mathbf{v}_{\mathrm{S,I-}})\} = -\gamma_{\mathrm{T}}/3$ as in Sec. 4.4, implying the dynamical stability of the pump under the presence of a small reverse signal. In the case of the forward-propagating signal, the two bands $Re\{\omega_{\mathrm{S}}(\mathbf{v}_{\mathrm{S,I+}})\}$ give again the frequencies of the transmittance doublet for each value of ℓ_{S}. This can be seen in Fig. 4.5a for $\ell_{\mathrm{S}} = 131$, where we have plotted the real parts of the eigenvalues as vertical dashed lines. Differently from the reverse signal case, the two bands are now closer between each other, implying that FWM produces an effective attraction between transmittance peaks. Furthermore, the real parts of $\omega_{\mathrm{S}}(\mathbf{v}_{\mathrm{S,I+}})$ coalesce in a non-integer neighborhood of $\ell_{\mathrm{P}} = 133$, taking the value $Re\{\omega_{\mathrm{S}}(\mathbf{v}_{\mathrm{S,I+}})\} = \omega_{\mathrm{P}}^{(0)}[1 - n_{\mathrm{NL}}|\tilde{a}_{P+}^{(0)}|^2/n_{\mathrm{L}}]$ of the Kerr-shifted resonance at $\ell_{\mathrm{P}} = 133$, and therefore closing the gap. In the same region, their corresponding imaginary parts $Im\{\omega_{\mathrm{S}}(\mathbf{v}_{\mathrm{S,I+}})\}$ depart from the value $-\gamma_{\mathrm{T}}/2$ and display the typical Goldstone and amplitude modes already studied in Sec. 4.4, which arise as a consequence of the U(1) symmetry breaking of the laser phase. Also in the TJR case, a smaller (negative) value of the curvature α will broaden the Goldstone and amplitude modes and therefore allow us to probe them at integer values of ℓ_{S}.

4.6 Conclusions

Our work establishes a route to optical isolation in silicon photonics devices that is not subjected to the dynamic reciprocity restrictions addressed in previous literature. This is done by considering ring and Taiji resonators in add-drop configuration strongly pumped in the forward direction. Signals injected in such a direction are coupled with the pump by means of four-wave mixing (FWM). However, conservation of energy and angular momentum prevents a similar FWM coupling between the pump and signals propagating in the opposite (reverse) direction. This leads to Lorentz reciprocity breaking as transmittance in the forward direction reaches its maximum value at a frequency for which transmittance is negligible in the reverse direction. Furthermore, this isolation from reverse-propagating signals takes place in a broad frequency range. The proposed configuration can also be realized by employing active ring resonators in which an external driving is initially employed to promote lasing in the forward direction and then can be switched off, or by using active Taiji resonators which grant unidirectional lasing even when a sizable backscattering is present into the system.

Our results are obtained by solving for the steady states of the temporal coupled-mode theory equations with a linearized treatment of the signal and idler fields as small perturbations to the pump, which is assumed to feature a much larger intensity. The transmittance spectrum across several modes and the different role of FWM for forward and reverse-propagating signals are also addressed by looking at the eigenvectors and eigenvalues of the Bogoliubov matrix coupling counterpropagating signal and idler fields. Such an analysis reveals a very powerful analogy between our results and the physics of polariton condensates.

Further research will address the stability of the lasing emission of the active optical isolators for growing signal intensity. Moreover, future work will be devoted to study the interplay between optical isolation based on asymmetrical FWM and the nontrivial band topologies and topological edge states that can be engineered in arrays of silicon ring (and Taiji) resonators [155, 13, 7, 12].

Chapter 5

The Taiji topological insulator laser

Topological insulators featuring a saturable gain at their boundaries display enhanced lasing properties due to the robustness of topologically protected edge modes against local defects and perturbations. Among these systems, arrays of micro-ring resonators realizing quantum spin-Hall insulator lasers without relying on magneto-optic materials that break time-reversal symmetry hold great promise due to their direct integration with state-of-the-art silicon photonics technology. Nevertheless, spurious backscattering can destroy the topological protection of the edge modes, thus decreasing the lasing performance.

In this Chapter we theoretically investigate lasing in such an active quantum spin-Hall topological insulator. Depending on the local or nonlocal character of the saturable gain the mode competition leads to different lasing behaviors. Employing a local saturable gain, we assess the effect of backscattering and conclude that it significantly reduces the lasing performance, ultimately suppressing the topological edge modes when it becomes comparable with the energy scale of the topological gap. The addition of Taiji resonators featuring an embedded S element that couples backscattered light back into the preferred direction imposes a well-defined chirality to the lasing emission and preserves the topological protection of a pair of edge modes. Finally, we also demonstrate that single-mode lasing can be obtained by combining Taiji resonators with the Kerr nonlinearity of the setup's material.

5.1 Introduction

As we learned in Chapter 1, the two-dimensional array of silicon ring-resonators of Ref. [11] realizes the photonic version of a quantum spin-Hall topological insulator in which the two whispering-gallery modes supported by each ring resonator (propagating in clockwise —CW— and counter-clockwise —CCW— directions) play the role of the pseudospins. Although time-reversal symmetry is globally preserved, the dynamics of each pseudospin are governed by Harper-Hofstadter Hamiltonians with opposite flux per plaquette and therefore opposite Chern number. The edge states of such a system are named *helical* modes.

A particularly interesting problem concerns the addition of saturable gain to a photonic topological insulator in order to promote lasing in the chiral surface modes. Such a non-Hermitian and nonlinear system is known as topological laser, or in short, *topolaser* [12]. The active analog of the quantum spin-Hall lattice of Ref. [11] represents the first realization of a two-dimensional non-magnetic topolaser [13]. Such a system lases in the one-dimensional helical states propagating along its boundaries. This work demonstrated that topolasers offer several advantages with respect to their trivial counterparts: single-frequency lasing, higher slope efficiency, and robustness against defects that the edge modes are able to bypass.

However, as we discussed in Chapter 1, due to the bosonic nature of photons, backscattering processes coupling the two pseudospins of a quantum spin-Hall insulator result in the suppression of the helical modes propagating along the lattice boundaries. In spite of this restriction Refs. [11, 13]

were able to engineer lattices with negligible backscattering in which the helical modes survive.

Instead of relying on our capacity to fabricate samples with a small enough level of defects causing backscattering and to maintain that level under control in spite of the operational degradation of the laser, a more effective strategy would be to promote and stabilize lasing in a single pseudospin. This motivated Ref. [13] to employ Taiji resonators (TJRs) as the building block of the photonic spin-Hall insulator. As a result, they found a unidirectional intensity flow in the rings of the array.

In this Chapter we capitalize in our previous study of TJR lasers (see Chapters 2 and 3) to analyze lasing in TJR-based spin-Hall topolasers in the presence of backscattering. We employ a set of coupled-mode theory equations describing the steady state of the field amplitudes in the two pseudospins of each resonator. We first focus on a passive array of ring resonators where we find the edge states at the frequencies of the topological gaps and ascertain their robustness against local defects and backscattering disorder. We then consider an active array and study the different lasing regimes that arise depending on the type of gain saturation employed. Backscattering results in a coupling between the two pseudospins that leads to reduced lasing performance. The introduction of TJRs as the site resonators of the spin-Hall topolaser drastically suppresses the undesired coupling between pseudospins and leads to lasing with enhanced properties, including a lasing threshold and slope efficiency very close to the single-resonator values. This effect is combined with an optical nonlinearity in order to promote lasing in a single helical mode.

The Chapter is structured as follows: A description of the physical system and the coupled-mode theory employed in the simulations is presented in Sec. 5.2. Sec. 5.3 analyzes the passive spin-Hall array of ring resonators. Our study of the ring resonator and TJR topolasers is found in Sec. 5.4. Conclusions are finally drawn in Sec. 5.5.

5.2   The physical system and the theoretical model

We consider a lattice of silicon resonators similar to the one studied in Ref. [11], but featuring TJRs as site resonators. A single 2×2 plaquette of the lattice is displayed in Fig. 5.1a. The TJRs are linked via racetrack resonators that do not host an S-shaped element inside. Every site resonator supports a pair of degenerate whispering-gallery modes propagating in CW and CCW directions. These correspond to the two pseudospins, up $(+)$ and down $(-)$, of the quantum spin-Hall insulator. To prevent confusions, on the following we will refer to the whispering-gallery modes simply as the $\pm$ pseudospins, while the CW/CCW directions will refer to the propagation of the helical modes along the lattice boundaries. Light couples between the different components of the array through directional couplers with transmission and coupling amplitudes $t_{\mathrm{w,S}}$ and $ik_{\mathrm{w,S}}$, respectively, where the w,S indices refer to the couplings between link and site resonators, and those between site resonators and the embedded S element, respectively. As usual, $t_{\mathrm{w,S}}$ and $k_{\mathrm{w,S}}$ are real numbers satisfying $t_{\mathrm{w,S}}^2 + k_{\mathrm{w,S}}^2 = 1$. The site resonators of an $N_x \times N_y$ lattice are labeled by the indices (n_x, n_y), where $n_x = 1, ..., N_x$ and $n_y = 1, ..., N_y$. The top-left resonator $(1, 1)$ is coupled to a bus waveguide that can be harnessed to probe the system by means of an external signal.

Let us assume that the site resonators have a perimeter $L_\circ = 2\pi R$, where R is their radius. We can then express the perimeter of the link resonators as $L_{\mathrm{L}} = L_\circ + 2\eta$. The parameter η takes into account the length difference between both types of resonators, and it is chosen in order to make the link resonators anti-resonant with the site resonators. This is done so that a photon resonant with the site resonators spends much more time in the sites than in the links. In such a case the system can be described by the Harper-Hofstadter tight-binding model (see Sec. 1.3). The anti-resonant condition is given by $\sin(\omega n_{\mathrm{L}} \eta / c) = 1$, where ω is the frequency of light, n_{L} is the linear refractive index of the material (we are neglecting nonlinear effects), and c is the vacuum speed of light. The hopping energy is given by $J = k_{\mathrm{w}}^2 c / (n_{\mathrm{L}} L_\circ)$ [11].

Each pseudospin must realize a copy of the Harper-Hofstadter model with opposite flux per plaquette $\Phi = \pm\alpha\Phi_0$, where $\Phi_0 = h/e$ is the magnetic flux quantum. Consider a photon describing a CCW-oriented closed loop along the 2×2 plaquette shown in Fig. 5.1a. When the photon jumps horizontally the link resonators have to introduce the corresponding Peierls phase appearing in the Harper-Hofstadter Hamiltonian (1.58). Of course, this phase has to be of opposite sign for photons belonging to different pseudospins. On the other hand, vertical hopping does not introduce any complex phase. The strategy of Ref. [11] achieves this by shifting the center of the link resonators coupling sites in the same row a quantity $\Delta x(n_y)$ which depends on the row number. For instance,
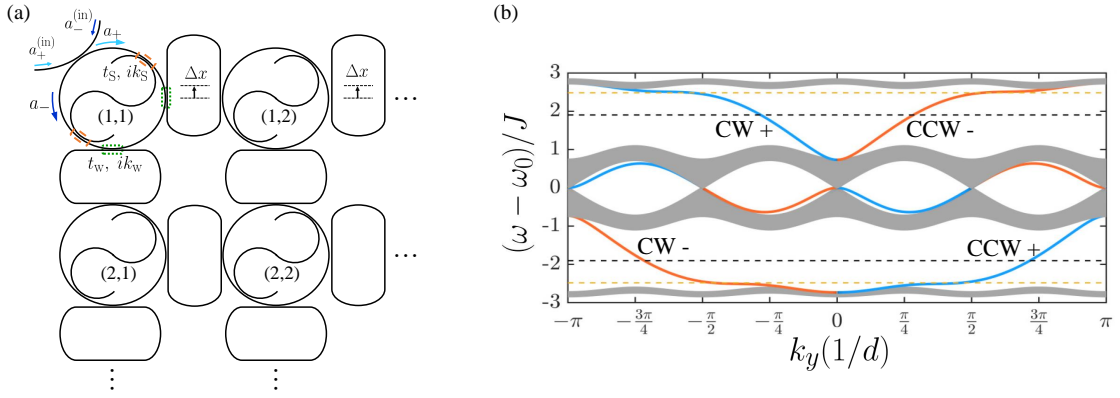
Figure 5.1: **(a)** Sketch of the top left 2×2 plaquette of the quantum spin-Hall topological insulator formed by TJRs. **(b)** Energy bands of a quantum spin-Hall topological insulator with $\alpha = 1/4$. The calculation was performed in a semi-infinite lattice featuring 399 sites in the x direction and periodic boundary conditions in the y direction. Only the edge states corresponding to one of the boundaries are plotted. ω is the frequency, ω_0 is the resonance frequency of the site resonators, J is the hopping energy, k_y is the lattice momentum along y, and d is the lattice spacing. Panel adapted from [165].

in our 2×2 plaquette the link resonators belonging to the first row are shifted upwards a quantity Δx, while those placed on the second row are not shifted. After enclosing the whole plaquette, a photon belonging to the $\pm$ pseudospin will pick up a phase $\pm 2\pi\alpha$, where $\alpha = 2\omega n_{\rm L} \Delta x/(2\pi c)$. We can now choose the values of Δx and λ such that we get the desired α for the Harper-Hofstadter model we want to implement. In the whole $N_x \times N_y$ lattice, the shift of the links connecting TJRs of the same row n_y will be given by $\Delta x(n_y) = \Delta x(N_y - n_y)$. Without loss of generality, in this Chapter we will focus on a quantum spin-Hall insulator formed by two copies of the Harper-Hofstadter model featuring opposite fluxes with $\alpha = 1/4$.

The dispersion of a quantum spin-Hall topological insulator featuring a flux $\alpha = 1/4$ is displayed in Fig. 5.1b. As we know from the Harper-Hofstadter model studied in Sec. 1.3, this system displays four energy bands. The two central bands, located within an energy scale set by the hopping energy J, touch each other by means of Dirac points at several values of the lattice momentum. On the other hand, the lower and upper gaps are topologically nontrivial and both feature a finite Chern number $\mathcal{C} = -1$. These two gaps contain the four helical modes that can propagate along the boundaries of the spin-Hall insulator. The lowest energy gap hosts two helical modes: In one of them light propagates in the $-$ pseudospin of the site resonators and travels in the CW direction along the lattice boundaries (this helical mode is labelled CW$-$). The other helical mode, named CCW$+$, is formed by photons of the $+$ whispering-gallery modes of the site resonators that propagate in the CCW direction along the edges of the topolaser. Similarly, the upper topological gap hosts the helical modes CW$+$ and CCW$-$.

In order to simulate the system we employ a temporal coupled-mode theory describing the field amplitudes $a_{\pm}^{(n_x,n_y)}$ of pseudospin $\pm$ in each resonator (n_x, n_y). The square modulus $|a_{\pm}^{(n_x,n_y)}|^2$ gives the corresponding intensity. By means of the bus waveguide we can probe the lattice by injecting a signal $a_{\pm}^{(\rm in)} = \tilde{a}_{\pm}^{(\rm in)} e^{-i\omega t}$ of frequency ω that couples with the $\pm$ pseudospin of the $(1,1)$ resonator. We can then rewrite the field amplitudes in each resonator as $a_{\pm}^{(n_x,n_y)} = \tilde{a}_{\pm}^{(n_x,n_y)} e^{-i\omega t}$.

The time-dependent coupled-mode equations read

$$
i\frac{d\tilde{a}_{\pm}^{(n_x,n_y)}}{dt} = (\omega_0 - \omega)\tilde{a}_{\pm}^{(n_x,n_y)} - \frac{n_{\rm NL}}{n_{\rm L}}\omega_0\left[|\tilde{a}_{\pm}^{(n_x,n_y)}|^2 + g|\tilde{a}_{\mp}^{(n_x,n_y)}|^2\right]\tilde{a}_{\pm}^{(n_x,n_y)}
$$

$$
+ i\frac{P_0^{(n_x,n_y)}}{1 + \frac{1}{n_{\rm S}}\left[|\tilde{a}_{\pm}^{(n_x,n_y)}|^2 + \xi|\tilde{a}_{\mp}^{(n_x,n_y)}|^2\right]}\tilde{a}_{\pm}^{(n_x,n_y)} - i\gamma_{\rm T}\tilde{a}_{\pm}^{(n_x,n_y)} - i\gamma_{\rm out}^{(n_x,n_y)}\tilde{a}_{\pm}^{(n_x,n_y)}
$$

$$
- i\left[\gamma_{\rm north}^{(n_x,n_y)} + \gamma_{\rm south}^{(n_x,n_y)} + \gamma_{\rm west}^{(n_x,n_y)} + \gamma_{\rm east}^{(n_x,n_y)}\right]\tilde{a}_{\pm}^{(n_x,n_y)}
$$

$$
+ \beta_{\rm north}^{(n_x,n_y)}\tilde{a}_{\pm}^{(n_x,n_y-1)} + \beta_{\rm south}^{(n_x,n_y)}\tilde{a}_{\pm}^{(n_x,n_y+1)} + \beta_{\rm west,\pm}^{(n_x,n_y)}\tilde{a}_{\pm}^{(n_x-1,n_y)} + \beta_{\rm east,\pm}^{(n_x,n_y)}\tilde{a}_{\pm}^{(n_x+1,n_y)}
$$

$$
+ \beta_{\pm,\mp}\tilde{a}_{\mp}^{(n_x,n_y)} + \beta_{\rm in}^{(n_x,n_y)}\tilde{a}_{\pm}^{(\rm in)}. \tag{5.1}
$$

A step-by-step derivation of the equations above can be found in Appendix C. By employing a 4th order Runge-Kutta algorithm we will solve them for the long-time stationary states $\tilde{a}_{\pm}^{(n_x,n_y)}(t \to \infty)$ of the field amplitudes. We denote by ω_0 the resonance frequency of the site resonators. The optical nonlinearity is accounted by means of a $n_{\rm NL}$ nonlinear refractive index and a g parameter describing its character (see Appendix A). The latter can take a value between $g = 1$, which corresponds to a purely nonlocal thermo-optic nonlinearity, and $g = 2$, which describes a local Kerr nonlinearity. In order to account for the addition of gain to the topological helical modes, we included a saturable gain featuring a pump rate $P_0^{(n_x,n_y)}$ that can be different for each resonator and a gain saturation coefficient $n_{\rm S}$. Similarly to the optical nonlinearity, we introduced a ξ parameter describing the type of saturable gain: $\xi = 1$ implies a nonlocal gain saturation typical of an inhomogeneously broadened gain medium, while $\xi = 2$ accounts for a local gain as displayed by a homogeneously broadened medium (see Chapter 3). In any case, for all values of ξ our model describes a class-A laser in which the dynamics of the reservoir triggering lasing is assumed to be much faster than any other timescale, and therefore it has been integrated out in the saturable gain term [161, 162].

The single resonator total loss rate $\gamma_{\rm T} = \gamma_{\rm A} + \gamma_{\rm S}$ is defined as the sum of the absorption losses $\gamma_{\rm A}$ and the loss rate due to the coupling with the S element $\gamma_{\rm S} = \frac{ck_{\rm S}^2}{L_{\circ}n_{\rm L}}$. The loss rate $\gamma_{\rm out}^{(n_x,n_y)}$ is due to the coupling of the $(1,1)$ resonator to the bus waveguide and is given by

$$
\gamma_{\rm out} = \begin{cases} \frac{ck_{\rm w}^2}{2L_{\rm s}n_{\rm L}} & if \quad n_x = n_y = 1 \\ \\ 0 & otherwise \end{cases}. \tag{5.2}
$$

The loss rates arising from the couplings between adjacent site resonators are

$$
\gamma_{\rm north} = \begin{cases} 0 & if \quad n_y = 1 \\ \\ \gamma_{\rm w} & if \quad n_y > 1 \end{cases}, \quad \gamma_{\rm south} = \begin{cases} 0 & if \quad n_y = N_y \\ \\ \gamma_{\rm w} & if \quad n_y < N_y \end{cases},
$$

$$
\gamma_{\rm west} = \begin{cases} 0 & if \quad n_x = 1 \\ \\ \gamma_{\rm w} & if \quad n_x > 1 \end{cases}, \quad \gamma_{\rm east} = \begin{cases} 0 & if \quad n_x = N_x \\ \\ \gamma_{\rm w} & if \quad n_x < N_x \end{cases}, \tag{5.3}
$$

where

$$
\gamma_{\rm w} = \frac{ck_{\rm w}^2}{2L_{\circ}n_{\rm L}}\frac{1 + e^{i\frac{\omega}{c}n_{\rm L}L_{\rm L}}}{1 - e^{i\frac{\omega}{c}n_{\rm L}L_{\rm L}}}. \tag{5.4}
$$

The link resonators are integrated out in the coupled-mode equations and their role is accounted by the couplings between site resonators

$$
\beta_{\rm north}^{(n_x,n_y)} = \begin{cases} 0 & if \quad n_y = 1 \\ \\ \beta_{\rm w} & if \quad n_y > 1 \end{cases}, \quad \beta_{\rm south}^{(n_x,n_y)} = \begin{cases} 0 & if \quad n_y = N_y \\ \\ \beta_{\rm w} & if \quad n_y < N_y \end{cases},
$$

$$
\beta_{\rm west,+}^{(n_x,n_y)} = \begin{cases} 0 & if \quad n_x = 1 \\ \\ \beta_{\rm w}e^{-i2\pi\alpha(N_y-n_y)} & if \quad n_x > 1 \end{cases}, \quad \beta_{\rm east,+}^{(n_x,n_y)} = \begin{cases} 0 & if \quad n_x = N_x \\ \\ \beta_{\rm w}e^{+i2\pi\alpha(N_y-n_y)} & if \quad n_x < N_x \end{cases},
$$

$$
\beta_{\rm west,-}^{(n_x,n_y)} = \begin{cases} 0 & if \quad n_x = 1 \\ \\ \beta_{\rm w}e^{+i2\pi\alpha(N_y-n_y)} & if \quad n_x > 1 \end{cases}, \quad \beta_{\rm east,-}^{(n_x,n_y)} = \begin{cases} 0 & if \quad n_x = N_x \\ \\ \beta_{\rm w}e^{-i2\pi\alpha(N_y-n_y)} & if \quad n_x < N_x \end{cases}, \tag{5.5}
$$

where

$$\beta_{\rm w} = \frac{ck_{\rm w}^2}{L_\circ n_{\rm L}} \frac{e^{i\frac{\omega}{c}n_{\rm L}L_{\rm L}/2}}{1 - e^{i\frac{\omega}{c}n_{\rm L}L_{\rm L}}}. \tag{5.6}$$

Note that, since the link resonators are anti-resonant with the site resonators, for frequencies ω in the neighborhood of ω_0 we have that $\exp(i\omega n_{\rm L}L_{\rm L}/c) \simeq -1$, therefore leading to $|\gamma_{\rm w}| \ll |\beta_{\rm w}|$. We can thus take $\gamma_{\rm w} = 0$ on the following.

The coupling parameters $\beta_{\pm,\mp} = \beta_{\pm,\mp}^{\rm (S)} + \beta_{\pm,\mp}^{\rm (BS)}$ describe the coupling between pseudospins belonging to the same resonator, which can be due to the S element ($\beta_{\pm,\mp}^{\rm (S)}$) or to backscattering ($\beta_{\pm,\mp}^{\rm (BS)}$). A backscattering-free ring resonator would feature $\beta_{\pm,\mp} = 0$. The addition of the 45°-tilted S element coupling the $+$ into the $-$ pseudospin introduces the couplings $\beta_{\pm} = 0$ and $\beta_{\mp} = -i2ck_{\rm S}^2 e^{i\omega_0 n_{\rm L}L_\circ/c}e^{i\omega_0 n_{\rm L}L_\circ/4c}/L_0 n_{\rm L}$. By switching $+ \leftrightarrow -$ we would describe the analog TJR coupling the $-$ into the $+$ pseudospin. As explained in Chapter 3, the effect of backscattering can be summarized by the Hermitian and non-Hermitian parameters

$$n = i\frac{\beta_{\mp}^{\rm (BS)} - \beta_{\pm}^{\rm (BS)*}}{2}, \quad h = -\frac{\beta_{\mp}^{\rm (BS)} + \beta_{\pm}^{\rm (BS)*}}{2}. \tag{5.7}$$

Finally, the coupling with the bus waveguide is given by

$$\beta_{\rm in}^{(n_x, n_y)} = \begin{cases} -\frac{ck_{\rm w}}{L_\circ n_{\rm L}} & if & n_x = n_y = 1 \\ \\ 0 & otherwise \end{cases}. \tag{5.8}$$

In the following Sections we will capitalize on this theoretical model to simulate a quantum spin-Hall insulator both in the presence and absence of a saturable gain, and to address the role of the TJRs in the preservation of the helical modes.

5.3   Passive spin-Hall insulator

In order to check the validity of our model, prior to studying topological lasing we first analyze the response of a backscattering-free passive spin-Hall insulator made of ring resonators by setting the S couplings to $k_{\rm S} = 0$ and the pump rate to $P_0 = 0$ for all resonators. In particular, we will assess the existence of chiral helical modes in the lattice boundaries when the system is probed by a signal propagating through the bus waveguide at a frequency lying in the topological gaps. Furthermore, we will check whether such helical modes exhibit topological protection against local perturbations and backscattering couplings of different strengths. We finally include finite couplings between site resonators and S waveguides in order to investigate if the passive spin-Hall insulator of TJRs can counteract the effect of backscattering while preserving the helical modes.

We consider an 8×8 lattice with realistic parameters for silicon photonics implementations: $n_{\rm L} = 3.5$, $L_\circ = 2\pi \times 20~\mu{\rm m}$, $L_{\rm S} = L_\circ/2$, $\omega_0 = 2\pi \times 194$ THz, $k_{\rm w} = 0.31$, and $\gamma_{\rm A}n_{\rm L}/c = 3.2 \times 10^{-5}~\mu{\rm m}^{-1}$. Moreover, such a value for the absorption losses will allow us to clearly identify the propagation direction of the helical modes in Fig. 5.2. These parameters result in a single-resonator quality factor $Q \simeq 4.5 \times 10^5$ and a tunneling energy $J \simeq 12\gamma_{\rm T}$. The width of each topological gap is approximately $1.5J \simeq 18\gamma_{\rm T}$. For the moment we assume that the shift of the resonance frequency of the resonators due to the optical nonlinearity is negligible, and therefore we set $n_{\rm NL} = 0$.

We now probe the system at different frequencies ω by means of a monochromatic signal injected through the bus waveguide and coupling to the $-$ pseudospins only. The spatial distribution of the steady-state intensities in the $-$ pseudospin calculated using Eq. (5.1) is shown in Fig. 5.2 for different frequencies belonging to the upper (panel a) and lower (panel c) topological gaps as well as to the two central bands (panel b). The intensity in each resonator is normalized in units of the intensity of the input signal, i.e. $|\tilde{a}_{-}^{(n_x, n_y)}|^2/|\tilde{a}_{-}^{\rm (in)}|^2$.

When the probe frequency ω belongs in the topological gaps the helical modes are observed propagating along the lattice surface. As expected, the propagation direction is the opposite for the two gaps: in the upper gap (panel a) light circulates in the CCW direction, while in the lower gap (panel c) the intensity propagates in the CW direction. Eventually, losses damp out the helical modes and propagation is no longer visible. This behavior was expected from the band
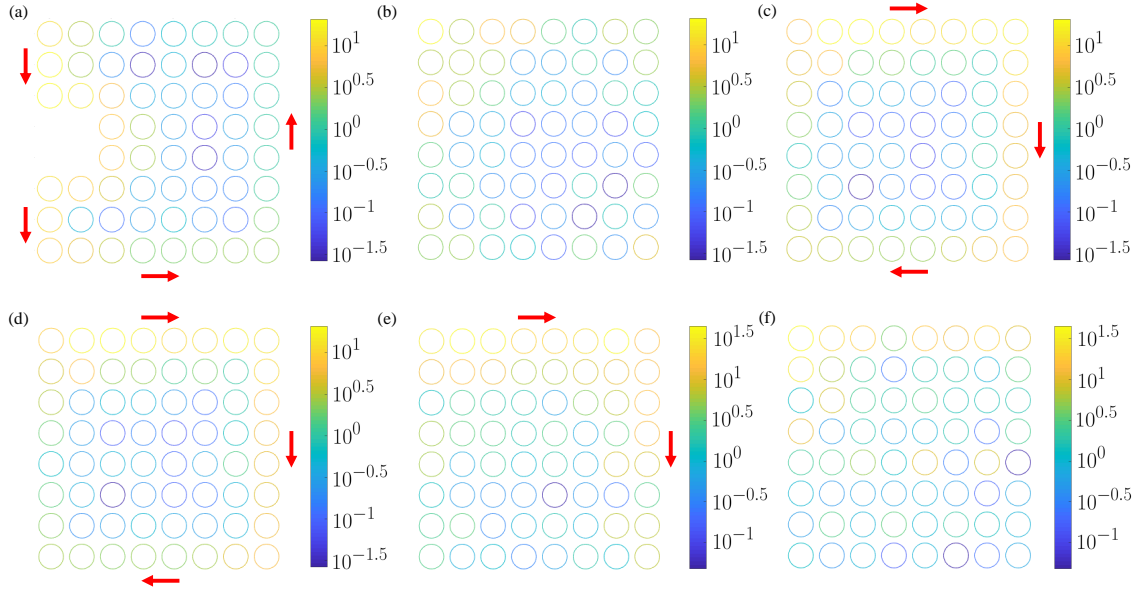
Figure 5.2: Steady-state intensity distribution $|\tilde{a}_+^{(0)} + \tilde{a}_-^{(0)}|^2 / |\tilde{a}_-^{(\mathrm{in})}|^2$ inside a passive 8×8 spin-Hall insulator of ring resonators with flux per plaquette $\alpha = 1/4$. Panels (a,b,c) show configurations without backscattering coupling counterpropagating pseudospins. In each case the top left resonator is driven by a signal $a_-^{(\mathrm{in})}$ with frequency $\omega = \omega_0 + 1.75J$ (panel a), $\omega = \omega_0$ (panel b), and $\omega = \omega_0 - 1.75J$ (panel c). Arrows indicate the propagation direction of the edge modes. Panels (d,e,f) correspond to a lattice driven by a signal with frequency $\omega = \omega_0 - 1.75J$ featuring a random Hermitian backscattering $|h| = 0.04J$ (panel d), $|h| = 0.5J$ (panel e), and $|h| = J$ (panel f).
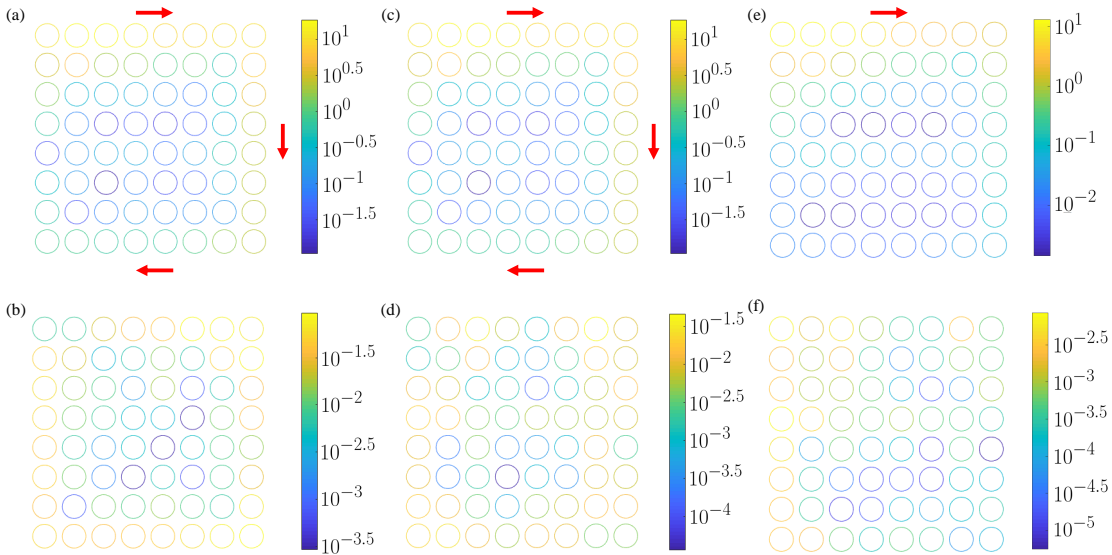

Figure 5.3: Passive 8×8 spin-Hall insulator with flux per plaquette $\alpha = 1/4$. The top left resonator is driven by a signal $a_-^{(\mathrm{in})}$ with frequency $\omega = \omega_0 - 1.75J$. The lattice features a random Hermitian backscattering $|h| = 0.04J$. Panels (a,c,e) and (b,d,f) show respectively the steady-state intensity distribution in the $-$ (normalized as $|\tilde{a}_-^{(0)}|^2 / |\tilde{a}_-^{(\mathrm{in})}|^2$) and $+$ (normalized as $|\tilde{a}_+^{(0)}|^2 / |\tilde{a}_-^{(\mathrm{in})}|^2$) pseudospins. Arrows indicate the propagation direction of the CW$-$ helical mode. Panels (a,b) are calculated for $\gamma_\mathrm{A} n_\mathrm{L} / c = 3.2 \times 10^{-5}$ $\mu\mathrm{m}^{-1}$ and $\gamma_\mathrm{S} = 0$. Panels (c,d) are calculated for $\gamma_\mathrm{A} = 0$ and $\gamma_\mathrm{S} n_\mathrm{L} / c = 3.2 \times 10^{-5}$ $\mu\mathrm{m}^{-1}$ (i.e. $k_\mathrm{S} = 0.06$). Panels (e,f) are calculated for $\gamma_\mathrm{A} n_\mathrm{L} / c = 3.2 \times 10^{-5}$ $\mu\mathrm{m}^{-1}$ and $\gamma_\mathrm{S} n_\mathrm{L} / c = 7.9 \times 10^{-5}$ $\mu\mathrm{m}^{-1}$ (i.e. $k_\mathrm{S} = 0.1$). The intensity inside the S waveguides is not plotted.

dispersion shown in Fig. 5.1b. In order to test the topological robustness of the helical modes against local perturbations we removed a 2×2 plaquette in the left boundary of the lattice (panel a). Notwithstanding the absence of these resonators, the helical mode is able to bypass the defect and continue propagating. On the other hand, when the probe frequency lies in the central trivial region (panel b) only the resonators near to the top left corner of the lattice (where the probing waveguide is coupled) host a large intensity, and no edge states are visible. A similar result is obtained when one sets $\alpha = 0$ and studies the topologically trivial lattice. Note that a probe signal $a_+^{(\text{in})}$ coupling into the $+$ pseudospin results in the same behavior, but interchanging the propagation directions CW $\leftrightarrow$ CCW of the helical modes observed at the respective topological gaps.

We now fix the frequency of the external driving $a_-^{(\text{in})}$ at $\omega = \omega_0 - 1.75J$ in the lower topological gap and include backscattering couplings featuring a random phase in all site resonators of the lattice. As in Chapter 3, we focus on Hermitian backscattering rather than including a non-Hermitian backscattering that can lead to spurious gain and losses if $|n| \simeq \gamma_{\text{T}}$. Panels (d), (e), and (f) of Fig. 5.2 show the spatial distribution inside the lattice of the normalized intensity $|\tilde{a}_+^{(n_x, n_y)} + \tilde{a}_-^{(n_x, n_y)}|^2 / |\tilde{a}_-^{(\text{in})}|^2$ for $|h| = 0.04J$, $|h| = 0.5J$, and $|h| = J$, respectively. Panel (d) actually corresponds to the level of backscattering present in the quantum spin-Hall insulator realized in Ref. [11]. In this case the CW$-$ mode is barely perturbed by the backscattering and no major changes in the intensity distribution with respect to the backscattering-free lattice of panel (c) are produced. This is in agreement with the experimental results of Ref. [11], where such a small coupling between pseudospins could not destroy the topological protection of the helical modes. However, a larger backscattering can rule out the edge modes: For $|h| = 0.5J$ the CW$-$ mode is still present but it is damped out before reaching the lower edge of the lattice. When we set $|h| = J$, the backscattering is of the order of the topological gap and the presence of the helical mode can only be hardly intuited along the upper boundary of the lattice.

Finally, it is worth asking whether we can capitalize on the recirculation of light from the $+$ into the $-$ pseudospin enabled by the embedded S element of TJRs in order to compensate the effect of a large backscattering leading to the vanishing of the helical modes. In order to check this assumption we introduce finite couplings $k_{\text{S}} > 0$ and study a passive spin-Hall insulator made of TJRs. Unfortunately, if the absorption losses γ_{A} remain constant, a larger coupling with the S waveguides also increases the total loss rate γ_{T} of the resonators, which can dump the propagation of the helical modes. This is especially compromising as the larger the backscattering present in the sample, the larger the value of k_{S} we will need in order to recirculate the backscattered intensity in the $+$ pseudospin into the $-$ one. Fig. 5.3 shows the spatial distribution of the intensity in our 8×8 spin-Hall insulator with a random Hermitian backscattering of modulus $|h| = 0.04J$. The $-$ pseudospin of the top-left site is driven by an external signal $a_-^{(\text{in})}$ with frequency in the lower topological gap ($\omega = \omega_0 - 1.75J$). As we know, this will excite the CW$-$ helical mode in the lattice boundaries. Panels (a) and (b) display the results for a lattice of ring resonators ($k_{\text{S}} = 0$) featuring $\gamma_{\text{A}} n_{\text{L}}/c = 3.2 \times 10^{-5} \ \mu\text{m}^{-1}$, and show respectively the intensities in the $-$ (normalized as $|\tilde{a}_-^{(n_x, n_y)}|^2 / |\tilde{a}_-^{(\text{in})}|^2$) and $+$ (normalized as $|\tilde{a}_+^{(n_x, n_y)}|^2 / |\tilde{a}_-^{(\text{in})}|^2$) pseudospins. In order to assess the effect of the S waveguide without altering the total loss rate γ_{T} of the lattice, panels (c,d) show the analog spatial intensity distributions in the $-$ and $+$ pseudospins for an array of TJRs (the intensity inside the S waveguides is not plotted) featuring $\gamma_{\text{A}} = 0$ and $\gamma_{\text{S}} n_{\text{L}}/c = 3.2 \times 10^{-5} \ \mu\text{m}^{-1}$ (which equivalently accounts for $k_{\text{S}} = 0.06$). This gives the same value of γ_{T} as in panels (a,b) and, as a consequence, the CW$-$ helical mode is unaffected by the S couplings. However, an absorptionless lattice is highly unrealistic. Besides, as it is evident from panel (d), such a small value of k_{S} only leads to a weak recirculation of the light scattered into the $+$ pseudospin. In order to further suppress the intensity in the $+$ pseudospin, we must include larger couplings k_{S}. Panels (e) and (f) show the spatial intensity distribution for a passive spin-Hall insulator featuring TJRs with S couplings $k_{\text{S}} = 0.1$—implying $\gamma_{\text{S}} n_{\text{L}}/c = 7.9 \times 10^{-5} \ \mu\text{m}^{-1}$—, and absorption losses $\gamma_{\text{A}} n_{\text{L}}/c = 3.2 \times 10^{-5} \ \mu\text{m}^{-1}$, in the $-$ and $+$ pseudospins, respectively. The resulting coupling with the S waveguide $|\beta_{\mp}^{(\text{S})}| = 0.4J$ reduces the intensity in the $+$ pseudospin in about one order of magnitude with respect to the calculations of panel (b). However, this comes at a cost: the total loss rate γ_{T} is now about 3.5 times larger than γ_{A}, thus producing the damping of the CW$-$ helical mode after having propagated through just the upper side of the lattice. For larger values of backscattering the situation is even more dramatic, as we would need a larger light recirculation through the S waveguide in order to suppress the backscattered intensity, therefore requiring a

larger value of k_S. The resulting increase in γ_T would lead to the total vanishing of the helical modes.

While the increase in the total loss rate of the system imposes limitations in the use of TJRs as the site resonators of passive spin-Hall insulators, in the following Section we will see that these restrictions are not present when a saturable gain is added to the edge resonators of the lattice. In that case, the incoherent pumping counteracts the effect of the incresed losses due to the finite couplings with the S waveguides, and therefore the only effect of TJRs is the intensity recirculation in the desired direction.

5.4   Active spin-Hall insulator

In this Section we add a saturable gain to the resonators located at the boundaries of the passive spin-Hall insulator studied in the previous Section. In Subsection 5.4.1 we investigate the possible lasing regimes in the backscattering-free ring resonator lattice and their relation with the type of saturable gain considered. In Subsection 5.4.2 we analyze the role of backscattering in the ring resonator topolaser and demonstrate that the Kerr nonlinearity of the material can be harnessed in order to promote lasing in a single topological gap. Finally, in Subsection 5.4.3 we show that the introduction of TJRs leads to single-pseudospin lasing with enhanced properties even in the presence of backscattering. We combine this effect with the optical nonlinearity of the material in order to grant topological protection to a single helical mode.

5.4.1   Saturable gain and lasing regimes in a backscattering-free ring resonator array

We start by considering the active analog of the 8×8 backscattering-free passive lattice of ring resonators explored in the previous Section. Only the edge resonators feature a saturable gain, which means that

$$P_0^{(n_x,n_y)} = \begin{cases} P_0 & if & n_x = 1, N_x \\ P_0 & if & n_y = 1, N_y \\ \\ 0 & otherwise \end{cases} . \tag{5.9}$$

In this case there is no probe signal and therefore the value of ω appearing in Eq. (5.1) is irrelevant as it just sets a reference frequency with respect to which the lasing frequency is measured. Without loss of generality, we set $\omega = \omega_0$. For the moment we do not take into account the shift of the resonance frequency of the site resonators due the optical nonlinearity, i.e. we set $n_{NL} = 0$. In each realization (i.e. each run of our code) we start from random initial conditions for the field amplitudes in each resonator, and we look for the long-time stationary states $\tilde{a}_{\pm}^{(n_x,n_y)}(t \to \infty)$ described by Eq. (5.1).

As we know from Chapter 3, whether a single backscattering-free ring resonator hosts unidirectional lasing depends on the type of gain saturation that the system features, which is accounted by the value of the ξ parameter. This plays a major role in the mode competition for gain: If $\xi \simeq 1$ none of the two pseudospins is able to get the whole gain and the resonator lases simultaneously in both counterpropagating directions. On the other hand, a saturable gain featuring $\xi > 1$ reinforces the imbalance in the mode competition as the gain saturation terms in the coupled-mode equations (3.1) are different for each pseudospin. Hence, the pseudospin featuring the smaller intensity experiences a smaller gain. Fluctuations then drive the resonator to a state of unidirectional lasing in a randomly chosen direction, provided that backscattering is sufficiently small.

In the case of the topolaser different ξ parameters also give rise to different lasing behaviors. In Fig. 5.4 we compare lasing in two backscattering-free spin-Hall lattices of ring resonators featuring $\xi = 1$ and $\xi = 2$. The $\xi = 2$ case summarizes the behavior of any $\xi > 1$ saturable gain. Panels (a,b,c,d) display the results for a single realization of the $\xi = 1$ topolaser. We first look at the average intensity in the edge resonators of the lattice

$$|\bar{a}_{\pm}|^2 = \left[\sum_{n_x=1}^{N_x} |\tilde{a}_{\pm}^{(n_x,1)}|^2 + \sum_{n_x=1}^{N_x} |\tilde{a}_{\pm}^{(n_x,N_y)}|^2 + \sum_{n_y=2}^{N_y-1} |\tilde{a}_{\pm}^{(1,n_y)}|^2 + \sum_{n_y=2}^{N_y-1} |\tilde{a}_{\pm}^{(N_x,n_y)}|^2 \right] \frac{1}{2(N_x + N_y - 2)} \tag{5.10}$$

as a function of the pump rate P_0. This is shown in panel (a). Above the lasing threshold, located at $P_0 = 1.09\gamma_T$, the average intensities in each pseudospin $|\bar{a}_\pm|^2$ depart linearly from zero with different slopes. The slope of the laser emission of each pseudospin is completely random and depends on the particular initial conditions randomly set for the realization. This behavior is identical to what was found for a single resonator. The increased lasing threshold with respect to the single resonator value (in which it is located at a pump rate $P_0 = \gamma_T$) is due to a weak penetration of the helical modes inside the passive bulk resonators. Panels (b,c) show the spatial distribution of the intensity in the lattice $|\tilde{a}_\pm^{(n_x,n_y)}|^2$ in units of n_S at a fixed pump rate $P_0 = 4.5\gamma_T$ for the $\pm$ pseudospins, respectively. The intensity is not homogeneously distributed along the boundary resonators and oscillates in time in each of them. In order to calculate the frequency spectrum of the $a_\pm(t)$ fields in each resonator we then performed a Fourier transform (FT) at a pump rate $P_0 = 4.5\gamma_T$. The transformed signals $FT(a_\pm)$ of all the edge resonators are shown in panel (d) as a function of the frequency ω_{FT}. The two pseudospins exhibit frequency components in the two topological gaps, which are the same for all the edge resonators. This indicates that our lattice is lasing in the four helical modes.

In the $\xi = 2$ topolaser two different behaviors are found. The first one is exemplified by panels (e,f,g,h) of Fig. 5.4 and is the analog of the $\xi = 2$ single resonator. Panel (e) shows the average intensity as a function of P_0. In this case the lasing threshold is located at the same pump rate $P_0 = 1.09\gamma_T$ as in the $\xi = 1$ realization. Above this value, the average intensity in a randomly chosen pseudospin which depends on the initial conditions of the realization (in this case the $-$ one) departs linearly with a slope $0.987 n_S/\gamma_T$, slightly smaller than the single resonator value n_S/γ_T. The intensity in the other pseudospin (the $+$ one) remains negligible. Panels (f,g) show the spatial distribution of the intensity at a pump rate $P_0 = 4.5\gamma_T$ in the two pseudospins $\pm$, respectively. Only in the latter one the edge resonators host a finite intensity which is concentrated at the corners of the lattice, since the corner resonators are not coupled with the lossy bulk. This prevents the intensity from leaking into the passive resonators. Panel (h) shows the frequency spectrum of the laser emission in this realization at a pump rate $P_0 = 4.5\gamma_T$. Only one peak is observed in the $-$ pseudospin at a frequency in the upper topological gap, indicating that the system is lasing in the CCW$-$ mode. Similar realizations in which single-mode lasing is triggered in another helical mode were also observed. However, no realizations in which the system lases in a single pseudospin at two distinct frequencies in the two topological gaps were found.

Contrary to what was observed in the single-resonator case, these are not the only possible outcomes in a $\xi = 2$ topolaser. Panels (i,j,k,l) show another realization in which the average intensity of the two pseudospins above threshold (located at a very similar value $P_0 = 1.10\gamma_T$ to that of the other realizations shown) takes the same value [1]. The slopes in this case are $0.399 n_S/\gamma_T$. Such a behavior was found to be unstable for a single resonator, but in the case of the topolaser it gives rise to a stationary pattern of intensity oscillations in the edge resonators in which the two pseudospins are in phase opposition. This can be regarded from the spatial intensity distributions at a pump rate $P_0 = 4.5\gamma_T$ shown in panels (j,k) in which the resonators emitting the larger intensity are alternatively distributed in each pseudospin. Panel (l) demonstrates that the emission spectrum of the two pseudospins at a pump rate $P_0 = 4.5\gamma_T$ features opposite frequency components belonging in the two topological gaps with the same spectral power. This implies that the system is lasing in the four helical modes. Therefore, even in a backscattering-free spin-Hall topolaser of ring resonators with a $\xi = 2$ gain saturation it is impossible to assure that the system will promote single-mode lasing when pumped above threshold.

On the following we will focus on the local saturable gain case (i.e. $\xi = 2$) which describes the homogeneously broadened gain medium of quantum spin-Hall topolasers.

5.4.2 Backscattering in a ring resonator topolaser

In order to apply our model to a more realistic system we now include in the ring resonator array a Hermitian backscattering of amplitude $|h| = 0.5\gamma_T = 0.04J$ —as was displayed by the setup of Ref. [11]— and a random complex phase in each site resonator. We also consider that the corresponding backscattering coupling rates $\beta_\pm^{(BS)}$ feature a random phase in every site resonator of the 8×8 lattice. As we found out in Sec. 5.3, it is important to take the backscattering

---

[1]Note that this is different from the behavior obtained for $\xi = 1$, where the average intensity in each pseudospin can take different values at fixed P_0. In the $\xi = 2$ case, solutions displaying multimode lasing always imply $|\bar{a}_+|^2 = |\bar{a}_-|^2$.
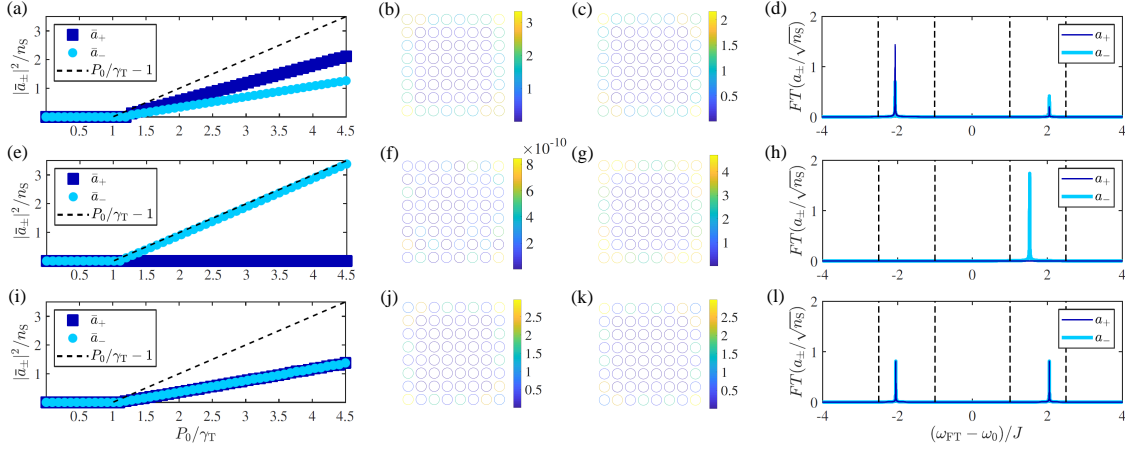
Figure 5.4: Topological lasing in a backscattering-free 8×8 quantum spin-Hall insulator of ring resonators with flux per plaquette $\alpha = 1/4$. Gain is only present in the edge resonators. Panels **(a,b,c,d)** correspond to a realization featuring a nonlocal saturable gain with $\xi = 1$. Two different realizations featuring a local saturable gain with $\xi = 2$ are shown in panels **(e,f,g,h)** and **(i,j,k,l)**, respectively. **(a,e,i)** Average intensity in the edge resonators of the lattice $|\bar{a}_\pm|^2$ as a function of the pump rate P_0. **(b,f,j)** Spatial distribution of the intensity $|\tilde{a}_+^{(n_x,n_y)}|^2$ in the + pseudospin (in units of n_S) at a pump rate $P_0 = 4.5\gamma_T$. **(c,g,k)** Spatial distribution of the intensity $|\tilde{a}_-^{(n_x,n_y)}|^2$ in the − pseudospin (in units of n_S) at a pump rate $P_0 = 4.5\gamma_T$. **(d,h,l)** Frequency spectrum for the two pseudospins as obtained from a Fourier transform (FT) of $a_\pm^{(n_x,n_y)}$ in all edge resonators at a pump rate $P_0 = 4.5\gamma_T$. ω_{FT} identifies the frequency of the transformed signal. The vertical dashed lines indicate the limits of the topological gaps.

rate much smaller than the width of the gap (which we remind the reader amounts for about $18\gamma_T \simeq 1.5J$; otherwise the edge modes disappear and light is localized in some resonators of the lattice boundaries. For the rest of the parameters, we employed the same values as in the calculations for the passive spin-Hall insulator.

We also investigate the effect of optical nonlinearities in the laser emission. As demonstrated in [162], when the nonlinear refractive index n_{NL} and the curvature of the helical mode have the same sign the imaginary part of the dispersion is positive and the system is dynamically unstable. Remarkably, the helical modes belonging to the same pseudospin but different topological gaps have opposite curvatures, and therefore for a given value of n_{NL} only one helical mode will be dynamically stable. We employ Kerr nonlinearities (i.e. featuring $g = 2$) of strength $|n_{NL}|n_S\omega_0/n_L = 0.1J$; this value is smaller than the width of the topological gap ($\simeq 1.5J$) and therefore the nonlinearity does not alter the topological protection of the helical modes. However, as we know from Chapters 2 and 3, it results in a shift of the resonance frequency of the site resonators proportional to the intensity circulating inside them. As we will see, this implies that the topological gaps will also be displaced in frequency with respect to the nonlinearity-free case. For such a small Kerr nonlinearity the anti-resonant condition for the link resonators remains well satisfied in spite of this shift (i.e. $\exp(i\omega_0(1 - n_{NL}n_S/n_L)n_L L_L/c) \simeq -1$).

Fig. 5.5 shows the average intensity $|\bar{a}_\pm|^2$ in the edge resonators for the two pseudospins as a function of the pump rate P_0 for three realizations of the ring resonator topolaser featuring $n_{NL} = 0$ (panel a), $n_{NL} < 0$ (panel e), and $n_{NL} > 0$ (panel i). To facilitate the comparison between the three cases, we choose all realizations to show lasing in the − pseudospin. However, note that while in the $n_{NL} = 0$ case solutions displaying multimode lasing with the same average intensity in each pseudospin are still possible, for $n_{NL} \neq 0$ one of the topological gaps is always dynamically unstable and therefore this kind of solutions cannot exist. The introduction of the Kerr nonlinearity does not significantly modify the slope and threshold of the lasing emission: in all the three cases it features a reduced slope of about $0.94n_S/\gamma_T$ and an increased lasing threshold $P_0 = 1.13\gamma_T$ compared with the backscattering-free case. The average intensity in the + pseudospin cannot be neglected and at pump rate $P_0 = 4.5\gamma_T$ it takes the value $|\bar{a}_+|^2 = 0.12n_S$. Contrary to what we had observed for the single-resonator laser (see Chapter 3), in the quantum spin-Hall topolaser the different
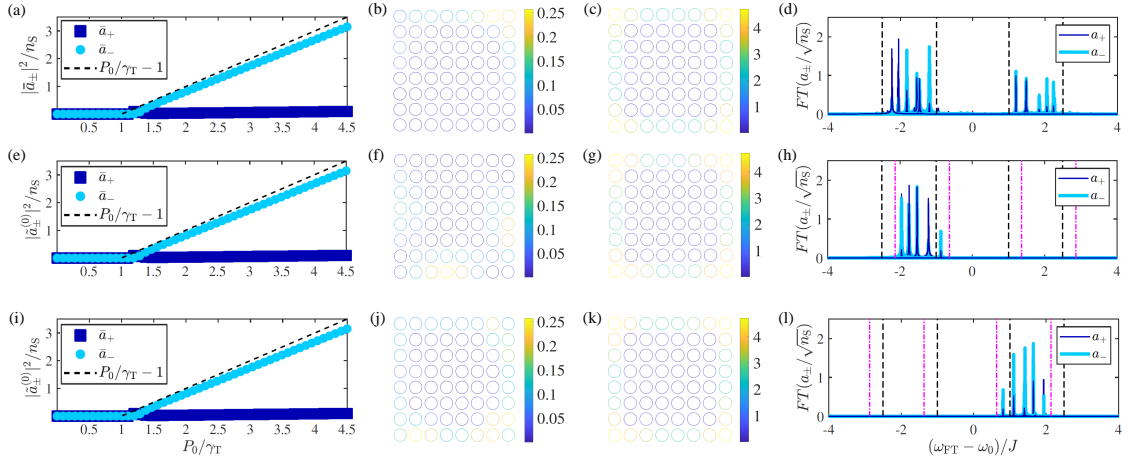
Figure 5.5: Topological lasing in an 8×8 quantum spin-Hall array of ring resonators with flux per plaquette $\alpha = 1/4$. Gain is only present in the edge resonators. The lattice hosts a Hermitian backscattering of strength $|h| = 0.04J$ and a random phase in each resonator. Panels **(a,b,c,d)** correspond to $n_{\mathrm{NL}} = 0$. Panels **(e,f,g,h)** display the results for $n_{\mathrm{NL}} < 0$. Panels **(i,j,k,l)** are obtained for $n_{\mathrm{NL}} > 0$. **(a,e,i)** Average intensity in the edge resonators of the lattice $|\bar{a}_\pm|^2$ as a function of the pump rate P_0. **(b,f,j)** Spatial distribution of the intensity $|\tilde{a}_+^{(n_x,n_y)}|^2$ in the $+$ pseudospin (in units of n_{S}) at a pump rate $P_0 = 4.5\gamma_{\mathrm{T}}$. **(c,g,k)** Spatial distribution of the intensity $|\tilde{a}_-^{(n_x,n_y)}|^2$ in the $-$ pseudospin (in units of n_{S}) at a pump rate $P_0 = 4.5\gamma_{\mathrm{T}}$. **(d,h,l)** Frequency spectrum for the two pseudospins over 100 realizations as obtained from a Fourier transform (FT) of $a_\pm^{(n_x,n_y)}$ in all edge resonators at a pump rate $P_0 = 4.5\gamma_{\mathrm{T}}$. ω_{FT} identifies the frequency of the transformed signal. The black dashed lines indicate the limits of the topological gaps in the $n_{\mathrm{NL}} = 0$ case. The pink dashed-dotted lines indicate the limits of the topological gaps in the $n_{\mathrm{NL}} \neq 0$ cases.

shift of the resonance frequency for the two pseudospins introduced by the Kerr nonlinearity (see Eq. (5.1)) does not lead to a suppression of the intensity circulating in the less populated one. This can be understood in terms of the small nonlinear refractive index $n_{\mathrm{NL}} n_{\mathrm{S}} \omega_0 / n_{\mathrm{L}} = 0.1J \simeq 1.2\gamma_{\mathrm{T}}$ employed in the topolaser. In contrast, the larger values of n_{NL} used in the single resonator laser, accounting for up to 50 times γ_{T}, yielded a larger splitting between the resonance frequencies for each pseudospin. However, in the topolaser the maximum value of n_{NL} that can be employed is limited by the frequency width of the gap: when $n_{\mathrm{NL}} n_{\mathrm{S}} \omega_0 / n_{\mathrm{L}}$ approaches J the helical modes disappear. In addition to this, a larger value of n_{NL} would pose the further inconvenient of a deviation from the anti-resonant condition for the link resonators.

Panels (b,f,j) and (c,g,k) of Fig. 5.5 display the spatial distribution of the intensity $|\tilde{a}_\pm^{(n_x,n_y)}|^2$ in the $+$ and $-$ pseudospins, respectively, for the same three realizations featuring $n_{\mathrm{NL}} = 0$ (panels b,c), $n_{\mathrm{NL}} < 0$ (panels f,g), and $n_{\mathrm{NL}} > 0$ (panels j,k). The pump rate in all cases was fixed at $P_0 = 4.5\gamma_{\mathrm{T}}$. As can be seen in panels (b,f,j) the intensity in the minority $+$ pseudospin is not homogeneously distributed across the lattice boundaries. Instead, only a few resonators host the majority of the intensity. In the case of the majority $-$ pseudospin, panels (c,g,k) show that the corner resonators feature a larger intensity than those located at the center of the lattice sides, as was found in the backscattering-free case.

We now analyze the frequency spectrum of the laser emission in all edge resonators of the quantum spin-Hall ring-resonator laser featuring $n_{\mathrm{NL}} = 0$ (panel d), $n_{\mathrm{NL}} < 0$ (panel h), and $n_{\mathrm{NL}} > 0$ (panel l). Each spectrum is calculated using 100 realizations, each one featuring different random initial conditions and different random backscattering phases. In all cases the pump rate is fixed at $P_0 = 4.5\gamma_{\mathrm{T}}$. Panel (d) shows that in the absence of the Kerr nonlinearity the spin-Hall lattice can lase in the two pseudospins at frequencies in the two topological gaps, whose limits are indicated by the black dashed lines. In each individual realization, as demonstrated in Subsection 5.4.1 for a $\xi = 2$ saturable gain, the system chooses between single-frequency lasing in one of the helical modes, or lases simultaneously in the four of them with equal average intensity in each pseudospin. However, when we employ a negative refractive index (panel h) the topolaser

can only emit in the two helical modes of positive curvature belonging in the lower topological gap. In each realization, the system displays single-mode lasing in one of them, which is arbitrarily chosen. Similarly, if the nonlinear refractive index is positive (panel l), lasing is only possible in the two helical modes of negative curvature in the upper topological gap. In each realization one of them is randomly chosen. Due to the finite Kerr nonlinearity, in the last two cases the resonance frequency of the site resonators is displaced a quantity $-n_{\mathrm{NL}}/n_{\mathrm{L}}\omega_0|\tilde{a}_-^{(n_x,n_y)}|^2$. This also shifts the frequencies of the topological gaps (although their width remains the same as in the absence of nonlinearity). Panels (h,l) show that the lasing frequency of all realizations falls into the limits of the nonlinearity-shifted topological gaps (delimited by the pink dashed-dotted lines) in each case and not into those of the $n_{\mathrm{NL}} = 0$ topological gaps (i.e. within the black dashed lines).

5.4.3 Backscattering in a TJR topolaser

In order to test the advantages of single-pseudospin lasing and intensity recirculation enabled by active TJRs we also investigate the analog lattice featuring S couplings of strength $k_{\mathrm{S}} = 0.31$ which couple the $+$ into the $-$ pseudospin [2]. The presence of the S waveguides increases the total loss rate γ_{T}; however, the inter-site couplings β_{w} remain the same and therefore the hopping energy $J \simeq 12\gamma_{\mathrm{A}} \simeq 0.48\gamma_{\mathrm{T}}$ remains unaltered. We consider an array featuring the same Hermitian backscattering with amplitude $|h| = 0.04J$ and a random complex phase in each site resonator as we did in the ring resonator topolaser: these parameters lead to a ratio $|h|/|\beta_{\mp}^{(\mathrm{S})}| \simeq 0.01$. As we know from Chapter 3, such a strong S coupling will always promote lasing in the $-$ pseudospin only. However, this system can still host a pair of helical modes propagating in CW and CCW directions along the lattice boundaries. Since each of these modes belongs in a different topological gap, they feature opposite curvatures and become dynamically unstable for opposite values of the optical nonlinearity of the material. Therefore, lasing in a single helical mode can be triggered by a proper choice of n_{NL}.

In this case we will solely focus on realizations featuring $n_{\mathrm{NL}} < 0$ and $n_{\mathrm{NL}} > 0$. In the first case lasing will only be possible in the CW$-$ helical mode located in the lower topological gap, which features a positive curvature, while in the latter one the lattice will only host lasing in the CCW$-$ mode of the upper gap, of negative curvature (see Fig. 5.1b). Panels (a) and (e) of Fig. 5.6 display the average intensity $|\bar{a}_\pm|^2$ in the two pseudospins for two realizations of the TJR topolaser featuring $n_{\mathrm{NL}} < 0$ and $n_{\mathrm{NL}} > 0$, respectively. In the two cases both the slope $(0.998n_{\mathrm{S}}/\gamma_{\mathrm{T}})$ and lasing threshold $(P_0 = 1.01\gamma_{\mathrm{T}})$ display very similar values to the single-resonator ones, and even outperform those of the backscattering-free ring resonator topolaser. The averaged residual intensity in the $+$ pseudospin at a pump rate $P_0 = 4.5\gamma_{\mathrm{T}}$ is $|\bar{a}_+|^2 = 3 \times 10^{-3}n_{\mathrm{S}}$, i.e. 40 times smaller than in the analog ring-resonator topolaser featuring a backscattering of the same strength. This can be understood by recalling our results for the single TJR laser discussed in Chapter 3: a sufficiently strong coupling with the embedded S element recirculates the backscattered intensity populating the unfavored $+$ pseudospin into the preferred $-$ one.

Panels (b,f) and (c,g) of Fig. 5.6 display the spatial distribution of the intensity $|\tilde{a}_\pm^{(n_x,n_y)}|^2$ in the $+$ and $-$ pseudospins, respectively, for the same two realizations of the TJR topolaser with $n_{\mathrm{NL}} < 0$ (panels b,c), and $n_{\mathrm{NL}} > 0$ (panels f,g). The pump rate in all cases was fixed at $P_0 = 4.5\gamma_{\mathrm{T}}$. As in the ring resonator topolaser, the intensity in the minority $+$ pseudospin is not homogeneously distributed across the lattice boundaries. However, for the majority $-$ pseudospin, in contrast to the light localization in the corner resonators observed in the ring resonator topolasers, panels (c,g) show that in the TJR topolaser the intensity presents a more homogeneous distribution across the lattice boundaries. This absence of localization is produced when the coupling rate between a given site resonator and the S waveguide $|\beta_{\mp}^{(\mathrm{S})}|$ overcomes that between adjacent site resonators $|\beta_{\mathrm{w}}|$, and it contributes to a slope closer to the single-resonator value $n_{\mathrm{S}}/\gamma_{\mathrm{T}}$ whenever a larger k_{S} is considered. The fact that $|\beta_{\mp}^{(\mathrm{S})}| \gg |\beta_{\mathrm{w}}|$ also produces a smaller penetration of the helical modes into the bulk resonators, therefore bringing the lasing threshold closer to $P_0/\gamma_{\mathrm{T}} = 1$.

We finally study the frequency spectrum of the laser emission of the TJR topolaser for $n_{\mathrm{NL}} < 0$ (panel d) and $n_{\mathrm{NL}} > 0$ (panel h) at a fixed pump rate $P_0 = 4.5\gamma_{\mathrm{T}}$. Each spectrum is calculated using 100 realizations, each one starting from different random initial conditions and featuring different random backscattering phases. As in the ring resonator topolaser, the resonance frequency

---

[2]Note that in the experiment of Ref. [13] the loss rate due to the S waveguide amounts to $\gamma_{\mathrm{S}}n_{\mathrm{L}}/c = 10$ cm^{-1}, or equivalently $k_{\mathrm{S}} = 0.35$.
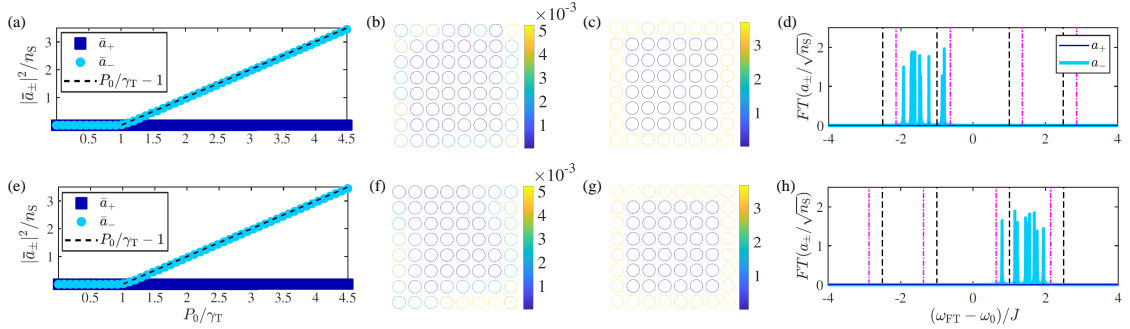
Figure 5.6: Topological lasing in an 8×8 quantum spin-Hall array of TJRs with flux per plaquette $\alpha = 1/4$. Gain is only present in the edge resonators. The lattice hosts a Hermitian backscattering of strength $|h| = 0.04J$ and a random phase in each resonator. Panels **(a,b,c,d)** correspond to a $n_{\mathrm{NL}} < 0$. Panels **(e,f,g,h)** are obtained for $n_{\mathrm{NL}} > 0$. **(a,e)** Average intensity in the edge resonators of the lattice $|\bar{a}_{\pm}|^2$ as a function of the pump rate P_0. **(b,f)** Spatial distribution of the intensity $|\tilde{a}_{+}^{(n_x,n_y)}|^2$ in the $+$ pseudospin (in units of n_{S}) at a pump rate $P_0 = 4.5\gamma_{\mathrm{T}}$. **(c,g)** Spatial distribution of the intensity $|\tilde{a}_{-}^{(n_x,n_y)}|^2$ in the $-$ pseudospin (in units of n_{S}) at a pump rate $P_0 = 4.5\gamma_{\mathrm{T}}$. **(d,h)** Frequency spectrum for the two pseudospins through 100 realizations as obtained from a Fourier transform (FT) of $a_{\pm}^{(n_x,n_y)}$ in all edge resonators at a pump rate $P_0 = 4.5\gamma_{\mathrm{T}}$. ω_{FT} identifies the frequency of the transformed signal. The black dashed lines indicate the limits of the topological gaps in the $n_{\mathrm{NL}} = 0$ case. The pink dashed-dotted lines indicate the limits of the topological gaps in the $n_{\mathrm{NL}} \neq 0$ cases.

ω_0 of the site resonators are displaced a quantity $-n_{\mathrm{NL}}n_{\mathrm{S}}\omega_0/n_{\mathrm{L}}$ due to the Kerr nonlinearity. Whilst this translates in a shift of the frequency at which the topological gaps appear, their width remains unaltered. Panel (d) shows that when the material features a Kerr nonlinearity with negative refractive index the system displays single-mode lasing in the CW− mode at some random frequency whithin the limits of the nonlinearity-shifted lower topological gap. Instead, when we employ a positive refractive index (panel h) the TJR topolaser can only emit in the CCW− mode at a frequency in the nonlinearity-shifted upper topological gap.

5.5   Conclusions

In this Chapter we studied lasing in active spin-Hall topological insulators based on arrays of silicon ring resonators supporting two pseudospin states that experience an opposite synthetic gauge field. As long as backscattering coupling the two pseudospins can be neglected, such a system hosts four helical modes topologically protected against local perturbations. Our analysis is based on solving for the steady state of the temporal coupled-mode equations for the field amplitudes in each resonator and pseudospin state.

   We first investigated the different lasing behaviors arising in a backscattering-free ring resonator lattice as a consequence of different gain saturation types which can suppress or reinforce the mode competition between pseudospin states. Even though we always consider a class-A laser featuring an instantaneous gain, we found that a nonlocal saturation promotes lasing in the four helical modes at the same time, while for a local gain saturation the two pseudospins experience a different gain. This latter case leads either to single-mode lasing in a random helical mode or to stationary intensity oscillations in the boundary resonators involving the four helical modes.

   When a realistic backscattering is considered the performance of such a spin-Hall laser decreases significantly and the backwards-propagating pseudospin hosts a finite intensity. However, we demonstrated that the combination of a unidirectional coupling between pseudospins enabled by TJRs and a non-zero optical Kerr nonlinearity grant single-mode topological lasing with a threshold and slope efficiency very similar to the backscattering-free single-resonator values, as well as a negligible backwards-propagating intensity.

   Our work has established the theoretical foundations behind the use of TJRs to promote single-mode lasing in active quantum spin-Hall topological insulators featuring a sizable backscattering. However, further research is needed in order to investigate in detail the role of a reservoir of

incoherent excitations that accounts for a more realistic gain saturation present in class-B lasers. In addition to this, the introduction of an asymmetrical four-wave mixing such as the one studied in Chapter 4 could reinforce the suppression of the backscattered light. This will be the subject of future work.

Chapter 6

Review of the fractional quantum Hall effect

The previous chapters have been devoted to the implementation of realistic non-trivial topological structures using a silicon photonics platform. Nevertheless, such a system has the clear disadvantage of providing weak nonlinearities which are only suitable for the study of IQH physics. In the following chapters we will focus on the fractional quantum Hall (FQH) effect, which requires strong interactions and hosts even more exotic phenomena. This physics involves strongly correlated phases of matter known as FQH liquids, which are characterized not by their symmetries—as in Landau's theory of phase transitions—but by a new kind of internal order known as *topological order* [166]. They display fascinating properties such as the existence of quasiparticle and quasihole excitations featuring a fraction of the electron charge and statistical properties different from those of bosons and fermions: the so-called *anyons*. Depending on the behavior of two such particles upon an exchange of their positions (a process known as *braiding*), which is determined by the topological order of the FQH liquid hosting them, these excitations can be classified into Abelian or non-Abelian. The latter type adds even more complexity as they involve a non-local storage of information in the system's wavefunction which gives rise to long-range entanglement [167].

One of the most promising paths opened by the study of non-Abelian FQH liquids is the perspective of building *fault-tolerant topological quantum computers* [168]. The topological protection of such a quantum computer arises from the nonlocal encoding of the qubit states, which makes it immune to errors caused by local perturbations.

Quantum simulators have also opened new perspectives for the study of FQH phases of matter. In fact, some of the challenges that electronic solid state setups pose to both experimentalists and theorists can be circumvented in alternative platforms like cold atomic gases and optical setups [169], which offer a large degree of experimental control due to the great technological advances they have experienced in the last decades.

In this Chapter we will first explain the physical origin and the theoretical treatment of the FQH effect, and we will then present the state-of-the-art implementations of such physics, focusing on cold atoms and optical systems. We refer the interested reader to [30] for a more comprehensive review of the topic.

6.1 Introduction

The topological revolution that physics has experienced in the last decades is rooted in the study of a rather simple setup: a 2D electron gas subjected to a strong perpendicular magnetic field. The pioneering experiments of [1] in solid state samples determined for the first time that the Hall
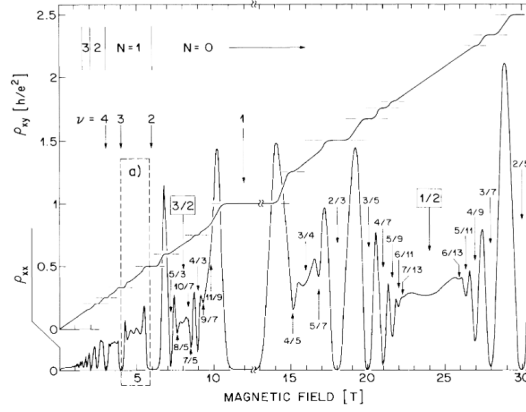
Figure 6.1: *The fractional quantum Hall effect.* Hall (ρ_{xy}) and longitudinal (ρ_{xx}) resistivities as a function of the magnetic field B. The numbers show the values of ν in Eq. (1.12) characterizing each plateau in ρ_{xy}. As can be seen, some of them take fractional values. This image was extracted from [173].

resistance is a quantized quantity that takes the discrete values

$$R_{\mathrm{H}} = \left(\frac{h}{e^2}\right)\frac{1}{\nu},\tag{6.1}$$

where, as we know from Chapter 1, ν was initially measured to be an integer number. This is the so-called integer quantum Hall (IQH) effect, that was successfully described in terms of the single-particle Landau levels (LLs) arising in the non-interacting picture (see Sec. 1.2).

However, shortly after the discovery of the IQH effect, in 1982 Tsui et al. [170] observed for the first time plateaux at rational values of ν. The first values discovered were $\nu = 1/3, 2/3$, but soon after many more followed (and even nowadays new ones continue to be observed! [171]): $\nu = 1/5, 2/5, 3/7, 4/9, 5/9, 3/5, 5/2, 12/5, 13/5...$ The most prominent plateaux are shown in Fig. 6.1. The appearance of these fractional plateaux could be understood by considering gaps inside the LLs at the particular values of ν where these are measured. A fractional value of ν would imply a fractional occupation of the LL considered. For instance, $\nu = 1/3$ means that only one third of the states belonging to the lowest Landau level (LLL) are occupied. This is why ν is known as *filling fraction*. Indeed, there is one ingredient that we left behind in our explanation of the IQH effect and that could account for this complicated gapped structure inside the LLs: the Coulomb repulsion between electrons. This would lift the degeneracy of each LL and produce a spectrum of states within the characteristic energy scale of the Coulomb interactions, E_{Coulomb}. On the other hand, disorder, for example produced by the presence of impurities inside the sample, can be characterized by a potential V_{disorder}. This would lead to localized states around the gap, therefore explaining the plateaux structure observed in the Hall resistance. In summary, we need the energy scales of our problem to satisfy

$$\hbar\omega_{\mathrm{c}} \gg E_{\mathrm{Coulomb}} \gg V_{\mathrm{disorder}}.\tag{6.2}$$

While in Chapter 1 the theoretical explanation of the IQH effect required only the single-particle spectrum of 2D charged particles inside a magnetic field, the crucial role of interactions makes the FQH effect much more difficult to understand. One cannot simply write down the matrix elements for the interacting Hamiltonian inside each macroscopically degenerate LL and diagonalize it exactly in order to find the spectrum of eigenvalues. This would be too computationally demanding—and it looked even more difficult forty years ago, when the FQH effect was observed for the first time. Instead, a much more efficient strategy would be to write down a wise Ansatz accounting for the relevant physics. Indeed, the first explanation of the origin of the fractional plateaux was due to Laughlin in 1983 [172], who derived a plausible Ansatz for the ground state of the FQH liquid at filling fractions $\nu = 1/m$, where m is a positive integer number (which, as we will see, is odd for a FQH liquid of fermions, and even for one formed by bosons). We will review his approach as well as its most significant predictions in the following Section.

6.2   The FQH ground state: Laughlin Ansatz

The so-called *Laughlin states* describe the ground state of FQH liquids at filling fractions $\nu = 1/m$, where m is a positive integer. The complexity of the problem due to the macroscopic degeneration of the Landau levels and the strong Coulomb repulsion between electrons makes very difficult to solve it exactly, even applying computational brute force. Instead, Laughlin provided an Ansatz which is actually really close to the exact solution and that captures all the relevant physics. Of course, his reasoning was motivated by physical insights that we will review on the following.

   Consider two particles in the LLL interacting via a central potential

$$V = V(|\mathbf{r}_1 - \mathbf{r}_2|). \tag{6.3}$$

We can exploit the rotational symmetry of the problem by working in the basis of eigenstates of the angular momentum operator. As we already saw in Chapter 1, this means that we should employ the symmetric gauge. The single-particle wavefunctions in the LLL can be written as

$$\psi_m \propto z^m e^{-|z|^2/4\ell_{\mathrm{B}}^2}, \tag{6.4}$$

where $z = x - iy$ is the complex in-plane coordinate and m labels the angular momentum quantum number. In fact, as we showed in Sec. 1.2.2, the wavefunctions (6.4) are eigenstates of the z component of the angular momentum. For clarity, on the following of this Section the wavefunctions will be presented unnormalized, unless stated otherwise.

   We now consider the total system of two interacting particles. If the energy scales determined by the cyclotron frequency and the central potential are well-separated (i.e. if $\hbar\omega_{\mathrm{c}} \gg V$), mixing between different LLs can be neglected. Therefore, as we saw in the single-particle case (see Sec. 1.2.2), the two-particles wavefunction must take the form of the usual Gaussian factor multiplied by a holomorphic function. More precisely, it can be written as

$$\psi \propto (z_1 + z_2)^M (z_1 - z_2)^m e^{-(|z_1|^2 + |z_2|^2)/4\ell_{\mathrm{B}}^2}, \tag{6.5}$$

being M and m a couple of non-negative integers, M related to the angular momentum of the center of mass, and m the relative angular momentum.

   In general, as long as LL mixing is not present, any N-particle wavefunction describing a state in the LLL must take the form

$$\psi(z_1, ..., z_N) = f(z_1, ..., z_N)e^{-\sum_{i=1}^{N}|z_i|^2/4\ell_{\mathrm{B}}^2}, \tag{6.6}$$

for some holomorphic function $f(z_1, ..., z_N)$. Moreover, the fermionic or bosonic statistics of the particles imposes that such a function must be antisymmetric or symmetric under any two-particle exchange $z_i \Longleftrightarrow z_j$, respectively.

   Laughlin generalized the two-particle state in Eq. (6.5) in order to account for N particles. His Ansatz for the ground state of the $\nu = 1/m$ FQH liquid reads

$$\psi_L = \prod_{i<j}(z_i - z_j)^m e^{-\sum_{i=1}^{N}|z_i|^2/4\ell_{\mathrm{B}}^2}. \tag{6.7}$$

It is easy to notice that when m is an odd integer this wavefunction is antisymmetric and therefore describes a fermionic state. On the other hand, when m is an even integer, the wavefunction is symmetric and describes a bosonic state. Note that, whatever the statistics of the particles, the probability of finding two of them close together is zero. This is a reflection of the incompressible character of FQH liquids. Besides, the Gaussian exponential tends to zero when the particles move far away from the origin. Altogether, these two facts imply that the spatial probability density stemming from the Laughlin wavefunction must be flat in the bulk of the FQH droplet, even though it can be difficult to realize at first sight given the shape of Eq. (6.7). We will justify this in the following Section.

   The first thing we would like to ensure is that the state described by Eq. (6.7) has the correct filling fraction. In order to do this we focus on a certain particle, let's say the one located at z_1. The polynomial of the Laughlin wavefunction can then be written as

$$\prod_{i<j}(z_i - z_j)^m = \prod_{i=2}^{N}(z_1 - z_i)^m, \tag{6.8}$$

which implies that there are $m(N-1)$ powers of z_1. What this is really telling us is that the maximum angular momentum of the particle at z_1 is $m(N-1)$ as well. This determines that the maximum radius of this particle will be $R = \sqrt{2m(N-1)}\ell_B \simeq \sqrt{2mN}\ell_B$, where we are considering a large number of particles $N \gg 1$. Thus, the area of the FQH droplet will be given by $A = \pi R^2 = 2\pi m N \ell_B^2$. As accounted in Eq. (1.55), the degeneracy of a given LL is

$$\mathcal{N} = \frac{A}{2\pi\ell_B^2} = mN. \tag{6.9}$$

We see that this lead to the correct result for the filling fraction, which is given by the number of particles N divided by the number of states $\mathcal{N}$:

$$\nu = \frac{N}{\mathcal{N}} = \frac{1}{m}. \tag{6.10}$$

Laughlin demonstrated in [172] that the overlap between the Ansatz in Eq. (6.7) and the true ground state for N electrons forming a FQH liquid is impressively large for small numbers of particles, around 99%. Of course, numerically finding the exact ground state of the system is difficult and can only be done for a couple of dozens of particles. However, when we consider very large numbers of particles, the overlap between the Laughlin state and the true ground state of the system is expected to tend to zero. At the end of the day, we should consider the Laughlin state as a state in the same universality class as the exact ground state of the system, meaning that both feature the same excitations and topological order.

6.3 The plasma analogy and the density of the Laughlin state

In order to demonstrate that the density of the Laughlin's state takes a constant value in the bulk of the FQH droplet, we will make use of Laughlin's plasma analogy [172, 30]. This is a very powerful analytical tool that relies on a mathematical analogy between the squared modulus of the Laughlin state (6.7) and the Boltzmann factor $e^{-\beta U}$ of a classical 2D Coulomb plasma.

In order to motivate this analogy, we first try to calculate the average density of the FQH liquid. This is done by taking the expectation value of the density operator

$$n(z) = \sum_{i=1}^{N} \delta(z - z_i), \tag{6.11}$$

which is given by

$$\langle \psi | n(z) | \psi \rangle = \frac{\int \prod_{i=1}^{N} d^2 z_i \, n(z) P[z_i]}{\int \prod_{i=1}^{N} d^2 z_i \, P[z_i]}. \tag{6.12}$$

In the equation above, $P[z_i]$ is the unnormalized probability density of the Laughlin state:

$$P[z_i] = \prod_{i<j} \frac{|z_i - z_j|^{2m}}{\ell_B^{2m}} e^{-\sum_{i=1}^{N} |z_i|^2 / 2\ell_B^2}. \tag{6.13}$$

A closer look at Eq. (6.12) reveals a clear similarity between the denominator on its right-hand side and the canonical partition function, which can be defined as

$$Z = \int \prod_{i=1}^{N} d^2 z_i \, P[z_i]. \tag{6.14}$$

Associating the probability density $P[z_i]$ to the Boltzmann distribution function

$$P[z_i] = e^{-\beta U(z_i)}, \tag{6.15}$$

we obtain an effective potential $U(z_i)$ of the form

$$U(z_i) = \frac{1}{\beta} \left[-2m \sum_{i<j} \log\left(\frac{|z_i - z_j|}{\ell_B}\right) + \frac{1}{2} \sum_{i=1}^{N} \frac{|z_i|^2}{\ell_B^2} \right]. \tag{6.16}$$

In the expressions above, the factor $\beta = 1/k_{\mathrm{B}}T$ sets a fictitious temperature T for the 2D plasma (but remember that the FQH droplet is not placed at a finite temperature!). In particular, by choosing the vale $\beta = 2/m$ we get

$$U(z_i) = -m^2 \sum_{i<j} \log\left(\frac{|z_i - z_j|}{\ell_{\mathrm{B}}}\right) + \frac{m}{4\ell_{\mathrm{B}}^2} \sum_{i=1}^{N} |z_i|^2, \tag{6.17}$$

which is the potential energy for a 2D Coulomb plasma of charged particles featuring an electric charge $q = -m$ each. The first term in Eq. (6.17) is indeed the 2D Coulomb potential between a pair of particles with charge $q = -m$. This stems from the 2D Poisson equation:

$$-\nabla^2 \phi = 2\pi q \delta^2(\mathbf{r}) \quad \rightarrow \quad \phi = -q\log\left(\frac{r}{\ell_{\mathrm{B}}}\right). \tag{6.18}$$

The potential energy will then be given by $U = q\phi$, which coincides with the first term in Eq. (6.17). On the other hand, the second term in Eq. (6.17) represents the interaction energy between a particle of charge $q = -m$ and a constant charge background that neutralizes it. For a background of charge density ρ_0 that gives rise to an electrostatic potential ϕ we can write the Poisson equation $-\nabla^2 \phi = 2\pi\rho_0$. Applying this to the second term of Eq. (6.17) we get

$$-\nabla^2 \phi = \nabla^2 \left(\frac{|z|^2}{4\ell_{\mathrm{B}}^2}\right) = \frac{1}{\ell_{\mathrm{B}}^2}, \tag{6.19}$$

and therefore the constant density ρ_0 must take the value

$$\rho_0 = \frac{1}{2\pi\ell_{\mathrm{B}}^2}. \tag{6.20}$$

Note that this is equal to the flux density in the FQH droplet.

To minimize the energy of the system, the plasma will be arranged in such a way that it neutralizes the background charge density. Given the fact that each particle carries a charge $q = -m$, the compensating density of particles n must satisfy $mn = \rho_0$, giving

$$n = \frac{1}{2\pi\ell_{\mathrm{B}}^2 m}, \tag{6.21}$$

which corresponds to the expected bulk density for a FQH droplet at filling fraction $\nu = 1/m$ [30]. Even though the shape of the Laughlin state in Eq. (6.7) may lead us to think otherwise, our calculation with the plasma analogy shows that the average density of particles of the FQH droplet is in fact constant. There is nothing special about the origin.

6.4 Topological order

It is now time to ask where do FQH liquids fit into our description of phases of matter. According to Landau's theory of symmetry breaking, different phases of matter are characterized by different symmetries. For example: Liquids are formed by randomly distributed atoms (or molecules), and therefore they are disordered states that do not break any symmetry. On the other hand, in crystals atoms are distributed according to a spatially-periodic geometrical pattern, and thus they only have a discrete translation symmetry. These two phases are connected via a spontaneous symmetry breaking.

At first glance it may seem that Landau's theory provides a satisfactory explanation of the whole spectrum of phases of matter arising in condensed matter physics. However, FQH liquids pose a remarkable exception. We have seen that there exist several types of FQH liquids classified according to their filling fraction ν. As we will see in the following Section, these display different types of excitations, namely quasiholes and quasiparticles with fractional charge and statistics determined by the value of ν. But being liquids, these different FQH phases do not feature any internal order: regardless of their filling fraction they all have the same symmetries and therefore cannot by distinguished by symmetry breaking. FQH liquids are not the only case of quantum phases of matter (i.e. phases at zero temperature) in which Landau's theory breaks down: another example is provided by the so-called chiral spin liquids [174].

It turns out that FQH liquids are characterized by a different type of order, named *topological order* [166, 175, 176]. This arises as a consequence of long-range entanglement in quantum many-body systems. Intuitively, we can interpret topological order as a global *dancing pattern* governing the motion of particles in the FQH droplet. Such a pattern arises from a set of local *dancing rules* aiming at lowering the energy of the local Hamiltonian perceived by each particle. For instance, in a FQH liquid of electrons these dancing rules are the quantized cyclotron motion determined by ν, the Fermi quantum statistics, and the repulsion due to the strong Coulomb interactions and the Pauli exclusion principle. This is different from the situation in a traditional symmetry-breaking phase, where all particles (or pairs of particles in the case of a superfluid of fermions) dance by themselves in the same way. The same way of dancing represents the long-range order.

Finally, how can we characterize phases with different topological order? Instead of looking at order parameters and long-range correlations as we are used to do in Landau symmetry-breaking theory, we must rely on physical properties such as the ground-state degeneracy [177], the fractional charge and statistics of the charged bulk excitations, and the properties of the gapless edge modes [178].

6.5   Excitations of the FQH liquid

So far we have only discussed the ground state for a $\nu = 1/m$ FQH liquid, being m a positive integer number. At this point it seems natural to wonder what kind of excitations does such a state feature. It turns out that the FQH droplet can host gapless edge excitations behaving as a 1D chiral quantum liquid [166, 41, 179] as well as gapped neutral collective excitations in the bulk somewhat similar to phonons in superfluids [180]. Nevertheless, here we will focus on the charged excitations of the bulk, which are quasiholes and quasiparticles featuring astonishing properties like fractional charge (in units of the elementary charge) and intermediate statistics between those of bosons and fermions.

6.5.1   Quasiholes

We start by writing the wavefunction that describes a quasihole excitation at a complex position $\eta = \eta_x - i\eta_y$ in the $x - y$ plane, namely

$$\psi_{\mathrm{QH}}(\eta, z) = \prod_{i=1}^{N}(z_i - \eta)\psi_{\mathrm{L}}(z) = \prod_{i=1}^{N}(z_i - \eta)\prod_{i<j}(z_i - z_j)^m e^{-\sum_{i=1}^{N}|z_i|^2/4\ell_{\mathrm{B}}^2}. \qquad (6.22)$$

A first inspection of this wavefunction reveals that the particle density vanishes precisely at the position of the quasihole η. In general, the wavefunction describing a state with M quasiholes located at positions η_μ, each one labeled by the index $\mu = 1, ..., M$, reads

$$\psi_{\mathrm{M-QH}} = \prod_{\mu=1}^{M}\prod_{i=1}^{N}(z_i - \eta_\mu)\prod_{i<j}(z_i - z_j)^m e^{-\sum_{i=1}^{N}|z_i|^2/4\ell_{\mathrm{B}}^2}. \qquad (6.23)$$

As mentioned before, the quasihole displays remarkable properties: in particular, it features fractional charge and statistics. In the following we will explore the origin of these properties.

Fractional charge

We will employ the plasma analogy again to demonstrate that the quasihole excitations carry a fraction of the charge of the particles forming the FQH liquid. The following calculations are made with the seminal case of a FQH liquid of electrons with charge $q = -e$ in mind, which is especially shocking as one would not think that an object carrying a fraction of the elementary charge can exist. However, the calculations applies as well to FQH liquids formed in synthetic systems like cold atomic gases or interacting photon systems, replacing the electron charge with the corresponding synthetic charge. In the case of a FQH liquid of electrons, the quasihole charge will be $q = +e/m$.

The plasma potential energy for a FQH droplet featuring a quasihole at η reads

$$U(z_i) = -m^2 \sum_{i<j} \log\left(\frac{|z_i - z_j|}{\ell_{\mathrm{B}}}\right) - m \sum_i \log\left(\frac{|z_i - \eta|}{\ell_{\mathrm{B}}}\right) + \frac{m}{4\ell_{\mathrm{B}}^2}\sum_i |z_i|^2. \qquad (6.24)$$

The equation above features an extra term with respect to Eq. (6.17), which can be interpreted as the interaction energy between the plasma particles and an impurity with unitary charge placed at a complex position η. Our physical intuition tells us that the particles of the plasma will try to screen this impurity. We know that each plasma particle carries a charge $q = -m$, and therefore only $1/m$ plasma particles are necessary in order to screen the impurity. Since we know that each plasma particle is in fact an electron of the FQH liquid, we conclude that the quasihole excitations must carry a fraction $1/m$ of the electron charge.

Another heuristic explanation of the fractional charge of the quasihole can be followed by looking at the Laughlin wavefunction for m quasiholes at a position η:

$$\psi_{m-QH}(\eta; z) = \prod_{i=1}^{N}(z_i - \eta)^m \prod_{k<l}(z_k - z_l)^m e^{-\sum_{i=1}^{n}|z_i|^2/4\ell_{\mathrm{B}}^2}. \tag{6.25}$$

In this context η plays the role of a fixed parameter. This implies that the wavefunction above describes the deficit of one electron at η (if it was a dynamical variable, Eq. (6.25) would be equivalent to the original ground state Laughlin wavefunction (6.7) featuring an extra electron at position η). Since m quasiholes produce the deficit of a single electron in the wavefunction, a single quasihole must feature $1/m$-th of the electron charge, i.e. it carries $q = +e/m$.

Fractional statistics

Now we will employ the plasma analogy again in order to demonstrate that quasiholes in the $\nu = 1/m$ Laughlin state are anyons featuring fractional statistics. Let us begin by considering a state of M quasiholes that we denote as $|\eta_1, ..., \eta_M\rangle$. The wavefunction of such a state in the position representation reads

$$\langle z, \bar{z}|\eta_1, ..., \eta_M\rangle = \prod_{j=1}^{M}\prod_{i=1}^{N}(z_i - \eta_j)\prod_{k<l}(z_k - z_l)^m e^{-\sum_{i=1}^{N}|z_i|^2/4\ell_{\mathrm{B}}^2}. \tag{6.26}$$

We now define the normalized $|\psi\rangle$ state as

$$|\psi\rangle = \frac{1}{\sqrt{Z}}|\eta_1, ..., \eta_M\rangle, \tag{6.27}$$

where Z is a normalization factor given by

$$Z = \int \prod_{i=1}^{N} d^2 z_i \exp\left(\sum_{i,j}\log|z_i - \eta_j|^2 + m\sum_{k,l}\log|z_k - z_l|^2 - \frac{1}{2\ell_{\mathrm{B}}^2}\sum_i |z_i|^2\right). \tag{6.28}$$

Remember that in the plasma analogy the normalization factor Z plays the role of the partition function, i.e.

$$Z = \int \prod_{i=1}^{N} d^2 z_i e^{-\beta U(z_i, \eta_j)}, \tag{6.29}$$

so we can write the potential energy for the 2D Coulomb plasma as

$$U(z_k; \eta_i) = -m^2 \sum_{k<l}\log\left(\frac{|z_k - z_l|}{\ell_{\mathrm{B}}}\right) - m\sum_{k,i}\log\left(\frac{|z_k - \eta_i|}{\ell_{\mathrm{B}}}\right) + \frac{m}{4\ell_{\mathrm{B}}^2}\sum_{k=1}^{N}|z_k|^2. \tag{6.30}$$

Nevertheless, if we want our description of the plasma to have a physical meaning, two terms are missing in the equation above: the Coulomb interaction potential between the unitary charged impurities and between them and the background charge. The total potential energy then reads

$$U(z_k; \eta_i) = -m^2 \sum_{k<l}\log\left(\frac{|z_k - z_l|}{\ell_{\mathrm{B}}}\right) - m\sum_{k,i}\log\left(\frac{|z_k - \eta_i|}{\ell_{\mathrm{B}}}\right) - \sum_{i<j}\log\left(\frac{|\eta_i - \eta_j|}{\ell_{\mathrm{B}}}\right)$$

$$+ \frac{m}{4\ell_{\mathrm{B}}^2}\sum_{k=1}^{N}|z_k|^2 + \frac{1}{4\ell_{\mathrm{B}}^2}\sum_{i=1}^{M}|\eta_i|^2. \tag{6.31}$$

This leads to the corrected plasma partition function

$$\int \prod_{i=1}^{N} d^2 z_i e^{-\beta U(z_i;\eta_j)} = \exp\left(-\frac{1}{m}\sum_{i<j}\log|\eta_i - \eta_j|^2 + \frac{1}{2m\ell_{\rm B}^2}\sum_{i=1}^{N}|\eta_i|^2\right)Z, \qquad (6.32)$$

being Z the old partition function given by Eq. (6.29).

At this point we can rely in our physical intuition about the behavior of the 2D Coulomb plasma. We know that the mobile charges (at positions z_i) will rearrange themselves in order to screen the impurities (at positions η_j) so that the presence of the latter will not be noticed at sufficiently large distances. In fact, the electric potential due to a single impurity will follow the exponential law $e^{-r/\lambda}$, where r is the distance and λ is a characteristic length called *Debye screening length*, which can be shown to be proportional to the square root of the ficticious temperature of the plasma (see [30]). This means that impurities will be completely screened at distances much larger than λ. This implies that as long as the distance between any two impurities satisfies $|\eta_i - \eta_j| \gg \lambda$ the corrected partition function should not depend on the impurities' positions η_i. This argument means that the normalization factor Z must take the value

$$Z = C \exp\left(\frac{1}{m}\sum_{i<j}\log|\eta_i - \eta_j|^2 - \frac{1}{2m\ell_{\rm B}^2}\sum_{i=1}^{M}|\eta_i|^2\right), \qquad (6.33)$$

where C is a constant (independent on η_i) that will be irrelevant for our calculations. This demonstrates the power of the plasma analogy: by appealing to our physical intuition about the screening of charges, we arrived at a much more simplified expression for Z (which is valid as long as the distance between the quasihole excitations is sufficiently large). The reader can compare Eqs. (6.29) and (6.33) to get an idea of the level of simplification achieved.

We can now compute the holomorphic and antiholomorphic Berry connections as

$$\mathcal{A}_{\eta_i}(\eta,\bar\eta) = -i\langle\psi|\partial_{\eta_i}|\psi\rangle = -\frac{i}{2}\frac{\partial\log Z}{\partial\eta_i} = -\frac{i}{2m}\sum_{j\neq i}\frac{1}{\eta_i-\eta_j}+, \frac{i\bar\eta_i}{4m\ell_{\rm B}^2} \qquad (6.34)$$

$$\mathcal{A}_{\bar\eta_i}(\eta,\bar\eta) = -i\langle\psi|\partial_{\bar\eta_i}|\psi\rangle = +\frac{i}{2}\frac{\partial\log Z}{\partial\bar\eta_i} = +\frac{i}{2m}\sum_{j\neq i}\frac{1}{\bar\eta_i-\bar\eta_j} - \frac{i\eta_i}{4m\ell_{\rm B}^2}. \qquad (6.35)$$

Remember that these expressions hold only as long as quasiholes do not get too close to each other.

We can use the Berry connection to compute both the fractional charge and statistics of the quasiholes. Let us start with the fractional charge: in order to do it, we shall adiabatically move one of the quasiholes in a closed path C that does not encircle any other quasiholes. This ensures that only the second term in the Berry connection gives a finite contribution

$$\mathcal{A}_{\eta} = \frac{i\bar\eta}{4m\ell_{\rm B}^2}, \quad \mathcal{A}_{\bar\eta} = -\frac{i\eta}{4m\ell_{\rm B}^2}. \qquad (6.36)$$

Once the quasihole completes the roundtrip around the path C the system's wavefunction picks a phase shift γ which corresponds to the Berry phase

$$e^{i\gamma} = \exp\left[-i\oint_C(\mathcal{A}_\eta d\eta + \mathcal{A}_{\bar\eta}d\bar\eta)\right]. \qquad (6.37)$$

Using the results from Eqs. (6.36) we get

$$\gamma = \frac{e\Phi}{m\hbar}, \qquad (6.38)$$

where Φ is the total magnetic flux enclosed by the path C. A closer inspection of the equation above leads to the conclusion that this is the Aharonov-Bohm phase [181] picked up by the quasihole (which, rememeber, is a charged particle moving inside a magnetic field). By comparing with the Aharonov-Bohm phase that an electron (of charge $q = -e$) would acquire, one can conclude that the charge of the quasihole is indeed

$$q = +e/m. \qquad (6.39)$$

We shall now take a look at the fractional statistics of quasiholes. We take again one of the quasiholes, for instance η_1, and move it adiabatically in a closed path C which now encloses another quasihole located at a position η_2. In this case both terms in Eq. (6.36) give a finite contribution to the Berry phase: The second term corresponds once again to the Aharonov-Bohm phase that we employed to ascertain the fractional charge. On the other hand, the Berry phase due to the first term can be expressed as

$$e^{i\gamma} = \exp\left(-\frac{1}{2m} \oint_C \frac{d\eta_1}{\eta_1 - \eta_2} + h.c.\right) = e^{2\pi i/m}, \tag{6.40}$$

and it represents the phase that the system's wavefunction picks when one quasihole encircles another. This implies that the phase that the system picks up upon the exchange of two such objects (which corresponds to a 180° rotation) is

$$e^{i\pi\alpha} = e^{i\pi/m} \quad \rightarrow \quad \alpha = \nu = \frac{1}{m}, \tag{6.41}$$

where we have defined the statistical parameter α in order to get $\alpha = 0$ for bosons and $\alpha = 1$ for fermions. Surprisingly, the statistical parameter for quasiholes is determined by the filling fraction ν of the FQH liquid hosting them. This implies that the charged excitations of the FQH bulk are neither bosonic nor fermionic. Instead, they represent a paradigmatic example of the so-called *anyons*. Nevertheless, in the fully-filled LLL case, we have $m = 1$ and therefore the quasiholes are as fermions, as the hole excitations of a trivial electron gas.

It is instructive to consider an exchange of n quasiholes around another group of n quasiholes. Assuming each group can be considered as a single object, the net statistical parameter will be $\alpha = n^2/m$.

6.5.2 Quasiparticles

Here we briefly comment on the existence of quasiparticles: bulk excitations of the FQH fluid featuring a charge of the same sign than that of the particles forming the Laughlin state, and opposite to their quasihole counterparts. In the case of electronic FQH liquids, quasiparticles have a charge $q = -e/m$. Quasiparticles are also anyons featuring a statistical parameter $\alpha = \nu = 1/m$, just as quasiholes. In spite of displaying the same exotic properties quasiholes do, due to the complexity of their theoretical treatment quasiparticles have not been as profusely studied as the former. The reader should remember from the previous Subsection that in order to insert quasiholes into the FQH droplet we reduced the electron density by including zeros in the wavefunction at the quasiholes' positions. This is done by multiplying the ground state of the system $\psi_{\rm L}$ by a polynomial prefactor of the form $\prod_i(z_i - \eta)$, being η the quasihole position. As a consequence, the relative angular momentum of the electron pairs of the system increases. In the case of the the quasiparticles we need to increase the electron density and reduce the relative angular momentum.

The first idea that can come to our minds is dividing $\psi_{\rm L}$ by a similar polynomial $\prod_i(z_i - \eta)$, but this would introduce singularities and lead to a non-holomorphic wavefunction. It turns out that the most promising candidate for a quasiparticle wavefunction can be obtained by differentiating with respect to z_i:

$$\psi_{\rm QP}(z, \bar\eta) = \left[\prod_{i=1}^N (2\partial_{z_i} - \bar\eta) \prod_{i<j} (z_i - z_j)^M\right] e^{-\sum_{i=1}^N |z_i|^2/4\ell_{\rm B}^2}. \tag{6.42}$$

This quasiparticle wavefunction has nevertheless a great downside with respect to the quasihole one: the derivatives make dealing with it analytically much tougher. For example, one can see that in this case there is no possible analogy between the squared modulus $|\psi_{\rm QP}|^2$ and the Boltzmann factor of a 2D Coulomb plasma.

6.6 All about anyons

In this Section we would like to take a step back and provide a more in-depth description about anyons and fractional statistics. We will also justify the huge interest they are attracting among

researchers of a variety of fields, not only due to their obviously exotic nature, but also because of their technological applications.

As we found in the previous Section, charged bulk excitations of the FQH droplet, namely quasiholes and quasiparticles, display a fraction of the electronic charge and intermediate statistics between bosons and fermions. This is a striking result that shocks our undergraduate textbook knowledge, where the boson-fermion dicotomy for indistinguishable particles seems to have a fundamental origin related to the Pauli exclusion principle and the symmetries of the global wavefunction of a quantum system ψ. Let us consider a couple of indistinguishable particles located at positions $\mathbf{r_1}$ and $\mathbf{r_2}$, respectively. Such a system is described by a wavefunction $\psi(\mathbf{r_1}, \mathbf{r_2})$. If we now move adiabatically the particles in order to interchange their positions, the wavefunction changes to $\psi(\mathbf{r_2}, \mathbf{r_1})$, but the indistinguishibility of the particles implies that the physics cannot depend on the particular position that they take, so at the level of probability densities the wavefunction must satisfy $|\psi(\mathbf{r_1}, \mathbf{r_2})| = |\psi(\mathbf{r_2}, \mathbf{r_1})|$. This leads to the conclusion that both wavefunctions can only differ in a phase, i.e. $\psi(\mathbf{r_2}, \mathbf{r_1}) = e^{i\pi\alpha}\psi(\mathbf{r_1}, \mathbf{r_2})$, where α is the statistical parameter introduced in the previous Section. Upon another adiabatic exchange the system must return to the original state, so $\psi(\mathbf{r_1}, \mathbf{r_2}) = e^{i2\pi\alpha}\psi(\mathbf{r_1}, \mathbf{r_2})$. From this last equation it is obvious that we should get the usual solutions $\alpha = 0$ for bosons and $\alpha = 1$ for fermions. For bosons one has that the wavefunction must be symmetric upong the exchange of two particles, i.e. $\psi(\mathbf{r_2}, \mathbf{r_1}) = +\psi(\mathbf{r_1}, \mathbf{r_2})$. On the other hand, in the case of fermions the wavefunction must be antisymmetric, i.e. $\psi(\mathbf{r_2}, \mathbf{r_1}) = -\psi(\mathbf{r_1}, \mathbf{r_2})$. This result is directly comparable with our calculation of Sec. 6.5.1 in which we took one particle in a closed path around the other, as exchanging both particles twice is equivalent to encircling one particle with the other.

So where is the loophole in this argument? Apparently only two solutions $\alpha = 0, 1$ can satisfy the requirement that the system must end up in the same state after taking one of the particles in a round trip around the other. And indeed everything we have considered up to this point is true in three dimensions, where encircling one particle with another is a topologically equivalent process to not moving the particles at all (i.e. they are homotopic processes). To see this, imagine that one takes the closed path and lifts it continuously above the encircled particle by means of the third dimension, making then the radius of the path tend to zero, as shown in the left panel of Fig. 6.2. From the point of view of topology both processes can be continuously deformed into one another, and therefore they are said to be in the same homotopy class. Thus, in 3D we can equate the initial and final wavefunctions $\psi(\mathbf{r_1}, \mathbf{r_2}) = e^{i2\pi\alpha}\psi(\mathbf{r_1}, \mathbf{r_2})$.

However, when we restrict ourselves to a two-dimensional plane the situation is different because we cannot make use of the third dimension any more. This was first realized in the seminal work of Leinaas and Myrheim [182]. The right panel of Fig. 6.2 shows two closed paths, A and B, performed by one of the particles of the pair. Path A encircles the other particle, while path B does not. In this case, both paths are not topologically equivalent because they cannot be smoothly deformed into one another. Transforming path A into path B, or viceversa, would require us to pierce the second particle. Therefore, in 2D interchanging twice the two particles is not topologically equivalent to not moving the particles at all and we cannot write the condition $\psi(\mathbf{r_1}, \mathbf{r_2}) = e^{i2\pi\alpha}\psi(\mathbf{r_1}, \mathbf{r_2})$ for the wavefunctions before and after the braiding. The double exchange process now leaves the system in a wavefunction $e^{i2\pi\alpha}\psi(\mathbf{r_1}, \mathbf{r_2})$, where the statistical parameter $\alpha \in [0, 2\pi)$ is a continuous variable defined modulo 2π. Thus, for a single exchange we get

$$\psi(\mathbf{r_2}, \mathbf{r_1}) = e^{i\pi\alpha}\psi(\mathbf{r_1}, \mathbf{r_2}), \quad \alpha \in [0, 2\pi). \tag{6.43}$$

In the particular case of FQH liquids described by the Laughlin's wavefunction, as we proved in Sec. 6.5.1, the statistical parameter of the charged bulk excitations is given by the filling fraction, i.e.

$$\alpha = \nu = \frac{1}{m}. \tag{6.44}$$

This kind of particles, whose braiding properties can be described by a phase factor, i.e. by elements of the $U(1)$ group, are labeled as *Abelian anyons*. Its defining property is that they commute, implying that the order in which anyons are interchanged is irrelevant. The existence of particles with intermediate statistics between bosons and fermions is already very exciting.

However, so far we are considering that, for a given spatial distribution of the anyons, only one non-degenerate ground state is available—and things can get even more alluring if we consider that the anyons live in an n-fold degenerate state! This possibility was first explored by [183]. In

that case, it is not sufficient to describe the braiding by an element of the $U(1)$ group, i.e. a phase factor $e^{i\pi\alpha}$. Instead, we need a unitary $n \times n$ matrix M belonging to the $U(n)$ group. We can write the relation between the initial (ψ_i) and final (ψ_f) states of the system upon an exchange of two particles as

$$\psi_f = \sum_i M_{fi}\psi_i \tag{6.45}$$

where the sum $\sum_i$ extends over the whole set of degenerate initial states. Note that there will be a matrix M describing each pair exchange. If the whole set of M matrices commute with each other, then the ground state degeneracy plays a trivial role and such anyons would be Abelian again. Nevertheless, if some matrices do not commute, anyon braiding can lead to nontrivial rotations within the degenerate set of ground states. This means that the final state in which the system ends is determined by the order in which the anyon exchanges are performed. Such fascinating objects are known as *non-Abelian anyons*.

But this is not the only exotic property that these particles can exhibit. Let us now consider what happens when we bring two anyons close together and look at them from far distances, as if they were a single particle. What kind of statistical properties should such an object exhibit? This process is known as *fusion* of anyons (although we warn the reader that it is not related to nuclear fusion or chemical reactions). The fusion of n Abelian anyons with statistical parameter α is trivial and, as we commented in the previous Section, it results in an object with statistical parameter $\alpha_n = n^2\alpha$. However, similarly to what happens when one adds up spins of different particles, there may exist more than a single manner to fuse a pair of non-Abelian anyons. In order to clarify this point we can introduce the concept of *topological charge* of the anyon, which can be thought of as a topological quantum number describing the nature of the considered object. In the Abelian case, the topological charge is identified with the statistical parameter α. On the other hand, for non-Abelian anyons one can have different *fusion channels*, i.e. different fusion possibilities depending on the topological charge of the considered anyons. This is usually denoted by

$$\phi_a \times \phi_b = \sum_c N_{ab}^c \phi_c, \tag{6.46}$$

which represents the fact that whenever $N_{ab}^c \neq 0$, if a couple of anyons with topological charges a and b fuse, one of the possible outcoumes is that the resulting object can be treated as a particle with topological charge c. The matrix N_{ab}^c determines the possible fusion channels. For instance, in the Abelian case we have that $N_{ab}^c = 1$ only for the fusion channel leading to a topological charge $c = \alpha_2 = 4\alpha$.

To add even more complexity to the subject, it can be shown that in FQH phases hosting non-Abelian anyonic excitations the dimension of the full Hilbert space is not given by the sum over the local degrees of freedom carried by the anyons, but it is instead a global property of the FQH liquid [30]. Such a non-local storage of information is a consequence of long-range entanglement [175, 176] arising in the FQH fluid and explains why physicists have a strong motivation to study non-Abelian anyons as a possible candidate for quantum computation, as we will see in the following Subsection.

As reviewed in [168, 30] there exist many non-Abelian theories featuring different fusion rules for the anyons that arise in each of them. For the purpose of giving a familiar example, here we will take a look at the so-called *Ising anyons* that arise in the theory describing the $\nu = 5/2$ FQH liquid. This implies that the LLL as well as the first LL are fully filled, while the second LL is half-filled. The ground state of this topological phase cannot be described by the Laughlin Ansatz, and there is no reason why its quasihole and quasiparticle excitations should follow the Abelian behavior studied in the previous Section. A promising candidate wavefunction to describe the ground state of such a system was proposed in 1991 by Moore and Read [184]. This theory leads to (and experimental observations up to date have been controversial [185, 186]) an anyon model where the particles can take three different topological charges represented by $\mathbb{1}, \sigma, \psi$. The fusion rules are the following:

$$\sigma \times \sigma = \mathbb{1} + \psi, \quad \sigma \times \psi = \sigma, \quad \psi \times \psi = \mathbb{1},$$
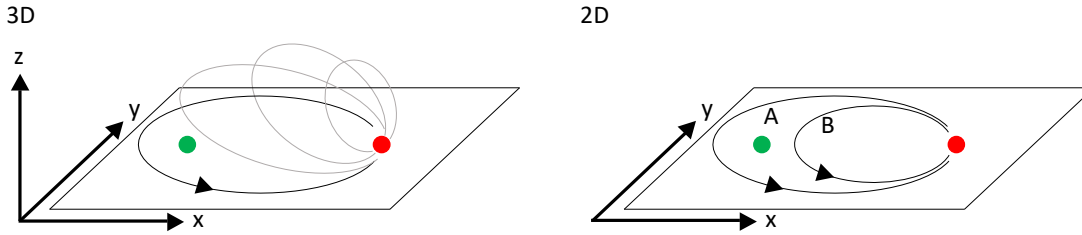$$\mathbb{1} \times x = x \quad \text{for} \quad x = \mathbb{1}, \sigma, \psi. \tag{6.47}$$

Figure 6.2: **Left:** Encircling one particle with another in 3D is topologically equivalent to not moving the particles at all because both paths can be smoothly transformed into one another. **Right:** In 2D, the two paths A and B are no longer topologically equivalent as we would have to pierce one of the particles in order to transform one into the other.

For example, when two σ anyons get close together the output can be either a $\mathbb{1}$ particle or a ψ particle. We can establish an analogy between the fusion rules for Ising anyons and the decomposition rules for tensor products of the $SU(2)$ representations, although taking 1 as the maximum spin.

The interested reader can check that there are plenty of anyon models describing different FQH states. However, an exhaustive review of each of them is far beyond the scope of this Thesis. Among these models, it is worth citing Fibonacci anyons that are supposed to arise in the $\nu = 12/5$ FQH liquid phase and are believed to be described by the Read-Rezayi wavefunction [187, 188]. In the next Subsection we will learn more about this anyon model and we will visit the most promising application of these exotic particles: topological quantum computing.

6.6.1 Topological quantum computing

Non-Abelian anyons are undoubtedly one of the most exotic objects that have arised in the last decades of physics history. At first glance, it may seem that the complexity of their theoretical treatment cannot lead to straightforward applications. However, this changed in 2003 when Kitaev [189] proposed to employ them as the building block of a quite ambitious project: a fault-tolerant topological quantum computer robust under local perturbations. In this Subsection we will not enter into details but instead try to distill the flavor of such a proposal.

Unfortunately, Ising anyons cannot be used for quantum computing as it has been shown that not every quantum logic gate can be constructed by braiding of these anyons [168]. This means that universal quantum computation would be out of reach in such a setup. Nevertheless, the already mentioned Fibonacci anyons do constitute a viable platform for topological quantum computing. This anyon model features two types of particles: the topological vacuum $\mathbb{1}$ and the anyon τ, which follow the fusion rules

$$\tau \times \tau = \mathbb{1} + \tau, \quad \mathbb{1} \times x = x \quad \text{for} \quad x = \mathbb{1}, \tau. \tag{6.48}$$

As shown by [190] each group of three Fibonacci anyons encodes a *qubit* (i.e. the two-level system which is the quantum analog of a classical bit). In this case, there is always a braid (i.e. a set of anyon interchanges) that approximates any single-qubit unitary operation up to arbitrary accuracy. The closer one wants to approximate a particular unitary operation, the longer the braid typically needs to be (i.e. the more anyon interchanges it must include). What is even more important is that also in a two-qubit Hilbert space braids exist that implement any desired two-qubit unitary operation [191]. Of course, braiding particles from different qubits is a necessary condition in order to perform operations on entangled states.

The main advantage of this proposal with respect to non-topological quantum computers is the fault-tolerant character of anyonic qubits and braiding operations. Topological quantum computers are expected to be immune against decoherence, since the anyon subspace is separated by a gap from the rest of the spectrum, and against systematic errors, since braiding does not care about the geometry or dynamics of the particular trajectories followed by the anyon. Because the qubit is stored non-locally in a group of anyons that are separated in space, the only possible errors that can occur in this kind of quantum computer are thermal excitations of anyon pairs in which both of them braid with a pair of qubit anyons. Nevertheless, the probability of this process decreases

exponentially with the inverse temperature and with the distance separating the qubit anyons. This weak point could therefore be under control by keeping our anyons well separated and at a sufficiently low temperature.

Any realistic quantum computer proposal must be able to realize the following three steps: First, we should be able to initialize the system in an arbitrary multi-qubit state. Second, a quantum computer must be able to perform an arbitrary sequence of operations (or logic gates) on the qubits. And finally, we need to measure the output state of the qubits somehow. All these three steps are expected to be performed using a topological quantum computer. The initialization step requires the production of quasiholes or quasiparticles in the FQH liquid. As we will see in Chapter 7, one possibility is to introduce impurities that interact repulsively with the system and thus are able to bind quasihole excitations from the bulk. The quasihole state has actually been shown to be the ground state of the system when it is cooled down in the presence of a repulsive potential [192]. Furthermore, we need to know the kind of particles in our anyon model these excitations belong to. As stated in [168], we can capitalize on the fact that the energies of degenerate fusion channels are split when anyons are brought together in order to measure the initial state of our qubits. Anyons of an unwanted type can then be discarded. Regarding the operations with the qubits, as we have already seen, any quantum logic gate involving one or two qubits can be approximated by a particular set of braiding operations, i.e. by swipping the anyons around each other. Finally, we can employ the same strategy as in the initialization step in order to measure the output state of the qubits.

6.7 Experiments in electronic FQH liquids

In this Section we would like to point out the most relevant experimental works aimed at demonstrating the presence of fractionally charged elementary excitations of anyonic nature in electronic FQH liquids.

Regarding the fractional charge, experiments have conclusively shown evidence of its existence. For instance, Ref. [193] imaged fractionally-charged states localized in the bulk of a two-dimensional electron gas forming a FQH liquid using a scanning single electron transistor. In addition to this, the existence of fractionally charged excitations also on the edges of the FQH droplet was confirmed by shot-noise measurements [194].

However, in contrast to the fractional charge, a clear signature of fractional statistics has long remained elusive. The authors of Ref. [195] employed an interferometric device for electric currents in the quantum Hall regime and observed features consistent with the existence of quasiparticles featuring anyonic statistics. Very recently, the consequences of fractional statistics were observed in a mesoscopic electronic device as a generalized exclusion principle in a current-current correlation measurement at the output of a beamsplitter [196].

As we see, demonstrating the existence of quasiparticles with fractional statistics is still an open problem. In the following Section we will explore the possibility to employ quantum simulators in order to obtain a direct evidence of the anyonic statistics.

6.8 Quantum simulators for the FQH effect

As we have seen in the previous Sections, although FQH liquids are expected to host an extraordinary amount of exotic physics, some of these features still lack a conclusive experimental demonstration. However, in Sec. 6.7 we only discussed experiments in electron gases. Therefore, at this point it is worth asking ourselves whether we can employ more experimentally-friendly platforms in order to access the FQH regime. In Sec. 1.5 we learned that the possibility to employ synthetic systems such as cold atomic gases and quantum fluids of light as quantum simulators is one of the main assets of modern physics, mainly because of the high degree of control one has over such platforms, even allowing to simulate specific Hamiltonians, and the well-established experimental techniques to address the system's properties. This of course poses a complicated challenge. The reader should keep in mind that the exotic physics arising in the FQH effect is a consequence of two ingredients: a magnetic field orthogonal to the plane of motion of the charged particles, and the strong Coulomb interactions between electrons. As we saw in Sec. 1.5, it is possible to design artificial gauge fields for neutral particles such as atoms and photons. Regarding the necessity for strong interactions, photons do not interact between each other in vacuum, and neutral atoms

alone can only display weak van der Waals forces. Nevertheless, as we will see in this Section, several schemes have been proposed to circumvent these apparent barriers and access FQH phases with synthetic platforms. In particular, we will focus on cold atomic gases and photonic systems.

6.8.1 Cold atoms

One of the more powerful tools available for cold atomic gases is the possibility to tune at will the strength of the effective interatomic interactions via the so-called Feshbach resonances [197]. These occur when the energy of a bound molecular state which is not accessible to the atoms approaches that of the accessible scattering state. The magnetic tuning of the energy difference between both states is the most common method in order to achieve a resonant coupling [198].

Although cold atomic gases represent one of the most promising platforms for the study of FQH physics, a convincing experimental realization of such a phase of matter in this system remains elusive to date. In the continuum (i.e. without a periodic potential), the authors of [199] tried for the first time to reach the FQH regime using small clusters of up to ten atoms set into rotation. Nevertheless, the small sample size limited the accuracy of the measurements, arising concerns about the actual Laughlin character of the droplet's ground state.

Regarding optical lattices, the recent work of [200] represents the first step towards the combination of strong interatomic interactions and synthetic magnetic fields in a spatially-periodic potential. The authors realized the interacting version of the Harper-Hofstadter model, in which they were able to demonstrate the chiral motion of pairs of atoms in a ladder-like lattice.

Overall, at the theoretical level different protocols to access the FQH regime are being proposed for both bosonic and fermionic cold atomic gases, both in lattices and continuum geometries [201, 202, 203, 204, 205, 206].

6.8.2 Photonic systems

In the case of photons, the absence of strong interactions is the most difficult challenge we must overcome if we want to access the FQH regime. In material media optical nonlinearities provide the necessary ingredient in order to bring photon-photon interactions to the table. However, we know that disorder in the samples imposes a lower limit in the interaction strength, and this can be a problem if we plan to use a typical Kerr nonlinearity. In order to enhance photon-photon interactions we can instead rely on polaritons, i.e. quasiparticles resulting from the strong coupling between electromagnetic waves and matter excitations which inherit their interaction properties from their matter part [53]. There exist many types of such quasiparticles, from exciton polaritons in semiconductor quantum wells to cavity polaritons formed by confined light coupled to atomic excitations.

This latter type is particularly interesting in order to study the FQH effect with photons in a continuum geometry. In fact, highly-excited Rydberg atoms employed as the matter constituent of cavity polaritons have been shown to provide ultra-strong dipolar interactions due to the blockade effect [207]. The groundbreaking idea of [16] was to combine these Rydberg polaritons with a twisted multimode cavity which induces a photon rotation in each round-trip [84]. Due to the previously explained analogy between rotating reference frames and magnetic fields, this design gives rise to photonic Landau levels. By putting together these two ingredients, Ref. [16] was able to experimentally demonstrate for the first time the formation of a two-photons Laughlin state.

Finally, we will briefly mention that strong photon-photon interactions can also be achieved in the microwave regime using superconducting qubits. Actually, the first experimental study of the interplay between strong photon-photon interactions and a synthetic magnetic field was reported for the three-sites system of [208], which can be thought of as a Bose-Hubbard model [209] where each qubit effectively behaves as a hard-core boson.

6.9 Concluding remarks

In this Chapter we have reviewed the most fundamental properties of fractional quantum Hall (FQH) liquids. Such topological phases of matter appear in two-dimensional systems with broken time-reversal symmetry and strong interactions. Remarkably, they cannot be described by Landau's theory of symmetry breaking, but rather by a global pattern of motion governing the dynamics of the constituent particles known as topological order. The ground state of a FQH

liquid featuring a filling fraction $\nu = 1/m$ —where m is a positive even (odd) integer in the case of bosonic (fermionic) particles— is described by the so-called Laughlin wavefunction. Strangely enough, such systems support bulk excitations featuring fractional charge and statistics. The existence of such objects —known as anyons— is only possible in two dimensions. Remarkably, other FQH liquids whose ground states cannot be described by the Laughlin wavefunction host even more exotic excitations known as non-Abelian anyons, which feature non-commutative braiding relations. These objects have arised a great expectation due to their possible application as qubits in a fault-tolerant topological quantum computer.

In spite of the exciting avenues opened up by the theory of FQH liquids, experiments in 2D electron gases are struggling to reach conclusive evidence of the existence of anyons. However, quantum simulators like cold atomic gases and quantum fluids of light are expected to host analog physics and offer a larger degree of experimental control and highly-developed measurement techniques which are not available for electron gases. Simultaneously to these exciting experimental advances, theorists have started investigating new strategies that harness the advantages of cold atomic gases and photonic systems to probe in an unambiguous way the anyonic nature of the excitations of FQH fluids. On the following we would like to point out some of these schemes (without the purpose of giving an exhaustive list).

A Ramsey-like interferometry scheme to detect the many-body braiding phase arising upon exchange of two anyons was proposed for a cold atom cloud in [210]. A related proposal exploiting the peculiarities of driven-dissipative photonic systems was presented in [211]. Spectroscopical consequences of the Haldane exclusion statistics were pointed out in [212] and soon translated to the photonic context in [213]. A subtle quantitative relation between the density profile of quasiholes (QHs) and their anyonic statistics was theoretically put forward in [214, 215] and numerically confirmed for discrete lattice geometries in [216]. Also, random unitary techniques to measure the many-body Chern number were investigated in [217].

To conclude, motivated by the possibility of exploring FQH liquids in synthetic systems, in Chapter 7 we will propose our own experimental strategy to measure the fractional charge and anyonic statistics in atomic and polaritonic FQH liquids. We expect that repulsively-interacting atomic impurities will bind the quasihole excitations of the FQH droplet, forming composite states that we label *anyonic molecules*. We anticipate that the quantum dynamics of such objects will reveal clear signatures of the fractional charge and statistics. Even though for the sake of concreteness we mainly focus on cold atomic gases, our scheme can be directly translated to quantum fluids of light such as Rydberg polaritons in a twisted optical cavity [16].

Chapter 7

Anyonic molecules in atomic fractional quantum Hall liquids

In this Chapter we study the quantum dynamics of heavy impurities embedded in a strongly interacting two-dimensional gas of lighter particles driven into the fractional quantum Hall (FQH) regime under the effect of a synthetic magnetic field. For suitable values of the impurity-light particle interaction strength, each impurity can capture one or more quasi-hole excitations of the FQH liquid, forming a bound molecular state with novel physical properties. An effective Hamiltonian for such anyonic molecules is derived within the Born-Oppenheimer approximation, which provides renormalized values for their effective mass, charge and statistics by combining the finite mass of the impurity with the fractional charge and statistics of the quasi-holes. The renormalized mass and charge of a single molecule can be extracted from the cyclotron orbit that it describes as a free particle in a magnetic field. The anyonic statistics introduces a statistical phase between the direct and exchange scattering channels of a pair of indistinguishable colliding molecules, and can be measured from the angular position of the interference fringes in the differential scattering cross section. Realistic implementations of such schemes for cold atomic gases are discussed, as well as for photonic systems.

7.1 Introduction

As reviewed in Chapter 6, the discovery of the fractional quantum Hall (FQH) effect in two-dimensional (2D) electron gases under a strong transverse magnetic field [170, 30, 218] changed the paradigm of the boson-fermion dicotomy when the possibility of observing quasi-particles with fractional statistics (and fractional charge) in 2D systems was proposed, the so-called *anyons* [182, 219, 220, 221, 222, 223]. Such exotic quasi-particles have been predicted to arise as emergent excitations of FQH fluids with different properties depending on the fluid density and the applied magnetic field [30]. Although the existence of fractionally charged excitations was experimentally confirmed in two-dimensional electron gases [194, 193], a clear evidence of fractional statistics has long remained elusive [195, 224, 196].

In parallel to these studies in the electronic context of solid-state physics, impressive developments in the experimental study of ultracold atomic gases [57] and quantum fluids of light [53, 225] opened the door to the exploration of strongly interacting topological phases of matter using these highly controllable quantum systems introduced in Chapter 1.

On the one hand, several protocols are available to generate synthetic gauge fields for a 2D gas of ultracold atoms. Conceptually, the most straightforward one relies on the Coriolis force experienced by neutral atoms set into rotation, which formally recovers the Lorentz force felt by charged particles in a magnetic field. Alternative strategies to induce effective Lorentz forces on neutral atoms involve the application of suitable optical and magnetic fields in order to associate a non-trivial Berry phase to the atomic motion and generate a synthetic magnetic field [67, 226]. At

sufficiently low temperatures and for sufficiently strong interactions, the atoms are then expected to turn into a sequence of strongly-correlated FQH liquid states for growing values of the angular speed or of the synthetic magnetic field strength [30, 218, 227]. Pioneering experimental investigations in this direction were reported in [199].

On the other hand, assemblies of photons in nonlinear optical devices are another promising platform to observe FQH physics. In addition to the effective mass (typically induced by the spatial confinement) and the synthetic gauge field, the interactions are provided by the nonlinearity of the medium. As we reviewed in Chapter 6, the realization of a two-particle Laughlin state was presented in [16] using the giant nonlinearity of Rydberg polaritons and the synthetic magnetic field of a twisted optical cavity [84].

Overall, these two platforms have raised great expectations due to the possibility to capitalize on the well-established experimental techniques avaliable in order to conclusively measure the anyonic statistics of the elementary excitations.

In particular, in analogy with polarons arising from the many-body dressing of an impurity immersed in a cloud of quantum degenerate atoms [228, 229, 230], a series of works [231, 232, 233] have anticipated the possibility of using impurity particles immersed in a FQH liquid to capture quasi-hole excitations (that is, flux tubes) and thus generate new anyonic molecules that inherit the fractional statistics of the quasi-hole. Observable consequences of the fractional statistics were pointed out in the fractional angular momentum of the impurities and, correspondingly, in their correlation functions and density profiles [231, 234]. An interferometric scheme to measure fractional charges by binding a mobile impurity to quasi-particles was proposed in [235]. Alternative models where heavy particles may acquire fractional statistics by interacting with phonons in the presence of strong magnetic fields and/or fast rotation were proposed in [236, 237]. The transport properties of impurities embedded in a Fermi gas in a (integer) Chern-insulating state were recently studied in [238]. Spectroscopic signatures of the fractional statistics were also anticipated for the threshold behaviour of the neutron scattering and particle tunneling cross sections of gapped quantum spin liquids and fractional Chern insulators [239].

In the present Chapter, we take inspiration from the aforementioned theoretical works and from the highly developed experimental techniques that are available to address and manipulate single atoms in large atomic gases to theoretically illustrate how such anyonic molecules are a very promising tool to observe fractional statistics and shine new light on the microscopic physics of FQH fluids. On the following we will focus on cold atoms implementations due to the conceptually straightforward experimental techniques available to generate synthetic magnetic fields and strong interactions, as well as the conservative nature of the system. However, all our conclusions directly extend to any other platform where quantum particles are made to experience a synthetic gauge field and strong interparticle interactions, for instance photons in twisted cavity set-ups where Landau levels [84] and Laughlin states [16] have been recently observed.

In particular, we investigate the quantum mechanical motion of a few anyonic molecules. Capitalizing on previous works, we provide a rigorous derivation of the effective Hamiltonian starting from a controlled Born-Oppenheimer (BO) approximation [240, 241] where the positions of the impurities play the role of the slow degrees of freedom and the surrounding FQH fluid provides the fast ones. Whereas bare quasi-holes typically do not support motional degrees of freedom [1], the anyonic molecule is found to display a fully fledged spatial dynamics, with a mass determined by the impurity mass supplemented by a non-trivial correction due to the quasi-hole inertia. Binding to the QH also modifies the effective charge of the impurity by including the Berry phase [243] that the QH accumulates during its motion in space. All together, an anyonic molecule then behaves as a free charged particle in a magnetic field, whose cyclotron radius provides detailed information on the renormalized mass and on the fractional charge.

In the presence of two anyonic molecules, the fractional statistics of the QHs results in a long-range Aharonov-Bohm-like interaction between them. We illustrate the consequences of this long-range topological interaction in the simplest scattering process where two such objects are made to collide. For both hard-disk and dipolar interaction potentials, we calculate the differential scattering cross section for indistinguishable impurities, finding that for large relative momenta it features alternate maxima and minima due to the interference of direct and exchange scattering

---

[1]In the simplest example of a Laughlin state, quasi-holes have a vanishing energy that does not depend on position and do not possess any intrinsic kinetic energy. In a trapped configuration, the position of a quasi-hole evolves in response to the trapping potential according to a first-order differential equation. This dynamics is analogous to the one of vortices in superfluids [242].

channels: analogously to textbook two-slit experiments, the interference pattern rigidly shifts when the statistical phase that the anyonic molecules acquire upon exchange is varied. This interference effect is instead suppressed when distinguishable impurities are considered. Experiments along these lines would therefore allow to confirm the existence of particles beyond the traditional boson-fermion classification and to quantitatively measure the statistics of the QHs in a direct way.

The structure of the Chapter is the following. In Sec. 7.2 we review the system Hamiltonian and in Sec. 7.3 we develop the rigorous Born-Oppenheimer framework that we employ to study the quantum dynamics of the anyonic molecules: In Subsec. 7.3.2 we establish the single particle parameters of the anyonic molecule and in Subsec. 7.3.3 we recover the interaction Hamiltonian between molecules. The theory of two-body scattering is presented in Sec. 7.4, where we summarize our predictions for the angular dependence of the differential scattering cross-section and we highlight the qualitative impact of the fractional statistics. Conclusions are finally drawn in Sec. 7.5.

7.2   The physical system and the model

We consider a system of quantum particles confined to the two-dimensional x-y plane and formed by a small number N of mobile impurities of mass M immersed in a large bath of $n \gg N$ particles of mass m in a FQH state. For simplicity, in what follows the former will be indicated as *impurities*, while the latter will be indicated as *atoms*. A transverse and spatially uniform synthetic magnetic field $\mathbf{B} = B\,\mathbf{u}_z$ is applied to the whole system (where $\mathbf{u}_z$ is the unit vector in the z direction), and we consider that the impurities and the atoms possess effective (synthetic) charges Q and q, respectively.

In the particular case in which the magnetic field is generated by rotating the trap around the z axis, the value of these quantities is set by the atomic masses and the rotation frequency of the trap ω_{rot} via $qB = 2m\omega_{\mathrm{rot}}$ and $QB = 2M\omega_{\mathrm{rot}}$ [66, 226]. In the spirit of Ref. [199], the corresponding centrifugal force can be compensated by harmonic trap potentials acting on each atomic species. Their strength has to be adjusted to give the same trapping frequency $\omega_{\mathrm{hc}} = \omega_{\mathrm{rot}}$ for the two species.

The proposed implementation can be straightforwardly generalized to quantum fluids of light by means of the twisted optical cavity setup of Refs. [84, 16]. In this case Rydberg atoms of two different species giving rise to strongly interacting Rydberg polaritons will play the role of the atoms and the impurities. Keeping this correspondence in mind, the model presented in this Section, as well as the experiments proposed in Secs. 7.3.2 and 7.4, can be directly translated to the optical platform.

In $\hbar = 1$ units, the system Hamiltonian then reads

$$H = T_{\mathrm{a}} + T_{\mathrm{i}} + V_{\mathrm{aa}} + V_{\mathrm{ia}} + V_{\mathrm{ii}} \,, \tag{7.1}$$

where

$$T_{\mathrm{a}}(\{\mathbf{r}_j\}) = \sum_{j=1}^{n} \frac{1}{2m} \left[-i\nabla_{\mathbf{r}_j} - q\mathbf{A}(\mathbf{r}_j) \right]^2 \,, \tag{7.2}$$

$$T_{\mathrm{i}}(\{\mathbf{R}_j\}) = \sum_{j=1}^{N} \frac{1}{2M} \left[-i\nabla_{\mathbf{R}_j} - Q\mathbf{A}(\mathbf{R}_j) \right]^2 \,, \tag{7.3}$$

$$V_{\mathrm{aa}}(\{\mathbf{r}_j\}) = g_{\mathrm{aa}} \sum_{i<j}^{n} \delta(\mathbf{r}_i - \mathbf{r}_j) \,, \tag{7.4}$$

$$V_{\mathrm{ia}}(\{\mathbf{r}_j\}, \{\mathbf{R}_j\}) = \sum_{i=1}^{n} \sum_{j=1}^{N} v_{\mathrm{ia}}(\mathbf{r}_i - \mathbf{R}_j) \,, \tag{7.5}$$

$$V_{\mathrm{ii}}(\{\mathbf{R}_j\}) = \sum_{i<j}^{N} v_{\mathrm{ii}}(\mathbf{R}_i - \mathbf{R}_j) \,. \tag{7.6}$$

We denote by $\mathbf{r}_j$ and $-i\nabla_{\mathbf{r}_j}$ the position and canonical momentum of the j-th atom, while $\mathbf{R}_j$ and $-i\nabla_{\mathbf{R}_j}$ represent those of the j-th impurity. $\mathbf{A}(\mathbf{r}_j) = B(-y_j/2, x_j/2, 0)$ and $\mathbf{A}(\mathbf{R}_j) =$

$B(-Y_j/2, X_j/2, 0)$ are the vector potentials corresponding to the synthetic magnetic field ($\mathbf{B} = \nabla \times \mathbf{A}$) at the positions of atoms and impurities, respectively.

The strength of the contact binary interaction between atoms is quantified by the g_{aa} parameter [2], whereas v_{ia} and v_{ii} denote the impurity-atom and impurity-impurity interaction potentials, respectively. When the synthetic magnetic field is large enough, the number of vortices n_{v} in the atomic fluid becomes comparable with the number n of atoms. At low enough temperatures and for sufficiently strong repulsive atom-atom interactions g_{aa}, the atomic gas enters the so-called FQH regime described by a rational value of the filling fraction $\nu = n/n_{\mathrm{v}}$ [30, 218, 66]. This incompressible state is characterized by excitations with fractional charge and statistics (quasi-holes and quasi-particles).

As it was first anticipated in [231, 232, 233] a repulsive interaction potential v_{ia} between the impurities and the atoms leads to the pinning of quasi-hole excitations at the impurities' positions. As a result, quasi-holes adiabatically follow the motion of the impurity forming composite objects that can be regarded as *anyonic molecules*. By looking at the density pattern of quasi-hole excitations shown in [244, 192], we anticipate that the number of quasi-holes pinned by each impurity can be controlled via the strength of v_{ia}: a stronger and/or longer-ranged interaction will provide space for more quasi-holes bound to each impurity. For the sake of simplicity, in this Chapter we will focus on the case of a single quasi-hole per impurity but generalization to the many quasi-holes case is straightforward.

As a final assumption, we will focus on impurity-impurity potentials v_{ii} of a far larger range than both the atom-atom and impurity-atom interactions and the QH extension. This will allow us to work with impurities that are separated enough in space to give independent and non-overlapping anyonic molecules that interact via the v_{ii} potential with no correction due to the microscopic structure of the quasi-holes. In particular we will focus on interaction potentials with hard-disk or dipolar spatial shapes.

7.3 The Born-Oppenheimer approximation

Several authors have theoretically addressed the quantum mechanics of mobile impurities immersed in FQH fluids and have written effective Hamiltonians for the motion of the resulting charge–flux-tube complexes [231, 232, 233, 235, 238, 236, 237]. Most such treatments were however based on heuristic models of the binding mechanism: while this was sufficient to get an accurate answer for the synthetic charge and the fractional statistics, it did not provide a quantitative prediction for the mass of the anyonic molecule: this is in fact determined by the bare mass of the impurity, supplemented by a correction due to the inertia of the FQH quasi-holes.

To fill this gap, in this Section we will summarize a rigorous approach to this problem. The reader that is already familiar with such effective Hamiltonians and is not interested in the technical details and in the quantitative value of the parameters can jump to the experimental remarks in the final Subsec. 7.3.2 and then move on to the scattering theory in Sec. 7.4.

7.3.1 General framework

Our theoretical description is based on a Born-Oppenheimer formalism in which we treat the impurities' positions as the slowly-varying degrees of freedom, while those of the surrounding atoms play the role of the fast ones [240, 245, 243]. For each position of the impurities, the atoms are assumed to be in their many-body ground state, which contains quasi-holes at the impurities' positions to minimize the repulsive interaction energy. Given the spatial coincidence of the impurity and the quasi-hole, in the following the positions of the resulting molecules will be indicated with the same variables $\mathbf{R}_i$. While our approach is known to be exact for fixed impurities, it extends to moving impurities as long as their kinetic energy is smaller than the energy gap between the quasi-hole state and its first excited state.

Under this approximation, the total wave function can be factorized as

$$\psi(\{\mathbf{r}_i\}, \{\mathbf{R}_i\}, t) = \varphi^{(0)}_{\{\mathbf{R}_i\}}(\{\mathbf{r}_i\}) \, \chi(\{\mathbf{R}_i\}, t) \,, \tag{7.7}$$

---

[2]Choosing a contact interaction potential, we are implicitly focusing on bosonic atomic fluids. Extension to fermionic fluids is straightforward and just requires using a finite-range form of the interaction potential v_{aa} to stabilize the FQH state. All our conclusions hold in this case as well.

where the wave function $\chi(\{\mathbf{R}_i\}, t)$ describes the quantum motion of the impurities and the atomic wave function $\varphi^{(0)}_{\{\mathbf{R}_i\}}(\{\mathbf{r}_i\})$ is the ground state of the Born-Oppenheimer atomic Hamiltonian

$$H_{\mathrm{BO}} = T_{\mathrm{a}} + V_{\mathrm{aa}} + V_{\mathrm{ia}} \tag{7.8}$$

that includes the kinetic and interaction energy of the atoms and the interaction potential between atoms and impurities. In what follows, we will use the shorthands $\mathbf{r}$ and $\mathbf{R}$ to denote the sets of atom coordinates $\{\mathbf{r}_i\}$ and of impurity coordinates $\{\mathbf{R}_i\}$.

In our specific FQH case with $\nu = 1/w$ with positive and integer-valued w, the atomic wave function can be written in terms of the magnetic length $\ell_{\mathrm{B}} = 1/\sqrt{qB}$ and the complex in-plane coordinates $z = x - iy$ of the atoms as a many-quasi-hole wave function of the Laughlin form

$$\varphi^{(0)}_{\mathbf{R}}(\mathbf{r}) = \frac{1}{\sqrt{\mathcal{N}}} \prod_{i=1}^{n} \prod_{j=1}^{N} (z_i - Z_j) \phi_{\mathrm{L}}(\{z_i\}). \tag{7.9}$$

The positions of the quasi-holes are parametrically fixed by the (complex) positions $Z = X - iY$ of the impurities, while the last factor ϕ_{L} is the well-known Laughlin wave function of the FQH state [172],

$$\phi_{\mathrm{L}}(\{z_i\}) = \prod_{i<j}^{n} (z_i - z_j)^{1/\nu} e^{-\sum_{i=1}^{n} |z_i|^2 / 4\ell_{\mathrm{B}}^2} . \tag{7.10}$$

In Eq. (7.9), the normalization constant $\mathcal{N}$ is chosen to ensure the partial normalization condition

$$\int d^{2n}\mathbf{r} \, |\varphi^{(0)}_{\mathbf{R}}(\mathbf{r})|^2 = 1 . \tag{7.11}$$

Provided that the impurities live in the bulk of the atomic cloud far from its edges and from each other, the energy $\epsilon^{(0)}_{\mathrm{BO}}$ of the Born-Oppenheimer ground state is independent of the impurities' positions $\mathbf{R}$ and can be safely neglected.

The dynamics of the anyonic molecules will be governed by an effective Hamiltonian acting on the molecule wave function $\chi(\mathbf{R})$,

$$H_{\mathrm{eff}} = \left\langle \varphi^{(0)}_{\mathbf{R}} \middle| H \middle| \varphi^{(0)}_{\mathbf{R}} \right\rangle , \tag{7.12}$$

which, as we will discuss in full detail in the following subsections, takes a form

$$H_{\mathrm{eff}} = \sum_{j=1}^{N} \frac{\left[-i\nabla_{\mathbf{R}_j} - \mathcal{Q}\mathbf{A}(\mathbf{R}_j) + \mathcal{A}_{\mathrm{stat},j}(\mathbf{R})\right]^2}{2\mathcal{M}} + V_{\mathrm{ii}}(\mathbf{R}) \tag{7.13}$$

that combines the properties of impurities and quasi-holes.

Within this picture, each molecule then features a mass $\mathcal{M}$ –only approximately equal to the one of the impurities, see Sec. 7.3.2– and a total charge $\mathcal{Q} = Q - \nu q$ resulting from the sum of the bare charge Q of the impurity and the one $-\nu q$ of the quasi-hole – see Sec. 7.3.2. These values are of course only accurate as long as the impurities are located in a region of constant density of the atomic cloud, that is, apart from each other in the bulk of an incompressible FQH phase. Under this condition, both the BO energy resulting from the interaction with the atoms $\epsilon^{(0)}_{\mathrm{BO}}$ and the scalar potential arising in the BO approximation give spatially constant energy shifts that can be safely neglected.

In addition to these single-particle properties, the molecules inherit the interaction potential $V_{\mathrm{ii}}(\mathbf{R})$ between the impurities and experience a Berry connection $\mathcal{A}_{\mathrm{stat},j}(\mathbf{R})$ that now depends on the position of all molecules and encodes their quantum statistics. For the Abelian FQH states under investigation here, we will see in Sec. 7.3.3 that the effect of the Berry connection $\mathcal{A}_{\mathrm{stat},j}$ can be summarized by a single statistical parameter determined by the filling ν of the FQH atomic fluid, which indicates that the statistical phase picked upon exchange of two molecules is $\exp(i\pi\nu)$. If more $N_{\mathrm{qh}} > 1$ quasi-holes were pinned to the same impurity, the statistical phase would grow quadratically as $N^2_{\mathrm{qh}}\nu$ [30].

Finally, note that we are restricting our attention to anyonic molecules that are separated enough in space for their internal structure not to be distorted by the interactions with the neighboring molecules. This is expected to be an accurate approximation if the inter-impurity distance

is much larger than the range of the atom-impurity potential and the internal size of the quasi-hole –typically of the order of the magnetic length ℓ_B [30]. Under this approximation, the values of the renormalized mass and of the synthetic charge that we obtain for single molecules directly translate to the many-molecule case, and the interaction potential reduces to the inter-impurity one v_{ii} with no corrections from the microscopic structure of the molecules.

7.3.2 Effective Hamiltonian for a single anyonic molecule

In this subsection we will investigate the parameters in the effective Hamiltonian (7.13) that control the single-particle physics of the molecules, namely the renormalized mass $\mathcal{M}$ and charge $\mathcal{Q}$. A simple experimental configuration to extract these values will also be proposed at the end of the subsection.

Mass renormalization

A crucial, yet often disregarded feature of the BO approximation is the renormalization of the effective mass of the slow degrees of freedom. In molecular physics such a renormalization affects the effective mass of the nuclei dressed by the electrons and is essential to guarantee consistency of the description [241, 243]. In our case it concerns the change of the effective mass of the impurity when this is dressed by the quasi-hole excitation in the surrounding FQH fluid. As far as we know, this feature was always overlooked in previous literature, even though it may give a quantitatively significant bias to observable quantities such as the effective magnetic length considered in [231].

In order to obtain a quantitative estimate for the effective mass $\mathcal{M}$, we generalize the molecular physics approach of Ref. [241] by including the synthetic magnetic field in the formalism (see Appendix D). As it is discussed in detail in Ref. [241], one needs to include the first perturbative correction to the BO adiabatic approximation, which amounts to taking into account the distortion of the quasi-hole profile due to the motion of the impurity. To this purpose we expand $\varphi_{\mathbf{R}}(\mathbf{r}, t) \simeq \varphi_{\mathbf{R}}^{(0)}(\mathbf{r}) + \varphi_{\mathbf{R}}^{(1)}(\mathbf{r}, t)$, where the BO wave function $\varphi_{\mathbf{R}}^{(0)}(\mathbf{r})$ is obtained as the ground state of the Hamiltonian (7.8) in the presence of a single impurity at $\mathbf{R}$ and has the quasi-hole form (7.9) with $N = 1$. While $\varphi_{\mathbf{R}}^{(0)}(\mathbf{r})$ only depends on the coordinate difference $\mathbf{r} - \mathbf{R}$, the first order perturbative correction $\varphi_{\mathbf{R}}^{(1)}(\mathbf{r}, t)$ depends on the impurity speed.

Following the theory of Ref. [241], the mass tensor of the molecule is then given at first order by

$$\underline{\underline{\mathcal{M}}} = \underline{\underline{M}} + \Delta \underline{\underline{M}} , \qquad (7.14)$$

where $\underline{\underline{M}}$ is the 2×2 unity matrix multiplied by the bare impurity mass and the correction is such that the corresponding kinetic energy

$$\frac{1}{2} \Delta M_{\alpha\beta} v_\alpha v_\beta = \int d\mathbf{r} \, \varphi_{\mathbf{R}}^{(1)*}(\mathbf{r}, t) \left[H_{\mathrm{BO}} - \epsilon_{\mathrm{BO}}^{(0)}(\mathbf{R}) \right] \varphi_{\mathbf{R}}^{(1)}(\mathbf{r}, t) \qquad (7.15)$$

recovers the increase in the BO energy due to the motion of the impurity.

The correction $\varphi_{\mathbf{R}}^{(1)}(\mathbf{r}, t)$ to the atomic wave function is obtained at the lowest perturbative level in the impurity speed $\underline{v} = (v_{\mathrm{X}}, v_{\mathrm{Y}})$ by applying the inverse of the fast Hamiltonian

$$\left[H_{\mathrm{BO}} - \epsilon_{\mathrm{BO}}^{(0)} \right] \varphi_{\mathbf{R}}^{(1)}(\mathbf{r}, t) = v_\alpha \, \nabla_\alpha \varphi_{\mathbf{R}}^{(0)}(\mathbf{r}) \qquad (7.16)$$

to the gradient of the atomic wave function with respect to the in-plane coordinates of the impurity $\alpha = \{X, Y\}$. In physical terms, this correction is such that the action of the fast BO Hamiltonian H_{BO} recovers the temporal evolution of the BO wave function $\varphi_{\mathbf{R}(t)}(\mathbf{r})$ due to the spatial displacement of the impurity.

In our Laughlin case, it is easy to show that the gradient of the atomic wave function with respect to $\mathbf{R}$ is proportional to the wavefunction of the lowest excited state of H_{BO},

$$\nabla_{\mathbf{R}} \varphi_{\mathbf{R}}^{(0)}(\mathbf{r}) = \frac{\tau}{\ell_B} \varphi_{\mathbf{R}}^{(e)}(\mathbf{r}) . \qquad (7.17)$$

This excited state corresponds to a chiral $\Delta L = -1$ oscillation of the quasi-hole around the impurity [3] and, for the simplest case of a single impurity located at $Z = 0$, its wavefunction

---

[3]In the case of many quasi-holes bound to a strong impurity potential, such an excitation mode can be viewed as the $\Delta L = -1$ chiral mode of the inner edge of the ring-shaped FQH fluid surrounding the impurity [192].

(normalized as in (7.11)) has the form

$$\varphi_{\mathbf{R}}^{(e)}(\mathbf{r}) = \frac{1}{\sqrt{\mathcal{N}^{(e)}}} \sum_{i_o=1}^{n} \prod_{\substack{i=1 \\ i \neq i_o}}^{n} z_i \, \phi_{\mathrm{L}}(\{z_i\}) \,. \tag{7.18}$$

While these results are enough to establish that the correction to the mass tensor is diagonal in the X, Y coordinates, a quantitative estimation of its magnitude needs microscopic insight on the overlap numerical factor τ and on the energy $\Delta\omega_{-1}$ of the excited state under consideration. This requires a few technical steps that are summarized on the following.

- τ FACTOR. We start by denoting $\left|\varphi_Z^{(0)}\right\rangle$ the quantum state of the atomic fluid with one quasi-hole at the position $\mathbf{R}$ corresponding to the complex variable $Z = X - iY$. We then expand the Z-dependent state vector around $Z = 0$ as

$$\left|\varphi_Z^{(0)}\right\rangle = \left|\varphi_{Z=0}^{(0)}\right\rangle + Z\left(\partial_Z\left|\varphi_Z^{(0)}\right\rangle\right) + Z^*\left(\partial_{Z^*}\left|\varphi_Z^{(0)}\right\rangle\right) + \frac{Z^2}{2}\left(\partial_Z^2\left|\varphi_Z^{(0)}\right\rangle\right) + \frac{Z^{*2}}{2}\left(\partial_{Z^*}^2\left|\varphi_Z^{(0)}\right\rangle\right)$$
$$+ |Z|^2\left(\partial_Z\partial_{Z^*}\left|\varphi_Z^{(0)}\right\rangle\right) + \mathcal{O}(Z^3) \,.$$

where all derivatives are evaluated at $Z = 0$.

We consider the atomic density operator $\hat{n}(r)$ evaluated at position r, indicated by the complex variable z. Taking advantage of the fact that

$$\hat{n}(z = Z)\left|\varphi_Z^{(0)}\right\rangle = 0 \,, \tag{7.19}$$

$$\left(\partial_{Z^*}\left|\varphi_Z^{(0)}\right\rangle\right)_{Z=0} = 0 \,, \tag{7.20}$$

$$\partial_Z\left|\varphi_Z^{(0)}\right\rangle = \frac{\tau}{\ell_B}\left|\varphi_Z^{(e)}\right\rangle \,, \tag{7.21}$$

we get that

$$\left\langle\varphi_Z^{(0)}\right|\hat{n}(z=0)\left|\varphi_Z^{(0)}\right\rangle \simeq |Z|^2\left(\partial_{Z^*}\left\langle\varphi_Z^{(0)}\right|\right)\hat{n}(z=0)\left(\partial_Z\left|\varphi_Z^{(0)}\right\rangle\right) =$$
$$= |Z|^2\frac{\tau^2}{\ell_{\mathrm{B}}^2}\left\langle\varphi_Z^{(e)}\right|\hat{n}(z=0)\left|(\varphi_Z^{(e)}\right\rangle \,. \tag{7.22}$$

For a quasi-hole living in the bulk of the FQH droplet we can take advantage of the local homogeneity of the atomic fluid to write

$$\left\langle\varphi_{Z=0}^{(0)}\right|\hat{n}(z)\left|\varphi_{Z=0}^{(0)}\right\rangle = \left\langle\varphi_{Z=z}^{(0)}\right|\hat{n}(z=0)\left|\varphi_{Z=z}^{(0)}\right\rangle \simeq |z|^2\frac{\tau^2}{\ell_{\mathrm{B}}^2}\left\langle\varphi_Z^{(e)}\right|\hat{n}(z=0)\left|\varphi_Z^{(e)}\right\rangle =$$
$$= |z|^2\frac{\tau^2}{\ell_{\mathrm{B}}^2}\left\langle\varphi_{Z=0}^{(e)}\right|\hat{n}(z)\left|\varphi_{Z=0}^{(e)}\right\rangle \,. \tag{7.23}$$

This expression relates the value of τ to the (normalized) radial density distribution $n_0(r)$ of the ground state $\varphi_{\mathbf{R}}^{(0)}$ and the distribution $n_e(r)$ in the first excited $\varphi_{\mathbf{R}}^{(e)}$ state. These two distributions can be numerically calculated using the expansion of $\varphi_{\mathbf{R}}^{(0)}$ and $\varphi_{\mathbf{R}}^{(e)}$ in terms of Jack polynomials developed in Ref. [192]. The results for a mesoscopic cloud of $n = 10$ particles are displayed in Fig. 7.1 and we have made sure that our results for the inner part of the profile are converged with respect to the number of particles n. In particular, we see in the figure that $n_0(\ell_{\mathrm{B}}/2) \simeq 0.028/\ell_{\mathrm{B}}^2$, while $n_e(0) \simeq 0.245/\ell_{\mathrm{B}}^2$. Substituting these values into Eq. (7.25) one obtains $\tau \simeq 0.7$.

- EXCITATION ENERGY $\Delta\omega_{-1}$ AND IMPURITY-ATOM INTERACTION. We now offer quantitative evidence of the binding of impurities to FQH quasi-holes in the presence of a repulsive interaction between the impurity and the atoms, and its relation with the energy gap $\Delta\omega_{-1}$ between the ground state and the first excited state.

To this purpose, we calculate the dependence of the energy difference between the ground state $\varphi^{(0)}$ displaying a quasi-hole located at the impurity's position (taken as the origin, i.e.
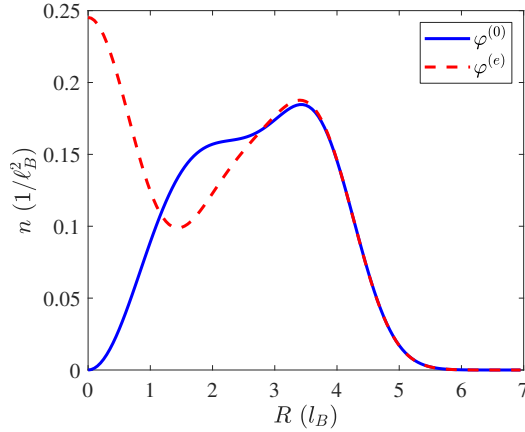
Figure 7.1: Density of the ground state $\varphi^{(0)}$ and the first excited state $\varphi^{(e)}$ as function of the distance to the quasi-hole located at $R = 0$ in the $\varphi^{(0)}$ case. Both curves were calculated for $n = 10$ particles in the FQH bath and are converged with respect to n.

$\mathbf{R} = 0$) and the lowest excited state $\varphi^{(e)}$ with the quasi-hole orbiting around the impurity with $\Delta L = -1$ with respect to the impurity-atom interaction. For simplicity, we employ a step-like interaction potential between the impurity and the atoms of the FQH fluid of the form

$$V_{\mathrm{ia}} = \bar{v}_{\mathrm{ia}} \sum_{i=1}^{n} \Theta(a - |\mathbf{r}_i|) \, , \tag{7.24}$$

where n is the number of atoms, $\bar{v}_{\mathrm{ia}} > 0$ and a is the step radius.

We first compute the states of interest using a Jack polynomials expansion [192] and then calculate the expectation values of the atom-impurity potentials in the ground and lowest excited states for different values of the step radius a. We have checked that the density profiles of the relevant many-body states in the vicinity of the impurity (i.e. for distances $\leq a$) do not depend on the total number n of atoms in the FQH state.

The expectation values in the ground state and in the lowest excited state for several values of a are shown in Fig. 7.2 as blue squares and red circles, respectively. While the ground state is almost insensitive to the presence of the impurity as long as the radius a of the interaction potential is much smaller than the spatial extension of the density depletion of the quasi-hole (on the order of the magnetic length ℓ_{B}, as shown by the blue curve in Fig. 7.1), the density in the excited state always has a significant overlap with the impurity (as shown in the red curve in Fig. 7.1), which gives a sizable energy shift of this state that grows quadratically with a and has a finite limit in the contact limit $a \to 0$ at a constant $\bar{v}_{\mathrm{ia}} a^2$.

The significant resulting energy gap $\Delta\omega_{-1}$ between the two states leads then to an efficient binding of the QH to the impurity. As the step radius or the potential strength are increased, its magnitude increases, thus reinforcing the rigidity of the impurity-quasihole molecule and, as we will see in the following lines, reducing the importance of the Born-Oppenheimer mass correction ΔM.

Quantitatively, the excitation energy $\Delta\omega_{-1}$ is at most on the order of a fraction of the bulk many-body gap above the fractional quantum Hall state, namely a fraction of the atom-atom interaction energy scale $V_0 = g_{\mathrm{aa}}/2\ell_{\mathrm{B}}^2$ [192]. Note also that the many-body gap can not exceed the cyclotron energy associated to the synthetic magnetic field acting on the atoms, $\omega_{\mathrm{cycl}} = 1/m\ell_B^2 = qB/m$.

The previous results can be plugged into Eq. (7.15), giving a mass correction

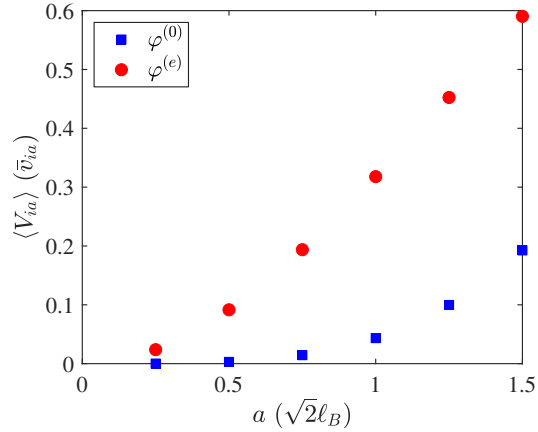$$\Delta M = \frac{2\tau^2}{\Delta\omega_{-1}\ell_{\mathrm{B}}^2} \, , \tag{7.25}$$

Figure 7.2: Expectation value of the step-like interaction between impurities and atoms V_{ia} in the ground state $\varphi^{(0)}$ (blue squares) and in the lowest excited state $\varphi^{(e)}$ (red circles) in units of $\bar{v}_{ia}$ as a function of its step radius a (in units of ℓ_{B}).

which, since $2\tau^2 \simeq 1$, provides the figure of merit

$$\frac{\Delta M}{M} \simeq \frac{m}{M} \frac{\omega_{\mathrm{cycl}}}{\Delta\omega_{-1}} \tag{7.26}$$

that can be used to quantify its relative importance.

For instance, a small m/M ratio can be obtained in a cold atoms experiment embedding heavy atoms like Erbium as impurities in a gas of light atoms such as Lithium. This already gives $m/M \simeq 0.04$ and can be further decreased replacing the heavy atom with a multi-atom molecule [246]. On the other hand, the $\Delta\omega_{-1}/\omega_{\mathrm{cycl}}$ factor is typically bound to values below unity, but can be maximized using strong (perhaps Feshbach-enhanced [197]) interactions among atoms and between atoms and impurities, so to push the many-body gap towards the cyclotron energy. All together, it is natural to expect that the correction to the effective impurity mass may be sizable and important to interpret the experimental observations.

Synthetic charge

As in the previous subsection, we consider the simplest situation in which a single quasi-hole is bound to a single impurity located at position $\mathbf{R}$. In this case the effective Hamiltonian (7.12) takes the form

$$H_{\mathrm{eff}} = \frac{[-i\nabla_{\mathbf{R}} - Q\mathbf{A}(\mathbf{R}) + \mathcal{A}(\mathbf{R})]^2}{2\mathcal{M}} + \Phi(\mathbf{R}) + \epsilon_{\mathrm{BO}}^{(0)}(\mathbf{R}) \,, \tag{7.27}$$

where

$$\mathcal{A}(\mathbf{R}) = -i \left\langle \varphi_{\mathbf{R}}^{(0)}(\mathbf{r}) \middle| \nabla_{\mathbf{R}} \middle| \varphi_{\mathbf{R}}^{(0)}(\mathbf{r}) \right\rangle \tag{7.28}$$

is the Berry connection related to the quasi-hole motion across the FQH fluid, which enters the equation above in the form of an effective vector potential [245, 243].

For the Laughlin states under consideration here, the Berry connection $\mathcal{A}(\mathbf{R})$ can be calculated making use of the plasma analogy [30] as reviewed in Chapter 6. This gives

$$\mathcal{A}(\mathbf{R}) = \frac{q\nu}{2\ell_{\mathrm{B}}^2} \mathbf{u}_{\mathrm{z}} \times \mathbf{R} = -\nu q \mathbf{A}(\mathbf{R}) \,, \tag{7.29}$$

which means that the QH feels the synthetic magnetic field as a fractional charge $-\nu q$ corresponding to the atomic density that has been displaced away from its surroundings. As a result, the effective single-molecule Hamiltonian can be recast in a compact form

$$H_{\mathrm{eff}} = \frac{\left[-i\nabla_{\mathbf{R}} - (Q - \nu q)\,\mathbf{A}(\mathbf{R})\right]^2}{2\mathcal{M}} \tag{7.30}$$

in terms of an effective charge

$$\mathcal{Q} = Q - \nu q \tag{7.31}$$

resulting from the sum of the bare charge Q of the impurity and the fractional charge $-\nu q$ of the quasi-hole that is bound to it.

The effective scalar potential is instead equal to

$$\Phi(\mathbf{R}) = \frac{-1}{2\mathcal{M}} \left[\left\langle \varphi_{\mathbf{R}}^{(0)}(\mathbf{r}) \right| \nabla_{\mathbf{R}}^2 \left| \varphi_{\mathbf{R}}^{(0)}(\mathbf{r}) \right\rangle + \mathcal{A}^2(\mathbf{R}) \right] : \tag{7.32}$$

as long as the impurity lives in the bulk of the (incompressible) FQH fluid where the fluid density is –to a high precision– constant, both the BO energy $\epsilon_{\mathrm{B}0}^{(0)}$ and the scalar potential are constant and can be safely neglected.

In order to facilitate the description of the two-body scattering process and isolate the features of interest, it will be beneficial to design an experiment where the effective charge $\mathcal{Q}$ of the anyonic molecules vanishes. From Eq. (7.31) one sees that if the gauge field is generated by rotation the $\mathcal{Q} = 0$ condition translates in a ratio $M/m = \nu$ between the masses of both atomic species, which is not straightforwardly compatible with the assumptions underlying the BO approximation. On the other hand, a careful design of the optical and magnetic fields applied to the atoms allows to tune the strength of the synthetic magnetic field acting on each of them, so to satisfy the required $\mathcal{Q} = 0$ condition.

As an alternative strategy, even though the $\mathcal{Q} = 0$ condition is not naturally fulfilled in the laboratory reference frame, the effect of the finite $\mathcal{Q}$ can be removed by looking at the system from a reference frame that rotates around the z axis at an angular frequency $\tilde{\Omega}$ such that

$$\tilde{\Omega} = -\frac{\mathcal{Q}\,\mathbf{B}}{2\mathcal{M}}. \tag{7.33}$$

Under this condition, the Coriolis force associated to the rotation is equal and opposite to the effective synthetic Lorentz force acting on the anyonic molecule. Inserting a value of the impurity mass on the order of the one of a heavy (e.g. Erbium) atom and a synthetic magnetic field on the order of $\mathcal{Q}\mathbf{B} \sim 1/\lambda^2$ with λ in the optical range $\lambda \sim 1\,\mu\mathrm{m}$, one finds a value for $\tilde{\Omega}$ in an accessible $100\,\mathrm{Hz}$ range.

But one must not forget that moving to the rotating frame not only introduces a Coriolis force, but also transforms the velocity appearing in the synthetic magnetic Lorentz force, which results in an additional force to be added to usual centrifugal force of rotating reference frames. In the system under consideration here, all such centrifugal/centripetal forces can be compensated in the rotating frame by introducing an additional anti-harmonic trapping potential $V_{\mathrm{i}}(\mathbf{R}) = -\frac{1}{2}\mathcal{M}\tilde{\Omega}^2\mathbf{R}^2$ acting on each impurity. Combining all different terms, the dynamics of isolated anyonic molecules in the rotating reference frame is then the desired one of free particles moving along straight lines [4] for which the scattering process will be the simplest.

Before concluding, it is worth stressing that the rotation at $\tilde{\Omega}$ considered here is just a way of looking at the effective dynamics of the anyonic molecules, and does not affect the underlying atoms that form a FQH state in the laboratory frame in the presence of the synthetic magnetic field [5].

Experimental remarks

Since the Hamiltonian (7.30) describes a free particle in a magnetic field, we can envisage a simple experiment to measure the fractional charge and the renormalized mass of the molecule from the radius of its cyclotron orbit, as sketched in Fig. 7.3. Once the molecule receives a momentum kick $\mathbf{p}$ (e.g. by applying a time-dependent force to the impurity), it starts describing a cyclotron orbit. For a given value of the momentum kick, the molecule mass $\mathcal{M}$ can be directly obtained from the

---

[4]The need for an unusual anti-trapping potential can be physically understood since we wish to transform localized cyclotron orbits into open straight lines going to infinity.

[5]The situation is of course slightly more complex if a rotating atomic gas is used to generate the FQH state. In this case the two rotations and the two contributions to the centrifugal potential must be carefully combined. Note also that, thanks to the R_{rel}^{-2} dependence of the two-body term in the Berry connection (7.39), the rotation at $\tilde{\Omega}$ has no effect on this latter term. Writing the Lagrangian associated to the Hamiltonian (7.38), transformation of the two-body term to the rotating frame only provides an additional constant term.
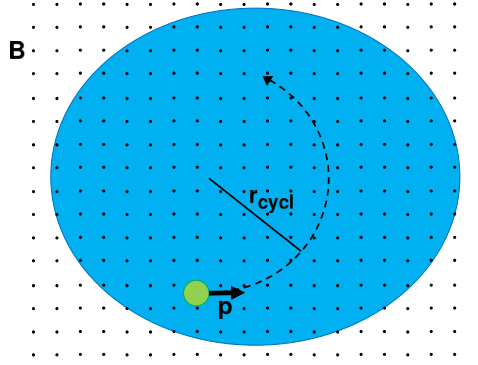
Figure 7.3: *Proposed experiment to measure the renormalized mass and the fractional charge of an anyonic molecule.* An impurity atom (green circle) is located in the bulk of a fractional quantum Hall fluid of atoms (blue region). Its repulsive interactions with the atoms make it bind one or more FQH quasi-holes, forming a composite *anyonic molecule* with renormalized mass $\mathcal{M}$, fractional (synthetic) charge $\mathcal{Q}$, and anyonic fractional statistics. To measure the renormalized mass and charge, one can impart a momentum kick $\mathbf{p}$ to a single such molecule initially at rest and follow the ensuing cyclotron motion.

actual speed via $\mathbf{p} = \mathcal{M}\mathbf{v}$. The charge is then extracted from the cyclotron radius via the textbook formula

$$ r_{\text{cycl}} = \frac{\mathcal{M}v}{\mathcal{Q}B}. \tag{7.34} $$

In order to determine the fractional charge, it is useful to consider the ratio $\mathcal{Q}/Q$ which is obtained by comparing the cyclotron radius for a molecule immersed in the FQH fluid with the one of the bare impurity in the absence of the surrounding FQH fluid. The relation (7.31) allows then to relate the observed charge $\mathcal{Q}$ to the fractional charge of the quasi-holes in the FQH fluid. If the synthetic magnetic field is generated by rotating the system, its calibration is made even simpler by the fact that the product qB (QB) is determined by the rotation speed ω_{rot} via $qB = 2m\omega_{\text{rot}}$ $(QB = 2M\omega_{\text{rot}})$ [226, 227].

Taking advantage of the different nature of the impurity particle as compared to the atoms forming the FQH fluid, reconstruction of the trajectory of the anyonic molecule can be done by imaging the position of the impurity at different evolution times after its deterministic preparation at a given location with a known momentum imparted, e.g. by an external potential. In this respect, we can expect that using impurities with a large mass offers the further advantage of a more accurate definition of the initial position and velocity against Heisenberg indetermination principle.

This issue can be put in quantitative terms by comparing the maximum kinetic energy of the molecule compatible with the BO approximation, with the cyclotron energy of the molecule in the synthetic magnetic field which quantifies its zero-point motion: in order for the cyclotron motion to be visible, several Landau levels must in fact be populated. The maximum kinetic energy can be estimated from $K_{\text{max}} = \mathcal{M}v_{\text{max}}^2/2$ using the velocity v_{max} at which the norm of the first-order correction $\varphi_{\mathbf{R}}^{(1)}$ in (7.16) becomes of order one, namely

$$ v_{\text{max}} = \frac{\Delta\omega_{-1}\,\ell_B}{\tau}\,. \tag{7.35} $$

The cyclotron energy is given by the usual formula using the effective charge $\mathcal{Q}$ of the molecule, namely $\Omega_{\text{cycl}} = \mathcal{Q}B/\mathcal{M}$. Imposing $K_{\text{max}} \gg \Omega_{\text{cycl}}$ then requires

$$ \sqrt{\frac{2\tau^2\mathcal{Q}}{q}}\,\frac{m}{\mathcal{M}}\,\frac{\omega_{\text{cycl}}}{\Delta\omega_{-1}} \ll 1 \tag{7.36} $$

which, recalling that $2\tau^2 \simeq 1$, is related to the condition (7.26) for a small mass correction and is well satisfied if the impurity mass is large enough.

In order for the anyonic molecule to behave as a rigid object and avoid its internal excitation and its dissociation, one must impose that the cyclotron frequency Ω_{cycl} is smaller than its lowest excitation mode at $\Delta\omega_{-1}$. This imposes a similar condition

$$\frac{\mathcal{Q}}{q}\frac{m}{\mathcal{M}}\frac{\omega_{\text{cycl}}}{\Delta\omega_{-1}} \ll 1 \tag{7.37}$$

that, again, is well satisfied in the heavy impurity limit. But it is also important to note that forming the bound impurity–quasi-hole state may be itself a non-trivial task since quasi-holes are associated to a global rotation of the FQH fluid. In [192, 216], it was shown that the quasi-hole state naturally forms when the atomic fluid is cooled to its ground state in the presence of the impurity provided that the atoms are able to exchange angular momentum with the external world. Alternatively, a quasi-hole can be created by inserting a localized flux through the cloud, and then introducing the impurity particle at its location [247, 248]. Finally, a speculative strategy yet to be fully explored may consist of inserting the impurity into the FQH fluid through its edge: provided the impurity's motion is slow enough, one can reasonably expect that it will be energetically favourable for the impurity to capture a quasi-hole from the edge and bring it along into the bulk of the FQH cloud.

Besides these technical difficulties, we anticipate that our proposed experiment for the measurement of the fractional charge will have great conceptual advantages over the shot noise measurements of electronic currents that were first used to detect charge fractionalization [194]. These experiments involve in fact complex mechanisms for charge transport and charge injection/extraction into/from the edge of the electron gas. On the other hand, we foresee that our proposed experiment has the potential to provide a direct and unambiguous characterization of the fractional charge of the quasi-hole excitations in the bulk of a fractional quantum Hall fluid.

7.3.3 Effective Hamiltonian for two anyonic molecules

After completing the calculation of the single-particle parameters $\mathcal{M}$ and $\mathcal{Q}$, we can now move on to the many-particle case. The two molecule case is already of particular interest as it allows to obtain information about the fractional statistics of the anyonic molecules. In the following we will focus on this case and we will leave the complexities of the three- and more-particle cases [223] to future investigations.

As already stated, we assume that the two impurities are located in the bulk of the FQH cloud, far apart from the edges and they are well separated by a distance much larger than the magnetic length. The effective molecule Hamiltonian is now given by

$$H_{\text{eff}} = \sum_{j=1}^{2}\frac{[-i\nabla_{\mathbf{R}_j} - Q\mathbf{A}(\mathbf{R}_j) + \mathcal{A}_j(\mathbf{R})]^2}{2\mathcal{M}}$$
$$+ \Phi(\mathbf{R}) + \epsilon_{\text{BO}}^{(0)}(\mathbf{R}) + V_{\text{ii}}(\mathbf{R})\,, \tag{7.38}$$

where $\mathbf{R}$ is again a shorthand for the whole set of impurity positions, $\{\mathbf{R}_k\}$. The Berry connection experienced by the j-th particle now contains two terms,

$$\mathcal{A}_j(\mathbf{R}) = \mathcal{A}_{\text{q}}(\mathbf{R}_j) + \mathcal{A}_{\text{stat},j}(\mathbf{R})$$
$$= \frac{\mathcal{B}_{\text{q}}}{2}\mathbf{u}_{\text{z}} \times \mathbf{R}_j + (-1)^j\frac{\nu}{R_{\text{rel}}^2}\mathbf{u}_{\text{z}} \times \mathbf{R}_{\text{rel}}\,. \tag{7.39}$$

The former term $\mathcal{A}_{\text{q}}$ is of single-particle nature and only depends on the position of the specific particle. Its Berry curvature $\mathcal{B}_{\text{q}} = \nu/\ell_{\text{B}}^2$ accounts for the synthetic magnetic field felt by each quasi-hole via their fractional charge $-\nu q$, as discussed in the previous section. The latter term $\mathcal{A}_{\text{stat}}$ has a two-body nature and depends on the relative position of the two impurities, $\mathbf{R}_{\text{rel}} = (X_{\text{rel}}, Y_{\text{rel}}) = \mathbf{R}_1 - \mathbf{R}_2$: each impurity experiences the vector potential corresponding to ν quanta of magnetic flux spatially localized on the other impurity. Since $\nabla \times \mathcal{A}_{\text{stat},j} = 0$, there is no Berry curvature involved in the interaction between spatially separated impurities and the effect can be viewed as an Aharonov-Bohm-like interaction [181].

Since the impurities are assumed to be located in the bulk of the FQH cloud and to be spatially separated to avoid any overlap, the Born-Oppenheimer energy $\epsilon_{\text{BO}}^{(0)}$ does not depend on the

positions and can be neglected [6]. The two-body generalization of the scalar potential Φ in (7.32) involves derivatives of the Laughlin wavefunction with respect to the impurity positions [7]. As it was discussed around (7.16), such derivatives only involve localized excitations in the atomic fluid around the quasi-hole. On this basis, for sufficiently separated impurities, we can safely approximate the two-body scalar potential with a relative-coordinate-independent energy shift that can be safely neglected in what follows.

Grouping the single-particle Berry connection due to the effective charge of each quasi-hole with the synthetic magnetic field directly felt by each impurity as done in the previous section, we can write the Hamiltonian in the compact form

$$
H_{\text{eff}} = \sum_{j=1}^{2} \frac{[-i\nabla_{\mathbf{R}_j} - \mathcal{Q}\mathbf{A}(\mathbf{R}_j) + \mathcal{A}_{\text{stat},j}(\mathbf{R})]^2}{2\mathcal{M}} \\
+ V_{\text{ii}}(\mathbf{R}) ,
\tag{7.40}
$$

in terms of the effective charge $\mathcal{Q} = Q - \nu q$ of each molecule. According to this Hamiltonian, the molecules interact via the interaction potential V_{ii} between the bare impurities and via the Aharonov-Bohm interaction encoded by the two-body vector potential $\mathcal{A}_{\text{stat},j}$ that depends on the relative position $\mathbf{R}_1 - \mathbf{R}_2$ between the two molecules.

Given the translational invariance of the configuration, we can separate the center of mass and the relative motion of the two molecules. Assuming a central impurity-impurity interaction $V_{\text{ii}}(\mathbf{R}_i - \mathbf{R}_j) = V_{\text{ii}}(R_{\text{rel}})$, we define the reduced and the total mass as usual as

$$
\mathcal{M}_{\text{rel}} = \mathcal{M}/2 , \quad \mathcal{M}_{\text{CM}} = 2\mathcal{M} ,
\tag{7.41}
$$

the relative and center of mass position

$$
\mathbf{R}_{\text{rel}} = \mathbf{R}_1 - \mathbf{R}_2 ,
\tag{7.42}
$$

$$
\mathbf{R}_{\text{CM}} = \frac{\mathbf{R}_1 + \mathbf{R}_2}{2} ,
\tag{7.43}
$$

the corresponding momenta

$$
\mathbf{P}_{\text{rel}} = \frac{\mathbf{P}_1 - \mathbf{P}_2}{2} ,
\tag{7.44}
$$

$$
\mathbf{P}_{\text{CM}} = \mathbf{P}_1 + \mathbf{P}_2 ,
\tag{7.45}
$$

and vector potentials

$$
\mathbf{A}_{\text{rel}}(\mathbf{R}_{\text{rel}}) = \frac{\mathcal{Q}}{2}\mathbf{A}(\mathbf{R}_{\text{rel}}) + \frac{\mathcal{A}_{\text{stat},1}(\mathbf{R}_1) - \mathcal{A}_{\text{stat},2}(\mathbf{R}_2)}{2} =
$$

$$
= \frac{\mathcal{Q}}{2}\mathbf{A}(\mathbf{R}_{\text{rel}}) + \frac{\nu}{R_{\text{rel}}^2}(-Y_{\text{rel}}, X_{\text{rel}}) ,
\tag{7.46}
$$

$$
\mathbf{A}_{\text{CM}}(\mathbf{R}_{\text{CM}}) = 2\mathcal{Q}\,\mathbf{A}(\mathbf{R}_{\text{CM}}) ,
\tag{7.47}
$$

to be included in the center of mass and relative Hamiltonians

$$
H_{\text{CM}} = \frac{[\mathbf{P}_{\text{CM}} - \mathbf{A}_{\text{CM}}(\mathbf{R}_{\text{CM}})]^2}{2\mathcal{M}_{\text{CM}}} ,
\tag{7.48}
$$

$$
H_{\text{rel}} = \frac{[\mathbf{P}_{\text{rel}} + \mathbf{A}_{\text{rel}}(\mathbf{R}_{\text{rel}})]^2}{2\mathcal{M}_{\text{rel}}} + V_{\text{ii}}(R_{\text{rel}}) .
\tag{7.49}
$$

The center of mass Hamiltonian (7.48) describes a free particle motion of total mass $2\mathcal{M}$ and charge $2\mathcal{Q}$. On the other hand, the relative Hamiltonian (7.49) contains the uniform magnetic field experienced by the reduced charge $\mathcal{Q}/2$ plus a non-trivial vector potential corresponding to ν quanta of magnetic flux localized at $R_{\text{rel}} = 0$.

---

[6]In the plasma analogy [30], this is easily understood in terms of the screening of the impurities by the charges which leads to a free energy independent of the impurity's positions.

[7]The analytic form (7.32) of the scalar potential only involves the projection of the derivative on orthogonal excited states. As required by gauge invariance, the contribution along the ground state cancels with the vector potential term.
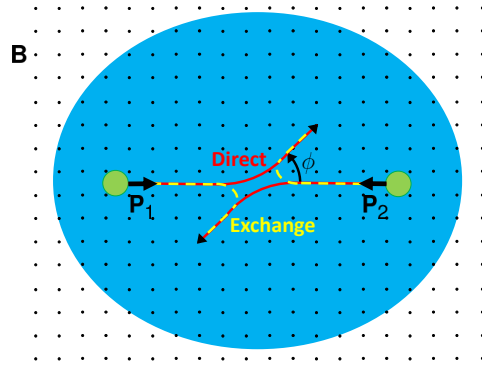

Figure 7.4: *Scattering of two anyonic molecules.* Similarly to Fig. 7.3, two indistinguishable anyonic molecules (green circles) formed by the binding of the same number of quasi-holes to a pair of identical impurities in the bulk of a FQH fluid (blue region) are considered. The two molecules are given momentum kicks against each other ($\mathbf{P}_1$ and $\mathbf{P}_2$, respectively). Due to their indistinguishability, two scattering channels contribute to the differential scattering cross section at an angle ϕ, see Eq. (7.68): the two channels are labelled as *direct* (red, solid trajectories) and *exchange* (yellow, dashed ones) and involve a relative phase determined by the anyonic statistics. As one can guess from textbook two-slit interference, information about the statistics can be extracted from the global position of the interference fringe pattern. This is illustrated in the next figures.

As it was discussed in the seminal works [182, 219, 220, 221, 222, 223], the presence of this latter vector potential is the key feature that encodes the fractional statistics of the anyonic molecules. In the following of this Chapter, we will study the effect of this vector potential onto the scattering cross section of two molecules. This is a measurable quantity that can serve as a probe of the statistical parameter of the molecules.

Depending on the bosonic vs. fermionic nature of the impurities, the effective Hamiltonian (7.40) will act on the Hilbert space of symmetric or anti-symmetric wavefunctions under the exchange of the two molecules, that is $\mathbf{R}_1 \leftrightarrow \mathbf{R}_2$ (or $\mathbf{R}_{\mathrm{rel}} \leftrightarrow -\mathbf{R}_{\mathrm{rel}}$). The combination of the intrinsic statistics of the impurities and the one inherited by the quasi holes can be encoded in the single statistical parameter $\alpha = \alpha_{\mathrm{i}} + \nu$, where the intrinsic contribution is $\alpha_{\mathrm{i}} = 0$ ($\alpha_{\mathrm{i}} = 1$) for bosonic (fermionic) impurities. In the next section, we will see how the scattering properties only depend on α and not on α_{i} and ν separately.

7.4 Scattering of anyonic molecules and fractional statistics

In the previous Section, we have summarized the conceptual framework to study the quantum mechanical motion and the interactions of anyonic molecules. Based on this complete and flexible framework, we can now attack the core subject of this Chapter, namely the observable consequences of the fractional statistics. As a simplest and most exciting example, we consider the differential cross section for the scattering of two anyonic molecules and, in particular, we will highlight a simple relation between the angular position of its maxima and minima and the fractional statistics.

To simplify our discussion, from now on we assume that the process underlying the synthetic magnetic field is designed in a way to have a vanishing effective charge $\mathcal{Q} = 0$ of the molecule. This condition is beneficial to have rectilinear trajectories in the asymptotic states of the scattering molecules. The only vector potential remaining in Eq. (7.40) will then be the Aharonov-Bohm interaction $\mathcal{A}_{\mathrm{rel}}$, which simplifies enormously the study of the scattering process.

A scheme of the proposed experimental strategy can be found in Fig. 7.4. If one prepares a pair of identical molecules inside the bulk of the FQH droplet, each one composed of the same kind of impurity and a bound quasi-hole excitation, and then makes them to collide, e.g. by pushing them against each other via a suitable external potential, the angular dependence of the differential scattering cross section will show a pattern of maxima and minima whose angular position can be directly related to the fractional statistics of the molecules, as we will show in Sec. 7.4.4.

7.4.1   General scattering theory

In order to study the two-molecule scattering we focus on the relative Hamiltonian (7.49) in 2D cylindrical coordinates and we consider the time-independent Schrödinger equation

$$
\left[\frac{\partial^2}{\partial r^2} + \frac{1}{r}\frac{\partial}{\partial r} + \frac{1}{r^2}\left(\frac{\partial}{\partial \phi} - i\nu \right)^2 - 2\mu V_{\mathrm{ii}}(r) + k^2 \right] \psi(r,\phi)
$$
$$
= 0 \, ,
$$
(7.50)

where $k^2 = 2\mu E$ is related to the energy E of the scattering process. For the sake of notational simplicity we use the shorthand r, μ in place of $R_{\mathrm{rel}}, \mathcal{M}_{\mathrm{rel}}$. Eq. (7.50) represents the scattering of a particle of mass μ by a flux tube of radius $r_0 \to 0$ giving a vector potential $\mathbf{A}_{\mathrm{rel}} = \nu \mathbf{u}_\phi / r$ that incorporates the fractional statistics ($\mathbf{u}_\phi$ is a unit vector in the ϕ coordinate). For a short-range potential (i.e. such that $rV_{\mathrm{ii}}(r) \to 0$ when $r \to \infty$) the solution far from the origin can be written as the sum of an incoming plane wave [8] and an outgoing cylindrical wave [251, 252]

$$
\psi(\mathbf{r}) = e^{i\mathbf{k}\cdot\mathbf{r}} + f(k,\phi)\frac{e^{ikr}}{\sqrt{r}} \, ,
$$
(7.51)

where $f(k,\phi)$ is the scattering amplitude.

   We will solve Eq. (7.50) using the method of partial waves. Given the cylindrical symmetry of the problem, we can look for factorized solutions $\psi(r,\phi) = e^{im\phi} u_{m,\nu}(r)/\sqrt{r}$ of angular momentum m with a radial function satisfying

$$
\frac{d^2 u_{m,\nu}}{dr^2} + \frac{u_{m,\nu}(r)}{4r^2} - \frac{(m-\nu)^2}{r^2} u_{m,\nu}(r)
$$
$$
- 2\mu V_{\mathrm{ii}}(r) u_{m,\nu}(r) + k^2 u_{m,\nu}(r) = 0 \, .
$$
(7.52)

In contrast to usual scattering problems, for any non-integer value of ν the centrifugal barrier is present here for all values of m. This guarantees that the wave function vanishes for $r = 0$ when the two particles overlap [223].

   The general solution of Eq. (7.52) in the free case $V_{\mathrm{ii}} = 0$ with $\nu = 0$ has the form

$$
u_m(r) \propto \sqrt{r}\, J_m(kr) \, ,
$$
(7.53)

in terms of the cylindrical Bessel function $J_m(kr)$. In the $r \to \infty$ limit the expression above tends to

$$
u_m(r) = \sqrt{\frac{2}{\pi k}}\cos\left(kr - m\frac{\pi}{2} - \frac{\pi}{4} \right) .
$$
(7.54)

For any short-range potential V_{ii} the solution of Eq. (7.52) in the $r \to \infty$ limit can be written with respect to the asymptotic form of the free solution (7.54) as

$$
u_{m,\nu}(r) = A_{m,\nu}(k)\cos\left[kr + \delta_{m,\nu}(k) - m\frac{\pi}{2} - \frac{\pi}{4} \right] \, ,
$$
(7.55)

where $\delta_{m,\nu}$ are the phase shifts.

   As usual, the scattering amplitude in Eq. (7.51) can be related to the phase shifts $\delta_{m,\nu}(k)$ of this asymptotic expansion: using the fact that the cylindrical harmonics are a complete basis and replacing all cylindrical Bessel functions with their asymptotic form at $r \to \infty$, we can write the

---

[8]It has been argued that in order to have a constant incoming current density one should have an incoming plane wave of the form $e^{i\mathbf{k}\cdot\mathbf{r}}e^{i\nu\phi}$ with a non-trivial angular dependence of the phase. Nevertheless, the only consequence of the absence of the phase factor is the appearance in $f(k,\phi)$ of a δ-function addend in the forward direction, namely around $\phi = 0$ [249]. Moreover, as $r \to \infty$ the incorrect incoming current density calculated with the plane wave in Eq. (7.51) tends to the correct, constant value that one would obtain if the factor $e^{i\nu\phi}$ was correctly included [250]. On this basis, in what follows we will for simplicity ignore both the correction to the incoming plane wave and the forward δ-function whose absence leads to.

wavefunction in Eq. (7.51) as:

$$\psi(\mathbf{r}) = \left[\sum_{m=-\infty}^{+\infty} i^m \sqrt{\frac{2}{\pi k r}} \cos\left(kr - m\frac{\pi}{2} - \frac{\pi}{4}\right) e^{im\phi} \right]$$

$$+ \left[\sum_{m=-\infty}^{\infty} a_{m,\nu}(k) e^{im\phi} \right] \frac{e^{ikr}}{\sqrt{r}} \tag{7.56}$$

$$= \sum_{m=-\infty}^{+\infty} A_{m,\nu}(k) \cos\left[kr + \delta_{m,\nu}(k) - m\frac{\pi}{2} - \frac{\pi}{4}\right] \frac{e^{im\phi}}{\sqrt{r}} ,$$

with

$$A_{m,\nu}(k) = \sqrt{\frac{2}{\pi k}} i^m e^{i\delta_{m,\nu}(k)} , \tag{7.57}$$

from which it is easy to obtain an expression of the scattering amplitude in terms of the phase shifts

$$f(k, \phi) = \sum_{m=-\infty}^{\infty} a_{m,\nu}(k) e^{im\phi} , \tag{7.58}$$

with

$$a_{m,\nu}(k) = \sqrt{\frac{2i}{\pi k}} e^{i\delta_{m,\nu}(k)} \sin\delta_{m,\nu}(k) . \tag{7.59}$$

7.4.2   A general result for short-range potentials

For a non-vanishing and non-integer ν the free solution of Eq. (7.52) changes to

$$u_{m,\nu}(r) \propto \sqrt{r}\, J_{|m-\nu|}(kr) , \tag{7.60}$$

which approaches

$$u_{m,\nu}(r) = C\sqrt{\frac{2}{\pi k}} \cos\left[kr - |m-\nu|\frac{\pi}{2} - \frac{\pi}{4}\right] \tag{7.61}$$

in the $r \to \infty$ limit.

For any short-range potential V_{ii}, the total phase shift in the cosine $\cos(kr + \Delta)$ in the asymptotic limit $r \to \infty$ can be referred to the fully free case with $V_{\mathrm{ii}} = 0$ and $\nu = 0$ [as done for $\delta_{m,\nu}(k)$ in Eq. (7.55)] or to the non-interacting case $V_{\mathrm{ii}} = 0$ with $\nu \neq 0$ considered in (7.61). These two choices give

$$\Delta = \delta_{m,\nu}(k) - m\frac{\pi}{2} - \frac{\pi}{4} , \tag{7.62}$$

$$\Delta = \Delta^V_{m,\nu} - |m-\nu|\frac{\pi}{2} - \frac{\pi}{4} , \tag{7.63}$$

respectively, where $\Delta^V_{m,\nu}$ is the phase shift exclusively due to the intermolecular potential V_{ii}. Combining these equations we obtain

$$\delta_{m,\nu}(k) = m\frac{\pi}{2} - |m-\nu|\frac{\pi}{2} + \Delta^V_{m,\nu}(k) , \tag{7.64}$$

where the total phase shift $\delta_{m,\nu}(k)$ is decomposed as the sum of the phase shift due to the topological flux attached to the impurities plus the one $\Delta^V_{m,\nu}(k)$ due to the interaction potential. In the non-interacting $V_{\mathrm{ii}} = 0$ case, this yields the same result as calculated in the original work by Aharonov and Bohm [181].

In the general case, assuming $0 < \nu < 1$, we can combine Eqs. (7.59) and (7.64) and decompose

the scattering amplitude as

$$f(k,\phi) = f_{\text{AB}}(k,\phi) + f_{\text{V}}(k,\phi) =$$

$$= \frac{1}{\sqrt{2\pi i k}} \left\{ \left[\sum_{m=1}^{\infty} e^{im\phi} \left(e^{i\pi\nu} - 1 \right) \right. \right.$$

$$+ \sum_{m=-\infty}^{0} e^{im\phi} \left(e^{-i\pi\nu} - 1 \right) \left] + \right.$$

$$+ \left[e^{i\pi\nu} \sum_{m=1}^{\infty} e^{im\phi} \left(e^{2i\Delta_{m,\nu}^{\text{V}}} - 1 \right) + \right.$$

$$\left. \left. + e^{-i\pi\nu} \sum_{m=-\infty}^{0} e^{im\phi} \left(e^{2i\Delta_{m,\nu}^{\text{V}}} - 1 \right) \right] \right\}. \quad (7.65)$$

The terms on the first two lines are geometric series that can be analytically summed up to $m = \infty$. They give the Aharonov-Bohm contribution to the scattering amplitude [181]

$$f_{\text{AB}}(k,\phi) = \sum_{m=-\infty}^{+\infty} a_{m,\nu}^{(\text{AB})}(k) e^{im\phi} = -\frac{\sin(\pi\nu)}{\sqrt{2\pi i k}} \frac{e^{i\phi/2}}{\sin\frac{\phi}{2}}, \quad (7.66)$$

and carry all information on the particle statistics. The terms on the third and fourth line summarize instead the contribution $f_{\text{V}}(k,\phi)$ of the interaction potential V_{ii} to the scattering amplitude. These terms must be evaluated by numerically summing the series.

This decomposition is of crucial technical importance as it enables to isolate the Aharonov-Bohm contribution f_{AB} that can be analytically computed, and restrict the numerical calculation to the potential contribution f_{V} only, for which convergence on the high angular-momentum side is straightforward. This is however much more than just a mathematical trick, since it tells us about the different physical nature of the two contributions to the scattering amplitude. The statistical part of the scattering amplitude f_{AB} originates from a vector potential $\mathcal{A}_{\text{rel}}$ that extends to infinity. As a result, it affects all angular momentum components. Its divergent behaviour for $\phi \to 0$ can be physically related to the step-like jump of the geometric phase that is accumulated when passing in the close vicinity of $r = 0$ on opposite sides. On the other hand, for a short-range interaction potential, the particles only see each other up to a certain distance, and therefore one only needs to sum up to a finite number of partial waves to achieve convergence in f_{V}.

7.4.3 Distinguishable and indistinguishable impurities

For distinguishable impurities, the differential scattering cross section is calculated directly from the scattering amplitude as

$$\frac{d\sigma_{\text{D}}}{d\phi} = |f(k,\phi)|^2. \quad (7.67)$$

Nevertheless, the scattering process is most interesting when the impurities are indistinguishable particles. In this case, the differential scattering cross section involves a sum over exchange processes according to

$$\frac{d\sigma_{\text{B,F}}}{d\phi} = |f(k,\phi) \pm f(k,\phi+\pi)|^2, \quad (7.68)$$

and may thus allow for interesting interference features in the angular dependence. As usual, the $\pm$ signs here correspond to bosonic and fermionic impurities, respectively. Indistinguishability guarantees that the cross section has the same value for ϕ and $\phi + \pi$.

Repeating the same calculation leading to (7.65) in the $1 < \nu < 2$ case and noting that $\Delta_{m,\nu}^{\text{V}}$ is a function of $m - \nu$ only, one can show that

$$f_{1+\nu}(k,\phi) = -e^{i\phi} f_{\nu}(k,\phi) \quad (7.69)$$

holds for any $0 < \nu < 1$. It is then immediate to deduce that the scattering cross sections in the bosonic and fermionic cases are related by [9]

$$\frac{d\sigma_{\mathrm{B},1+\nu}}{d\phi}(\phi) = \frac{d\sigma_{\mathrm{F},\nu}}{d\phi}(\phi) \ . \tag{7.70}$$

Noting the scattering cross sections are periodic of period 2 in ν, one can thus summarize the statistics into a single statistical parameter α, defined as $\alpha = \alpha_{\mathrm{i}} + \nu$ with $\alpha_{\mathrm{i}} = 0$ ($\alpha_{\mathrm{i}} = 1$) for bosonic (fermionic) impurities, which fully determines the scattering properties as a general scattering cross section $d\sigma_\alpha/d\phi$.

A similar reasoning leads to the interesting relation

$$f_{1-\nu}(k,\phi) = -e^{i\phi} f_\nu(k,-\phi) \ , \tag{7.71}$$

from which one extracts the symmetry relation

$$\frac{d\sigma_{\mathrm{B},\nu}}{d\phi}(\pi - \phi) = \frac{d\sigma_{\mathrm{F},1-\nu}}{d\phi}(\phi) \ , \tag{7.72}$$

that translates into the compact form

$$\frac{d\sigma_\alpha}{d\phi}(\pi - \phi) = \frac{d\sigma_{2-\alpha}}{d\phi}(\phi) \ . \tag{7.73}$$

7.4.4   Numerical results for the differential scattering cross section

The key feature of the Aharonov-Bohm contribution (7.66) to the scattering amplitude in the absence of interaction potential V_{ii} is a divergent behaviour in the forward direction for any non-integer ν. This was traced back by Ref. [253] to the infinite-range nature of the Aharonov-Bohm interaction and is known to pose mathematical difficulties related to the optical theorem. In the following of this Chapter, we are going to focus on the scattering at finite angles ϕ where such problems do not arise.

The situation gets much more interesting when the interaction potential V_{ii} is included. This introduces a more complex angular dependence of the scattering amplitude $f_V(k,\phi)$ and clear features in the differential scattering cross section. Keeping an eye on possible experimental realizations of this work we choose a dipolar form of the repulsive interaction potential [254], $V_{\mathrm{ii}} = b/r^3$, for which a dipolar length can be defined as $a_{\mathrm{D}} = \mu b$. As we shall see better in Sec. 7.4.5, this specific choice of the interaction potential is motivated by the extremely strong dipolar potentials that can be obtained using heteronuclear molecules. As an additional check, we have also calculated the differential scattering cross section for the case of a hard-wall potential of radius a_{HD},

$$V(r) = \begin{cases} \infty & if \quad r \leq a_{\mathrm{HD}} \\ 0 & if \quad r > a_{\mathrm{HD}} \end{cases} \ , \tag{7.74}$$

for which we can benchmark our predictions against the semi-analytical results available in Ref. [255].

In order to calculate the differential cross section $d\sigma/d\phi$ in the different cases, we have to first calculate the phase shift $\delta_{m,\nu}(k)$ by solving the radial Schrödinger equation Eq. (7.52) in the presence of the interaction potential V_{ii} and the vector potential $\mathbf{A}_{\mathrm{rel}}$. This was done numerically, employing Numerov's method [256], which gives a global error of order $\mathcal{O}(h^4)$, being $h = r_{i+1} - r_i$ the numerical step size in the r coordinate. Identifying the interaction contribution $\Delta_{m,\nu}^V$ to the phase shift, one can separate the different terms in Eq. (7.65): the first two lines are analytically computed giving f_{AB} of Eq. (7.66). The interaction-induced amplitude f_V is evaluated by numerically performing the sum in the last two lines up to large values of m until convergence is reached. The desired differential cross section $d\sigma/d\phi$ is finally obtained by summing the resulting f_V to the analytically computed f_{AB} and plugging the outcome into Eq. (7.68).

Figs. 7.5 and 7.6 show the differential scattering cross section as function of the scattering angle ϕ for a hard-disk and a dipolar interaction between bosonic impurities, respectively. The filling

---

[9]Extending our theory to the $\nu = 1$ integer quantum Hall (IQH) regime, the relation (7.70) has the direct physical interpretation that a boson immersed in the IQH transmutes into a fermion upon binding a quasi-hole, which in this case corresponds to one missing particle in the underlying IQH fluid.

---

fraction of the FQH bath is fixed in both cases to $\nu = 0.5$, while the different solid curves represent different values of the relative incident momentum $ka_{\mathrm{HD,D}}$ for indistinguishable impurities. The qualitative behavior of $d\sigma/d\phi$ is identical for the two potentials: for small momenta ($ka_{\mathrm{HD,D}} \ll 1$) the only effect of the fractional statistics beyond the divergences in $\phi = 0, \pi$ is the slight breaking of the $\phi \leftrightarrow \pi - \phi$ symmetry (or, equivalently, of the $\phi \leftrightarrow -\phi$ symmetry), so that the minimum of the curve is displaced to angles larger than $\phi = \pi/2$, as was first found in Ref. [255]. For larger momenta $ka_{\mathrm{HD,D}} \gtrsim 1$, the peaks around $\phi = 0, \pi$ persist, and marked oscillations appear in the angular dependence because of interference effects, with a strong suppression of the differential scattering cross section occurring at some particular angles $\phi_{\min}$.

This oscillating behavior is reached for smaller $ka_{\mathrm{HD,D}}$ in the case of hard-disk interactions. For $ka_{\mathrm{HD}} = 5$ (the largest value of the momentum considered here) four periods of oscillations are clearly visible. For dipolar interactions, a larger value of ka_{D} is required to develop a comparable oscillating pattern. For instance for $ka_{\mathrm{D}} = 5$, the curve only shows a single oscillation period between $\phi = 0$ and π An oscillating behaviour is however recovered for far larger momenta, for instance the curve for $ka_{\mathrm{D}} = 50$ features four well-developed minima.

This seeming difference can be reconciled by drawing a qualitative analogy with the textbook double slit experiment where, for a fixed incident wavevector, the larger the separation between the slits, the smaller the angular separation between the fringes observed in the screen. In our case, the role of the slit separation is played by the effective radius of the repulsive potential: in the hard-disk case the wavefunction is restricted to the outer $r > a_{\mathrm{HD}}$ region, setting the effective radius to $\bar{r}_{\mathrm{HD}} = a_{\mathrm{HD}}$. For the smoother dipolar potential the wavefunction has a finite tail in the inner region, but we can estimate the radius as the inversion point $\bar{r}_{\mathrm{D}}$ at which the kinetic energy equals the the dipolar potential, i.e. the distance at which

$$\frac{k^2}{2m} = \frac{a_{\mathrm{D}}}{m\bar{r}_{\mathrm{D}}^3} \ . \tag{7.75}$$

One can expect that the differential cross section for the two potentials should display oscillations of comparable period if the two effective radii are equal $\bar{r}_{\mathrm{D}} = \bar{r}_{\mathrm{HD}}$. This implies that the incident momenta are related by

$$2ka_{\mathrm{D}} = (ka_{\mathrm{HD}})^3 : \tag{7.76}$$

the different powers appearing on either side of this equation explain why a much larger ka_{D} is needed to recover a $ka_{\mathrm{HD}} > 1$ oscillatory pattern. Quite remarkably, this relation is approximately satisfied by the pair $ka_{D} = 50$ and $ka_{HD} = 5$: by comparing the solid cyan lines in Figs. 7.5 and 7.6, one sees that the oscillations of these curves indeed have a very similar angular period. The same reasoning on the effective radii $\bar{r}_{\mathrm{HD,D}}$ suggests that the angular period of the oscillations should scale as $(ka_{\mathrm{HD}})^{-1}$ and $(ka_{\mathrm{D}})^{-1/3}$, respectively. We can hint at such a dependence in the plots of Figs. 7.5 and 7.6.

A quantitative confirmation of this scaling law is provided in Fig. 7.7. Here we compare the angular dependence of the differential scattering cross section for the hard-disk (left panel) and dipolar (central panel) cases for several parameter choices that pairwise satisfy the relation Eq. (7.76) between the incident wavevectors. As expected, the oscillation periods are almost identical within each pair (represented by the same color in Fig. 7.7). As a further illustration, panel c) demonstrates the linear dependence of the oscillation period with respect to $(ka_{\mathrm{HD}})^{-1}$ and $(2ka_{\mathrm{D}})^{-1/3}$ in each case, which confirms our intuitive interpretation in terms of the textbook double slit experiment.

To better highlight the role of indistinguishability in determining the differential cross section, Figs. 7.5 and 7.6 also show, as dashed curves, the angular dependence of the differential scattering cross section for distinguishable impurities. In this case, a single scattering channel contributes to the scattering cross section in each direction so the oscillating behaviour is absent and the differential cross section has a rather flat and featureless angular dependence.

The small oscillations that are visible in the vicinity of the forward scattering direction $\phi = 0, 2\pi$ for the hard-disk case are due to diffraction effects from the sharp edges of the potential and do not have a statistical origin, as they are visible also for $\alpha = 0$, as we explicitly demonstrate in Fig. 7.8. This Figure shows the angular dependence of the differential scattering cross section for distinguishable bosons ($\alpha = 0$; black curve) and for distinguishable anyonic molecules with $\alpha = 0.1$ (dark blue curve) and $\alpha = 0.5$ (cyan curve) interacting via a hard-disk potential for a fixed relative incident momentum $ka_{\mathrm{HD}} = 5$. The latter case was previously displayed as the dashed line in Fig. 7.5. The three curves present a very similar and featureless behavior for angles
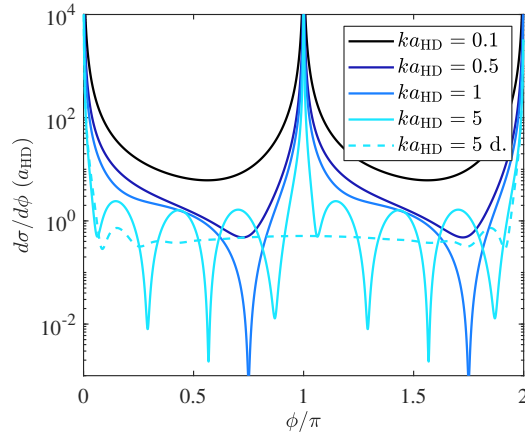
Figure 7.5: Differential scattering cross section $d\sigma/d\phi$ in units of the hard-core radius a_{HD} as function of the scattering angle ϕ for a hard-disk interaction potential V_{ii} between bosonic impurities immersed in a $\nu = 0.5$ FQH fluid. The different solid curves correspond to indistinguishable impurities with different values of the relative incident momentum ka_{HD}. The larger ka_{HD}, the more visible is the fringe pattern resulting from the interference of direct and exchange scattering channels. For comparison, the dashed curve is for distinguishable impurities at $ka_{\mathrm{HD}} = 5$: in this case, no interference fringe is visible.
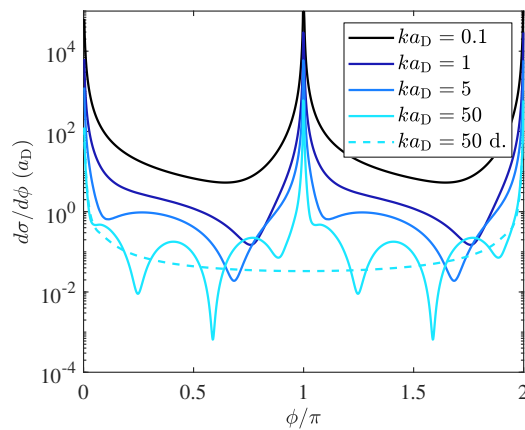

Figure 7.6: Differential scattering cross section $d\sigma/d\phi$ in units of the dipolar length a_{D} as function of the scattering angle ϕ for a dipole interaction potential V_{ii} between bosonic impurities immersed in a $\nu = 0.5$ FQH fluid. The different solid curves correspond to indistinguishable impurities with different values of the relative incident momentum ka_{D}. The larger ka_{D}, the more visible is the fringe pattern resulting from the interference of direct and exchange scattering channels. For comparison, the dashed curve is for distinguishable impurities at $ka_{\mathrm{D}} = 50$: in this case, no interference fringe is visible.
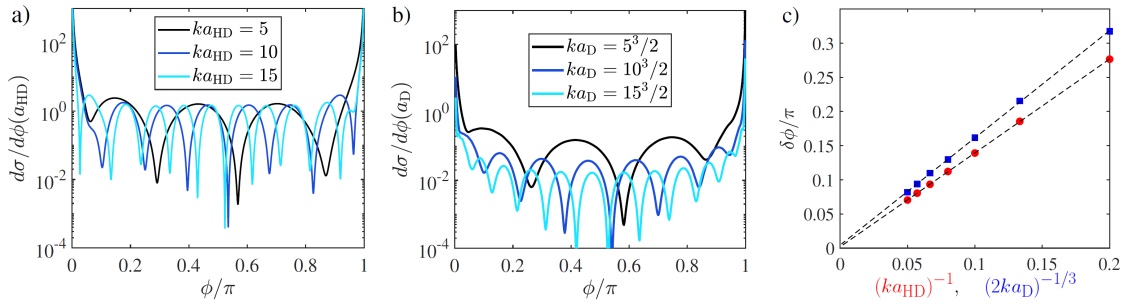
Figure 7.7: Differential scattering cross section $d\sigma/d\phi$ as function of the scattering angle ϕ for indistinguishable molecules with statistical parameter $\alpha = 0.5$ and several values of the relative incident momentum $ka_{\mathrm{HD,D}}$ in the hard-disk **a)** and dipolar **b)** interaction cases. The curves plotted with the same color in these two panels satisfy the relation Eq. (7.76) and are thus expected to have the same angular oscillation period. Panel **c)** shows the oscillation period $\delta\phi$ (calculated as the difference between the angular position of the two central minima) as a function of $(ka_{\mathrm{HD}})^{-1}$ for hard-disk impurities (red circles) and as a function of $(2ka_{\mathrm{D}})^{-1/3}$ for dipolar ones (blue squares). The dashed black lines are the respectives linear fits.
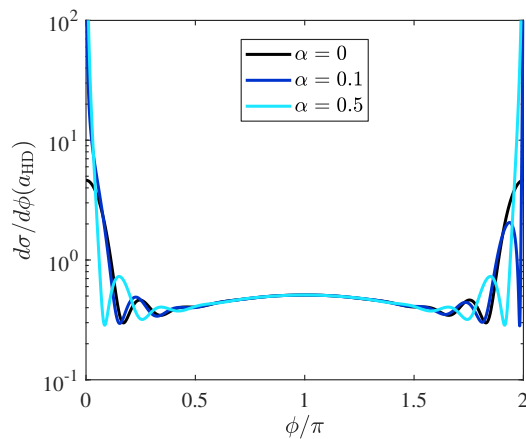

Figure 7.8: Differential scattering cross section $d\sigma/d\phi$ in units of the hard-core radius a_{HD} as function of the scattering angle ϕ for a hard-disk interaction potential V_{ii} between distinguishable impurities with a relative incident momentum $ka_{\mathrm{HD}} = 5$, and for three values of the statistical parameter α.
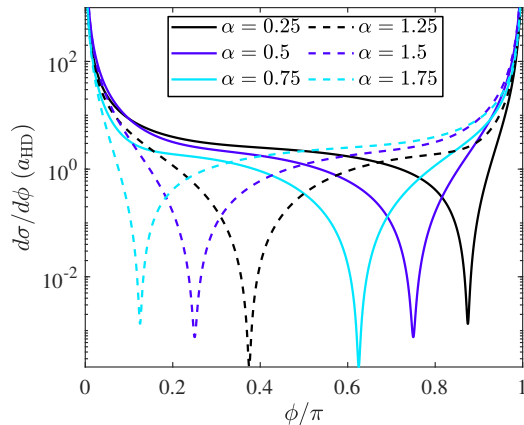
Figure 7.9: Differential scattering cross section $d\sigma/d\phi$ in units of the hard-core radius a_{HD} as function of the scattering angle ϕ for a hard-disk interaction potential V_{ii} between indistinguishable impurities, a relative incident momentum $ka_{\mathrm{HD}} = 1$ and different values of the statistical parameter α, defined as $\alpha = \nu$ for bosons and $\alpha = 1 + \nu$ for fermions. Solid (dashed) lines correspond to bosonic (fermionic) impurites inside a FQH bath of filling fraction $0 < \nu < 1$.

$0.5\pi < \phi < 1.5\pi$, confirming the crucial role of indistinguishability and of interference between the direct and exchange scattering channels. The oscillations around $\phi = 0, 2\pi$ are in fact present in the three curves with a comparable angular period. However, a finite α introduces a phase shift of the diffraction pattern and, for values $\alpha \neq 0.5$, an asymmetry between the oscillations to the left and to the right of the forward direction (see the dark blue curve).

For curves displaying the same angular period in the indistinguishable case (e.g. the cyan lines in Figs. 7.5 and 7.6), the larger contrast of the fringes observed for a hard-disk potential with respect to the dipolar potential can be related to the flatter angular dependence of the distinguishable differential scattering cross section in the first case, which enhances the destructive interference.

As a next step, it is interesting to compare the two cases of bosonic and fermionic impurities (from now on, we will always consider the indistinguishable case). Fig. 7.9 displays $d\sigma/d\phi$ for hard-disk bosonic and fermionic impurities with the same value $ka_{\mathrm{HD}} = 1$ of the relative incident momentum and a range of values of ν. The most visible feature is a drift of the minimum towards small angles as ν is increased, with a smooth connection of the bosonic case for $\nu \to 1$ and the fermionic case for $\nu \to 0$. The Bose-Fermi symmetry relations Eqs. (7.72)-(7.73) also manifest in this plot.

Fig. 7.10 gives more details on the dependence of the differential scattering cross section on the statistical parameter ν. The different panels correspond to dipolar [in a) and b)] and hard-disk [in c) and d)] interactions and to different (fixed) values of $ka_{\mathrm{HD,D}} = 0.1$ [in a) and c)] and $ka_{\mathrm{HD,D}} = 5$ [in b) and d)]. For standard bosons and fermions at $\nu = 0$, we recover a symmetric and smooth cross section with no peaks at $\phi = 0, \pi$. For bosons at intermediate values of $0 < \nu < 1$, the peaks at $\phi \to 0, \pi$ appear and, more interestingly, the oscillation pattern at large $ka_{\mathrm{HD,D}}$ features a global shift towards smaller angles for growing ν, with again a smooth recovery to the fermionic case when $\nu \to 1$.

The linearity of this shift as a function of ν is illustrated in Fig. 7.11 for both choices of interaction potential. In order to have a good contrast in the oscillations, a relatively large $ka_{\mathrm{HD,D}}$ is chosen. The deviations that are visible for the dipolar case disappear when even larger values of ka_{D} are chosen. For $\alpha = 1$, the minimum recovers the usual location at $\phi_{\min} = \pi/2$ of standard $\nu = 0$ fermions. The smaller slope of the hard-disk case is a consequence of the faster angular periodicity of the oscillations that is visible when comparing the panels in Figs. 7.10 b) and d), both plotted for $ka_{\mathrm{D,HD}} = 5$.

This simple dependence on ν of the angular interference pattern shown in Fig. 7.11 is a key conclusion of our study. From an experimental perspective, it provides a quantitatively accurate way to extract the fractional statistics of the quasi-holes in the FQH cloud just by detecting the oscillations in the angular dependence of the differential cross section and measuring the position of the minimum ($\phi_{\min}$) in different conditions. For instance, a quantitative value of ν for a given FQH liquid can be interpolated by repeating the measurement of $\phi_{\min}$ with bosonic impurities in
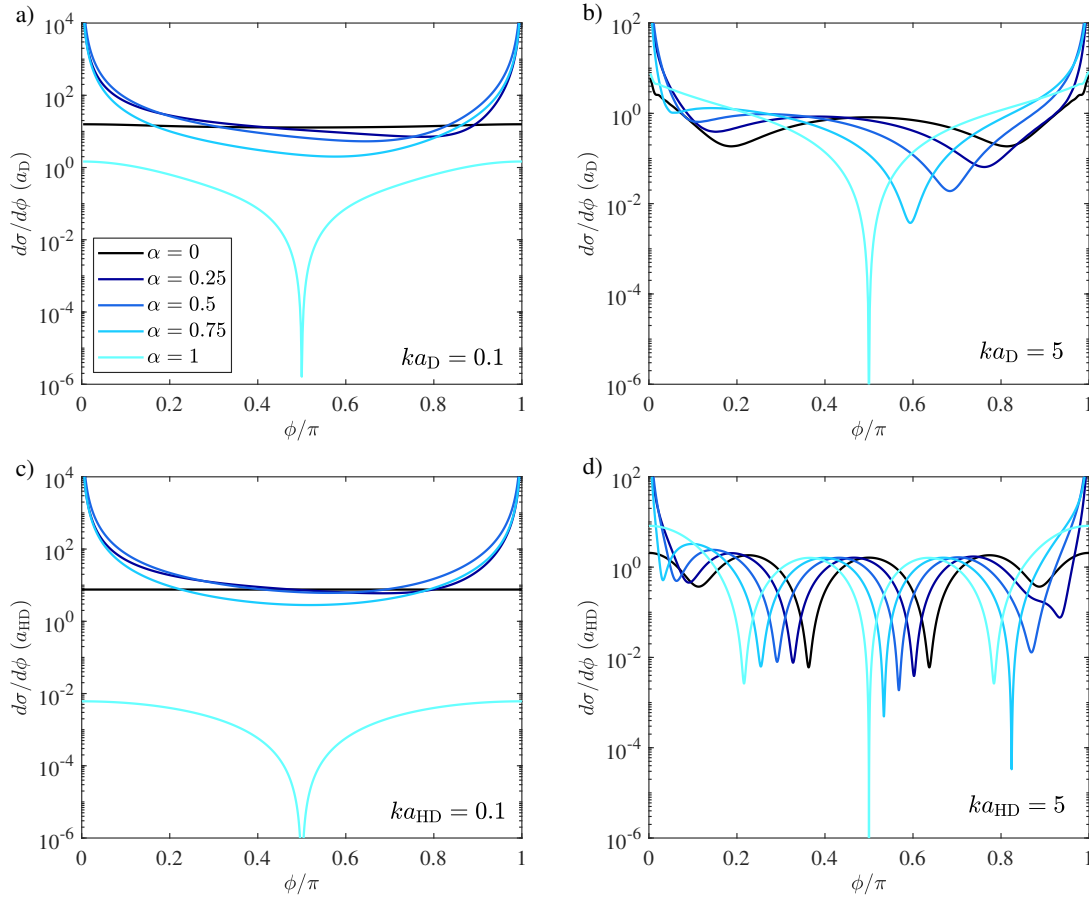
Figure 7.10: Differential scattering cross section $d\sigma/d\phi$ as function of the scattering angle ϕ for several values of the statistical parameter ν. The different panels refer to different values of the relative incident momentum k and different forms of the interaction potential V_{ii} between the impurities. In particular: **a)** Dipolar interactions and $ka_D = 0.1$. **b)** Dipolar interactions and $ka_D = 5$ **c)** Hard-disk interactions and $ka_{HD} = 0.1$ **d)** Hard-disk interactions and $ka_{HD} = 5$. The different curves refer to different values of the statistical parameter as indicated in the legend in a): $\alpha = 0, 0.25, 0.5, 0.75$ correspond to bosonic impurities at growing values of ν, while $\alpha = 1$ is the fermionic case with $\nu = 0$. To avoid overcrowding the figure, no other curve for fermionic impurities is displayed. As it was shown in Fig. 7.9, such curves are immediately obtained from the bosonic ones via the symmetry relations in Eqs. (7.72)-(7.73).
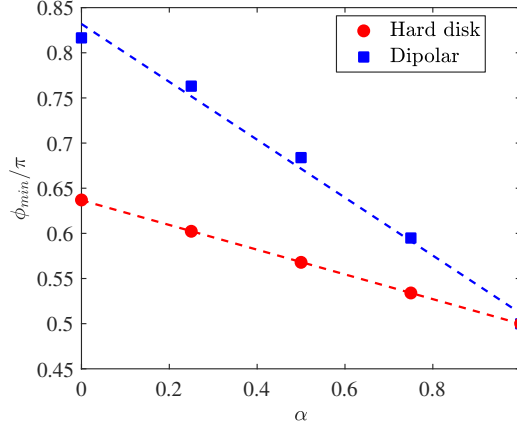
Figure 7.11: Angular position $\phi_{\min}$ of the minimum of the differential scattering cross section extracted from Fig. 7.10**b)**,**d)** for a dipolar and a hard-disk interaction potential, respectively, as a function of the statistical parameter $\alpha = \nu$ of anyonic molecules formed by bosonic impurities bound to a single quasi-hole in a FQH fluid at filling ν. The dashed lines are linear fits.

the presence and in the absence (i.e. $\nu = 0$) of the FQH liquid, keeping in mind that for $\nu = 1$ the minimum is at an angle $\phi_{\min} = \pi/2$, and assuming the linear dependence on $\nu = \alpha$ shown in Fig. 7.11. Perhaps less challenging, a qualitative signature of the fractional statistics for $0 < \nu < 1$ is already offered by the asymmetry of the differential cross section for $\phi \leftrightarrow \pi - \phi$ (or, equivalently, for $\phi \leftrightarrow -\phi$ or $\phi \leftrightarrow 2\pi - \phi$), that indicates a preferential chirality in the scattering process.

From a conceptual viewpoint, the linear dependence of the fringe position on ν suggests an intuitive understanding of the underlying physical mechanism: the oscillations can be interpreted as an interference pattern for the two scattering channels contributing to the scattering in a given direction, say at an angle ϕ. In one channel, each particle is deflected by an angle ϕ during the scattering process. In the other channel, each particle is deflected by $\pi + \phi$. Because of indistinguishability, the two processes have to be summed up with a relative phase α resulting from the sum of the intrinsic statistics $\alpha_i = 0, 1$ of the bosonic/fermionic impurities and of the fractional statistics ν of the attached quasi-holes. As it happens in generic interference experiments, e.g. two-slit interference, a phase-shift on one of the two arms results in a rigid shift of the whole fringe pattern. This intuitive interpretation is further confirmed by the complete disappearance of the fringe pattern when distinguishable impurities are considered.

7.4.5   Experimental remarks

In practice, a scattering experiment will begin with the simultaneous generation of a pair of anyonic molecules at different and controlled spatial locations. The two molecules will then have to be pushed against each other at a controlled speed with suitable potentials. This can be done following one of the schemes discussed in Sec. 7.3.2.

The angular dependence of their differential scattering cross section will be finally extracted by repeating the experiment many times and collecting the statistical distribution of the trajectories of the scattering products. For instance, the position of the impurities after the scattering event can be measured using absorption imaging as in Ref. [257]. In order to directly access the differential scattering cross section in a single shot, one may follow the route of [258] and consider the collision between two clouds of independent impurities embedded in the FQH droplet. A possible alternative is to follow a similar strategy to that of neutron scattering in liquid helium [259] and make use of a detector placed at several angular positions outside the FQH droplet. This of course has the inconvenient that the impurities may excite undesired edge modes on their way out and get their energy and momentum modified. In all cases, as we have mentioned at the beginning of Sec. 7.4, the analysis of the scattering experiment could be made simpler if the system parameters were chosen in such a way to give a vanishing effective charge $\mathcal{Q}$ for the anyonic molecules.

To check the actual feasibility of our proposal, it is important to estimate the maximum value of ka_D that one can realistically obtain in experiments. Combining the definition of a_D with the results of Sec. 7.3.2 for the maximum momentum $k_{\max} = \mathcal{M}v_{\max}$ that is compatible with the

Born-Oppenheimer approach, one gets

$$k_{\max} a_{\mathrm{D}} = \frac{\mathcal{M}}{m\tau} \frac{\Delta\omega_{-1}}{\omega_{\mathrm{cycl}}} \frac{a_{\mathrm{D}}}{\ell_B} \, . \tag{7.77}$$

As we have seen in the previous subsection, a large value of this quantity is needed to see a well developed system of fringes in the differential scattering cross section.

As a first concrete example, we can consider the case of the magnetic interaction between two magnetic atoms, e.g. ^{166}Er atoms with a relatively large magnetic dipole of $7\,\mu_B$ [260]. Estimating $\mathcal{M}/m \simeq 25$, $\ell_B \simeq 1\,\mu$m, $\Delta\omega_{-1}/\omega_{\mathrm{cycl}} = 0.1$, we obtain a not-so-optimistic value $k_{\max} a_{\mathrm{D}} \simeq 0.02$. However, a huge enhancement of the dipolar interaction is found if electric rather than magnetic interactions are used, e.g. between ground state heteronuclear diatomic molecules [246]. For a typical dipole moment $d_{\mathrm{E}} \sim 1$ Debye, an enhancement on the order of ≈ 200's can be obtained, leading to a promising $k_{\max} a_{\mathrm{D}} \approx 5$. Thanks to the quadratic dependence of the dipolar force on the dipole moment d_E, a sizable further increase is achievable with specific choices of molecules which display larger dipole moments of several Debye [261], e.g. 1.25 Debye for RbCs, 2.4 Debye for NaK, up to 5.5 Debye for LiCs, and are presently under active experimental investigation in the ultracold quantum gases community [262, 263, 264, 265, 266, 267]. Note that a large value of a_{D} is also essential to fulfill (for a given ka_{D}) the condition

$$\frac{\Delta\omega_{-1}}{\omega_{\mathrm{cycl}}} \frac{\mathcal{M}}{m} \left(\frac{a_{\mathrm{D}}}{\ell_B}\right)^2 \gg (ka_{\mathrm{D}})^2 \tag{7.78}$$

that guarantees, according to our discussion in Sec. 7.3.2, that the kinetic energy is low enough for the anyonic molecule to behave as a rigid object during the collision process.

7.5 Conclusions

In this Chapter we have shown how the quantum dynamics of heavy impurity particles immersed in a two-dimensional fractional quantum Hall (FQH) fluid of lighter particles may reveal crucial information about the fractional charge and statistics of the FQH quasi-hole excitations. Even though the discussion was carried out with a special attention to realizations in ultracold atomic gas platforms, equally promising candidates for experimental observation of the fractional charge and statistics are offered by FQH fluids of photons [7, 16] or hybrid electronic-optical systems [268, 269].

In full generality, we considered impurities that repulsively interact with the atoms of the FQH fluid. In this case, for suitable parameters the impurities can form bound states with quasi-hole excitations, the so-called anyonic molecules. A rigorous Born-Oppenheimer [240, 241] framework was set up to derive the effective charge and statistics of the anyonic molecules. Quite remarkably, this same formalism provides a quantitative prediction for the effective mass of the molecules, which combines the bare impurity mass with a correction due to the quasi-hole inertia.

As a main result of our work we proposed and characterized specific configurations where the fractional charge and statistics can be experimentally highlighted with state-of-the-art technology. If a single anyonic molecule is prepared inside the FQH fluid with some initial momentum, the values of the renormalized mass and of the fractional charge can be extracted from the experimentally accessible cyclotron orbit that it describes as a free charged particle in a magnetic field. This provides direct and unambiguous information on the fractional charge of FQH quasi-holes.

In the case of two anyonic molecules, the fractional statistics of the quasi-holes provides a long-range Aharonov-Bohm-like interaction between the molecules with dramatic consequences on two-body scattering processes. For sufficiently large values of the relative incident momentum, the differential cross section displays a clear oscillatory pattern due to the interference of direct and exchange processes and the non-trivial fractional statistical phase that the quasi-holes acquire upon exchange is directly observable as a rigid shift of the angular interference pattern.

As future perspectives, we envision to extend our approach to the case of impurities binding with different numbers of quasi-holes, leading to molecules with different anyonic statistics, and to the case of a larger number of molecules forming few-body complexes with a richer structure of eigenstates determined by the interplay of the inter-impurity interaction and the fractional statistics [223]. An even more intriguing development will be to extend our treatment to more subtle FQH fluids supporting non-Abelian excitations [30] and explore the consequences of the topological degeneracy on the quantum dynamics of the non-Abelian anyonic molecules [270, 232].

Finally, we would like to generalize our approach in order to account for driven-dissipative systems. This will allow us to implement the proposed strategy to quantum fluids of light, in particular the cavity Rydberg polaritons of Ref. [16]. We anticipate that such a setup will require the use of two different Rydberg excitations: one will give rise to the FQH fluid and the other will be associated to the impurities. The polariton dynamics will be determined by the cavity modes accesible to their photonic part. In order to give a momentum kick to the impurity polaritons one could employ a digital micromirror device allowing to inject photons with different angular momenta. Experimental insight can be obtained by looking at the spatial correlations of the emerging output photons as a function of the angle between them. All these technical details need to be accounted for in an explicit calculation for such a platform.

Conclusions and outlooks

This Thesis is devoted to the study of topological phases of matter in optical platforms, focusing on non-Hermitian systems with gain and losses involving nonreciprocal elements, and fractional quantum Hall liquids where strong interactions play a central role.

In the first part we investigated nonlinear Taiji micro-ring resonators in passive and active silicon photonics setups. Such resonators establish a unidirectional coupling between the two whispering-gallery modes circulating in their perimeter, and have raised a great expectation due to their promising role in preserving quantum spin-Hall topological insulator lasers even in the presence of a time-reversal symmetry breaking backscattering.

We started by demonstrating that a single nonlinear Taiji resonator coupled to a bus waveguide breaks Lorentz reciprocity. The space-reversal symmetry breaking geometry of the Taiji resonator produces an enhancement of the intensity when the resonator is pumped in a certain direction. This fact, combined with the optical nonlinearity of the material, leads to a different shift of the resonance frequency of the resonator that results in a different transmittance when light is injected from opposite sides of the waveguide.

When a saturable gain is added to a single Taiji resonator, a sufficiently strong unidirectional coupling rules out the possibility of lasing in one of the whispering-gallery modes with independence of the type of optical nonlinearity and gain saturation displayed by the material. This can be regarded as a dynamical time-reversal symmetry breaking. As long as the unidirectional coupling is larger than the amount of backscattering present into the sample, Taiji resonators grant unidirectional lasing and recirculate backscattered light into the lasing direction. This effect is further enhanced by an optical Kerr nonlinearity.

We showed that both ring and Taiji resonators can work as optical isolators over a broad frequency band in realistic operating conditions. Our proposal relies on the presence of a strong pump in a single direction: as a consequence four-wave mixing can only couple the pump with small intensity signals propagating in the same direction. The resulting nonreciprocal devices circumvent the restrictions imposed by dynamic reciprocity.

We then studied two-dimensional arrays of ring and Taiji resonators realizing quantum spin-Hall topological insulator lasers. In ring resonator lattices it is impossible to impose a definite chirality to the laser emission. Furthermore, when backscattering is present in such a system the lasing properties significantly deteriorate. However, the strong unidirectional coupling present in Taiji resonator lattices promotes lasing with a well-defined chirality while considerably improving the slope efficiency and reducing the lasing threshold. Finally, we demonstrated that lasing in a single helical mode can be obtained in quantum spin-Hall lasers of Taiji resonators by exploiting the optical nonlinearity of the material.

As future work, we will explicitly include in our calculations for the quantum spin-Hall lasers the dynamics of a reservoir providing the saturable gain. Such kind of models are known as class-B lasers and they are more suitable to describe the physics of topological lasers. We will also capitalize on our proposal for optical isolators in order to exploit the effect of asymmetrical four-wave mixing to further suppress the effect of backscattering in the quantum spin-Hall array. Furthermore, the interplay between topological photonics and nonlinear optics deserves much more attention and leads to interesting phenomena like topological bulk and edge solitons protected against local

disorder [271, 21, 272]. Finally, the use of Taiji resonators opens up exciting perspectives in relation with exceptional points and parity-symmetry breaking [149, 273, 274].

In the second part of this Thesis we dived into more speculative waters and explored fractional quantum Hall liquids of cold atoms and photons. We proposed strategies to experimentally access the fractional charge and anyonic statistics of the quasihole excitations arising in the bulk of such systems. Heavy impurities introduced inside a fractional quantum Hall droplet will bind quasiholes, forming composite objects that we label as anyonic molecules. Restricting ourselves to molecules formed by one quasihole and a single impurity, we find that the bound quasihole gives a finite contribution to the impurity mass, that we are able to ascertain by considering the first-order correction to the Born-Oppenheimer approximation. The effective charge and statistical parameter of the molecule are given by the sum of those of the impurity and the quasihole, respectively. While the mass and charge of such objects can be directly assessed by imaging the cyclotron orbit described by a single molecule, the anyonic statistics manifest as a rigid shift of the interference fringes in the differential scattering cross section describing a collision between two molecules.

An exciting outlook for this work would be to use the impurities in order to explore the physics of non-Abelian quasihole excitations which are expected to arise in higher-order fractional quantum Hall liquids. Moreover, an extension of our theory is necessary in order to describe molecules binding with several quasiholes, and therefore displaying different anyonic statistics. Future research will address the interaction between several such objects.

To conclude, topological photonics has grown far beyond its initial purpose of being a platform for quantum simulation. It constitutes a field in its own right, leading to the observation of completely new physics with no analog in other systems. In particular, the interplay between optical nonlinearities, nonreciprocity, and non-Hermitian systems featuring topological band structures opens up exciting perspectives for both theorists and experimentalists. The call to adventure is right in front of us, and we will respond.

Appendices

Appendix A

Coupled-mode theory for the single Taiji resonator

$\mathbb{I}$n this Appendix we derive the coupled-mode theory (2.15-2.16) employed in Chapter 2 to study the passive nonlinear Taiji resonator (TJR). We also calculate the most general expressions for the nonlinear refractive index n_{NL} and the g parameter.

We will first compute the coupled-mode equations in the linear regime ($n_{\mathrm{NL}} = 0$) and then include the effect of a finite optical nonlinearity, which is a shift of the resonance frequency. Fig. A.1 shows a sketch of the TJR coupled to a bus waveguide. The bus waveguide-ring resonator and S waveguide-ring resonator directional couplers are described by transmission $t_{\mathrm{w,S}}$ and coupling $ik_{\mathrm{w,S}}$ amplitudes satisfying $\sqrt{t_{\mathrm{w,S}}^2 + k_{\mathrm{w,S}}^2} = 1$, being $t_{\mathrm{w,S}}$ and $k_{\mathrm{w,S}}$ real numbers. The perimeter of the external ring resonator is L, and the length of the S waveguide between the two points at which it is coupled with the ring is L_{S}. The equations relating the field amplitudes $E_{\pm}^{(1,2)}$ in each mode (labelled CW + and CCW −) at the bus waveguide-ring resonator directional coupler read

$$E_{-}^{(1)} = t_{\mathrm{S}}^2 e^{i\frac{\omega}{c} n_{\mathrm{L}} L} E_{-}^{(2)} - 2k_{\mathrm{S}}^2 t_{\mathrm{S}} e^{i\frac{\omega}{c} n_{\mathrm{L}} L} e^{i\frac{\omega}{c} n_{\mathrm{L}} L_{\mathrm{S}}} E_{+}^{(1)}, \tag{A.1}$$

$$E_{+}^{(1)} = t_{\mathrm{w}} E_{+}^{(2)} + ik_{\mathrm{w}} E_{\mathrm{R}}^{(\mathrm{in})}, \tag{A.2}$$

$$E_{-}^{(2)} = t_{\mathrm{w}} E_{-}^{(1)} + ik_{\mathrm{w}} E_{\mathrm{L}}^{(\mathrm{in})}, \tag{A.3}$$

$$E_{+}^{(2)} = t_{\mathrm{S}}^2 e^{i\frac{\omega}{c} n_{\mathrm{L}} L} E_{+}^{(1)}, \tag{A.4}$$

where $E_{\mathrm{L,R}}^{(\mathrm{in})}$ are the external driving fields injected in the bus waveguide from its left and right side, respectively. The superindices $(1, 2)$ refer to the relative position of the fields with respect to the directional coupler: (1) to its left and (2) to its right.

We now combine Eqs. (A.1-A.3) to get an expression relating $E_{-}^{(1)}$ and $E_{+}^{(2)}$ only:

$$E_{-}^{(1)} e^{-i\frac{\omega}{c} n_{\mathrm{L}} L} = \left(1 - k_{\mathrm{S}}^2 - \frac{k_{\mathrm{w}}^2}{2}\right) E_{-}^{(1)} + ik_{\mathrm{w}} E_{\mathrm{L}}^{(\mathrm{in})} - 2k_{\mathrm{S}}^2 e^{i\frac{\omega}{c} n_{\mathrm{L}} L_{\mathrm{S}}} E_{+}^{(2)}, \tag{A.5}$$

where we have assumed $k_{\mathrm{w,S}} \ll 1$ and therefore dropped terms of higher order than $\mathcal{O}(k_{\mathrm{w,S}}^2)$. We will also be working in the vicinity of the resonance frequency of the resonator ω_0. Therefore we have that

$$e^{-i\frac{\omega}{c} n_{\mathrm{L}} L} = e^{-i\frac{\omega - \omega_0}{c} n_{\mathrm{L}} L} \simeq \left(1 - i\frac{\omega}{c} n_{\mathrm{L}} L + i\frac{\omega_0}{c} n_{\mathrm{L}} L\right). \tag{A.6}$$

After making this substitution in Eq. (A.5) we can use a Fourier transform to go from the frequency to the real-time space, i.e.

$$-i\omega E_{-}^{(1)}(\omega) \to \frac{d}{dt} E_{-}^{(1)}(t). \tag{A.7}$$
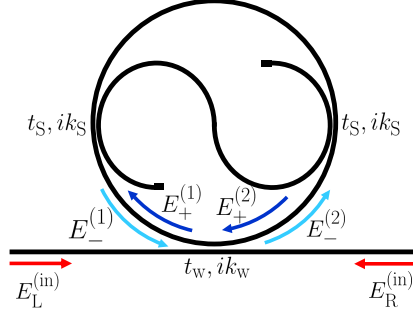
Figure A.1: Sketch of the Taiji resonator (TJR) coupled to a bus waveguide. The electric field amplitudes $E_\pm^{(1,2)}$ in the $\pm$ modes are measured immediately to the left (1) and right (2) of the bus waveguide-ring resonator coupling. $E_{\mathrm{L,R}}^{(\mathrm{in})}$ are the driving signals entering the bus waveguide from its left and right side, respectively. $t_{\mathrm{w,S}}$ and $ik_{\mathrm{w,S}}$ are the transmission and coupling amplitudes at the directional couplers.

This leads to the temporal coupled-mode equation for the CCW ($-$) mode:

$$i\dot{E}_-^{(1)} = \omega_0 E_-^{(1)} - i\frac{c}{n_{\mathrm{L}}L}k_{\mathrm{S}}^2 E_-^{(1)} - i\frac{c}{n_{\mathrm{L}}L}\frac{k_{\mathrm{w}}^2}{2}E_-^{(1)} - \frac{c}{n_{\mathrm{L}}L}k_{\mathrm{w}}E_{\mathrm{L}}^{(\mathrm{in})} - i\frac{c}{n_{\mathrm{L}}L}e^{i\frac{\omega}{c}n_{\mathrm{L}}L_{\mathrm{S}}}2k_{\mathrm{S}}^2 E_+^{(2)}. \quad (A.8)$$

Similarly, we can employ Eqs. (A.2) and (A.4) to derive the analog expression for the CW ($+$) mode:

$$i\dot{E}_+^{(2)} = \omega_0 E_+^{(2)} - i\frac{c}{n_{\mathrm{L}}L}k_{\mathrm{S}}^2 E_+^{(2)} - i\frac{c}{n_{\mathrm{L}}L}\frac{k_{\mathrm{w}}^2}{2}E_+^{(2)} - \frac{c}{n_{\mathrm{L}}L}k_{\mathrm{w}}E_{\mathrm{R}}^{(\mathrm{in})}. \quad (A.9)$$

From these expressions we can ascertain the value of the radiative losses due to the coupling of the ring with the bus (γ_{w}) and S (γ_{S}) waveguides:

$$\gamma_{\mathrm{S}} = \frac{c}{n_{\mathrm{L}}L}k_{\mathrm{S}}^2, \quad (A.10)$$

$$\gamma_{\mathrm{w}} = \frac{c}{n_{\mathrm{L}}L}\frac{k_{\mathrm{w}}^2}{2}. \quad (A.11)$$

Finally, we can complete our description of the TJR by including in the coupled-mode equations (A.8-A.9) terms accounting for the shift of the linear resonance frequency ω_0 due to the optical nonlinearity of the material. Consider the spatial and temporal dependence of the electric field amplitudes in the two directions

$$E_+(z,t) = \tilde{E}_+ e^{i(kz-\omega t)}, \quad (A.12)$$

$$E_-(z,t) = \tilde{E}_- e^{-i(kz+\omega t)}, \quad (A.13)$$

where k is the wavenumber, z is a spatial coordinate, ω is the frequency, and t is time. On the following we drop the $(1,2)$ superindices on the field amplitudes.

In the case of a local Kerr nonlinearity ($g = 2$) with nonlinear refractive index n_{K}, the resonance frequency shift at some location z will be proportional to the intensity at that particular point, i.e. Eqs. (A.8-A.9) will feature terms proportional to

$$|E_+ + E_-|^2(E_+ + E_-). \quad (A.14)$$

By expanding the squared modulus above, we obtain

$$|E_+ + E_-|^2(E_+ + E_-) = (|E_+|^2 + 2|E_-|^2)E_+ + (|E_-|^2 + 2|E_+|^2)E_- + E_+^2 E_-^* + E_-^2 E_+^*$$
$$\simeq (|E_+|^2 + 2|E_-|^2)E_+ + (|E_-|^2 + 2|E_+|^2)E_-. \quad (A.15)$$

The last two terms in the second step oscillate fast and average to zero in the context of the rotating-wave approximation; therefore they can be safely neglected. As we see, we have obtained the $g = 2$ factor for the Kerr shift due to counterpropagating waves in each case.

On the other hand, for a nonlocal thermo-optic nonlinearity ($g = 1$) with nonlinear refractive index n_T the resonance frequency shift at z will be proportional to the intensity circulating in the whole ring, i.e.

$$\left[\int_z |E_+ + E_-|^2 dz\right](E_+ + E_-) = \left[\int_z (|E_+|^2 + |E_-|^2 + E_+^* E_- + E_+ E_-^*)dz\right](E_+ + E_-)$$
$$= (|E_+|^2 + |E_-|^2)(E_+ + E_-). \quad \text{(A.16)}$$

In the passage from the second to the third step we took into account that the first and second terms in the integral do not depend on z, while the third and fourth terms average to zero when we integrate the whole perimeter of the ring resonator. This leads to the same shift for waves propagating in the two directions, summarized by the $g = 1$ factor.

Altogether, we can include these terms into Eqs. (A.8-A.9), giving the steady-state equations

$$\omega E_+ = \omega_0 E_+ - \frac{n_\mathrm{K}}{n_\mathrm{L}}\omega_0(|E_+|^2 + 2|E_-|^2)E_+$$
$$- \frac{n_\mathrm{T}}{n_\mathrm{L}}\omega_0(|E_+|^2 + |E_-|^2)E_+ - i\gamma_\mathrm{T} E_+ - \frac{c}{Ln_\mathrm{L}}k_\mathrm{w}E_\mathrm{in}^{(\mathrm{R})}, \quad \text{(A.17)}$$
$$\omega E_- = \omega_0 E_- - \frac{n_\mathrm{K}}{n_\mathrm{L}}\omega_0(|E_-|^2 + 2|E_+|^2)E_-$$
$$- \frac{n_\mathrm{T}}{n_\mathrm{L}}\omega_0(|E_-|^2 + |E_+|^2)E_- - i\gamma_\mathrm{T} E_- - \frac{c}{Ln_\mathrm{L}}k_\mathrm{w}E_\mathrm{in}^{(\mathrm{L})}$$
$$- i\frac{c}{Ln_\mathrm{L}}2k_\mathrm{S}^2 e^{i\frac{\omega}{c}n_\mathrm{L}L_\mathrm{S}}E_+. \quad \text{(A.18)}$$

By properly grouping both nonlinear terms it is easy to show that

$$\omega E_+ = \omega_0 E_+ - \frac{n_\mathrm{K} + n_\mathrm{T}}{n_\mathrm{L}}\omega_0\left(|E_+|^2 + \frac{2n_\mathrm{K} + n_\mathrm{T}}{n_\mathrm{K} + n_\mathrm{T}}|E_-|^2\right)E_+$$
$$- i\gamma_\mathrm{T} E_+ - \frac{c}{Ln_\mathrm{L}}k_\mathrm{w}E_\mathrm{in}^{(\mathrm{R})}, \quad \text{(A.19)}$$
$$\omega E_- = \omega_0 E_- - \frac{n_\mathrm{K} + n_\mathrm{T}}{n_\mathrm{L}}\omega_0\left(|E_-|^2 + \frac{2n_\mathrm{K} + n_\mathrm{T}}{n_\mathrm{K} + n_\mathrm{T}}|E_+|^2\right)E_-$$
$$- i\gamma_\mathrm{T} E_- - \frac{c}{Ln_\mathrm{L}}k_\mathrm{w}E_\mathrm{in}^{(\mathrm{L})} - i\frac{c}{Ln_\mathrm{L}}2k_\mathrm{S}^2 e^{i\frac{\omega}{c}n_\mathrm{L}L_\mathrm{S}}E_+, \quad \text{(A.20)}$$

and therefore

$$n_\mathrm{NL} = n_\mathrm{K} + n_\mathrm{T}, \quad g = \frac{2n_\mathrm{K} + n_\mathrm{T}}{n_\mathrm{K} + n_\mathrm{T}}. \quad \text{(A.21)}$$

Upon replacing $\omega \to i\partial_t$, these equations can be used to describe the evolution of the system in time under the assumption of a temporally local nonlinearity. While this is usually a good approximation for Kerr media, one must keep in mind that thermal nonlinearities are typically slow so this approximation must be explicitly verified on a case-by-case basis.

Appendix B

Finite-element model

$\mathbf{H}$ere we derive the finite-element equations to be employed in the fits of the experimental results for the single nonlinear Taiji resonator studied in Chapter 2. We start by dividing each waveguide in the sample into segments of equal length $\Delta z_{\mathrm{r,S,w}} = L_{\mathrm{r,S,w}}/N_{r,S,w} = z_j - z_{j-1}$, being $L_{\mathrm{r,S,w}}$[1] the total length of each component (ring, S, and bus waveguides), $N_{\mathrm{r,S,w}}$ the number of segments in which it is divided, and z_j the spatial coordinate of each segment $j = 1, ..., N_{\mathrm{r,S,w}}$. The segment length in each case is assumed to be much longer than the light wavelength, i.e. $\Delta z_{\mathrm{r,S,w}} \gg \lambda$. The aim of the finite-element model is to relate the amplitude of the electric field E at a position z_{j+1} to the amplitude in the precedent segment z_j. To simplify the notation, on the following we will drop the subindices referring to the sample components as the equations are valid regardless of which waveguide is considered. We started from a modified Helmholtz's equation including a local Kerr nonlinearity with refractive index n_{K}, and a nonlocal thermo-optical nonlinearity with refractive index n_{T}. It reads

$$\frac{\partial^2 E}{\partial z^2} = -\left(\frac{\omega}{c}\right)^2 \left[\left(n_{\mathrm{L}} + i\alpha\frac{c}{\omega}\right) + n_{\mathrm{K}}|E(z)|^2 \right.$$
$$\left. + n_{\mathrm{T}}\frac{\Delta z}{L}\sum_{j=1}^{N}|E(z_j)|^2 \right]^2 E(z), \tag{B.1}$$

where ω and c correspond to the angular frequency and speed of light in free space, respectively, n_{L} is the linear refractive index, and α is the absorption coefficient. Note that the thermal nonlinearity shifts the refractive index at each sample component proportionally to the average intensity inside it. In our case we have that $n_{\mathrm{L}} \gg n_{\mathrm{K,T}}|E(z)|^2 \ \forall z$, which implies that the field oscillation due to the linear part of the material's response will be much faster than that of the nonlinear part. Therefore one can employ the Ansatz

$$E(z) = E_+(z) + E_-(z)$$
$$= \xi_+(z)e^{i\frac{\omega}{c}(n_{\mathrm{L}}+i\alpha c/\omega)z} + \xi_-(z)e^{-i\frac{\omega}{c}(n_{\mathrm{L}}+i\alpha c/\omega)z}, \tag{B.2}$$

where $E_{\pm}$ are the electric field amplitudes and $\xi_{\pm}$ are the slowly-evolving parts of the field propagating in the clockwise $(+)$ and counterclockwise $(-)$ directions.

After inserting Eq. (B.2) into Eq. (B.1) we use the rotating wave approximation to neglect those terms oscillating with spatial frequency on the order of ω/c or faster, which average to zero in a segment much longer than the optical wavevelength, as well as the smaller terms proportional

---

[1]Note that here and in the following we use the compact notation of repeated indices for different quantities, i.e. $L_{\mathrm{r,S,w}}$ corresponds to L_{r}, L_{S} and L_{w}.

to $\partial^2 \xi_{+,-}/\partial z^2$ and those of order $\mathcal{O}(n_{\mathrm{K,T}}^2)$. Identifying the energy-conserving processes we obtain

$$
\begin{aligned}
\frac{\partial \xi_\pm}{\partial z} = \pm i \frac{\omega}{c} \Bigg[& n_{\mathrm{K}} \left(|\xi_\pm(z)|^2 + 2|\xi_\mp(z)|^2 \right) \\
& + n_{\mathrm{T}} \frac{\Delta z}{L} \sum_{j=1}^{N} \left(|\xi_\pm(z_j)|^2 + |\xi_\mp(z_j)|^2 \right) \Bigg] \xi_\pm(z).
\end{aligned}
\tag{B.3}
$$

By integrating these differential equations along a single segment where the slowly-evolving intensities $|\xi_\pm|^2$ can be considered as constant in our weak absorption regime and employing the Ansatz (B.2) one finally arrives to

$$
\begin{aligned}
E_\pm(z \pm \Delta z) = exp \Bigg\{ i \Bigg[& \left(n + i\alpha \frac{c}{\omega} \right) \\
& + n_{\mathrm{K}} \left(|E_\pm(z)|^2 + 2|E_\mp(z)|^2 \right) \\
& + n_{\mathrm{T}} \frac{\Delta z}{L} \sum_{j=1}^{N} \left(|E_\pm(z_j)|^2 + |E_\mp(z_j)|^2 \right) \Bigg] \frac{\omega}{c} \Delta z \Bigg\} E_\pm(z).
\end{aligned}
\tag{B.4}
$$

which generalizes Eq. (2.17) to generic nonlinearities. Actually, this result also provides a rigorous mathematical explanation of the different character of the $g = 1, 2$ parameters describing the thermo-optic and Kerr optical nonlinearities.

The fields in the different components of the sample are coupled in reciprocal and lossless directional couplers in which the output and input field amplitudes are related by a scattering matrix

$$
\begin{pmatrix} E_{\mathrm{out},1} \\ E_{\mathrm{out},2} \end{pmatrix} = \begin{pmatrix} t_{\mathrm{w,S,m}} & ik_{\mathrm{w,S,m}} \\ ik_{\mathrm{w,S,m}} & t_{\mathrm{w,S,m}} \end{pmatrix} \begin{pmatrix} E_{\mathrm{in},1} \\ E_{\mathrm{in},2} \end{pmatrix},
\tag{B.5}
$$

where $t_{\mathrm{w,S}}$ and $ik_{\mathrm{w,S}}$ represent the transmission and coupling amplitudes in the ring-bus and ring-S couplers, respectively. On the other hand, t_{m} and ik_{m} correspond to the transmission and reflection amplitudes at the facets of the bus waveguide, which give rise to Fabry-Pérot oscillations. Note that $t_{\mathrm{w,S,m}}$ and $k_{\mathrm{w,S,m}}$ are taken as real numbers satisfying $t_{\mathrm{w,S,m}}^2 + k_{\mathrm{w,S,m}}^2 = 1$.

Altogether, the set of Eqs. (B.4-B.5) for all elements of our set-up represent the electric field propagation throughout the sample and can be solved with standard numerical techniques providing a complete and quantitative description of the nonlinear light propagation at the steady-state.

Appendix C

Coupled-mode theory for the spin-Hall topolaser

In this Appendix we explicitly derive the coupled-mode theory equations (5.1) for the quantum spin-Hall insulator studied in Chapter 5.

A diagram of the top-left 1×2 plaquette of the lattice is shown in Fig. C.1. The two site resonators of circumference perimeter $L_\circ$ are coupled via a racetrack ring resonator of perimeter L_L. The left site resonator is also coupled to a bus waveguide. For the moment we do not consider neither the tilted S elements inside the site ring resonators, nor the saturable gain. We also assume that the position of the link resonator is not shifted with respect to the central horizontal axis of the plaquette, and that nonlinear effects are negligible. For further simplicity, we will not consider absorption losses.

When the plaquette is probed by means of signal with field amplitude $E^{(\text{in})}$, the $-$ pseudospin (corresponding with the CCW whispering-gallery modes of the site resonators) is excited. We label by $a_{1,2}^{(1)}$ the field amplitudes in the $-$ pseudospin in the left site resonator before and after the coupling with the bus waveguide. In a similar manner, $b_{1,2}$ are the field amplitudes in the link resonator before and after the coupling with the left site resonator. Finally, $a^{(2)}$ is the field amplitude in the right site resonator at an opposite position in the circumference to the coupling with the link resonator. The output amplitude through the bus waveguide is labelled $E^{(\text{out})}$.

We now write down the system of six equations relating our six unknowns and the inhomogeneous term given by the input field:

$$a_1^{(1)} = a_2^{(1)} e^{i \frac{\omega}{c} n_L \frac{L_\circ}{2}} t_w e^{i \frac{\omega}{c} n_L \frac{L_\circ}{2}} + i k_w b_1 e^{i \frac{\omega}{c} n_L \frac{L_\circ}{2}} \tag{C.1}$$

$$a_2^{(1)} = t_w a_1^{(1)} + i k_w E^{(\text{in})} \tag{C.2}$$

$$b_1 = b_2 e^{i \frac{\omega}{c} n_L \frac{L_L}{2}} t_w e^{i \frac{\omega}{c} n_L \frac{L_L}{2}} + i k_w a_1^{(2)} e^{i \frac{\omega}{c} n_L \frac{L_\circ}{2}} e^{i \frac{\omega}{c} n_L \frac{L_L}{2}} \tag{C.3}$$

$$b_2 = t_w b_1 + i k_w e^{i \frac{\omega}{c} n_L \frac{L_\circ}{2}} a_2^{(1)} \tag{C.4}$$

$$a_1^{(2)} = e^{i \frac{\omega}{c} n_L \frac{L_\circ}{2}} t_w e^{i \frac{\omega}{c} n_L \frac{L_\circ}{2}} a_1^{(2)} + i k_w b_2 e^{i \frac{\omega}{c} n_L \frac{L_L}{2}} e^{i \frac{\omega}{c} n_L \frac{L_\circ}{2}} \tag{C.5}$$

$$E^{(\text{out})} = t_w E^{(\text{in})} + i k_w a_1^{(1)}. \tag{C.6}$$

The objective is to end with a couple of equations describing $a_1^{(1)}$ and $a^{(2)}$ (which we want to promote to dynamical variables) as a function of all the other field amplitudes. We first combine Eqs. (C.2-C.5) in order to integrate out the fields in the link resonator. After a bit of manipulation,
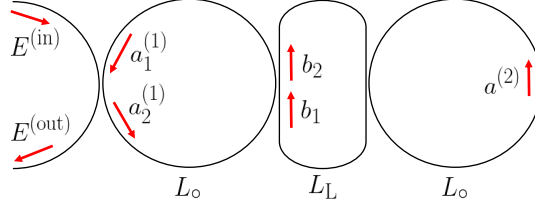
Figure C.1: Sketch of a couple of site resonators (of circumference length $L_\circ$) of the quantum spin-Hall insulator connected by means of a link resonator (of length L_{L}). The left site resonator is coupled to a bus waveguide. The arrows indicate the propagation direction of the fields.

we arrive to the equation for $a^{(2)}$:

$$a^{(2)}e^{-i\frac{\omega}{c}n_{\mathrm{L}}L_\circ} = t_{\mathrm{w}}\left(1 - k_{\mathrm{w}}^2\frac{e^{i\frac{\omega}{c}n_{\mathrm{L}}L_{\mathrm{L}}}}{1 - t_{\mathrm{w}}^2 e^{i\frac{\omega}{c}n_{\mathrm{L}}L_{\mathrm{L}}}}\right)a^{(2)}$$

$$-k_{\mathrm{w}}^2\left(1 + t_{\mathrm{w}}^2\frac{e^{i\frac{\omega}{c}n_{\mathrm{L}}L_{\mathrm{L}}}}{1 - t_{\mathrm{w}}^2 e^{i\frac{\omega}{c}n_{\mathrm{L}}L_{\mathrm{L}}}}\right)e^{i\frac{\omega}{c}n_{\mathrm{L}}L_{\mathrm{L}}}\left(t_{\mathrm{w}}a^{(1)} + ik_{\mathrm{w}}E^{(\mathrm{in})}\right). \tag{C.7}$$

Since we know that at the resonance frequency of the site resonators ω_0 we have that

$$e^{i\frac{\omega_0}{c}n_{\mathrm{L}}L_\circ} = 1, \tag{C.8}$$

it is legitimate to introduce the complex phase above in the right-hand side of Eq. (C.7). Assuming that ω is always in the vicinity of the resonance frequency, we can Taylor expand the right-hand side, giving

$$a^{(2)}\left(1 - i\frac{\omega}{c}n_{\mathrm{L}}L_\circ + i\frac{\omega_0}{c}n_{\mathrm{L}}L_\circ\right). \tag{C.9}$$

At this point we can change from reciprocal to real space by employing the Fourier relation

$$-i\omega a^{(2)}(\omega) \rightarrow \frac{d}{dt}a^{(2)}(t). \tag{C.10}$$

By keeping terms up to quadratic order in the coupling k_{w} we finally arrive to the temporal coupled-mode equation for the right site resonator:

$$i\dot{a}^{(2)} = \omega_0 a^{(2)} - i\frac{c}{n_{\mathrm{L}}L_\circ}k_{\mathrm{w}}^2\frac{1}{2}\frac{1 + e^{i\frac{\omega}{c}n_{\mathrm{L}}L_{\mathrm{L}}}}{1 - e^{i\frac{\omega}{c}n_{\mathrm{L}}L_{\mathrm{L}}}}a^{(2)} - i\frac{c}{n_{\mathrm{L}}L_\circ}k_{\mathrm{w}}^2\frac{e^{i\frac{\omega}{c}n_{\mathrm{L}}\frac{L_{\mathrm{L}}}{2}}}{1 - e^{i\frac{\omega}{c}n_{\mathrm{L}}L_{\mathrm{L}}}}a^{(1)}, \tag{C.11}$$

where we can identify the second and third terms in the right-hand side of the equation with the losses and incoming light due to the coupling with the left site resonator enabled by the link resonator, respectively. The great advantage of this equation is that we have got rid of the field amplitudes in the link resonators. The role of the link resonators is in fact implicitly accounted by the losses and couplings terms.

Following a similar procedure, we employ Eqs. (C.1-C.4) to derive an expression for the field amplitude in the left site resonator $a_1^{(1)}$, i.e.

$$a_1^{(1)}e^{-i\frac{\omega}{c}n_{\mathrm{L}}L_\circ} = t_{\mathrm{w}}\left(t_{\mathrm{w}}a_1^{(1)} + ik_{\mathrm{w}}E^{(\mathrm{in})}\right)\left(1 - k_{\mathrm{w}}^2\frac{e^{i\frac{\omega}{c}n_{\mathrm{L}}L_{\mathrm{L}}}}{1 - t_{\mathrm{w}}^2 e^{i\frac{\omega}{c}n_{\mathrm{L}}L_{\mathrm{L}}}}\right) - k_{\mathrm{w}}^2\frac{e^{i\frac{\omega}{c}n_{\mathrm{L}}\frac{L_{\mathrm{L}}}{2}}}{1 - t_{\mathrm{w}}^2 e^{i\frac{\omega}{c}n_{\mathrm{L}}L_{\mathrm{L}}}}a_1^{(2)}. \tag{C.12}$$

By changing to real space and keeping terms up to second order in the couplings k_{w}, as we did for the right site resonator, we finally arrive to the temporal coupled-mode equation

$$i\dot{a}_1^{(1)} = \omega_0 a_1^{(1)} - i\frac{c}{n_\circ L_{\mathrm{L}}}k_{\mathrm{w}}^2\frac{1}{2}\frac{1 + e^{i\frac{\omega}{c}n_{\mathrm{L}}L_{\mathrm{L}}}}{1 - e^{i\frac{\omega}{c}n_{\mathrm{L}}L_{\mathrm{L}}}}a_1^{(1)} - i\frac{c}{n_{\mathrm{L}}L_\circ}\frac{k_{\mathrm{w}}^2}{2}a_1^{(1)} - i\frac{c}{n_{\mathrm{L}}L_\circ}k_{\mathrm{w}}^2\frac{e^{i\frac{\omega}{c}n_{\mathrm{L}}\frac{L_{\mathrm{L}}}{2}}}{1 - e^{i\frac{\omega}{c}n_{\mathrm{L}}L_{\mathrm{L}}}}a_1^{(2)}$$

$$-\frac{c}{n_{\mathrm{L}}L_\circ}k_{\mathrm{w}}E^{(\mathrm{in})}. \tag{C.13}$$

On the right-hand side of this equation, the second and third terms represent the radiative losses into the link resonator and bus waveguide, respectively. On the other hand, light coupled into the

left site resonator from the right site resonator and the bus waveguide is accounted by means of the third and fourth terms, respectively.

In the notation employed in Chapter 5, the field amplitudes $a_1^{(1)}$ and $a^{(2)}$ would be labelled $a_-^{(1,1)}$ and $a_-^{(1,2)}$, respectivelly. Similar equations can be obtained for the amplitudes belonging to the $+$ pseudospin. It is straightforward to generalize these equations to account for the position shift of the link resonators, and to include the couplings with resonators located on top and on the bottom of the considered plaquette, which give rise to analogous coupling and losses terms as those appearing in Eqs. (C.11) and (C.13).

The 45°-tilted S element of length L_S embedded by the site ring resonators adds a term in the $-$ pseudospin equations of the form

$$-i\frac{c}{n_L L_\circ} 2 k_S^2 e^{i\frac{\omega}{c} n_L \frac{L_\circ}{4}} e^{i\frac{\omega}{c} n_L L_S} a_+,\tag{C.14}$$

which can be understood by considering the length of the optical path connecting the points of the resonator in which the $a_\pm$ amplitudes are measured, and the fact that light can couple into the S waveguide at two different positions.

Appendix D

Mass renormalization for anyonic molecules

$\boxed{\text{I}}$n this Appendix, we show how the Born-Oppenheimer (BO) approach of Ref. [241] can be straightforwardly extended to include synthetic magnetic fields. Such a step is necessary in order to correctly account for the mass renormalization of the anyonic molecules studied in Chapter 7.

We start by writing the full action functional

$$\mathcal{S}[\varphi_{\mathbf{R}}^*, \varphi_{\mathbf{R}}, \chi^*, \chi] = \langle \psi | H - i\partial_t | \psi \rangle = \int_{t_i}^{t_f} dt \int d\mathbf{R} \int d\mathbf{r} \left[|\chi|^2 \varphi_{\mathbf{R}}^* \left(H_{\text{BO}} + \sum_{j=1}^{N} \frac{(-i\nabla_{\mathbf{R}_j})^2}{2M} - i\partial_t \right) \varphi_{\mathbf{R}} \right.$$

$$\left. + |\varphi_{\mathbf{R}}|^2 \chi^* \left(\sum_{j=1}^{N} \frac{(-i\nabla_{\mathbf{R}_j} - Q\mathbf{A}(\mathbf{R}_j))^2}{2M} - i\partial_t \right) \chi + |\chi|^2 \varphi_{\mathbf{R}}^* \sum_{j=1}^{N} \frac{1}{M} \frac{(-i\nabla_{\mathbf{R}_j} - Q\mathbf{A}(\mathbf{R}_j))\chi}{\chi} \cdot (-i\nabla_j) \varphi_{\mathbf{R}} \right] ,$$
(D.1)

in terms of the atoms and impurities wavefunctions $\varphi_{\mathbf{R}}(t)$ and $\chi(t)$. The time dependence of the former is a finite order contribution and it is dropped when one refers to the zeroth order ground state $\varphi_{\mathbf{R}}^{(0)}$. As in the main text, the shorthands $\mathbf{R}$ and $\mathbf{r}$ refer to the set of impurity and atom positions $\{\mathbf{R}_i\}$ and $\{\mathbf{r}_i\}$, respectively. $\mathbf{A}(\mathbf{R}_j)$ is the vector potential (not present in the original formulation of Ref. [241]) evaluated at the position of the impurity j. Requiring

$$\frac{\delta \mathcal{S}[\varphi_{\mathbf{R}}^*, \varphi_{\mathbf{R}}, \chi^*, \chi]}{\delta \varphi_{\mathbf{R}}^*} = 0 , \qquad \frac{\delta \mathcal{S}[\varphi_{\mathbf{R}}^*, \varphi_{\mathbf{R}}, \chi^*, \chi]}{\delta \chi^*} = 0 , \tag{D.2}$$

and using Eqs. (7.7) and (7.11) we obtain the expressions to be satisfied by the factorized wave functions

$$[H_{\text{BO}} + U_{\text{ia}}[\varphi_{\mathbf{R}}, \chi] - \epsilon(\mathbf{R}, t)]\varphi_{\mathbf{R}} = i\partial_t \varphi_{\mathbf{R}} , \tag{D.3}$$

$$\left[\frac{(-i\nabla_{\mathbf{R}_j} - Q\mathbf{A}(\mathbf{R}_j) + \mathcal{A}_j(\mathbf{R}, t))^2}{2M} + \epsilon(\mathbf{R}, t) \right] \chi = i\partial_t \chi , \tag{D.4}$$

where

$$U_{\text{ia}}[\varphi_{\mathbf{R}}, \chi] = \sum_{j=1}^{N} \frac{1}{M} \left[\frac{(-i\nabla_{\mathbf{R}_j} - \mathcal{A}_j(\mathbf{R}, t))^2}{2} + \right.$$

$$\left. \left(\frac{(-i\nabla_{\mathbf{R}_j} - Q\mathbf{A}(\mathbf{R}_j))\chi}{\chi} + \mathcal{A}_j(\mathbf{R}, t) \right) \cdot (-i\nabla_{\mathbf{R}_j} - \mathcal{A}_j(\mathbf{R}, t)) \right] \tag{D.5}$$

is the impurity-bath coupling operator,

$$\mathcal{A}_j(\mathbf{R}, t) = -i \langle \varphi_{\mathbf{R}}(t) | \nabla_{\mathbf{R}_j} | \varphi_{\mathbf{R}}(t) \rangle \tag{D.6}$$

is the Berry connection arising from the parametric dependence of the bath wave function on the position of the impurities and

$$\epsilon(\mathbf{R}, t) = \langle \varphi_{\mathbf{R}}(t) | H_{\mathrm{BO}} + U_{\mathrm{ia}} - i\partial_t | \varphi_{\mathbf{R}}(t) \rangle \tag{D.7}$$

is the BO potential energy surface experienced by the moving impurities, which mediates the exact coupling between fast and slow degrees of freedom.

We see that the complete expressions in Eqs. (D.3)-(D.7) do not include any additional first order modification beyond those calculated in Ref. [241]. Therefore, the renormalized mass of the molecule keeps the same form as in the case without vector potential $\mathbf{A}(\mathbf{R}_j)$, which we show in Eqs. (7.14)-(7.16).

Bibliography

[1] K. v. Klitzing, G. Dorda, and M. Pepper. New method for high-accuracy determination of the fine-structure constant based on quantized hall resistance. *Phys. Rev. Lett.*, 45:494–497, Aug 1980. (cited on pp. 1, 8, and 87)

[2] D. J. Thouless, M. Kohmoto, M. P. Nightingale, and M. den Nijs. Quantized hall conductance in a two-dimensional periodic potential. *Phys. Rev. Lett.*, 49:405–408, Aug 1982. (cited on pp. 1, 14, and 16)

[3] L. D. Landau, E. M. Lifshitz, J. B. Sykes, J. S. Bell, and M. E. Rose. Quantum mechanics, non-relativistic theory: Vol. 3 of course of theoretical physics. *Physics Today*, 11(12):56–59, 1958. (cited on pp. 1 and 8)

[4] M. Z. Hasan and C. L. Kane. *Colloquium: Topological insulators. Rev. Mod. Phys.*, 82:3045–3067, Nov 2010. (cited on pp. 1, 8, and 15)

[5] Zhaoju Yang, Fei Gao, Xihang Shi, Xiao Lin, Zhen Gao, Yidong Chong, and Baile Zhang. Topological acoustics. *Phys. Rev. Lett.*, 114:114301, Mar 2015. (cited on pp. 1 and 18)

[6] Grazia Salerno, Tomoki Ozawa, Hannah M. Price, and Iacopo Carusotto. Floquet topological system based on frequency-modulated classical coupled harmonic oscillators. *Phys. Rev. B*, 93:085105, Feb 2016. (cited on pp. 1 and 18)

[7] Tomoki Ozawa, Hannah M. Price, Alberto Amo, Nathan Goldman, Mohammad Hafezi, Ling Lu, Mikael C. Rechtsman, David Schuster, Jonathan Simon, Oded Zilberberg, and Iacopo Carusotto. *Topological photonics. Rev. Mod. Phys.*, 91:015006, Mar 2019. (cited on pp. 1, 5, 40, 55, 58, 72, and 127)

[8] Eli Yablonovitch. Inhibited spontaneous emission in solid-state physics and electronics. *Phys. Rev. Lett.*, 58:2059–2062, May 1987. (cited on pp. 1 and 20)

[9] Sajeev John. Strong localization of photons in certain disordered dielectric superlattices. *Phys. Rev. Lett.*, 58:2486–2489, Jun 1987. (cited on pp. 1 and 20)

[10] Zheng Wang, Yidong Chong, J. D. Joannopoulos, and Marin Soljačić. Observation of unidirectional backscattering-immune topological electromagnetic states. *Nature*, 461(7265):772–775, Oct 2009. (cited on pp. 1, 20, 23, 27, and 30)

[11] M. Hafezi, S. Mittal, J. Fan, A. Migdall, and J. M. Taylor. Imaging topological edge states in silicon photonics. *Nature Photonics*, 7(12):1001–1005, Dec 2013. (cited on pp. 2, 18, 20, 24, 25, 73, 74, 79, and 81)

[12] Yasutomo Ota, Kenta Takata, Tomoki Ozawa, Alberto Amo, Zhetao Jia, Boubacar Kante, Masaya Notomi, Yasuhiko Arakawa, and Satoshi Iwamoto. Active topological photonics. *Nanophotonics*, 9(3):547–567, 2020. (cited on pp. 2, 5, 21, 23, 37, 40, 58, 72, and 73)

145

[13] Miguel A. Bandres, Steffen Wittek, Gal Harari, Midya Parto, Jinhan Ren, Mordechai Segev, Demetrios N. Christodoulides, and Mercedeh Khajavikhan. Topological insulator laser: Experiments. *Science*, 359(6381), 2018. (cited on pp. 2, 3, 24, 25, 26, 40, 55, 58, 72, 73, 74, and 84)

[14] J. P. Hohimer, G. A. Vawter, and D. C. Craft. Unidirectional operation in a semiconductor ring diode laser. *Applied Physics Letters*, 62(11):1185–1187, 1993. (cited on pp. 2, 37, 39, and 58)

[15] Dirk Jalas, Alexander Petrov, Manfred Eich, Wolfgang Freude, Shanhui Fan, Zongfu Yu, Roel Baets, Miloš Popović, Andrea Melloni, John D. Joannopoulos, Mathias Vanwolleghem, Christopher R. Doerr, and Hagen Renner. What is — and what is not — an optical isolator. *Nature Photonics*, 7(8):579–582, Aug 2013. (cited on pp. 2, 27, 28, and 57)

[16] Logan W. Clark, Nathan Schine, Claire Baum, Ningyuan Jia, and Jonathan Simon. *Observation of Laughlin states made of light*. *Nature*, 582(7810):41–45, Jun 2020. (cited on pp. 2, 100, 101, 104, 105, 127, and 128)

[17] A. Muñoz de las Heras, R. Franchi, S. Biasi, M. Ghulinyan, L. Pavesi, and I. Carusotto. Nonlinearity-induced reciprocity breaking in a single nonmagnetic taiji resonator. *Phys. Rev. Applied*, 15:054044, May 2021. (cited on pp. 3, 27, and 57)

[18] A. Muñoz de las Heras and I. Carusotto. Unidirectional lasing in nonlinear taiji microring resonators. *Phys. Rev. A*, 104:043501, Oct 2021. (cited on pp. 3 and 39)

[19] Yu Shi, Zongfu Yu, and Shanhui Fan. Limitations of nonlinear optical isolators due to dynamic reciprocity. *Nature Photonics*, 9(6):388–392, Jun 2015. (cited on pp. 3, 37, and 57)

[20] A. Muñoz de las Heras, E. Macaluso, and I. Carusotto. Anyonic molecules in atomic fractional quantum hall liquids: A quantitative probe of fractional charge and anyonic statistics. *Phys. Rev. X*, 10:041058, Dec 2020. (cited on p. 4)

[21] Daria Smirnova, Daniel Leykam, Yidong Chong, and Yuri Kivshar. Nonlinear topological photonics. *Applied Physics Reviews*, 7(2):021306, 2020. (cited on pp. 5, 37, and 130)

[22] N. W. Ashcroft and N. D. Mermin. *Solid State Physics*. Holt-Saunders, 1976. (cited on p. 6)

[23] Mahito Kohmoto. Topological invariant and the quantization of the hall conductance. *Annals of Physics*, 160(2):343–354, 1985. (cited on p. 7)

[24] J. E. Avron, R. Seiler, and B. Simon. Homotopy and quantization in condensed matter physics. *Phys. Rev. Lett.*, 51:51–53, Jul 1983. (cited on p. 7)

[25] Barry Simon. Holonomy, the quantum adiabatic theorem, and berry's phase. *Phys. Rev. Lett.*, 51:2167–2170, Dec 1983. (cited on p. 7)

[26] Qian Niu, D. J. Thouless, and Yong-Shi Wu. Quantized hall conductance as a topological invariant. *Phys. Rev. B*, 31:3372–3377, Mar 1985. (cited on pp. 7 and 16)

[27] Ching-Kai Chiu, Jeffrey C. Y. Teo, Andreas P. Schnyder, and Shinsei Ryu. Classification of topological quantum matter with symmetries. *Rev. Mod. Phys.*, 88:035005, Aug 2016. (cited on p. 8)

[28] S. M. Girvin. Course 2: The Quantum Hall Effect: Novel Excitations and Broken Symmetries. In A. Comtet, T. Jolicoeur, S. Ouvry, and F. David, editors, *Topological Aspects of Low Dimensional Systems*, volume 69, page 53, January 1999. (cited on p. 8)

[29] M. O. Goerbig. Quantum hall effects, 2009. (cited on p. 8)

[30] David Tong. *Lectures on the quantum Hall effect*. *arXiv e-prints*, page arXiv:1606.06687, Jun 2016. (cited on pp. 8, 15, 87, 90, 91, 94, 97, 103, 104, 106, 107, 108, 111, 115, and 127)

[31] Ryogo Kubo. Statistical-mechanical theory of irreversible processes. i. general theory and simple applications to magnetic and conduction problems. *Journal of the Physical Society of Japan*, 12(6):570–586, 1957. (cited on p. 14)

[32] Fenner Harper, Steven H. Simon, and Rahul Roy. Perturbative approach to flat chern bands in the hofstadter model. *Phys. Rev. B*, 90:075104, Aug 2014. (cited on pp. 15 and 17)

[33] Yasuhiro Hatsugai. Edge states in the integer quantum hall effect and the riemann surface of the bloch function. *Phys. Rev. B*, 48:11851–11862, Oct 1993. (cited on p. 15)

[34] Xiao-Liang Qi, Yong-Shi Wu, and Shou-Cheng Zhang. General theorem relating the bulk topological number to edge states in two-dimensional insulators. *Phys. Rev. B*, 74:045125, Jul 2006. (cited on p. 15)

[35] P G Harper. Single band motion of conduction electrons in a uniform magnetic field. *Proceedings of the Physical Society. Section A*, 68(10):874–878, oct 1955. (cited on p. 16)

[36] Douglas R. Hofstadter. Energy levels and wave functions of bloch electrons in rational and irrational magnetic fields. *Phys. Rev. B*, 14:2239–2249, Sep 1976. (cited on pp. 16 and 17)

[37] R. Peierls. Zur theorie des diamagnetismus von leitungselektronen. *Zeitschrift für Physik*, 80(11):763–791, Nov 1933. (cited on p. 16)

[38] J. M. Luttinger. The effect of a magnetic field on electrons in a periodic potential. *Phys. Rev.*, 84:814–817, Nov 1951. (cited on p. 16)

[39] U. Kuhl and H.-J. Stöckmann. Microwave realization of the hofstadter butterfly. *Phys. Rev. Lett.*, 80:3232–3235, Apr 1998. (cited on p. 16)

[40] Takahiro Fukui, Yasuhiro Hatsugai, and Hiroshi Suzuki. Chern numbers in discretized brillouin zone: Efficient method of computing (spin) hall conductances. *Journal of the Physical Society of Japan*, 74(6):1674–1677, 2005. (cited on p. 16)

[41] A. M. Chang, L. N. Pfeiffer, and K. W. West. Observation of chiral luttinger behavior in electron tunneling into fractional quantum hall edges. *Phys. Rev. Lett.*, 77:2538–2541, Sep 1996. (cited on pp. 16 and 92)

[42] Di Xiao, Ming-Che Chang, and Qian Niu. Berry phase effects on electronic properties. *Rev. Mod. Phys.*, 82:1959–2007, Jul 2010. (cited on p. 16)

[43] Mikio Nakahara. *Geometry, topology and physics*. Graduate student series in physics. Hilger, Bristol, 1990. (cited on p. 17)

[44] M Mochol-Grzelak, A Dauphin, A Celi, and M Lewenstein. Efficient algorithm to compute the second chern number in four dimensional systems. *Quantum Science and Technology*, 4(1):014009, nov 2018. (cited on p. 17)

[45] B. ANDREI BERNEVIG and Taylor L. Hughes. *Topological Insulators and Topological Superconductors*. Princeton University Press, stu - student edition edition, 2013. (cited on p. 17)

[46] C. L. Kane and E. J. Mele. Quantum spin hall effect in graphene. *Phys. Rev. Lett.*, 95:226801, Nov 2005. (cited on p. 17)

[47] B. Andrei Bernevig and Shou-Cheng Zhang. Quantum spin hall effect. *Phys. Rev. Lett.*, 96:106802, Mar 2006. (cited on p. 17)

[48] Markus König, Steffen Wiedmann, Christoph Brüne, Andreas Roth, Hartmut Buhmann, Laurens Molenkamp, Xiao-Liang Qi, and Shou-Cheng Zhang. Quantum spin hall insulator state in hgte quantum wells. *Science (New York, N.Y.)*, 318:766–70, 12 2007. (cited on p. 18)

[49] Liang Fu, C. L. Kane, and E. J. Mele. Topological insulators in three dimensions. *Phys. Rev. Lett.*, 98:106803, Mar 2007. (cited on p. 18)

[50] Mohammad Hafezi, Eugene A. Demler, Mikhail D. Lukin, and Jacob M. Taylor. Robust optical delay lines with topological protection. *Nature Physics*, 7(11):907–912, Nov 2011. (cited on p. 18)

[51] Richard P. Feynman. Simulating physics with computers. *International Journal of Theoretical Physics*, 21(6):467–488, Jun 1982. (cited on p. 18)

[52] Immanuel Bloch, Jean Dalibard, and Sylvain Nascimbène. Quantum simulations with ultracold quantum gases. *Nature Physics*, 8(4):267–276, Apr 2012. (cited on p. 18)

[53] Iacopo Carusotto and Cristiano Ciuti. *Quantum fluids of light. Rev. Mod. Phys.*, 85:299–366, Feb 2013. (cited on pp. 18, 22, 58, 59, 67, 70, 100, and 103)

[54] Alán Aspuru-Guzik and Philip Walther. Photonic quantum simulators. *Nature Physics*, 8(4):285–291, Apr 2012. (cited on p. 18)

[55] Andrew A. Houck, Hakan E. Türeci, and Jens Koch. On-chip quantum simulation with superconducting circuits. *Nature Physics*, 8(4):292–299, Apr 2012. (cited on p. 18)

[56] R. Blatt and C. F. Roos. Quantum simulations with trapped ions. *Nature Physics*, 8(4):277–284, Apr 2012. (cited on p. 18)

[57] L.P. Pitaevskii and S. Stringari. *Bose-Einstein condensation and superfluidity.* International series of monographs on physics. Oxford University Press, 2016. (cited on pp. 19 and 103)

[58] Immanuel Bloch, Jean Dalibard, and Wilhelm Zwerger. Many-body physics with ultracold gases. *Rev. Mod. Phys.*, 80:885–964, Jul 2008. (cited on p. 19)

[59] Waseem S. Bakr, Jonathon I. Gillen, Amy Peng, Simon Fölling, and Markus Greiner. A quantum gas microscope for detecting single atoms in a hubbard-regime optical lattice. *Nature*, 462(7269):74–77, Nov 2009. (cited on p. 19)

[60] Jacob F. Sherson, Christof Weitenberg, Manuel Endres, Marc Cheneau, Immanuel Bloch, and Stefan Kuhr. Single-atom-resolved fluorescence imaging of an atomic mott insulator. *Nature*, 467(7311):68–72, Sep 2010. (cited on p. 19)

[61] D. Jaksch and P. Zoller. The cold atom hubbard toolbox. *Annals of Physics*, 315(1):52–79, 2005. Special Issue. (cited on p. 19)

[62] Oliver Morsch and Markus Oberthaler. Dynamics of bose-einstein condensates in optical lattices. *Rev. Mod. Phys.*, 78:179–215, Feb 2006. (cited on p. 19)

[63] Maciej Lewenstein, Anna Sanpera, Veronica Ahufinger, Bogdan Damski, Aditi Sen(De), and Ujjwal Sen. Ultracold atomic gases in optical lattices: mimicking condensed matter physics and beyond. *Advances in Physics*, 56(2):243–379, 2007. (cited on p. 19)

[64] M. Aidelsburger, M. Lohse, C. Schweizer, M. Atala, J. T. Barreiro, S. Nascimbène, N. R. Cooper, I. Bloch, and N. Goldman. Measuring the chern number of hofstadter bands with ultracold bosonic atoms. *Nature Physics*, 11(2):162–166, Feb 2015. (cited on p. 19)

[65] N. R. Cooper, J. Dalibard, and I. B. Spielman. *Topological bands for ultracold atoms. Rev. Mod. Phys.*, 91:015005, Mar 2019. (cited on p. 19)

[66] N.R. Cooper. *Rapidly rotating atomic gases. Advances in Physics*, 57(6):539–616, 2008. (cited on pp. 19, 105, and 106)

[67] Jean Dalibard, Fabrice Gerbier, Gediminas Juzeliūnas, and Patrik Öhberg. *Colloquium: Artificial gauge potentials for neutral atoms. Rev. Mod. Phys.*, 83:1523–1543, Nov 2011. (cited on pp. 19 and 103)

[68] Vincent Bretin, Sabine Stock, Yannick Seurin, and Jean Dalibard. Fast rotation of a bose-einstein condensate. *Phys. Rev. Lett.*, 92:050403, Feb 2004. (cited on p. 19)

[69] V. Schweikhard, I. Coddington, P. Engels, V. P. Mogendorff, and E. A. Cornell. Rapidly rotating bose-einstein condensates in and near the lowest landau level. *Phys. Rev. Lett.*, 92:040404, Jan 2004. (cited on p. 19)

[70] R. Dum and M. Olshanii. Gauge structures in atom-laser interaction: Bloch oscillations in a dark lattice. *Phys. Rev. Lett.*, 76:1788–1791, Mar 1996. (cited on p. 19)

[71] G. Juzeliūnas and P. Öhberg. Slow light in degenerate fermi gases. *Phys. Rev. Lett.*, 93:033602, Jul 2004. (cited on p. 19)

[72] G. Juzeliūnas, J. Ruseckas, P. Öhberg, and M. Fleischhauer. Light-induced effective magnetic fields for ultracold atoms in planar geometries. *Phys. Rev. A*, 73:025602, Feb 2006. (cited on p. 19)

[73] N Goldman, G Juzeliūnas, P Öhberg, and I B Spielman. Light-induced gauge fields for ultracold atoms. *Reports on Progress in Physics*, 77(12):126401, nov 2014. (cited on p. 19)

[74] Y.-J. Lin, R. L. Compton, K. Jiménez-García, J. V. Porto, and I. B. Spielman. Synthetic magnetic fields for ultracold neutral atoms. *Nature*, 462(7273):628–632, Dec 2009. (cited on p. 19)

[75] D Jaksch and P Zoller. Creation of effective magnetic fields in optical lattices: the hofstadter butterfly for cold neutral atoms. *New Journal of Physics*, 5:56–56, may 2003. (cited on p. 20)

[76] M. Aidelsburger, M. Atala, M. Lohse, J. T. Barreiro, B. Paredes, and I. Bloch. Realization of the hofstadter hamiltonian with ultracold atoms in optical lattices. *Phys. Rev. Lett.*, 111:185301, Oct 2013. (cited on p. 20)

[77] Hirokazu Miyake, Georgios A. Siviloglou, Colin J. Kennedy, William Cody Burton, and Wolfgang Ketterle. Realizing the harper hamiltonian with laser-assisted tunneling in optical lattices. *Phys. Rev. Lett.*, 111:185302, Oct 2013. (cited on p. 20)

[78] J. Struck, C. Ölschläger, M. Weinberg, P. Hauke, J. Simonet, A. Eckardt, M. Lewenstein, K. Sengstock, and P. Windpassinger. Tunable gauge potential for neutral and spinless particles in driven optical lattices. *Phys. Rev. Lett.*, 108:225304, May 2012. (cited on p. 20)

[79] Gregor Jotzu, Michael Messer, Rémi Desbuquois, Martin Lebrat, Thomas Uehlinger, Daniel Greif, and Tilman Esslinger. Experimental realization of the topological haldane model with ultracold fermions. *Nature*, 515(7526):237–240, Nov 2014. (cited on p. 20)

[80] John David Jackson. *Classical electrodynamics; 2nd ed.* Wiley, New York, NY, 1975. (cited on p. 20)

[81] F. D. M. Haldane and S. Raghu. Possible realization of directional optical waveguides in photonic crystals with broken time-reversal symmetry. *Phys. Rev. Lett.*, 100:013904, Jan 2008. (cited on pp. 20 and 23)

[82] S. Raghu and F. D. M. Haldane. Analogs of quantum-hall-effect edge states in photonic crystals. *Phys. Rev. A*, 78:033834, Sep 2008. (cited on pp. 20 and 23)

[83] Mikael C. Rechtsman, Julia M. Zeuner, Yonatan Plotnik, Yaakov Lumer, Daniel Podolsky, Felix Dreisow, Stefan Nolte, Mordechai Segev, and Alexander Szameit. Photonic floquet topological insulators. *Nature*, 496(7444):196–200, Apr 2013. (cited on p. 21)

[84] Nathan Schine, Albert Ryou, Andrey Gromov, Ariel Sommer, and Jonathan Simon. *Synthetic Landau levels for photons.* *Nature*, 534:671 EP –, Jun 2016. (cited on pp. 21, 100, 104, and 105)

[85] Yi Chen Hu and Taylor L. Hughes. Absence of topological insulator phases in non-hermitian *pt*-symmetric hamiltonians. *Phys. Rev. B*, 84:153101, Oct 2011. (cited on p. 21)

[86] Kenta Esaki, Masatoshi Sato, Kazuki Hasebe, and Mahito Kohmoto. Edge states and topological phases in non-hermitian systems. *Phys. Rev. B*, 84:205128, Nov 2011. (cited on p. 21)

[87] P. St-Jean, V. Goblot, E. Galopin, A. Lemaître, T. Ozawa, L. Le Gratiet, I. Sagnes, J. Bloch, and A. Amo. Lasing in topological edge states of a one-dimensionallattice. *Nature Photonics*, 11(10):651–656, Oct 2017. (cited on pp. 21 and 22)

[88] Babak Bahari, Abdoulaye Ndao, Felipe Vallini, Abdelkrim El Amili, Yeshaiahu Fainman, and Boubacar Kanté. Nonreciprocal lasing in topological cavities of arbitrary geometries. *Science*, 358(6363):636–640, 2017. (cited on p. 23)

[89] R J Potton. Reciprocity in optics. *Reports on Progress in Physics*, 67(5):717–754, apr 2004. (cited on pp. 27 and 57)

[90] D. A. B. Miller. Rationale and challenges for optical interconnects to electronic chips. *Proceedings of the IEEE*, 88(6):728–749, 2000. (cited on p. 27)

[91] I. P. Kaminow. Optical integrated circuits: A personal perspective. *Journal of Lightwave Technology*, 26(9):994–1004, 2008. (cited on p. 27)

[92] R. Nagarajan, M. Kato, J. Pleumeekers, P. Evans, S. Corzine, S. Hurtt, A. Dentai, S. Murthy, M. Missey, R. Muthiah, R. A. Salvatore, C. Joyner, R. Schneider, M. Ziari, F. Kish, and D. Welch. Inp photonic integrated circuits. *IEEE Journal of Selected Topics in Quantum Electronics*, 16(5):1113–1125, 2010. (cited on p. 27)

[93] Horst Dötsch, Norbert Bahlmann, Oleksandr Zhuromskyy, Manfred Hammer, Ludger Wilkens, Reinald Gerhardt, Peter Hertel, and Anatoly F. Popkov. Applications of magneto-optical waveguides in integrated optics: review. *J. Opt. Soc. Am. B*, 22(1):240–253, Jan 2005. (cited on pp. 27, 30, and 57)

[94] Zheng Wang and Shanhui Fan. Optical circulators in two-dimensional magneto-optical photonic crystals. *Opt. Lett.*, 30(15):1989–1991, Aug 2005. (cited on pp. 27 and 30)

[95] Lei Bi, Juejun Hu, Peng Jiang, Dong Hun Kim, Gerald F. Dionne, Lionel C. Kimerling, and C. A. Ross. On-chip optical isolation in monolithically integrated non-reciprocal optical resonators. *Nature Photonics*, 5(12):758–762, Dec 2011. (cited on pp. 27, 30, and 57)

[96] Yuya Shoji, Masatoshi Ito, Yuya Shirato, and Tetsuya Mizumoto. Mzi optical isolator with si-wire waveguides by surface-activated direct bonding. *Opt. Express*, 20(16):18440–18448, Jul 2012. (cited on pp. 27, 30, and 57)

[97] Tomoki Ozawa, Hannah M. Price, Alberto Amo, Nathan Goldman, Mohammad Hafezi, Ling Lu, Mikael C. Rechtsman, David Schuster, Jonathan Simon, Oded Zilberberg, and Iacopo Carusotto. Topological photonics. *Rev. Mod. Phys.*, 91:015006, Mar 2019. (cited on pp. 27 and 37)

[98] Wei Yan, Yucong Yang, Shuyuan Liu, Yan Zhang, Shuang Xia, Tongtong Kang, Weihao Yang, Jun Qin, Longjiang Deng, and Lei Bi. Waveguide-integrated high-performance magneto-optical isolators and circulators on silicon nitride platforms. *Optica*, 7(11):1555–1562, Nov 2020. (cited on pp. 27 and 57)

[99] S. Bhandare, S. K. Ibrahim, D. Sandel, Hongbin Zhang, F. Wust, and R. Noe. Novel nonmagnetic 30-db traveling-wave single-sideband optical isolator integrated in iii/v material. *IEEE Journal of Selected Topics in Quantum Electronics*, 11(2):417–421, 2005. (cited on pp. 27 and 57)

[100] Zongfu Yu and Shanhui Fan. Complete optical isolation created by indirect interband photonic transitions. *Nature Photonics*, 3(2):91–94, Feb 2009. (cited on pp. 27, 30, and 57)

[101] Kejie Fang, Zongfu Yu, and Shanhui Fan. Realizing effective magnetic field for photons by controlling the phase of dynamic modulation. *Nature Photonics*, 6(11):782–787, Nov 2012. (cited on pp. 27 and 57)

[102] Christophe Galland, Ran Ding, Nicholas C. Harris, Tom Baehr-Jones, and Michael Hochberg. Broadband on-chip optical non-reciprocity using phase modulators. *Opt. Express*, 21(12):14500–14511, Jun 2013. (cited on pp. 27 and 57)

[103] C. R. Doerr, L. Chen, and D. Vermeulen. Silicon photonics broadband modulation-based isolator. *Opt. Express*, 22(4):4493–4498, Feb 2014. (cited on pp. 27 and 57)

[104] Li Fan, Jian Wang, Leo T. Varghese, Hao Shen, Ben Niu, Yi Xuan, Andrew M. Weiner, and Minghao Qi. An all-silicon passive optical diode. *Science*, 335(6067):447–450, 2012. (cited on pp. 27 and 57)

[105] Ang Li and Wim Bogaerts. Reconfigurable nonlinear nonreciprocal transmission in a silicon photonic integrated circuit. *Optica*, 7(1):7–14, Jan 2020. (cited on p. 28)

[106] Parinaz Aleahmad, Mercedeh Khajavikhan, Demetrios Christodoulides, and Patrick LiKamWa. Integrated multi-port circulators for unidirectional optical information transport. *Scientific Reports*, 7(1):2129, May 2017. (cited on p. 28)

[107] Bo Peng, Şahin Kaya Özdemir, Fuchuan Lei, Faraz Monifi, Mariagiovanna Gianfreda, Gui Lu Long, Shanhui Fan, Franco Nori, Carl M. Bender, and Lan Yang. Parity–time-symmetric whispering-gallery microcavities. *Nature Physics*, 10(5):394–398, May 2014. (cited on pp. 28 and 57)

[108] Long Chang, Xiaoshun Jiang, Shiyue Hua, Chao Yang, Jianming Wen, Liang Jiang, Guanyu Li, Guanzhong Wang, and Min Xiao. Parity–time symmetry and variable optical isolation in active–passive-coupled microresonators. *Nature Photonics*, 8(7):524–529, Jul 2014. (cited on pp. 28 and 57)

[109] Leonardo Del Bino, Jonathan M. Silver, Sarah L. Stebbings, and Pascal Del'Haye. Symmetry breaking of counter-propagating light in a nonlinear resonator. *Scientific Reports*, 7(1):43142, Feb 2017. (cited on pp. 28, 30, and 58)

[110] Leonardo Del Bino, Jonathan M. Silver, Michael T. M. Woodley, Sarah L. Stebbings, Xin Zhao, and Pascal Del'Haye. Microresonator isolators and circulators based on the intrinsic nonreciprocity of the kerr effect. *Optica*, 5(3):279–282, Mar 2018. (cited on pp. 28, 30, and 58)

[111] Lukas J. Maczewsky, Matthias Heinrich, Mark Kremer, Sergey K. Ivanov, Max Ehrhardt, Franklin Martinez, Yaroslav V. Kartashov, Vladimir V. Konotop, Lluis Torner, Dieter Bauer, and Alexander Szameit. Nonlinearity-induced photonic topological insulator. *Science*, 370(6517):701–704, 2020. (cited on p. 28)

[112] A. Calabrese, F. Ramiro-Manzano, H. M. Price, S. Biasi, M. Bernard, M. Ghulinyan, I. Carusotto, and L. Pavesi. Unidirectional reflection from an integrated taiji microresonator. *Photon. Res.*, 8(8):1333–1341, Aug 2020. (cited on pp. 28, 32, and 33)

[113] Wouter Van Parys, Bart Moeyersoon, Dries Van Thourhout, Roel Baets, Mathias Vanwolleghem, Beatrice Dagens, Jean Decobert, Odile Le Gouezigou, Dalila Make, Reinier Vanheertum, and Liesbet Lagae. Transverse magnetic mode nonreciprocal propagation in an amplifying algainas-inp optical waveguide isolator. *Applied Physics Letters*, 88(7):071115, 2006. (cited on p. 30)

[114] Hugo Lira, Zongfu Yu, Shanhui Fan, and Michal Lipson. Electrically driven nonreciprocity induced by interband photonic transition on a silicon chip. *Phys. Rev. Lett.*, 109:033901, Jul 2012. (cited on p. 30)

[115] M. M. Krause, H. Renner H., and E. Brinkmeyer. Optical isolation in silicon waveguides based on nonreciprocal raman amplification. *Electronics Letters*, 44:691–693(2), May 2008. (cited on p. 30)

[116] Christopher G. Poulton, Ravi Pant, Adam Byrnes, Shanhui Fan, M. J. Steel, and Benjamin J. Eggleton. Design for broadband on-chip isolator using stimulated brillouin scattering in dispersion-engineered chalcogenide waveguides. *Opt. Express*, 20(19):21235–21246, Sep 2012. (cited on p. 30)

[117] Michael D. Tocci, Mark J. Bloemer, Michael Scalora, Jonathan P. Dowling, and Charles M. Bowden. Thin-film nonlinear optical diode. *Applied Physics Letters*, 66(18):2324–2326, 1995. (cited on p. 30)

[118] Katia Gallo, Gaetano Assanto, Krishnan R. Parameswaran, and Martin M. Fejer. All-optical diode in a periodically poled lithium niobate waveguide. *Applied Physics Letters*, 79(3):314–316, 2001. (cited on p. 30)

[119] D.F. Walls and G.J. Milburn. *Quantum Optics*. Springer Study Edition. Springer Berlin Heidelberg, 2012. (cited on p. 30)

[120] Mher Ghulinyan, Fernando Ramiro Manzano, Nikola Prtljaga, Martino Bernard, Lorenzo Pavesi, Georg Pucker, and Iacopo Carusotto. Intermode reactive coupling induced by waveguide-resonator interaction. *Phys. Rev. A*, 90:053811, Nov 2014. (cited on p. 30)

[121] R. Y. Chiao, P. L. Kelley, and E. Garmire. Stimulated four-photon interaction and its influence on stimulated rayleigh-wing scattering. *Phys. Rev. Lett.*, 17:1158–1161, Nov 1966. (cited on p. 31)

[122] A. E. Kaplan. Light-induced nonreciprocity, field invariants, and nonlinear eigenpolarizations. *Opt. Lett.*, 8(11):560–562, Nov 1983. (cited on p. 31)

[123] George N. Ghalanos, Jonathan M. Silver, Leonardo Del Bino, Niall Moroney, Shuangyou Zhang, Michael T. M. Woodley, Andreas Ø. Svela, and Pascal Del'Haye. Kerr-nonlinearity-induced mode-splitting in optical microresonators. *Phys. Rev. Lett.*, 124:223901, Jun 2020. (cited on p. 31)

[124] V. Ilchenko and M. L. Gorodetskii. Thermal nonlinear effects in optical whispering gallery microresonators. *Laser Physics*, 2:1004–1009, 1992. (cited on p. 31)

[125] R. W. Boyd. *Nonlinear Optics*. Academic Press, 2008. (cited on p. 32)

[126] P. N. Butcher and D. Cotter. *The elements of nonlinear optics*. Cambridge Studies in Modern Optics. Cambridge University Press, 2008. (cited on p. 32)

[127] Hyatt M. Gibbs. *Optical Bistability: Controlling Light with Light*. Academic Press, 1985. (cited on p. 32)

[128] F. Ramiro-Manzano, N. Prtljaga, L. Pavesi, G. Pucker, and M. Ghulinyan. Thermo-optical bistability with si nanocrystals in a whispering gallery mode resonator. *Opt. Lett.*, 38(18):3562–3565, Sep 2013. (cited on p. 32)

[129] Martino Bernard, Fernando Ramiro Manzano, Lorenzo Pavesi, Georg Pucker, Iacopo Carusotto, and Mher Ghulinyan. Complete crossing of fano resonances in an optical microcavity via nonlinear tuning. *Photon. Res.*, 5(3):168–175, Jun 2017. (cited on p. 32)

[130] A. Trenti, M. Borghi, S. Biasi, M. Ghulinyan, F. Ramiro-Manzano, G. Pucker, and L. Pavesi. Thermo-optic coefficient and nonlinear refractive index of silicon oxynitride waveguides. *AIP Advances*, 8(2):025311, 2018. (cited on pp. 33 and 59)

[131] C. Castellan, S. Tondini, M. Mancinelli, C. Kopp, and L. Pavesi. Reflectance reduction in a whiskered soi star coupler. *IEEE Photonics Technology Letters*, 28(17):1870–1873, 2016. (cited on pp. 33 and 40)

[132] Riccardo Franchi, Stefano Biasi, Alberto Mu noz de las Heras, Mher Ghulinyan, Iacopo Carusotto, and Lorenzo Pavesi. Influence of the bus waveguide on the linear and nonlinear response of a taiji microresonator. *Opt. Express*, 29(19):29615–29630, Sep 2021. (cited on p. 33)

[133] W. W. Chow, J. Gea-Banacloche, L. M. Pedrotti, V. E. Sanders, W. Schleich, and M. O. Scully. The ring laser gyro. *Rev. Mod. Phys.*, 57:61–104, Jan 1985. (cited on p. 39)

[134] Stephan Burkhardt, Matthias Liertzer, Dmitry O. Krimer, and Stefan Rotter. Steady-state ab initio laser theory for fully or nearly degenerate cavity modes. *Phys. Rev. A*, 92:013847, Jul 2015. (cited on p. 39)

[135] Surendra Singh and L. Mandel. Mode competition in a homogeneously broadened ring laser. *Phys. Rev. A*, 20:2459–2463, Dec 1979. (cited on p. 39)

[136] P. Lett, W. Christian, Surendra Singh, and L. Mandel. Macroscopic quantum fluctuations and first-order phase transition in a laser. *Phys. Rev. Lett.*, 47:1892–1895, Dec 1981. (cited on p. 39)

[137] H. Zeghlache, Paul Mandel, N. B. Abraham, L. M. Hoffer, G. L. Lippi, and T. Mello. Bidirectional ring laser: Stability analysis and time-dependent solutions. *Phys. Rev. A*, 37:470–497, Jan 1988. (cited on p. 39)

[138] G. Mezosi, M. J. Strain, S. Furst, Z. Wang, S. Yu, and M. Sorel. Unidirectional bistability in algainas microring and microdisk semiconductor lasers. *IEEE Photonics Technology Letters*, 21(2):88–90, 2009. (cited on p. 39)

[139] Fuad Rawwagah and Surendra Singh. Nonlinear dynamics of a modulated bidirectional solid-state ring laser. *J. Opt. Soc. Am. B*, 23(9):1785–1792, Sep 2006. (cited on p. 39)

[140] Sylvain Schwartz, Gilles Feugnet, Philippe Bouyer, Evguenii Lariontsev, Alain Aspect, and Jean-Paul Pocholle. Mode-coupling control in resonant devices: Application to solid-state ring lasers. *Phys. Rev. Lett.*, 97:093902, Aug 2006. (cited on p. 39)

[141] Sylvain Schwartz, Gilles Feugnet, Evguenii Lariontsev, and Jean-Paul Pocholle. Oscillation regimes of a solid-state ring laser with active beat-note stabilization: From a chaotic device to a ring-laser gyroscope. *Phys. Rev. A*, 76:023807, Aug 2007. (cited on pp. 39 and 52)

[142] G. Morthier and P. Mechet. Theoretical analysis of unidirectional operation and reflection sensitivity of semiconductor ring or disk lasers. *IEEE Journal of Quantum Electronics*, 49(12):1097–1101, 2013. (cited on p. 39)

[143] Jean-Baptiste Ceppe, Patrice Féron, Michel Mortier, and Yannick Dumeige. Dynamical analysis of modal coupling in rare-earth whispering-gallery-mode microlasers. *Phys. Rev. Applied*, 11:064028, Jun 2019. (cited on pp. 39 and 52)

[144] Anthony E. Siegman. *Lasers*. University Science Books, 1986. (cited on p. 39)

[145] J. P. Hohimer and G. A. Vawter. Unidirectional semiconductor ring lasers with racetrack cavities. *Applied Physics Letters*, 63(18):2457–2459, 1993. (cited on pp. 39 and 58)

[146] Yuan Shi, M. Sejka, and O. Poulsen. A unidirectional er/sup 3+/-doped fiber ring laser without isolator. *IEEE Photonics Technology Letters*, 7(3):290–292, 1995. (cited on p. 39)

[147] Svyatoslav Kharitonov and Camille-Sophie Brès. Isolator-free unidirectional thulium-doped fiber laser. *Light: Science & Applications*, 4(10):e340–e340, Oct 2015. (cited on p. 39)

[148] Wesley D. Sacher, Michael L. Davenport, Martijn J. R. Heck, Jared C. Mikkelsen, Joyce K. S. Poon, and John E. Bowers. Unidirectional hybrid silicon ring laser with an intracavity s-bend. *Opt. Express*, 23(20):26369–26376, Oct 2015. (cited on p. 39)

[149] Jinhan Ren, Yuzhou G. N. Liu, Midya Parto, William E. Hayenga, Mohammad P. Hokmabadi, Demetrios N. Christodoulides, and Mercedeh Khajavikhan. Unidirectional light emission in pt-symmetric microring lasers. *Opt. Express*, 26(21):27153–27160, Oct 2018. (cited on pp. 40 and 130)

[150] Yuzhou G. N. Liu, Omid Hemmatyar, Absar U. Hassan, Pawel S. Jung, Jae-Hyuck Choi, Demetrios N. Christodoulides, and Mercedeh Khajavikhan. Engineering interaction dynamics in active resonant photonic structures. *APL Photonics*, 6(5):050804, 2021. (cited on p. 40)

[151] S. Soleymani, Q. Zhong, M. Mokim, S. Rotter, R. El-Ganainy, and S. K. Ozdemir. Chiral Coherent Perfect Absorption on Exceptional Surfaces. *arXiv e-prints*, page arXiv:2107.06019, July 2021. (cited on p. 40)

[152] Jin-Woong Lee, Kyoung-Youm Kim, Hee-Jong Moon, and Kyung-Sook Hyun. Selection of lasing direction in single mode semiconductor square ring cavities. *Journal of Applied Physics*, 119(5):053101, 2016. (cited on p. 40)

[153] Bo Peng, Şahin Kaya Özdemir, Matthias Liertzer, Weijian Chen, Johannes Kramer, Huzeyfe Yılmaz, Jan Wiersig, Stefan Rotter, and Lan Yang. Chiral modes and directional lasing at exceptional points. *Proceedings of the National Academy of Sciences*, 113(25):6845–6850, 2016. (cited on pp. 40 and 49)

[154] Qi-Tao Cao, Ruishan Liu, Heming Wang, Yu-Kun Lu, Cheng-Wei Qiu, Stefan Rotter, Qi-huang Gong, and Yun-Feng Xiao. Reconfigurable symmetry-broken laser in a symmetric microcavity. *Nature Communications*, 11(1):1136, Feb 2020. (cited on p. 40)

[155] Gal Harari, Miguel A. Bandres, Yaakov Lumer, Mikael C. Rechtsman, Y. D. Chong, Mercedeh Khajavikhan, Demetrios N. Christodoulides, and Mordechai Segev. Topological insulator laser: Theory. *Science*, 359(6381), 2018. (cited on pp. 40, 58, and 72)

[156] C. Henry. Theory of the linewidth of semiconductor lasers. *IEEE Journal of Quantum Electronics*, 18(2):259–264, 1982. (cited on p. 41)

[157] D. F. Walls and G. J. Milburn. *Quantum optics*. Springer-Verlag Berlin Heidelberg, New York, 2008. (cited on p. 41)

[158] Iacopo Carusotto and Cristiano Ciuti. Quantum fluids of light. *Rev. Mod. Phys.*, 85:299–366, Feb 2013. (cited on p. 41)

[159] Mher Ghulinyan, Fernando Ramiro Manzano, Nikola Prtljaga, Martino Bernard, Lorenzo Pavesi, Georg Pucker, and Iacopo Carusotto. Intermode reactive coupling induced by waveguide-resonator interaction. *Phys. Rev. A*, 90:053811, Nov 2014. (cited on p. 41)

[160] J. Hambenne and M. Sargent. Physical interpretation of bistable unidirectional ring-laser operation. *IEEE Journal of Quantum Electronics*, 11(2):90–92, 1975. (cited on p. 41)

[161] Ivan Amelio and Iacopo Carusotto. Theory of the coherence of topological lasers. *Phys. Rev. X*, 10:041060, Dec 2020. (cited on pp. 41, 61, and 76)

[162] Aurelian Loirette-Pelous, Ivan Amelio, Matteo Seclì, and Iacopo Carusotto. Linearized theory of the fluctuation dynamics in 2d topological lasers, 2021. (cited on pp. 41, 61, 76, and 82)

[163] S. Biasi, F. Ramiro-Manzano, F. Turri, P. Larré, M. Ghulinyan, I. Carusotto, and L. Pavesi. Hermitian and non-hermitian mode coupling in a microdisk resonator due to stochastic surface roughness scattering. *IEEE Photonics Journal*, 11(2):1–14, 2019. (cited on pp. 47 and 50)

[164] N. Bender, S. Factor, J. D. Bodyfelt, H. Ramezani, D. N. Christodoulides, F. M. Ellis, and T. Kottos. Observation of asymmetric transport in structures with active nonlinearities. *Phys. Rev. Lett.*, 110:234101, Jun 2013. (cited on p. 57)

[165] Matteo Seclì, Massimo Capone, and Iacopo Carusotto. Theory of chiral edge state lasing in a two-dimensional topological system. *Phys. Rev. Research*, 1:033148, Dec 2019. (cited on p. 75)

[166] X. G. Wen. Vacuum degeneracy of chiral spin states in compactified space. *Phys. Rev. B*, 40:7387–7390, Oct 1989. (cited on pp. 87 and 92)

[167] Xie Chen, Zheng-Cheng Gu, and Xiao-Gang Wen. Local unitary transformation, long-range quantum entanglement, wave function renormalization, and topological order. *Phys. Rev. B*, 82:155138, Oct 2010. (cited on p. 87)

[168] Chetan Nayak, Steven H. Simon, Ady Stern, Michael Freedman, and Sankar Das Sarma. *Non-Abelian anyons and topological quantum computation. Rev. Mod. Phys.*, 80:1083–1159, Sep 2008. (cited on pp. 87, 97, 98, and 99)

[169] I. M. Georgescu, S. Ashhab, and Franco Nori. Quantum simulation. *Rev. Mod. Phys.*, 86:153–185, Mar 2014. (cited on p. 87)

[170] D. C. Tsui, H. L. Stormer, and A. C. Gossard. *Two-dimensional magnetotransport in the extreme quantum limit. Phys. Rev. Lett.*, 48:1559–1562, May 1982. (cited on pp. 88 and 103)

[171] Hailong Fu, Yijia Wu, Ruoxi Zhang, Jian Sun, Pujia Shan, Pengjie Wang, Zheyi Zhu, L. N. Pfeiffer, K. W. West, Haiwen Liu, X. C. Xie, and Xi Lin. 3/2 fractional quantum hall plateau in confined two-dimensional electron gas. *Nature Communications*, 10(1):4351, Sep 2019. (cited on p. 88)

[172] R. B. Laughlin. *Anomalous quantum Hall effect: An incompressible quantum fluid with fractionally charged excitations. Phys. Rev. Lett.*, 50:1395–1398, May 1983. (cited on pp. 88, 90, and 107)

[173] R. Willett, J. P. Eisenstein, H. L. Störmer, D. C. Tsui, A. C. Gossard, and J. H. English. Observation of an even-denominator quantum number in the fractional quantum hall effect. *Phys. Rev. Lett.*, 59:1776–1779, Oct 1987. (cited on p. 88)

[174] X. G. WEN. Topological orders in rigid states. *International Journal of Modern Physics B*, 04(02):239–271, 1990. (cited on p. 91)

[175] Xiao-Gang Wen. Colloquium: Zoo of quantum-topological phases of matter. *Rev. Mod. Phys.*, 89:041004, Dec 2017. (cited on pp. 92 and 97)

[176] Xiao-Gang Wen. Choreographed entanglement dances: Topological states of quantum matter. *Science*, 363(6429), 2019. (cited on pp. 92 and 97)

[177] X. G. Wen and Q. Niu. Ground-state degeneracy of the fractional quantum hall states in the presence of a random potential and on high-genus riemann surfaces. *Phys. Rev. B*, 41:9377–9396, May 1990. (cited on p. 92)

[178] Xiao-Gang Wen. Topological orders and edge excitations in fractional quantum hall states. *Advances in Physics*, 44(5):405–473, 1995. (cited on p. 92)

[179] A. M. Chang. Chiral luttinger liquids at the fractional quantum hall edge. *Rev. Mod. Phys.*, 75:1449–1505, Nov 2003. (cited on p. 92)

[180] S. M. Girvin, A. H. MacDonald, and P. M. Platzman. Magneto-roton theory of collective excitations in the fractional quantum hall effect. *Phys. Rev. B*, 33:2481–2494, Feb 1986. (cited on p. 92)

[181] Y. Aharonov and D. Bohm. *Significance of electromagnetic potentials in the quantum theory.* *Phys. Rev.*, 115:485–491, Aug 1959. (cited on pp. 94, 114, 118, and 119)

[182] J. M. Leinaas and J. Myrheim. *On the theory of identical particles.* *Il Nuovo Cimento B (1971-1996)*, 37(1):1–23, Jan 1977. (cited on pp. 96, 103, and 116)

[183] Jürg Fröhlich. *Statistics of Fields, the Yang-Baxter Equation, and the Theory of Knots and Links*, pages 71–100. Springer US, New York, NY, 1988. (cited on p. 96)

[184] Gregory Moore and Nicholas Read. Nonabelions in the fractional quantum hall effect. *Nuclear Physics B*, 360(2):362–396, 1991. (cited on p. 97)

[185] M. Dolev, M. Heiblum, V. Umansky, Ady Stern, and D. Mahalu. Observation of a quarter of an electron charge at the $\nu = 5/2$ quantum hall state. *Nature*, 452(7189):829–834, Apr 2008. (cited on p. 97)

[186] R. L. Willett, C. Nayak, K. Shtengel, L. N. Pfeiffer, and K. W. West. Magnetic-field-tuned aharonov-bohm oscillations and evidence for non-abelian anyons at $\nu = 5/2$. *Phys. Rev. Lett.*, 111:186401, Oct 2013. (cited on p. 97)

[187] N. Read and E. Rezayi. Beyond paired quantum hall states: Parafermions and incompressible states in the first excited landau level. *Phys. Rev. B*, 59:8084–8092, Mar 1999. (cited on p. 98)

[188] E. H. Rezayi and N. Read. Non-abelian quantized hall states of electrons at filling factors 12/5 and 13/5 in the first excited landau level. *Phys. Rev. B*, 79:075306, Feb 2009. (cited on p. 98)

[189] A.Yu. Kitaev. Fault-tolerant quantum computation by anyons. *Annals of Physics*, 303(1):2–30, 2003. (cited on p. 98)

[190] Louis H Kauffman and Samuel J Lomonaco. Braiding operators are universal quantum gates. *New Journal of Physics*, 6:134–134, oct 2004. (cited on p. 98)

[191] Michael H. Freedman, Michael Larsen, and Zhenghan Wang. A modular functor which is universal¶for quantum computation. *Communications in Mathematical Physics*, 227(3):605–622, Jun 2002. (cited on p. 98)

[192] E. Macaluso and I. Carusotto. *Ring-shaped fractional quantum Hall liquids with hard-wall potentials.* Phys. Rev. A, 98:013605, Jul 2018. (cited on pp. 99, 106, 108, 109, 110, and 114)

[193] Jens Martin, Shahal Ilani, Basile Verdene, Jurgen Smet, Vladimir Umansky, Diana Mahalu, Dieter Schuh, Gerhard Abstreiter, and Amir Yacoby. *Localization of fractionally charged quasi-particles.* Science, 305(5686):980–983, 2004. (cited on pp. 99 and 103)

[194] R. de Picciotto, M. Reznikov, M. Heiblum, V. Umansky, G. Bunin, and D. Mahalu. *Direct observation of a fractional charge.* Nature, 389(6647):162–164, 1997. (cited on pp. 99, 103, and 114)

[195] R. L. Willett, L. N. Pfeiffer, and K. W. West. *Measurement of filling factor 5/2 quasiparticle interference with observation of charge e/4 and e/2 period oscillations.* Proceedings of the National Academy of Sciences, 106(22):8853–8858, 2009. (cited on pp. 99 and 103)

[196] H. Bartolomei, M. Kumar, R. Bisognin, A. Marguerite, J.-M. Berroir, E. Bocquillon, B. Plaçais, A. Cavanna, Q. Dong, U. Gennser, Y. Jin, and G. Fève. *Fractional statistics in anyon collisions.* Science, 368(6487):173–177, 2020. (cited on pp. 99 and 103)

[197] Cheng Chin, Rudolf Grimm, Paul Julienne, and Eite Tiesinga. *Feshbach resonances in ultracold gases.* Rev. Mod. Phys., 82:1225–1286, Apr 2010. (cited on pp. 100 and 111)

[198] A. J. Moerdijk, B. J. Verhaar, and A. Axelsson. Resonances in ultracold collisions of ^{6}Li, ^{7}Li, and ^{23}Na. *Phys. Rev. A*, 51:4852–4861, Jun 1995. (cited on p. 100)

[199] Nathan Gemelke, Edina Sarajlic, and Steven Chu. *Rotating few-body atomic systems in the fractional quantum Hall regime*, 2010. (cited on pp. 100, 104, and 105)

[200] M. Eric Tai, Alexander Lukin, Matthew Rispoli, Robert Schittko, Tim Menke, Dan Borgnia, Philipp M. Preiss, Fabian Grusdt, Adam M. Kaufman, and Markus Greiner. Microscopy of the interacting harper–hofstadter model in the two-body limit. *Nature*, 546(7659):519–523, Jun 2017. (cited on p. 100)

[201] M. Popp, B. Paredes, and J. I. Cirac. *Adiabatic path to fractional quantum Hall states of a few bosonic atoms.* Phys. Rev. A, 70:053612, Nov 2004. (cited on p. 100)

[202] Anders S. Sørensen, Eugene Demler, and Mikhail D. Lukin. *Fractional Quantum Hall States of Atoms in Optical Lattices.* Phys. Rev. Lett., 94:086803, Mar 2005. (cited on p. 100)

[203] N. Regnault and B. Andrei Bernevig. *Fractional Chern insulator.* Phys. Rev. X, 1:021014, Dec 2011. (cited on p. 100)

[204] Fabian Grusdt, Fabian Letscher, Mohammad Hafezi, and Michael Fleischhauer. *Topological growing of Laughlin states in synthetic gauge fields.* Phys. Rev. Lett., 113:155301, Oct 2014. (cited on p. 100)

[205] L Palm, F Grusdt, and P M Preiss. *Skyrmion ground states of rapidly rotating few-fermion systems.* New Journal of Physics, 22(8):083037, aug 2020. (cited on p. 100)

[206] Bárbara Andrade, Valentin Kasper, Maciej Lewenstein, Christof Weitenberg, and Tobias Graß. *Preparation of the 1/2-Laughlin state with atoms in a rotating trap*, 2020. (cited on p. 100)

[207] Ningyuan Jia, Nathan Schine, Alexandros Georgakopoulos, Albert Ryou, Logan W. Clark, Ariel Sommer, and Jonathan Simon. A strongly interacting polaritonic quantum dot. *Nature Physics*, 14(6):550–554, Jun 2018. (cited on p. 100)

[208] P. Roushan, C. Neill, A. Megrant, Y. Chen, R. Babbush, R. Barends, B. Campbell, Z. Chen, B. Chiaro, A. Dunsworth, A. Fowler, E. Jeffrey, J. Kelly, E. Lucero, J. Mutus, P. J. J. O'Malley, M. Neeley, C. Quintana, D. Sank, A. Vainsencher, J. Wenner, T. White, E. Kapit, H. Neven, and J. Martinis. *Chiral ground-state currents of interacting photons in a synthetic magnetic field.* Nature Physics, 13(2):146–151, 2017. (cited on p. 100)

[209] H. A. Gersch and G. C. Knollman. Quantum cell model for bosons. *Phys. Rev.*, 129:959–967, Jan 1963. (cited on p. 100)

[210] B. Paredes, P. Fedichev, J. I. Cirac, and P. Zoller. $\frac{1}{2}$-anyons in small atomic Bose-Einstein condensates. Phys. Rev. Lett., 87:010402, Jun 2001. (cited on p. 101)

[211] R.O. Umucalılar and I. Carusotto. Many-body braiding phases in a rotating strongly correlated photon gas. Physics Letters A, 377(34):2074 – 2078, 2013. (cited on p. 101)

[212] Nigel R. Cooper and Steven H. Simon. Signatures of fractional exclusion statistics in the spectroscopy of quantum Hall droplets. Phys. Rev. Lett., 114:106802, Mar 2015. (cited on p. 101)

[213] R. O. Umucalılar and I. Carusotto. Generation and spectroscopic signatures of a fractional quantum Hall liquid of photons in an incoherently pumped optical cavity. Phys. Rev. A, 96:053808, Nov 2017. (cited on p. 101)

[214] R. O. Umucalılar, E. Macaluso, T. Comparin, and I. Carusotto. Time-of-flight measurements as a possible method to observe anyonic statistics. Phys. Rev. Lett., 120:230403, Jun 2018. (cited on p. 101)

[215] E. Macaluso, T. Comparin, L. Mazza, and I. Carusotto. Fusion channels of non-Abelian anyons from angular-momentum and density-profile measurements. Phys. Rev. Lett., 123:266801, Dec 2019. (cited on p. 101)

[216] E. Macaluso, T. Comparin, R. O. Umucalılar, M. Gerster, S. Montangero, M. Rizzi, and I. Carusotto. Charge and statistics of lattice quasiholes from density measurements: A tree tensor network study. Phys. Rev. Research, 2:013145, 2020. (cited on pp. 101 and 114)

[217] A. Elben, B. Vermersch, C. F. Roos, and P. Zoller. Statistical correlations between locally randomized measurements: A toolbox for probing entanglement in many-body quantum states. Phys. Rev. A, 99:052323, 2019. (cited on p. 101)

[218] M. O. Goerbig. Quantum Hall effects, 2009. (cited on pp. 103, 104, and 106)

[219] Frank Wilczek. Quantum mechanics of fractional-spin particles. Phys. Rev. Lett., 49:957–959, Oct 1982. (cited on pp. 103 and 116)

[220] B. I. Halperin. Statistics of quasiparticles and the hierarchy of fractional quantized Hall states. Phys. Rev. Lett., 52:1583–1586, Apr 1984. (cited on pp. 103 and 116)

[221] Daniel Arovas, J. R. Schrieffer, and Frank Wilczek. Fractional statistics and the quantum Hall effect. Phys. Rev. Lett., 53:722–723, Aug 1984. (cited on pp. 103 and 116)

[222] Yong-Shi Wu. General theory for quantum statistics in two dimensions. Phys. Rev. Lett., 52:2103–2106, Jun 1984. (cited on pp. 103 and 116)

[223] Yong-Shi Wu. Multiparticle quantum mechanics obeying fractional statistics. Phys. Rev. Lett., 53:111–114, Jul 1984. (cited on pp. 103, 114, 116, 117, and 127)

[224] V. Mourik, K. Zuo, S. M. Frolov, S. R. Plissard, E. P. A. M. Bakkers, and L. P. Kouwenhoven. Signatures of Majorana fermions in hybrid superconductor-semiconductor nanowire devices. Science, 336(6084):1003–1007, 2012. (cited on p. 103)

[225] Iacopo Carusotto, Andrew A. Houck, Alicia J. Kollár, Pedram Roushan, David I. Schuster, and Jonathan Simon. Photonic materials in circuit quantum electrodynamics. Nature Physics, 16(3):268–279, 2020. (cited on p. 103)

[226] Jean Dalibard. Introduction to the physics of artificial gauge fields. arXiv e-prints, page arXiv:1504.05520, Apr 2015. (cited on pp. 103, 105, and 113)

[227] N. R. Cooper. Rapidly rotating atomic gases. Advances in Physics, 57(6):539–616, 2008. (cited on pp. 104 and 113)

[228] Pietro Massignan, Matteo Zaccanti, and Georg M Bruun. Polarons, dressed molecules and itinerant ferromagnetism in ultracold Fermi gases. Reports on Progress in Physics, 77(3):034401, feb 2014. (cited on p. 104)

[229] Ming-Guang Hu, Michael J. Van de Graaff, Dhruv Kedar, John P. Corson, Eric A. Cornell, and Deborah S. Jin. *Bose polarons in the strongly interacting regime*. *Phys. Rev. Lett.*, 117:055301, Jul 2016. (cited on p. 104)

[230] Nils B. Jørgensen, Lars Wacker, Kristoffer T. Skalmstang, Meera M. Parish, Jesper Levinsen, Rasmus S. Christensen, Georg M. Bruun, and Jan J. Arlt. *Observation of attractive and repulsive polarons in a Bose-Einstein condensate*. *Phys. Rev. Lett.*, 117:055302, Jul 2016. (cited on p. 104)

[231] Yuhe Zhang, G. J. Sreejith, N. D. Gemelke, and J. K. Jain. *Fractional angular momentum in cold-atom systems*. *Phys. Rev. Lett.*, 113:160404, Oct 2014. (cited on pp. 104, 106, and 108)

[232] Yuhe Zhang, G. J. Sreejith, and J. K. Jain. *Creating and manipulating non-Abelian anyons in cold atom systems using auxiliary bosons*. *Phys. Rev. B*, 92:075116, Aug 2015. (cited on pp. 104, 106, and 127)

[233] Douglas Lundholm and Nicolas Rougerie. *Emergence of fractional statistics for tracer particles in a Laughlin liquid*. *Phys. Rev. Lett.*, 116:170401, Apr 2016. (cited on pp. 104 and 106)

[234] Tobias Graß, Bruno Juliá-Díaz, Niccolò Baldelli, Utso Bhattacharya, and Maciej Lewenstein. *Fractional angular momentum and anyon statistics of impurities in Laughlin liquids*. *Physical Review Letters*, 125:136801, 2020. (cited on p. 104)

[235] F. Grusdt, N. Y. Yao, D. Abanin, M. Fleischhauer, and E. Demler. *Interferometric measurements of many-body topological invariants using mobile impurities*. *Nature Communications*, 7(1):11994, 2016. (cited on pp. 104 and 106)

[236] E. Yakaboylu and M. Lemeshko. *Anyonic statistics of quantum impurities in two dimensions*. *Phys. Rev. B*, 98:045402, Jul 2018. (cited on pp. 104 and 106)

[237] Enderalp Yakaboylu, Areg Ghazaryan, Douglas Lundholm, Nicolas Rougerie, Mikhail Lemeshko, and Robert Seiringer. *A quantum impurity model for anyons*, 2019. (cited on pp. 104 and 106)

[238] A. Camacho-Guardian, N. Goldman, P. Massignan, and G. M. Bruun. *Dropping an impurity into a Chern insulator: A polaron view on topological matter*. *Phys. Rev. B*, 99:081105, Feb 2019. (cited on pp. 104 and 106)

[239] Siddhardh C. Morampudi, Ari M. Turner, Frank Pollmann, and Frank Wilczek. *Statistics of fractionalized excitations through threshold spectroscopy*. *Phys. Rev. Lett.*, 118:227201, May 2017. (cited on p. 104)

[240] M. Born and R. Oppenheimer. *Zur quantentheorie der molekeln*. *Annalen der Physik*, 389(20):457–484, 1927. (cited on pp. 104, 106, and 127)

[241] Arne Scherrer, Federica Agostini, Daniel Sebastiani, E. K. U. Gross, and Rodolphe Vuilleumier. *On the mass of atoms in molecules: Beyond the Born-Oppenheimer approximation*. *Phys. Rev. X*, 7:031035, Aug 2017. (cited on pp. 104, 108, 127, 143, and 144)

[242] Alexander L Fetter and Anatoly A Svidzinsky. *Vortices in a trapped dilute Bose-Einstein condensate*. *Journal of Physics: Condensed Matter*, 13(12):R135, 2001. (cited on p. 104)

[243] Raffaele Resta. *Manifestations of Berry's phase in molecules and condensed matter*. *Journal of Physics: Condensed Matter*, 12(9):R107–R143, feb 2000. (cited on pp. 104, 106, 108, and 111)

[244] E. Macaluso and I. Carusotto. *Hard-wall confinement of a fractional quantum Hall liquid*. *Phys. Rev. A*, 96:043607, Oct 2017. (cited on p. 106)

[245] C. Alden Mead. *The geometric phase in molecular systems*. *Rev. Mod. Phys.*, 64:51–85, Jan 1992. (cited on pp. 106 and 111)

[246] Lincoln D Carr, David DeMille, Roman V Krems, and Jun Ye. *Cold and ultracold molecules: science, technology and applications*. *New Journal of Physics*, 11(5):055049, may 2009. (cited on pp. 111 and 127)

[247] Fabian Grusdt, Fabian Letscher, Mohammad Hafezi, and Michael Fleischhauer. *Topological growing of Laughlin states in synthetic gauge fields*. Phys. Rev. Lett., 113:155301, Oct 2014. (cited on p. 114)

[248] Shovan Dutta and Erich J Mueller. *Coherent generation of photonic fractional quantum Hall states in a cavity and the search for anyonic quasiparticles*. Physical Review A, 97(3):033825, 2018. (cited on p. 114)

[249] C. R. Hagen. *Aharonov-Bohm scattering amplitude*. Phys. Rev. D, 41:2015–2017, Mar 1990. (cited on p. 117)

[250] Didier Caenepeel and Richard MacKenzie. *Parity violation, anyon scattering, and the mean field approximation*. Phys. Rev. D, 50:5418–5424, Oct 1994. (cited on p. 117)

[251] I. Richard Lapidus. *Quantum-mechanical scattering in two dimensions*. American Journal of Physics, 50(1):45–47, 1982. (cited on p. 117)

[252] Sadhan K. Adhikari. *Quantum scattering in two dimensions*. American Journal of Physics, 54(4):362–367, 1986. (cited on p. 117)

[253] Charles M. Sommerfield and Hisakazu Minakata. *Aharonov-Bohm and Coulomb scattering near the forward direction*. arXiv e-prints, pages hep–th/0006092, June 2000. (cited on p. 120)

[254] T Lahaye, C Menotti, L Santos, M Lewenstein, and T Pfau. *The physics of dipolar bosonic quantum gases*. Reports on Progress in Physics, 72(12):126401, nov 2009. (cited on p. 120)

[255] Akira Suzuki, M. K. Srivastava, R. K. Bhaduri, and J. Law. *Scattering of anyons with hard-disk repulsion and the second virial coefficient*. Phys. Rev. B, 44:10731–10735, Nov 1991. (cited on pp. 120 and 121)

[256] B. V. Noumerov. *A method of extrapolation of perturbations*. Monthly Notices of the Royal Astronomical Society, 84(8):592–602, 06 1924. (cited on p. 120)

[257] B. Olmos, W. Li, S. Hofferberth, and I. Lesanovsky. *Amplifying single impurities immersed in a gas of ultracold atoms*. Phys. Rev. A, 84:041607, Oct 2011. (cited on p. 126)

[258] Niels Kjærgaard, Angela S Mellish, and Andrew C Wilson. *Differential scattering measurements from a collider for ultracold atoms*. New Journal of Physics, 6:146–146, oct 2004. (cited on p. 126)

[259] J. L. Yarnell, G. P. Arnold, P. J. Bendt, and E. C. Kerr. *Excitations in liquid helium: neutron scattering measurements*. Phys. Rev., 113:1379–1386, Mar 1959. (cited on p. 126)

[260] L. Chomaz, S. Baier, D. Petter, M. J. Mark, F. Wächtler, L. Santos, and F. Ferlaino. *Quantum-fluctuation-driven crossover from a dilute Bose-Einstein condensate to a macro-droplet in a dipolar quantum fluid*. Phys. Rev. X, 6:041039, Nov 2016. (cited on p. 127)

[261] J Deiglmayr, M Aymar, R Wester, M Weidemüller, and O Dulieu. *Calculations of static dipole polarizabilities of alkali dimers: prospects for alignment of ultracold molecules*. The Journal of chemical physics, 129(6):064309–064309, 2008. (cited on p. 127)

[262] Tetsu Takekoshi, Lukas Reichsöllner, Andreas Schindewolf, Jeremy M. Hutson, C. Ruth Le Sueur, Olivier Dulieu, Francesca Ferlaino, Rudolf Grimm, and Hanns-Christoph Nägerl. *Ultracold dense samples of dipolar RbCs molecules in the rovibrational and hyperfine ground state*. Phys. Rev. Lett., 113:205301, Nov 2014. (cited on p. 127)

[263] Jee Woo Park, Sebastian A. Will, and Martin W. Zwierlein. *Ultracold dipolar gas of fermionic $^{23}Na^{40}K$ molecules in their absolute ground state*. Phys. Rev. Lett., 114:205302, May 2015. (cited on p. 127)

[264] Kai K. Voges, Philipp Gersema, Mara Meyer zum Alten Borgloh, Torben A. Schulze, Torsten Hartmann, Alessandro Zenesini, and Silke Ospelkaus. *Ultracold gas of bosonic $^{23}Na^{39}K$ ground-state molecules*. Phys. Rev. Lett., 125:083401, Aug 2020. (cited on p. 127)

[265] Timur M. Rvachov, Hyungmok Son, Ariel T. Sommer, Sepehr Ebadi, Juliana J. Park, Martin W. Zwierlein, Wolfgang Ketterle, and Alan O. Jamison. *Long-lived ultracold molecules with electric and magnetic dipole moments.* Phys. Rev. Lett., 119:143001, Oct 2017. (cited on p. 127)

[266] Mingyang Guo, Bing Zhu, Bo Lu, Xin Ye, Fudong Wang, Romain Vexiau, Nadia Bouloufa-Maafa, Goulven Quéméner, Olivier Dulieu, and Dajun Wang. *Creation of an ultracold gas of ground-state dipolar ^{23}Na^{87}Rb molecules.* Phys. Rev. Lett., 116:205303, May 2016. (cited on p. 127)

[267] J. Deiglmayr, A. Grochola, M. Repp, K. Mörtlbauer, C. Glück, J. Lange, O. Dulieu, R. Wester, and M. Weidemüller. *Formation of ultracold polar molecules in the rovibrational ground state. Phys. Rev. Lett.*, 101:133004, Sep 2008. (cited on p. 127)

[268] Sylvain Ravets, Patrick Knüppel, Stefan Faelt, Ovidiu Cotlet, Martin Kroner, Werner Wegscheider, and Atac Imamoglu. *Polaron polaritons in the integer and fractional quantum Hall regimes. Phys. Rev. Lett.*, 120:057401, Jan 2018. (cited on p. 127)

[269] Ovidiu Cotleţ, Falko Pientka, Richard Schmidt, Gergely Zarand, Eugene Demler, and Atac Imamoglu. *Transport of neutral optical excitations using electric fields. Phys. Rev. X*, 9:041019, Oct 2019. (cited on p. 127)

[270] Parsa Bonderson, Victor Gurarie, and Chetan Nayak. *Plasma analogy and non-Abelian statistics for Ising-type quantum Hall states. Phys. Rev. B*, 83:075303, Feb 2011. (cited on p. 127)

[271] Sebabrata Mukherjee and Mikael C. Rechtsman. Observation of floquet solitons in a topological bandgap. *Science*, 368(6493):856–859, 2020. (cited on p. 130)

[272] N. Pernet, P. St-Jean, D. D. Solnyshkov, G. Malpuech, N. Carlon Zambon, B. Real, O. Jamadi, A. Lemaître, M. Morassi, L. Le Gratiet, T. Baptiste, A. Harouri, I. Sagnes, A. Amo, S. Ravets, and J. Bloch. Topological gap solitons in a 1d non-hermitian lattice, 2021. (cited on p. 130)

[273] Ramy El-Ganainy, Konstantinos G. Makris, Mercedeh Khajavikhan, Ziad H. Musslimani, Stefan Rotter, and Demetrios N. Christodoulides. Non-hermitian physics and pt symmetry. *Nature Physics*, 14(1):11–19, Jan 2018. (cited on p. 130)

[274] Ş K. Özdemir, S. Rotter, F. Nori, and L. Yang. Parity–time symmetry and exceptional points in photonics. *Nature Materials*, 18(8):783–798, Aug 2019. (cited on p. 130)